Study of the stellar and cluster populations and identification of X-ray sources in the central regions of the Small Magellanic Cloud

Strantzalis Achilles

Department of Physics, Section of Astrophysics,
Astronomy and Mechanics
National and Kapodistrian University of Athens
Greece
March 2021

Ευχαριστίες

Η διατριβή αυτή εκπονήθηκε στον Τομέα Αστροφυσικής, Αστρονομίας και Μηχανικής του Τμήματος Φυσικής του Εθνικού και Καποδιστριακού Πανεπιστημίου Αθηνών στα πλαίσια της απόκτησης διδακτορικού διπλώματος και επικεντρώνεται στο Μικρό Νέφους του Μαγγελάνου. Πραγματεύεται την μελέτη αστρικών πληθυσμών και αστρικών σμηνών στην κεντρική περιοχή του γαλαξία αυτού.

Φτάνοντας στο τέλος αυτής της προσπάθειας θα ήθελα να εκφράσω την ευγνωμοσύνη μου σε όλους όσους συνέβαλαν σε αυτή τη διατριβή, η οποία δεν θα μπορούσε να ολοκληρωθεί χωρίς την υποστήριξη και την ενθάρρυνσή τους.

Θα ήθελα αρχικά να ευχαριστήσω τα μέλη της Επταμελούς Εξεταστικής Επιτροπής, Καθηγητή Απόστολο Μαστιχιάδη, Καθηγητή Βασίλη Χαρμανδάρη, Αν.Καθηγητή Θεοχάρη Αποστολάτο, Επίκ. Καθηγητή Στέλιο Καζαντζίδη, και Επικ. Καθηγήτρια Καλλιόπη Δασύρα για τις επιστημονικές παρατηρήσεις και τα σχόλιά τους.

Θα ήθελα να ευχαριστήσω τους κο Νικόλαο Ρέσκο και κα Στέλλα Τσιλιά, για την συνεργασία μας, στα πλάισια της προπτυχιακής τους εργασίας, που με βοήθησαν εκληρώσω, να μελετήσω και να κατανοήσω ανοιχτά θέματα του διδακτορικού.

Επίσης, θα ήθελα να ευχαριστήσω τον κο Μιχάλη Παπαχρήστου και την κα Γωγώ Λουκαΐδου, που με την συνύπαρξή μας στο ίδιο γραφείο όλα αυτά τα χρόνια, οι συζητήσεις και οι εύστοχες παρατηρήσεις και οι ανταλλαγές επιστημονικών απόψεων στήριξαν την μελέτη μου. Την δεσποινίδα Σοφία Ζαρμπούτη για τη βοήθεια και την στήριξή της σε όλη την διάρκεια της εκπόνησης του διδακτορικού σε τεχνικά θέματα.

Θα ήθελα να ευχαριστήσω επίσης την κα Σοφία Λιανού για την υποστήριξη και την συμβολή της σε μέρος της διατριβής καθώς επίσης και τους κο Δημήτρη Λαζάρου και κο Πέτρο Δραζίνο για την συνεργασία μας στα πλαίσια της μελέτης των αστρικών σμηνών στο κέντρο του γαλαξία. Τον κο Γρηγόρη Μαραβέλια για την ουσιαστική του βοήθεια για την εξοικίωσή μου με την Python και την PyRAF.

Θα ήθελα να ευχαριστήσω τον Αν. Καθηγητή Ζέζα Ανδρέα που σε όλα τα θέματα του διδακτορικού με καθοδήγησε στην εκπλήρωσή τους ή με βοήθησε στην κατανόηση τους και την κα Βάλια Αντωνίου που καθ' όλη τη διάρκεια της διατριβής με τις εύστοχες επιστημονικές παρατηρήσεις της, την ενθάρρυνσή και την υποστήριξή της, με βοήθησε στην εκπόνησης της.

Ιδιαίτερα τέλος, θα ήθελα να ευχαριστήσω την Καθηγήτρια Χατζηδημητρίου Δέσποινα, που αρχικά με εμπιστεύτηκε και στην συνέχεια με στήριξε και με καθοδήγησε σε όλη την διάρκεια της διατριβής και με ενέμπνευσε με το πάθος και την αγάπη της για την επιστημονική έρευνα, την εργασία και την Αστρονομία.

4 Μαρτίου 2021

KEY WORDS: Small Magellanic Cloud, galaxy, star formation history, star clusters, X-ray sources.

ΛΕΞΕΙΣ ΚΛΕΙΔΙΑ: Μικρό Νέφος του Μαγγελάνου, γαλαξίας, ιστορία αστρικής δημιουργίας, αστρικά σμήνη, πηγές στις ακτίνες Χ.

Abstract

The Small Magellanic Cloud (SMC) is one of the closest star forming dwarf galaxies and the second nearest dwarf irregular galaxy to our own. The SMC is gas rich and about two orders of magnitude less massive than our own galaxy. It is a member of an interacting galaxy pair (the other member being the Large Magellanic Cloud - LMC), which is believed to be infalling to (and interacting with) the Milky Way Galaxy. The aim of this study is to analyze the stellar populations in the inner denser regions of this galaxy and determine its star formation history and its star cluster population. Recent star formation is exemplified by the presence of a large population of high mass X-ray binaries (of the Be type). One of the aims of this thesis is to identify the optical counterparts of known X-ray sources in the SMC central regions and ultimately link them to star forming events.

Observations of four fields in the SMC central regions were obtained with the 6.5m Magellan Telescope at the Las Campanas Observatory in Chile on October 4th, 2004, using the Inamori Magellan Areal Camera and Spectrograph (IMACS). Each field had a 0.44^o diameter (SMC3: RA 00 56 53.6, DEC -72 17 16.7, SMC4: RA 00 49 36.1, DEC -73 16 18.0, SMC5: RA 00 53 22.4, DEC -72 26 36.2, SMC6: RA 00 53 15.0, DEC -72 42 06.8).

The images were reduced following standard procedures. After bias subtraction and flat fielding (using *IRAF*), an astrometric solution was calculated and applied to the data using the 2MASS catalog as reference. The absolute astrometric accuracy of the reference catalog is approximately 0.1 arcsec. The final mosaic image in each filter and field was constructed using *SWarp*. Point spread function (PSF) photometry was then performed, using the *DAOPHOT* package in IRAF, separately for each constituent CCD. Absolute photometric calibration was achieved by using a set of secondary standards selected from isolated relatively bright stars (B$\leq$17.5mag and I$\leq$18mag) in the Zaritsky et al. [2002] photometric catalog. This analysis yielded a photometric catalogue of 1.068.893 stars with a limiting magnitude of $B \sim 24.5$, significantly deeper by at least 2 magnitudes than any other published optical survey in the inner regions of the SMC, to date. Extensive artificial star experiments were performed in order to estimate the level of completeness of the data.

The photometric data were used to construct colour magnitude diagrams (B versus B-I) in the four fields studied. These diagrams show a well defined main sequence (MS), the subgiant (SG) and red giant (RGB) branches as well as the red clump (RC) and its vertical extension to brighter magnitudes caused by the presence of younger stellar populations in the fields studied. It is noted that in the case of field SMC4,the RC appears to be strongly elongated (and strongly inclined, essentially along the reddening vector) towards redder colours. This is caused by differential interstellar reddening, which is particularly severe in this field.

The CMDs were used to study the stellar populations present in the SMC central regions and estimate the star formation history (SFH), i.e. the star formation rate as a function of look-back time. The latter was achieved by applying the method of Dohm-Palmer et al. [1997] to MS stars. The method is more sensitive to relatively recent star formation, as the time resolution and accuracy degrade with increasing look-back time. A general conclusion of this analysis was that in all four fields star formation has been more intense recently (in the past 1Gyr). More specifically, the star formation activity seems to have been intense over the past $\sim$100Myr, decreasing rapidly over a period of few hundred Myr (look-backtime). In fields SMC4 and SMC6, there appears to have been a small enhancement in SF around 700-800 Myr ago. Beyond 1Gyr, from about 1 to about 3Gyr ago, star formation activity seems to have been lower, while it peaked again between 4 and 8 Gyr ago. Our results also confirmed that most of the stars in the SMC seem to have been formed over the past 8 Gyr. In the two fields with fainter completeness limits (fields SMC3 and SMC5) the peak in star formation rate occurred close to an age of 6-7 Gyr. The SFH beyond the 50% completeness limit is less reliable, therefore for fields 4 and 6 the displacement to somewhat different ages of the SFR peaks beyond 4 Gyr is most probably the result of increased uncertainties and biases.

To investigate probable differences in the mixture of stellar populations across the SMC central regions, we followed a different approach, which takes full account of the differences in completeness in the regions studied. The Luminosity Function (LF) of the MS

stars encodes information on the ages of the stellar populations present. Combining the LF of MS stars with the completeness of our data, we derived the completeness corrected LF (CCLF). The MS CCLF can be used for a rough comparison of the mixture of stellar populations of different ages present in the different fields. The CCLFs have been normalized to older stars, assuming that older populations are more evenly distributed spatially than younger ones. Based on this analysis, it was found that fields SMC3 and SMC5, which are located in the North-Northeast, have a significantly higher contribution from younger populations compared to the Southern-Southwestern fields SMC4 and SMC6. Younger populations therefore, seem to be more abundant in the North-NorthEasern regions, which was also noted in near-infrared studies (e.g. Rubele et al. [2018])). Our analysis confirmed that the history of star formation is not uniform along the so called SMC Bar. Therefore, the "Bar" may not be considered as a unique entity, at least in terms of stellar populations.

CMDs constructed over large regions may suffer from small but non-negligible residual systematic photometric errors due to PSF variability, different completeness levels, differential interstellar absorption and possibly line-of-sight distance variations. All these factors may result in "blurring" specific features, such as distinct main sequence turnoffs, in CMDs constructed over extended areas. In order to overcome these limitations, we focused our study on smaller regions with optimal sizes of about 1.1 arcmin in radius. Regions of this size contain enough stars to allow for detection of stellar evolutionary features in the CMD, and at the same time they are small enough to be less influenced by the previously mentioned systematic effects. We found that in a few regions (favoured by low dust absorption) there are clear indications of distinct MS turnoffs (MSTOs), at 2.7 and 4 Gyr ago. This confirms beyond doubt that SF has not been continuous over this period and that intense SF activity has been followed by periods of low SF. This may be secular, or connected to the SMC-LMC interaction.

Apart from distinct turnoffs in intermediate ages, we also noted the existence of a distinct turnoff around 56-120Myr old. Enhanced SF for this period was also reported by Harris and Zaritsky [2004], Rubele et al. [2015] and Auchettl et al. [2019] who showed that a large fraction of the supernova remnants in the SMC indicated a burst of star formation between 50 and 200 Myr ago. We have investigated the kinematic behaviour of this population using proper motion measurements from Gaia DR2. It was found that the 56-120Myr stars are kinematically distinct from very young stars that still lie on the zero-age main sequence (at least up to the saturation limit of the IMACS data). This is a tentative result that needs to be further investigated using the new Gaia EDR3 data and it alludes to the presence of distinct substructures proposed by Murray et al. [2019] who also found that non-rotational motions are prevalent throughout the SMC. A first analysis of the EDR3 data have shown that significant systematic errors were present in the DR2 data, that probably created false kinematic trends.

Star clusters are often considered as the building blocks of galactic disks, as star formation is generally clustered. The identification of star clusters (mostly small clusters) in the SMC is an ongoing endeavour. It is only relatively recently that machine learning and data mining methods and techniques have been employed to detect star clusters in the Magellanic Clouds. Our data provide a unique opportunity to investigate the validity of these identifications and classifications and have superior spatial resolution to most data used to date to search for star clusters. Applying criteria based on CMDs corrected for the field contribution, number density profiles and image inspection, we examined all known clusters and candidates in our fileds. We could only confirm about 70% of the objects classified as clusters in the most recent compilation of Bica et al. [2020]. Most of the non-confirmed objects are artifacts, caused by the inferior spatial resolution of some of the older surveys. We also applied the well-known data clustering algorithm, "Density-based Spatial Clustering of Applications with Noise" (DBSCAN), to both the IMACS data and to Gaia DR2 data. DBSCAN is a non-parametric algorithm based on density.The results from the application of DBSCAN confirmed the classification resulting from the use of the three criteria described above. The combined use of the two methods is a very useful tool for the discovery and verification of star clusters in resolved galaxies.

The last part of the thesis concerns the optical identification of X-ray sources that have been discovered in the direction of the SMC central regions. To identify candidate high mass X-ray binaries, we cross-correlated the most recent X-ray source catalogue in

the SMC central regions Antoniou et al. [2019] with the IMACS photometric catalogue. In order to correctly interpret the results of the cross-correlation, we calculated statistical tables of chance coincidence in different regions of the CMD: the CMD was divided in colour-magnitude cells. For each cell, we calculated the "chance coincidence", i.e. the probability to detect one or more optical matches (inside the specified cell) to a X-ray source, within a search radius determined by the positional uncertainty. The resulting chance coincidence probabilities in the various CMD cells for different search radii were extracted. As expected, the chance coincidence probability is higher for regions of the CMD with high stellar density, and increases with increasing search radius. We found a total of 9 new candidate high mass X-ray binaries of the Be type, within a 2 sigma search radius. Optical spectroscopy is needed to confirm these identifications.

Περίληψη

Εισαγωγή

Η μελέτη αυτή επικεντρώνεται στο Μικρό Νέφος του Μαγγελάνου (Small Magellanic Cloud, SMC), που είναι ένας κοντινός, πλούσιος σε αέριο γαλαξίας, ο οποίος αλληλεπιδρά τόσο με το Μεγάλο Νέφος του Μαγγελάνου (Large Magellanic Cloud, LMC), όσο και με τον δικό μας Γαλαξία. Εξαιτίας της μικρής του μάζας, των ενδογαλαξιακών αλληλεπιδράσεων τόσο με το Μεγάλο Νέφος του Μαγγελάνου όσο και με τον Γαλαξία μας (Besla et al. 2016, Hammer et al. 2015,Kallivayalil et al. 2013) καθώς και της περίπλοκης γεωμετρίας του (Hatzidimitriou et al. 1993, Subramanian and Subramaniam 2015, Ripepi et al. 2017) παρουσιάζει ιδιαίτερο ενδιαφέρον τόσο ως προς την ιστορία της αστρικής δημιουργίας σε γαλαξιακή κλίμακα, όσο και ως προς τον πληθυσμό των αστρικών σμηνών που τον αποτελούν.

Έχουν πραγματοποιηθεί αρκετές μελέτες για την ιστορία της αστρικής δημιουργίας του SMC (π.χ. Harris and Zaritsky 2004, Sabbi et al. 2009, Cignoni et al. 2012, Rubele et al. 2015, Rubele et al. 2018 κλπ) χρησιμοποιώντας τόσο επίγεια τηλεσκόπια όσο και δεδομένα από το Hubble Space Telescope (HST), καμία όμως από αυτές δεν έγινε με δεδομένα που έχουν μεγάλη χωρική ανάλυση και ταυτόχρονα μεγάλο εύρος πεδίου. Μέσα από τα αποτελέσματα των μελετών φαίνεται ότι το SMC έχει έντονη αστρική δημιουργία ακόμα και στο πρόσφατο παρελθόν. Επίσης, το SMC χαρακτηρίζεται από πλήθος αστρικών σμηνών και έχουν πραγματοποιηθεί μελέτες τόσο ώς προς την ταξινόμησή τους (Bica et al. 2008, Bitsakis et al. [2018], Bica et al. 2020) όσο και την ιστορία δημιουργίας τους (Nayak et al. 2018). Παρ' όλα αυτά η ανίχνευση και ταξινόμηση μικρών αστρικών σμηνών στην κεντρική περιοχή του SMC παραμένει ανοιχτό πρόβλημα εξαιτίας της υψηλής πυκνότητας του πεδίου.

Τα δεδομένα

Για την μελέτη του SMC χρησιμοποιήθηκαν φωτομετρικές παρατηρήσεις που ελήφθησαν με το τηλεσκόπιο Magellan 6.5m στο Αστεροσκοπείο Las Campanas στην Χιλή, με την κάμερα IMACS, μέσω τεσσάρων διαφορετικών οπτικών φίλτρων (B, V, R, I), καλύπτοντας τέσσερα πεδία διαμέτρου 0.44^o το καθένα, στην κεντρική περιοχή του SMC (SMC3: RA 00:56:53.6, DEC -72:17:16.7, SMC4: RA 00:49:36.1, DEC -73:16:18.0, SMC5: RA 00:53:22.4, DEC -72:26:36.2, SMC6: RA 00:53:15.0, DEC -72:42:06.8). Η θέση των τεσσάρων πεδίων στο SMC φαίνεται στο σχήμα. 9. Σκοπός αυτής της διατριβής είναι (i) η συστηματική μελέτη των αστρικών πληθυσμών και του ρυθμού αστρικής δημιουργίας σαν συνάρτηση του χρόνου, στις πιο κεντρικές και επομένως μεγάλης πυκνότητας περιοχές του γαλαξία, όπου άλλες μελέτες επιδεικνύουν σημαντικές ελλείψεις (είτε ως προς την επιφανειακή κάλυψη, είτε ως προς την ποιότητα/βάθος των φωτομετρικών δεδομένων), (ii) η σύγκριση της ηλικιακής κατανομής των αστρικών σμηνών με τους αστρικούς πληθυσμούς πεδίου (ο στόχος αυτός προαπαιτεί αναθεώρηση των καταλόγων αστρικών σμηνών στις περιοχές ενδιαφέροντος, με μεθόδους που περιλαμβάνουν τεχνικές Machine Learning) και (iii) η ταυτοποίηση και ο χαρακτηρισμός πηγών ακτίνων X (που έχουν ανακαλυφθεί με το Chandra Deep Survey) με οπτικές πηγές.

Επεξεργασία και ανάλυση δεδομένων

Αφαίρεση BIAS-"Επιπεδοποίηση"-Αστρομετρία

Αρχικά λοιπόν, αφαιρέθηκε ο ηλεκτρονικός θόρυβος (BIAS) της CCD κάμερας, έγινε διόρθωση για τη σχετική ευαισθησία των pixels ("επιπεδοποίηση", FLAT FIELDING) και συντέθηκε το τελικό "μωσαϊκό" όλων των τμημάτων των εικόνων (frames), μετά από κατάλληλη επεξεργασία και αστρομετρική βαθμονόμηση, με την χρήση καταλόγων από το 2MASS. Για όλες τις παραπάνω διεργασίες χρησιμοποιήθηκε το πακέτο επεξεργασίας εικόνων IRAF. Η διαδικασία αυτή πραγματοποιήθηκε και για τα τέσσερα διαφορετικά φίλτρα B, V, R, I. Η χωρική διακριτική ικανότητα ήταν εξαιρετική, χάρη στη χρήση τεχνικών προσαρμοστικής οπτικής στη διάρκεια των παρατηρήσεων.

Φωτομετρία

Στην συνέχεια αναπτύχθηκε και εφαρμόστηκε αλγόριθμος φωτομετρικής ανάλυσης, που συνδυάζει το πακέτο επεξεργασίας εικόνων IRAF, με τη γλώσσα προγραμματισμού Python (PyRAF). Η φωτομετρία έγινε με την χρήση της συνάρτησης Point Spread Function (PSF). Με τον αλγόριθμο αυτό εξήχθησαν όλες οι βασικές οπτικές παράμετροι για κάθε άστρο στα φίλτρα B, R, V, I. Αναγωγή της φωτομετρίας στο σύστημα BVRI έγινε μόνο για τις μετρήσεις στα φίλτρα B, I, με την χρήση δευτερογενών άστρων βαθμονόμησης (secondary standards) από τον φωτομετρικό κατάλογο των Harris and Zaritsky [2004]. Λόγω της χωρικής μεταβλητότητας του υποβάθρου και της συνάρτησης PSF, ο ορισμός των φωτομετρικών παραμέτρων και η αναγωγή της φωτομετρίας έγιναν για κάθε CCD, κάθε πεδίου, ξεχωριστά. Πρέπει να αναφερθεί ότι τα μεγέθη στο φίλτρο R δεν μπόρεσαν να βαθμονομηθούν γιατί τα δευτερογενή άστρα που χρημοποιήθηκαν από τον κατάλογο Harris and Zaritsky [2004] δεν είχαν μεγέθη στο συγκεκριμένο φιλτρο. Παρόλο που υπάρχουν άλλοι κατάλογοι (βλ. Massey [2002]), αυτοί περιλαμβάνουν κυρίως λαμπρά άστρα, που εμφανίζουν "κορεσμένα" είδωλα στις εικόνες του IMACS και δεν μπορούν να χρησιμοποιηθούν.

Από την ανάλυση των αποτελεσμάτων της φωτομετρίας στο φίλτρο V διαπιστώθηκε ότι έπρεπε να το εξαιρέσουμε από την μελέτη μας, καθώς υπήρχαν συστηματικά σφάλματα που σχετίζονταν με την χρήση της μεθόδου adaptive optics κατά την διάρκεια της παρατήρησης. Παράδειγμα αυτού του συστηματικού σφάλματος μπορούμε να δούμε στο σχήμα 18 όπου παρατηρούμε μια συστηματική μετατόπιση του δείκτη χρώματος σε συγκεκριμένες περιοχές του πεδίου παρατήρησης. Οπότε, αν και το πεδίο V θα μας έδινε την δυνατότητα να ανιχνεύσουμε και να μελετήσουμε πιο αμυδρά άστρα, επειδή είχε τον μεγαλύτερο χρόνο έκθεσης στην παρατήρηση, δεν μπορέσαμε τελικά να το χρησιμοποιήσουμε. Επισης, αναφέρουμε εδώ ότι είχαν γίνει παρατηρήσεις και σε ένα πέμπτο πεδίο (SMC7). Οι μετρήσεις αυτές δεν χρησιμοποιήθηκαν καθόλου γιατί έγιναν στην διάρκεια του λυκαυγούς, με αποτέλεσμα να έχουν υπόβαθρο μεταβλητής και υψηλής εντασης, που οδηγεί σε μεγάλα σφάλματα στην φωτομετρία. Η κατανομή σφαλματων αυτών φαίνεται στο σχήμα 19.

Εκτίμηση της πληρότητας (completeness)

Ο τελικός κατάλογος περιλαμβάνει βαθμονομημένα μεγέθη B και I και τα σφάλματα αυτών για 1.068.893 άστρα, με οριακό μέγεθος περίπου 24mag. Για να ελεγχθεί η αξιοπιστία και η πληρότητα (completeness) της φωτομετρίας ως προς το μέγεθος, ακολουθήσαμε τη μέθοδο της προσθήκης "τεχνητών άστρων" στις εικόνες (artificial star experiments). Το πλήθος των τεχνητών άστρων είναι $\sim 8\%$ του αρχικού πληθυσμού των άστρων της περιοχής που μελετάμε. Τα τεχνητά άστρα έχουν ομοιόμορφη χωρική κατανομή και κατανομή μεγεθών. Στην συνέχεια εξάγουμε τη φωτομετρία με την ίδια διαδικασία που περιγράφηκε προηγουμένως. Συγκρίνουμε τον αριθμό των τεχνητών άστρων που ανακτήθηκαν με τον αρχικό τους αριθμό, για διαφορετικές τιμές αστρικών μεγεθών. Για να μπορέσουμε να μελετήσουμε καλύτερα την χωρική μεταβολή του ποσοστού πληρότητας, η μελέτη πραγματοποιήθηκε για επιμέρους τμήματα των CCDs. Τις μεσαίες CCDs (που είναι μεγαλύτερες) τις χωρίσαμε σε 8 ισοεμβαδικά τμήματα και τις ακραίες (που είναι μικρότερες) σε 4. Για να έχουμε μεγαλύτερο στατιστικό δείγμα επαναλάβαμε την παραπάνω διαδικασία 10 φορές σε κάθε τμήμα CCD, προσθέτοντας κάθε φορά καινούργια τεχνητά άστρα. Στην συνέχεια υπολογίσαμε σε ποιο μέγεθος (για κάθε φίλτρο) η πληρότητα είναι 50% και 20%. Η χωρική κατανομή των διαφόρων μεγεθών με πληρότητα 50% και 20% στο B φαίνεται στα σχήματα 20, 21. Από τα διαγράμματα στην εικόνα 22, προκύπτει ότι η πληρότητα είναι καλύτερη στο φίλτρο B, και στα πεδία SMC3 και SMC5. Η διαδικασία αυτή επαναλήφθηκε πολλές φορές, καθώς είναι αναγκαία η βελτίωση της ακρίβειας των υπολογιζόμενων διορθώσεων πληρότητας ανά μέγεθος, οι οποίες με την σειρά τους χρειάζονται για την ακριβέστερη εξαγωγή της ιστορίας της αστρικής δημιουργίας από τα φωτομετρικά δεδομένα (π.χ. Cole et al. 2007, εικόνες 23, 24).

Διαγράμματα δείκτη χρώματος - μεγέθους (B-I, B)

Για την μελέτη των αστρικών πληθυσμών των πεδίων κατασκευάστηκαν διαγράμματα δείκτη χρώματος-μεγέθους (B, B-I). Στα διαγράμματα αυτά (εικόνες 25, 26, 27, 28) διακρίνονται άστρα σε διαφορετικές φάσεις εξέλιξης (Κύρια Ακολουθία, κλάδος των γιγάντων, οριζόντιος

κλάδος). Οι κόκκινες γραμμές στα διαγράμματα παριστάνουν το όρια κάτω από τα οποία τα άστρα έχουν ποσοστά πληρότητας κάτω από 50% και 20% αντίστοιχα. Όπως αναφέραμε και προηγούμενως στα πεδία SMC3, SMC5 τα ποσοστά πληρότητας 50% και 20% είναι σε μεγαλύτερα μεγέθη, που σημαίνει ότι η φωτομετρία στα πεδία αυτά είναι πιο αξιόπιστη για τα πιο αμυδρά άστρα. Επίσης, αριστερά απεικονίζεται ανά διάφορα μεγέθη στο B το μέσο σφάλμα μεγέθους (είναι συνδυασμός του σφάλματος που προκύπτει από την φωτομετρία και του σφάλματος μέσης τιμής της βαθμονόμησης, μέσω της διάδοσης σφαλμάτων) και το σφάλμα χρώματος που προκύπτει από τα σφάλματα μεγεθών στο φίλτρο B και I.

Παρατηρούμε ότι το πεδίο SMC4 έχει πιο ευρεία κύρια ακολουθία (εικόνα 26), και επιμηκυμένο οριζόντιο κλάδο. Αυτό αφείλεται στο γεγονός ότι στο πεδίο SMC4 υπάρχουν περιοχές με μεγάλη μεσοαστρική απορρόφηση οπότε δημιουργούνται έντονα φαινόμενα ερύθρωσης με συνέπεια να έχουμε την ερυθρομετατόπιση του χρώματος των άστρων των συγκεκριμένων περιοχών (βλ. σχήμα 30).

Ιστορία αστρικής δημιουργίας

Για την μελέτη του ρυθμού αστρικής δημιουργίας συναρτήσει του χρόνου χρησιμοποιούμε την μέθοδο που ανέπτυξε ο Dohm-Palmer et al. [1997] για κάθε ένα από τα 4 πεδία που μελετήσαμε. Η μέθοδος εφαρμόστηκε σε άστρα της Κύριας Ακολουθίας (ΚΑ). Για τον σκοπό αυτό χωρίσαμε τα άστρα της ΚΑ σε οριζόντιες λωρίδες συγκεκριμένο εύρους του μεγέθους B. Υπόθέτουμε επίσης ότι η αρχική συνάρτηση μάζας (Initial Mass Function, IMF) που θα την χρειαστούμε στην μέθοδό μας είναι ανεξάρτητη του χρόνου και εξαρτάται μόνο από το μέγεθος και το χρώμα. Αυτή η σύμβαση γίνεται ακόμα πιο αποδεκτή δεδομένου ότι τα άστρα της ΚΑ έχουν στενό εύρος χρώματος. Επίσης, δεχόμαστε ότι τα άστρα της ΚΑ που βρίσκονται στην ίδια οριζόντια λωρίδα έχουν την ίδια IMF. Πρέπει να προσέξουμε εδώ ότι μία λωρίδα έχει άστρα ίδια μάζας αλλά διαφορετικών ηλικιών. Δηλαδή άστρα που έχουν εξελιχθεί και θα φύγουν από την ΚΑ και άστρα νεότερα ίδιας μάζας με τα προηγούμενα που θα συνεχίσουν να είναι άστρα κύριας ακολουθίας. Για να λάβουμε υπόψη την μείωση των ποσοστών πληρότητας σε αμυδρότερα άστρα διαιρούμε το πλήθος των άστρων σε μία συγκεκριμένη λωρίδα με το αντίστοιχο ποσοστό πληρότητας σε αυτό το μέγεθος. Δηλαδή αν μία λωρίδα σε ένα συγκεκριμένο μέγεθος, έχει N άστρα της ΚΑ και ποσοστό πληρότητας σε αυτό το μέγεθος 50% θεωρούμε ότι τα άστρα τελικά είναι N/0.5. Η εξέλιξη του ρυθμού αστρικής δημιουργίας συναρτήσει του χρόνου για τα 4 πεδία φαίνεται στις εικόνες 31 και 32. Έχουμε υποθέσει δύο διαφορετικές μεταλλικότητες, μία για τα τελευταία $\sim 1.2Gyr$ (Z=0.004) και μία για τα παλαιότερα άστρα (μέχρι $\sim 12Gyr$). Οι επιλογές αυτές βασίστηκαν σε σχέσεις ηλικίας μεταλλικότητας καθώς επίσης και σε μελέτες που έχουν γίνει σε αστρικούς πλυθησμούς στο SMC (Da Costa and Hatzidimitriou 1998, Kayser et al. 2007, Rubele et al. 2018. Η IMF που χρησιμποιήσαμε είναι η Salpeter (Salpeter [1955]), την οποία χρησοποίησαν στα μοντέλα τους οι Harris and Zaritsky [2004] για την μελέτη της αστρικής δημιουργίας στο SMC. Χρήση άλλων IMF δεν έχει σημαντική επίπτωση στα αποτελέσματά μας. Στα διαγράμματα 33, 34 βλέπουμε με μεγαλύτερη λεπτομέρεια τον ρυθμό αστρικής δημιουργίας για $t \leq 1.2Gyr$. Παρατηρούμε ότι για $t \leq 1.2Gyr$) παρουσιάζεται ενίσχυση του ρυθμού αστρικής δημιουργίας και στα 4 πεδία. Ο ρυθμός αυτός μειώνεται όσο πηγαίνουμε προς τα πίσω στον χρόνο. Στα πεδία SMC4 και SMC6 μετά τα 800Myr εμφανίζεται επίσης μια (μικρότερη) ενίσχυση της αστρικής δημιουργίας. Εν συνεχεία, ο ρυθμός μειώνεται από 1 έως 3Gyr ενώ στην συνέχεια παρατηρείται μία αύξηση μεταξύ $\sim 4 - 8Gyr$. Στα πεδία όπου τα ποσοστά πληρότητας είναι βέλτιστα (SMC3, SMC5), παρατηρείται ένα μέγιστο αστρικής δημιουργίας μεταξύ 6-7Gyr. Το πεδίο SMC4 είναι σε μεγαλύτερη απόσταση από εμάς σε σχέση με τα άλλα πεδία και αυτό οφείλεται στην κλήση που έχει το SMC ως προς την γραμμή παρατήρησης, παρ' όλα αυτά τα αποτελέμσατα είναι ίδια στα όρια του σφάλματος για μικρές μεταβολές στη τιμή που υιοθετούμε για το μέτρο απόστασης.

Τα αποτελέσματα που αναφέραμε πριν είναι σε γενικές γραμμές σε συμφωνία με την βιβλιογραφία. Πράγματι επεισόδιο ενίσχυσης αστρικής δημιουργίας στα $\sim 4 - 6Gyr$ προτείνεται από τους Rezaeikh et al. [2014], Weisz et al. [2013], Cignoni et al. [2012] και Noël et al. [2009]. Επίσης οι Bitsakis et al. [2018] και Nayak et al. [2018] πρότειναν αυξημένο ρυθμό αστρικής δημιουργίας τα τελευταία 100-200Myr.

Συναρτήσεις λαμπρότητας

Για τη μελέτη των αστρικών πληθυσμών χρησιμοποιήθηκαν επίσης συναρτήσεις λαμπρότητας των άστρων κύριας ακολουθίας που κατασκευάστηκαν με βαση τα διαγράμματα δείκτη χρώματος-μεγέθους, σε ένα τετραγωνικό πλέγμα υποπεριοχών (στις οποίες υποδιαιρέθηκαν τα αρχικά πεδία), που επέτρεψε την μελέτη της χωρικής κατανομής των διαφορετικών πληθυσμών.

Οι συναρτήσεις λαμπρότητας διορθώθηκαν με την χρήση των τιμών πληρότητας (completeness corrections) σε όλο το φάσμα των μεγεθών για κάθε υποπεριοχή. Έτσι προκύπτει η διορθωμένη για τη πληρότητα συνάρτηση λαμπρότητας. Στην εικόνα 37 παριστάνονται οι διορθωμένες συναρτήσεις λαμπρότητας των 4 πεδίων παρατήρησης. Οι συναρτήσεις έχουν κανονικοποιηθεί με τέτοιο τρόπο ώστε να έχουν το ίδιο πληθυσμό άστρων για B$\leq$ 21.6. Η κανονικοποίηση έγινε με το σκεπτικό ότι άστρα αυτού του μεγέθους ή αυτής της ηλικίας είναι ομοιόμορφα κατανεμημένα σε όλο τον γαλαξία, οπότε κάθε πεδίο πρέπει να περιέχει τον ίδιο αριθμό άστρων από αυτή την ηλικία και πάνω. Με βάση τις συναρτήσεις λαμπρότητας τα πεδία SMC3 και SMC5 που βρίσκονται βόρεια και βορειοανατολικά της μπάρας του γαλαξία αντίστοιχα έχουν μεγαλύτερο αριθμό νέων άστρων από τα πεδία SMC4, SMC6 που βρίσκονται νότια και νοτιοδυτικά της μπάρας.

Επίσης, χρησιμοποιώντας τις συναρτήσεις λαμπρότητας κατασκευάστηκαν χάρτες χρωματικής απεικόνισης της κλίσης της διορθωμένης συνάρτησης λαμπρότητας, που επέτρεψαν την αναγνώριση περιοχών με σημαντικές διαφοροποιήσεις ως προς τη μίξη αστρικών πληθυσμών. Η χωρική μεταβολή της κλίσης των συναρτήσεων λαμπρότητας φαίνεται στην εικόνα 39. Παρατηρούμε ότι η μίξη των αστρικών πληθυσμών διαφοροποείται κατά μήκος της μπάρας του SMC, δηλ. η αστρική δημιουργία δεν είναι ομοιόμορφη στην μπάρα.

Διακριτά γεγονότα αστρικής δημιουργίας

Συμβάντα αστρικής δημιουργίας στα 2.7 και 4 Gyr

Μελετήθηκαν τα διαγράμματα δείκτη χρώματος μεγέθους (CMD) σε δίκτυο υποπεριοχών ακτίνας 1 arcmin - αρκετά μικρών, ώστε να μην επηρεάζονται από μεταβολές της ερύθρωσης και από τη μεταβολή του PSF, και ταυτόχρονα αρκετά μεγάλων ώστε να έχουν στατιστικά σημαντικό αριθμό άστρων σε όλο το CMD. Η εξαιρετική φωτομετρία και χωρική ανάλυση επέτρεψαν, για πρώτη φορά, την ανακάλυψη διακεκριμένων συμβάντων αστρικής δημιουργίας, πριν από 2.7 και 4 Gyr, χωρίς την ανάγκη μοντελοποίησης, αλλά απευθείας από παρατήρηση των διαγραμμάτων δείκτη χρώματος μεγέθους. Τα διακριτά αυτά συμβάντα παρατηρήθηκαν σε υποπεριοχές στα πεδία SMC3 και SMC5 όπου έχουμε πολύ καλή ποιότητα της φωτομετρίας ακόμα και σε αμυδρά άστρα. Μάλιστα οι συγκεκριμένες υποπεριοχές χαρακτηρίζονται από ακόμα καλύτερη ποιότητα φωτομετρίας σε σχέση με τις υπόλοιπες υποπεριοχές του ίδου πεδίου (κάτω διάγραμμα 46). Οι διορθωμένες συναρτήσεις λαμπρότητας των υποπεριοχών έχουν ένα στενό εύρος τιμών 0.011-0.014 (πάνω διάγραμμα 46). Τα παραπάνω συνοψίζονται στο ότι οι υποπεριοχές αυτές χαρακτηρίζονται από υψηλής ποιότητας φωτομετρικά δεδομένα και παρουσιάζουν παρόμοια χαρακτηριστικά ως προς τον πλυθησμό των άστρων της ΚΑ. Η χωρική κατανομή των περιοχών αυτων παρουσιάζεται στην εικόνα 45. Συνολικά, επιβεβαιώνεται ότι το μεγαλύτερο μέρος των άστρων στο SMC δημιουργήθηκαν τα τελευταία 6-7 Gyr, και ότι η αστρική δημιουργία στον γαλαξία αυτό δεν είναι συνεχής: περίοδοι έντονης αστρικής δημιουργίας φαίνεται να ακολουθούνται από περιόδους χαμηλής αστρικής δημιουργίας. Αυτή η διακοπτόμενη δραστηριότητα μπορεί να σχετίζεται (εν μέρει τουλάχιστον) με την τροχιακή ιστορία του Μαγγελανικού συστήματος.

Περίοδος αστρικής δημιουργίας $90 Myr$

Ένα άλλο αποτέλεσμα προέκυψε από τον συνδυασμό των φωτομετρικών μας δεδομένων με την εξαιρετική αστρομετρία του δορυφόρου Gaia (Gaia Data Release 2). Κυρίως στα CMD του πεδίου SMC5 παρατηρείται σαφής διακεκριμένη ακολουθία άστρων που αντιστοιχεί σε αστρικό πληθυσμό με ηλικία περίπου 56-120 Myr (εικόνα 48. Παρόμοιος πληθυσμός εντοπίστηκε και στα άλλα πεδία (SMC3) χωρίς όμως να είναι τόσο διακριτός όσο στο πεδίο SMC5. Ενίσχυση της αστρικής δημιουργίας κατά την περίοδο 50-200 Myr έχει προταθεί και από άλλους συγγραφείς Harris and Zaritsky [2004], Rubele et al. [2015] και Auchettl et al. [2019]. Στην περίπτωση, ο

εντοπισμός του πληθυσμού είναι άμεσος, πάνω σε ένα διάγραμμα δείκτη χρώματος - μεγέθους, και δεν βασιζεται σε κάποια στατιστική ανάλυση, όπως συνέβαινε σε προγενέστερες μελέτες. Το εντυπωσιακό είναι ότι Ο πληθυσμός αυτός παρουσιάζει κινηματικό προφίλ που τον ξεχωρίζει από τα υπόλοιπα νέα άστρα στην περιοχή. Η κινηματική αυτή μελέτη έγινε με βάση δεδομένα για τις ίδιες κινήσεις και τις παραλλάξεις από το Gaia DR2. Η στατιστική σημασία των αποτελεσμάτων ελέγχθηκε με τη χρήση τεστ Kolmogorov-Smirnov. Στις δύο διευθύνσεις (ορθή αναφορά, RA και απόκλιση, DEC) η πιθανότητα οι δύο πληθυσμοί να είχαν ίδια κατανομή στην ιδία κίνηση ήταν 3.1% και 0.013% αντίστοιχα. Τα αποτελέσματα αυτής της έρευνας προετοιμάστηκαν για δημοσίευση στο MNRAS (Strantzalis et al. 2020). Τα νέα δεδομένα όμως που δημοσιεύτηκαν από το Gaia eDR3 για τα ίδια άστρα έδωσαν διαφορετικές κινηματικές παραμέτρους που μείωσαν σημαντικά τη στατιστική σημασία των παραπάνω συσχετίσεων.

Αναγνώριση και ταυτοποίηση αστρικών σμηνών

Στις κεντρικές περιοχές του SMC, η αναγνώριση αστρικών σμηνών (κυρίως μικρών) παρεμποδίζεται από την υψηλή αστρική πυκνότητα. Το πρόβλημα είναι μεγαλύτερο όταν τα δεδομένα δεν έχουν επαρκή χωρική διακριτική ικανότητα. Οι περισσότεροι πρόσφατοι κατάλογοι αστρικών σμηνών στο SMC έχουν βασιστεί κυρίως σε δεδομένα χαμηλότερης ποιότητας από τα δεδομένα που έχουμε τώρα στη διάθεσή μας (Bica et al. 2008, Bitsakis et al. 2018, Bica et al. 2020). Ο Bica et al. [2008], παρουσίασε έναν από τους μεγαλύτερους και πιο ολοκληρωμένους καταλόγους αστρικών σμηνών όλων των μεγεθών, οι Bitsakis et al. [2018] παρουσίασαν έναν κατάλογο στην ευρύτερη περιοχή του SMC που περιείχε 1319 αντικείμενα χαρακτηρισμένα ως αστρικά σμήνη, τα περισσότερα αναφερόντουσαν για πρώτη φορά. Πολύ πρόσφατα, οι Bica et al. [2020] παρουσίασαν έναν ανανεωμένο κατάλογο που κυρίως ήταν βασισμένος στους ήδη υπάρχοντες καταλόγους, και περιείχε ελάχιστα αντικείμενα από τον κατάλογο του Bitsakis et al. [2018], γιατί τα περισσότερα είχαν αποχαρακτηριστεί από αστρικά σμήνη. Η μελέτη μας βασίστηκε στην ταξινόμηση των διάφορων αντικειμένων που έχουν χαρακτηριτεί ως αστρικά σμήνη στους δύο τελευταίους καταλόγους, στα 4 πεδία που μελετήσαμε.

Ο έλεγχος έγινε με βάση συγκεκριμένα κριτήρια, όπως ακτινικά διαγράμματα επιφανειακής αριθμητικής αστρικής πυκνότητας (Radial Profiles, RD) διαγράμματα δείκτη χώματος-μεγέθους (CMD) και σύγκρισή τους με το CMD άστρων πεδίου με την χρήση του κριτηρίου Kolmogorov-Smirnov). Επίσης χρησιμοποιήσαμε ως δευτερεύον κριτήριο την εικόνα της περιοχής του σμήνους στις παρατηρήσεις μας με το Magellan Telescope, δεδομένης της καλύτερης χωρικής ανάλυσης, σε σχέση με τα δεδομένα που είχαν χρησιμοποιηθεί στις περιπσότερες περιπτώσεις για τον εντοπισμό και ταξινόμηση των αστρικών σμηνών. Πράγματι άμεσα φαίνεται από τις εικόνες ότι κάποια "αντικείμενα" που έχουν χαρακτηριστεί ως αστρικά σμήνη, δεν φαίνεται να είναι (βλ τις δύο τελευταίες περιοχές της εικόνας 53.

Όπως προαναφέρθηκε, κατασκευάσαμε το προφίλ ακτινικής κατανομής της επιφανειακής πυκνότητας κάθε περιοχής με κέντρο, το κέντρο που έδιναν οι κατάλογοι για κάθε αστρικό σμήνος. Αυτό που αναμένουμε είναι εκθετική μείωση της επιφανειακής πυκνότητας (βλ. τα 4 πάνω διαγράμματα της εικόνας 54), όμως σε κάποιες περιπτώσεις η επιφανειακή πυκνότητα παραμένει σταθερή μέσα στα πλαίσια διακυμάνσεων του υποβάθρου (βλ. τα 2 κάτω διαγράμματα της εικόνας 54). Ένα αστρικό σμήνος κατά πάσα πιθανότητα θα παρουσιάσει ένα CMD με διαφορετικά χαρακτηριστικά με το CMD του υποβάθρου γύρω του. Για να διορθώσουμε το CMD του υποψήφιου σμήνους από το υπόβαθρο, εφαρμόσαμε μίσ Μπαεσιανή μέθοδο (BEHR, Park et al. 2006). Τα τελικά διαγράμματα προέκυψαν από την σύγκριση του CMD της περιοχής του σμήνους και το CMD μιας ισοεμβαδικής περιοχής του υποβάθρου γύρω από το σμήνος. Το υπόβαθρο ορίζεται σε ένα δακτύλιο γύρω από την περιοχή του σμήνους. Για παράδειγμα στην περίπτωση του αστρικού σμήνους NGC306 (βλ. εικόνα 56), λαμβάνοντας υπόψη το ελάχιστο της τιμής που δίνει ο αλγόριθμος (κάτω δεξιά, εικόνα 56) προκύπτει ένα διάγραμμα με πλήθος άστρων πάνω στην κύρια ακολουθία. Αντίθετα στην περίπτωση του BS259 (βλ. εικόνα 59) παρατηρούμε ότι δεν υπάρχουν άστρα που παραμένουν μετά την αφαίρεση. Αυτό οφείλεται στο γεγονός ότι το CMD της περιοχής του BS259 παρουσιάζει τα ίδια χαρακτηριστικά με το υπόβαθρο γύρω από αυτή την περιοχή.

Χρησιμοποιώντας τα τρία παραπάνω κριτήρια 1) εικόνα, 2) ακτινικό προφίλ επιφανειακής πυκνότητας, 3) τα διαγράμματα CMD που προκύπτουν από την Μπαεσιανή ανάλυση, βρήκαμε

ποια από τα αντικείμενα που έχουν κατηγοριοποιηθεί σαν σμήνη στους κατάλογους δεν μπορεί να είναι πράγματι αστρικά σμήνη. Από τον κατάλογο των Bica et al. [2020], το 30% των σμηνών (που βρίσκονται στα 4 πεδία μας) αποχαρακτηρίστηκαν, ενώ το ποσοστό αυτό ήταν πολύ μεγαλύτερο για τον κατάλογο των Bitsakis et al. [2018] (με το 87% των σμηνών να έχουν απορριφθεί). Στην εικόνα 60 φαίνεται η χωρική κατανομή των σμηνών από τους 2 καταλόγους, στα 4 πεδία που μελετήσαμε, όπως ταξινομήθηκαν με τα παραπάνω κριτήρια. Επισης, μελετήσαμε τις κατανομές των άστρων ΚΑ της περιοχής του σμήνους σε σύγκριση με του υποβάθρου ως προς το μέγεθος και ως προς τον δείκτη χρώματος με την χρήση του κριτηρίου Kolmogorov-Smirnov (βλ. εικόνα 62. Στην εικόνα 63 μπορούμε να δούμε ότι για αντικείμενα που αποχαρακτηρίστηκαν από αστρικά σμήνη, η πιθανότητα η κατανομή των άστρων της ΚΑ του "σμήνους" σε σύγκριση με την κατανομή των άστρων της ΚΑ του υποβάθρου να προέρχονται από τον ίδιο πληθυσμό είναι μεγάλη.

Επιπλέον, επιχειρήθηκε ανεξάρτητη ταυτοποίηση αστρικών σμηνών τόσο από τα δικά μας δεδομένα όσο και από τα δεδομένα από τη GAIA eDR3, με την εφαρμογή του αλγόριθμου DBSCAN (Density-Based Spatial Clustering of Applications with Noise). Πρόκειται για ένα αλγόριθμο machine learning και έχει δώσει εξαιρετικά αποτελέσματα κυρίως για τα δεδομένα από την Gaia, λόγω της ομοιογένειας τους. Τα αποτελέσματα της μελέτης αυτής θα δημοσιευτούν στο MNRAS (Strantzalis et al. 2021a)

Πηγές ακτίνων X στο SMC

Τέλος, έγινε χωρική συσχέτιση μεταξύ του νέου καταλόγου πηγών ακτίνων X στη κατεύθυνση του SMC που προέκυψε από παρατηρήσεις με τον δορυφόρο *Chandra* (XVP, P.I. Andreas Zezas, Antoniou et al. [2019]), με τον κατάλογο των οπτικών πηγών που καταγράφηκαν και φωτομετρήθηκαν στα 4 πεδία που μελετήσαμε, με στόχο την ταυτοποίηση των πηγών ακτίνων X. Για κάθε πηγή για την οποία βρέθηκε οπτικό counterpart εντός του κύκλου αστρομετρικού σφάλματος, υπολογίστηκε η πιθανότητα να είναι η συσχέτιση τυχαία. Τα αποτελέσματα φαίνονται στην εικόνα 68.

Στην συνέχεια ανιχνεύθυκαν υποψήφια BeXRB για διάφορες ακτίνες εύρεσης (μία, δύο, τρεις φορές του αστρομετρικού σφάλματος της πηγής ακτίνων, (εικόνα 69) . Με αυτό τον τρόπο ταυτοποιήθηκαν (για ακτίνα έρευνας 1σ) 54 υποψήφια συστήματα BeXRB (που είναι συστήματα ακτίνων X με συνοδό αστέρα μεγάλης μάζας, και συγκεκριμένα φασματικού τύπου Be). Για ακτινα 2σ έχουμε 9 νέα υποψήφια συστήματα (δηλ. χωρίς προηγούμενη αναφορά), ενώ για ακτίνα 3σ έχουμε 70. Ένας μικρός αριθμός πηγών ακτίνων X συσχετίστηκε με γαλαξίες ($\sim 5.7\%$) με βάση τις εικόνες από το Magellan Telescope και κυρίως από το Hubble Space Telescope (εικόνα 70. Τα αποτελέσματα της μελέτης αυτης θα δημοσιευτούν στο Strantzalis et al. 2021b).

Contents

1 Introduction

1.1 General features of the Small Magellanic Cloud galaxy

The Small Magellanic Cloud (SMC) is one of the closest late type star forming dwarf galaxies and the second nearest dwarf irregular galaxy to our own, the closest being the disrupted Canis Major dwarf (Martin et al. [2004], Conn et al. [2008]). The SMC is a gas rich galaxy about two orders of magnitude less massive than our own galaxy and a member of the Magellanic Cloud interacting galaxy pair, which is believed to be infalling to (and interacting with) the Milky Way Galaxy. A detailed understanding of the star formation history, structure and evolution of the SMC has important implications about galaxy interactions, star formation (SF) in dwarf galaxies and "near field cosmology".

The distance of the SMC has been estimated by many authors using different methods. Hilditch et al. [2005] used forty eclipsing binaries of spectral types O and B and estimated a distance of $61 \pm 1 kpc$. Inno et al. [2013] used a large near infrared (NIR) data set of Cepheids and derived a similar value of $61 \pm 3 kpc$. A combination of different types of distance indicators [de Grijs and Bono, 2015], including eclipsing binaries systems, pulsating stars, stellar population tracers and star cluster properties resulted in a weighted average distance of $61.94 \pm 0.57 kpc$. In agreement with this result, Scowcroft et al. [2016] using Spitzer observations of classical Cepheids confirmed a distance of $62.0 \pm 0.3 kpc$. Based on Gaia DR2 data of RR Lyrae variables a similar distance of $59.9 \pm 2.9 kpc$ was reached by Neeley et al. [2019].

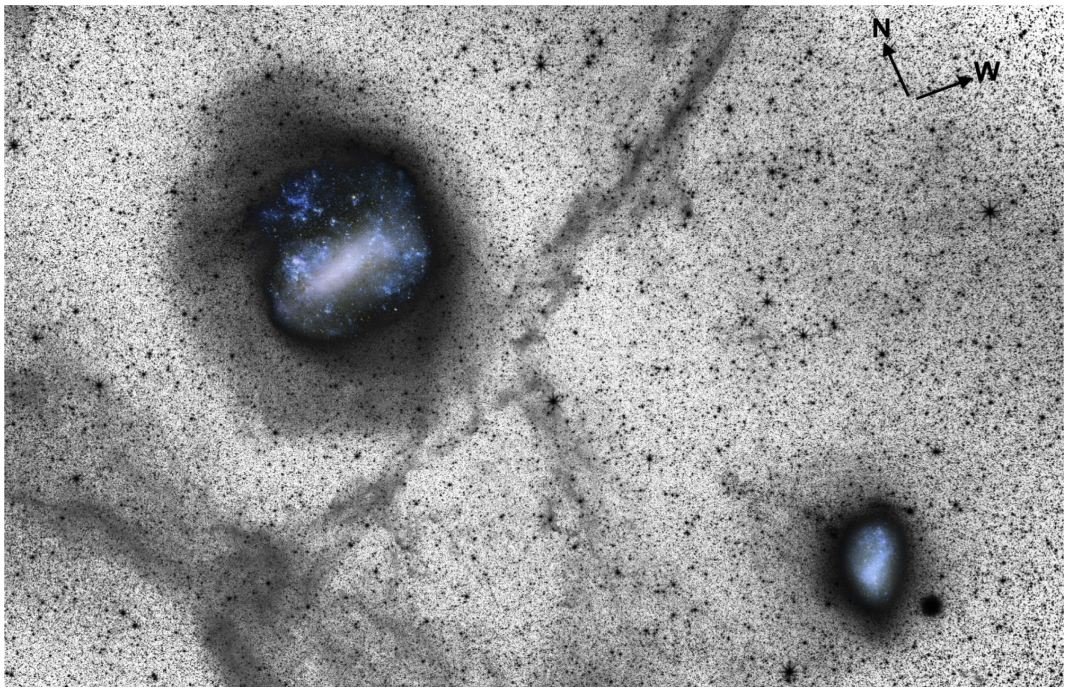

Figure 1: Wide-field Luminance Filter image of the Magellanic System ($39° \times 27°$). The LMC is located toward the top left and the SMC is to the bottom right. The Milky Way globular cluster 47 Tuc is visible to the west of the SMC. A tail of stars stretches out from the SMC in the direction of the LMC. The outskirts of the LMC disk display pronounced asymmetries. For illustrative purposes, colour insets of the inner regions of the LMC and SMC (from Besla et al. 2016) are also shown.

The SMC interacts (D'Onghia and Fox 2016, Besla et al. 2012, 2010) both with its neighbouring Large Magellanic Cloud (LMC) and with the Milky Way Galaxy (MW). These interactions have produced the Magellanic Stream (Mathewson et al. 1974), a trail of gas extending than 180°across the sky, and a "counter-tail", the so-called Leading Arm. The ongoing LMC-

SMC interaction is furthermore clearly shown by the stream of gas and stars linking the two galaxies, commonly referred to as the Magellanic Bridge (McGee and Newton 1981). These gravitational interactions have had a significant impact on the evolution of the MCs (Putman et al. 1998). Studying the current properties of the MCs is the key to understanding their recent evolution and interaction mechanisms between each other and with the MW. According to Besla et al. [2016] and Hammer et al. [2015], the MCs are on their first infall towards the MW, having entered the Local Group as a small group of dwarf galaxies [Sales et al., 2017]. Due to the relatively small mass of the SMC compared to the LMC and the MW, its star and cluster formation histories, morphology and overall dynamics are expected to be significantly affected by these interactions.

The traditional picture of the orbits of the MCs began to change with the work of Kallivayalil et al. [2006a], Kallivayalil et al. [2006b] and Kallivayalil et al. [2013], who inferred that both galaxies move faster around MW than originally thought. Also, Besla et al. [2007], Patel et al. [2017] suggested that the MCs are passing for the first time close to the MW , or have a long period orbit, depending on the mass of the MW and the LMC. van der Marel and Kallivayalil [2014] were the first to measure the internal proper motion field of the LMC, revealing a clockwise rotation of the disk in the plane of the sky, consistent with previous results of van der Marel and Sahlmann [2016] who used proper motions from the Tycho-Gaia Astrometric Solution (TGAS). Furthermore, the velocity map of LMC obtained by Gaia Collaboration et al. [2018a] revealed a high degree of order in the rotational motion of this system, while the proper motion residuals indicated a streaming motion along the Bar (Fig. 2). The periphery of LMC showed evidence of more complicated substructure, indicative of tidal stripping by the MW (Mackey et al. 2018, Nidever et al. 2019, Belokurov and Koposov 2016) and interactions with the SMC, as presented by Belokurov and Koposov [2016] who studied the distribution of blue horizontal branch stars.

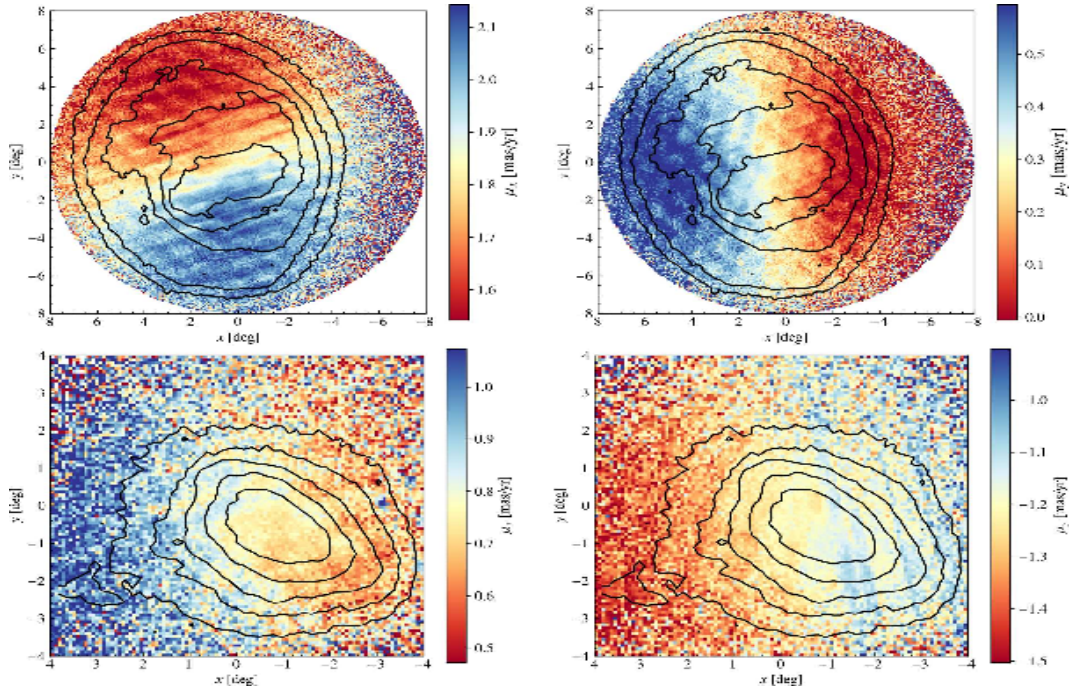

Figure 2: Proper motions of stars in the LMC (upper) and SMC (lower) showing the components x (left) and y (right). The colour shows the median PM in each pixel. The black density contours are logarithmically spaced, such that the outermost contour is at a source density 100 times lower than the highest density. The centre of each colour bar is chosen to be the median PM of all sources (Gaia Collaboration et al. 2018a).

On the other hand the SMC seems to have a more complex kinematical structure. Dobbie et al. [2014] studied radial velocities of intermediate age red giant branch stars and found signs of tidal stripping in the outer regions of the SMC as well as a velocity gradient along the northwest-southeast axis. The young stellar populations also show a similar velocity gradient, with even higher velocities encountered in the direction of the SMC Wing (an almost horizontal eastwward extension of the SMC, Evans and Howarth 2008). An extensive study of proper motions in the central region of the SMC has been presented by Nidever et al. [2018], who used data from the near-infrared VISTA survey of the MCs system. The map of proper motions as a function of position within the SMC revealed a nonuniform velocity pattern indicating of a tidal feature behind the SMC and a flow of stars in the southeast moving predominantly along the line of sight.

In recent study by De Leo et al. [2020] used a combination of spectroscopic data and proper motions to conclude that the gaseous component of the SMC is probably far from dynamical equilibrium. They also found evidence that the SMC is currently undergoing tidal disruption by the LMC within 2 kpc of its centre and possibly all the way into the very core. A detailed kinematic analysis of proper motions of stars in the Magellanic Bridge based on the Gaia Data Release 2 and on Hubble Space Telescope ACS data is presented in Zivick et al. [2019], who found a general pattern in the Bridge proper motions pointing away from the SMC toward the LMC.

During the last two decades realistic dynamical simulations of the MCs have been presented by many authors (e.g. Besla et al. 2010, Besla et al. 2012, Diaz and Bekki 2012), based on new proper motions data together with improved estimates of the parameters of the galaxies. Connors et al. [2006] conducted an N-body simulation of the MCs-MW system and compared the results with HI data from the Parkes All-Sky-Survey (HIPASS). They showed that the interaction between the SMC and the LMC results in both a spatial and kinematical bifurcation of both the Stream and the Leading Arm. Tepper-García et al. [2019] questioned the interpretation of the Leading Arm formation, showing that a hot MW corona would inhibit it. On the other hand Bekki and Chiba [2009], Diaz and Bekki [2012] using chemodynamical simulations suggested that the Magellanic Bridge and a structure away from the SMC ("Counter Bridge") also formed as a result of the LMC-SMC interactions.

1.2 Three dimensional structure of the SMC

The SMC has a complex geometry. One of the first studies that suggested that the SMC has a large line of sight depth was by Mathewson et al. [1986], who used Cepheid distances to derive an overall depth of about 32kpc. The large line of sight depth was confirmed for the older stellar population and was found to be very significant in the north eastern outer regions of the SMC, using intermediate age red clump stars as distance indicators by Hatzidimitriou and Hawkins [1989] and Hatzidimitriou et al. [1993]). Since then there have been numerous studies of the SMC structure and geometry (e.g. Subramanian and Subramaniam 2009, Subramanian and Subramaniam 2012, Subramanian and Subramaniam 2015, Ripepi et al. 2017, Deb et al. 2019). Subramanian and Subramaniam [2009] confirmed the large line of sight depth in the outer regions of the SMC, using a similar method as in Hatzidimitriou and Hawkins [1989]. Using red clump stars as well as RR-Lyrae variables, representing intermediate age and the old stellar populations respectively, Subramanian and Subramaniam [2012] claimed a large line of sight depth ($\sim 14kpc$, (Fig. 3)) for both populations. The older populations generally seem to follow a spheroidal or slightly ellipsoidal distribution. Jacyszyn-Dobrzeniecka et al. [2016], based on the analysis of a large sample of Cepheids, also described the SMC as an extended ellipsoidal galaxy. They identified two large ellipsoidal off-axis structures, with the northern one located closer to us and younger, while the south-western is further away and older.

More recently, Deb et al. [2019] using classical Cepheids and modeling the observed 3D distribution as a trixial ellipsoid obtained the geometrical and viewing parameters of the SMC. More specifically, the viewing angle parameter have inclination angle i= $3.465^\circ \pm 0.030^\circ$ with respect to longest axis from the line of sight and position angle of line of major axis is $=63.086^\circ \pm 0.117^\circ$. Also, the SMC is not a planar but heavily elongated for more than 25-30

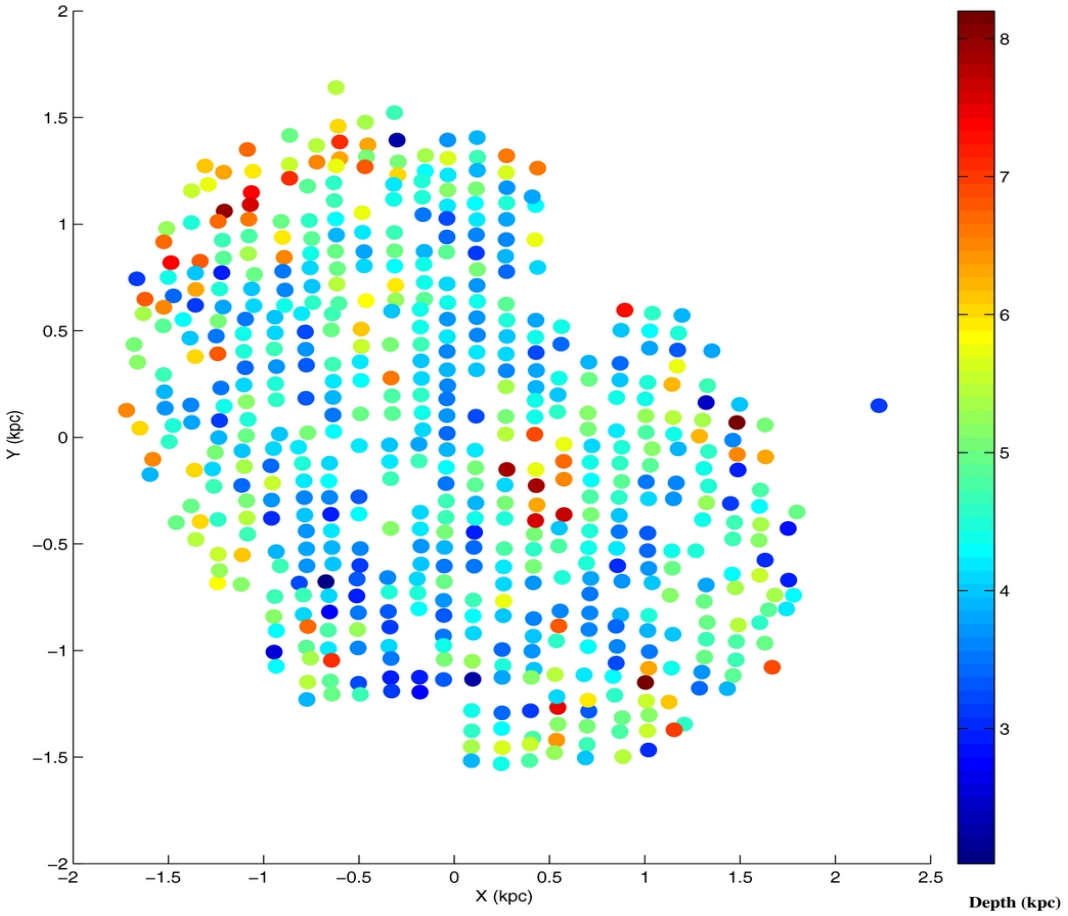

Figure 3: Two-dimensional plot of the depth in the sub-regions of the SMC obtained from the analysis of the red clump stars (Subramanian2012).

kpc approximately in the north-east towards south-west direction (Ripepi et al. 2017, Ripepi et al. 2016). Subramanian and Subramaniam [2012],

1.3 Star Formation History of the Small Magellanic Cloud

The stellar populations and star formation history (SFH) of the SMC have been the subject of numerous investigations over the past 4 decades [e.g. Gardiner and Hatzidimitriou, 1992, Noël et al., 2007, Cignoni et al., 2013, Nidever et al., 2017, Rubele et al., 2018], employing both ground-based and space observations. More recent studies are generally characterised by increased photometric accuracy and depth, improved spatial resolution and increased sophistication of stellar models and SFH simulation codes. The first extensive study of the distribution of populations of different ages over an area of 100 square degrees (excluding the inner densest regions) was published in the early 1990's (Gardiner and Hatzidimitriou 1992) and was based on photographic photometry. They claimed that only 7% of the stellar mass in the outer regions could be attributed to old populations. About a decade later Harris and Zaritsky [2004] published the first comprehensive study of the SFH of the SMC, based on CCD photometry. They studied the central area (4 x 4.5 deg^2) of the galaxy, using data from the Magellanic Cloud Photometric Survey obtained with the 1-m Swope Telescope

[Zaritsky et al., 2002]. They concluded that approximately 50% of the stars that have ever been formed in the SMC, did so more than about 8.4 Gyr ago, and that only a small amount of stars formed between 8.4 and 3 Gyr ago. They also claimed that during the last 3 Gyr there

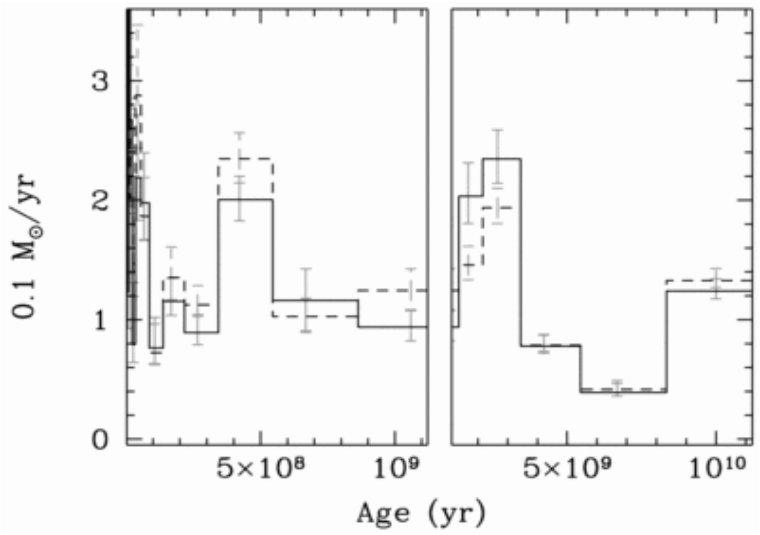

Figure 4: Comparing the global SFH solution, with and without the BV colour offset by Harris and Zaritsky [2004]. The original SFH solution is shown as the solid histogram.

has been a rise in the mean star formation rate (SFR) with three main bursts occurring at 2.5, 0.4 and 0.06 Gyr ago (Fig. 4).

The claim for low SF rate between 3 and 8 Gyr ago has been largely challenged by several subsequent studies, with the more recent one based on the Vista Magellanic Cloud Survey (VMC, Rubele et al. 2018). The VMC covers the entire region of the MCs and Magellanic Bridge (Fig. 5). In this study it was found that half of the stellar mass of the SMC formed prior to an age of 6.3 Gyr, while $\simeq$80% of the stellar mass formed between 8 and 3.5 Gyr ago. Similar results, supporting enhanced star formation at intermediate ages between $\simeq$4 and $\simeq$6 Gyr have also been found in specific (small) regions (Noël et al. 2009, Cignoni et al. 2012, Weisz et al. 2013). In particular Noël et al. [2009] found one peak of SF rate (SFR) at $\sim$4-5 Gyr and an old one at $\simeq$10 Gyr almost in all fields. In the W fields, this old enhancement splits into two, one peaked at $\simeq$8 Gyr old and another at $\sim$12 Gyr. Concerning the oldest population, as exemplified by RR-Lyrae variables (e.g. Muraveva et al. 2018) and one bona-fide old star cluster, NGC 121 (Glatt et al. 2008), it comprises only a small percentage of the total stellar mass of the galaxy [Soszynski et al., 2002]. Noël et al. [2009] and Sabbi et al. [2009] provide an age of about 12Gyr for the oldest stars although they both agree that SF was low at that time and that the old population is similar at all radii and at azimuth. Moreover, spatial variations in the SFH of the SMC were found to be consistent with gas drawn into the center of the SMC about at 3.5 Gyr ago, which simultaneously shut down star formation in the outer regions while dramatically increasing the star formation rate in the centre (Weisz et al. 2013).

Over the past $\sim$500Myr there has been a significant enhancement in SF, strongly concentrated in the Bar and the Wing areas [Cignoni et al., 2013, Sabbi et al., 2009]. Stars younger than $\sim$100Myr have a highly inhomogeneous spatial distribution [Sabbi et al., 2009], with a clear offset to the North-East and the Wing regions. Also, Noël et al. [2009] found a strong dichotomy between SE and W in the current irregular shape of the SMC. This dichotomy is produced by the youngest population and began $\sim$1 Gyr ago.

Additional tracers of the SFH of the SMC include variable stars and AGB stars or core collapse progenitors, although these involve a smaller number of objects. Rezaeikh et al. [2014] used long period variable stars to find two formation epochs, one at $\sim$6 Gyr and another at 0.7 Gyr. Cioni et al. [2006] studying AGB stars concluded that old stars (7-9Gyr) are located at the periphery of the SMC, while younger stars ($<$ 7Gyr) are present in the direction of the LMC. Auchettl et al. [2019] studying 23 supernovae remnants proposed that a burst of SF occurred 50 and 200 Myr ago.

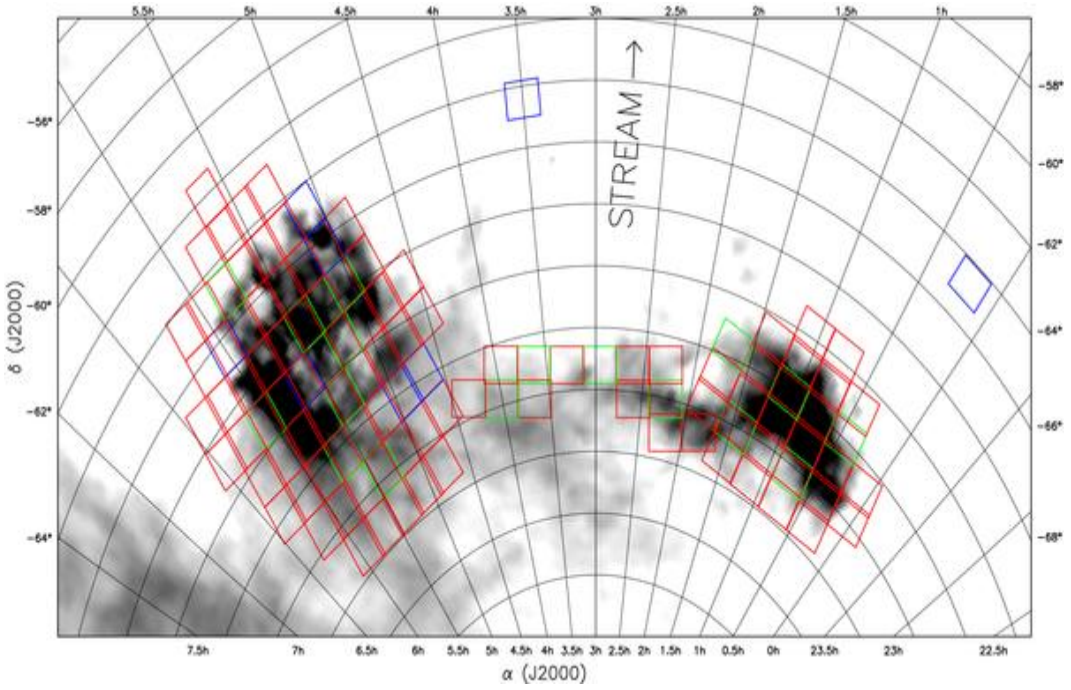

Figure 5: Magellanic system area tiled for VMC observations (Cioni et al. 2011). The underlying image shows the HI distribution (McClure-Griffiths et al. 2009).

Possible correlations between the SFHs of the SMC, the LMC and the MW due to their interactions have also been studied by some authors. Harris and Zaritsky [2004] suggested that two bursts of SF that apparently took place 2.5 and 0.4 Gyr ago in the SMC were temporally coincident with past perigalactic passages of the SMC with the MW. It is noted that at the time it was thought that the MCs have been orbiting the MW for several Gyrs (as mentioned earlier, the data available today suggest that the MCs are falling towards the MW for the first time). Rezaeikh et al. [2014] found a common burst of SF in both Clouds at 0.7 Gyr which may be linked to the interaction between the MCs. Generally, there is no strong evidence for periodic behaviour in the SFHs of the MCs, suggesting that repeated encounters with the MW are unlikely (Weisz et al. 2013), as indeed seems to be the case according to the most recent estimates of the orbit of the MC system. Moreover, the different initial star formation epochs of MCs, suggest that the two galaxies may not have formed as a pair and at least the SMC formed in isolation (Rezaeikh et al. 2014).

1.4 Star Clusters in the SMC

The study of star clusters (SCs) is a unique tool for understanding the star formation history of a galaxy. Several studies have been carried out over the past century with the purpose of discovering and characterising the star cluster population of the SMC, with the first recorded attempt being that of Shapley and Wilson [1925]. Hodge and Wright [1974] presented for the first time a comprehensive study of the structural parameters of the then known SMC clusters. A year later Bruck [1975] presented a list of candidate star clusters based on UK 48-inch Schmidt Telescope photographic plates. In 1986 Hodge [1986] revised the SMC cluster catalog based on CTIO 4m photographic plates, adding 213 new clusters (and candidates), thus bringing the total number of known clusters (and candidates) to 601. Taking into account the incompleteness of the data Hodge [1986] estimated that the total number of star clusters in the SMC could be around 2000. About ten years later, Bica and Schmitt [1995] compiled an updated catalogue of 554 clusters in the SMC and MC Bridge, using all available information at the time (Fig. 8). Using the Optical Gravitational Lensing Experiment (OGLE)survey

data, Pietrzynski et al. [1998] provided another catalog of star clusters in the central region of the SMC, using an automatic algorithm detecting overdensities. The catalog contained 238 clusters, 72 of which were new objects. In 2008, Bica et al. [2008] combined data from previous catalogs to compile a comprehensive catalog of star clusters in the SMC, also providing structural parameters for many of them.

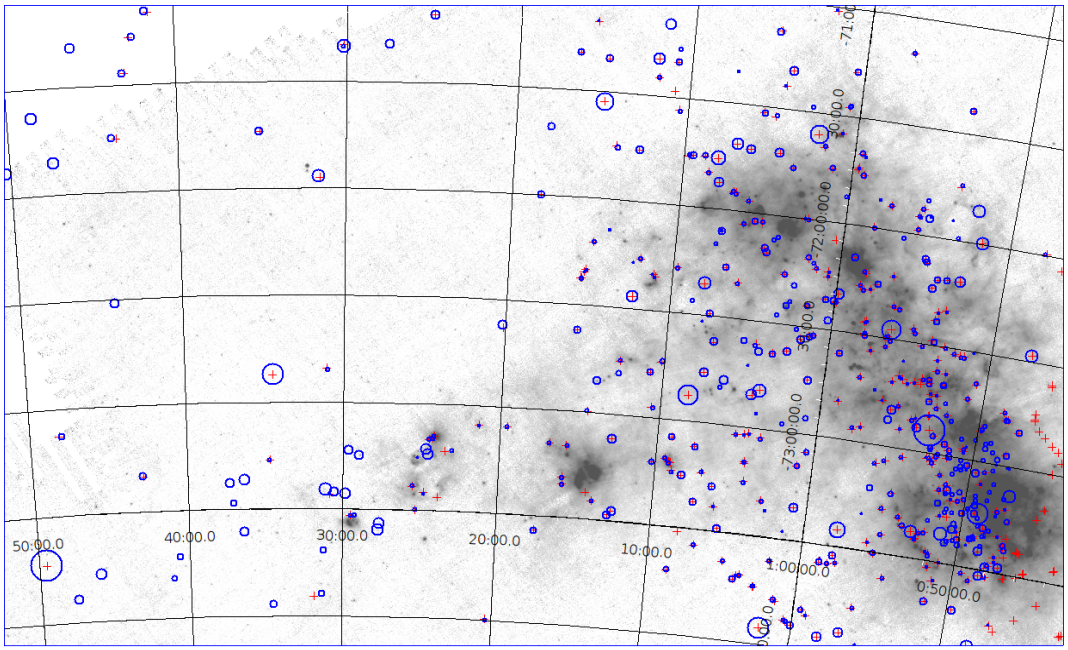

Figure 6: The extended objects that characterized as star clusters (C), clusters associations (CA), clusters nelula (CN) in the catalog of Bica and Schmitt [1995] (red crosses) and of Bica et al. [2020] (blue circles).

The great majority of the above studies were mainly based on visual inspection of images (at least as a first step). Recently, automated clustering algorithms have been employed to study the cluster population in the Magellanic Clouds, and in the SMC in particular, with varying success. Piatti (2017, 2016) applied Machine Learning algorithms to identify clusters, particularly smaller and lower density ones, from the SMASH-VMC survey. Some of the 38 new clusters they identified are hardly recognizable on optical images, without the help of a robust field star decontamination. Bitsakis et al. [2018], also following an automated detection method (Bitsakis et al. [2017]), detected a total of 1319 candidate star clusters in the central area of the SMC, of which 1108 were new identifications, although according to Piatti [2018] this unprecedented number of clusters could be greatly overestimated. One of the more severe deficiencies of the Bitsakis et al. catalog is that it failed to recover $\sim$ 50% of the known relatively bright clusters located in the SMC main body. At the same time, the number of new cluster candidates per time unit as a function of time was noticeably different from the intrinsic SMC cluster frequency. The most recent updated catalog of star clusters in the SMC has been presented by Bica et al. [2020] (Fig. 8). They published a list of star clusters, associations and related objects in the SMC and the Magellanic Bridge (MB) with 2741 entries, a factor of 2 larger than the previous version. A major contribution of this work is a new sample of 45 clusters and candidate clusters in the SMC and the Magellanic Bridge. It is also noted that in this catalog the majority of the Bitsakis et al. [2018] identifications are classified as associations.

The age distribution of SMC star clusters has been the subject of several studies. Chiosi et al. [2006] derived the ages of 311 SCs younger than 1Gyr and found an enhancement of

formation between 15 and 90 Myr. Glatt et al. [2010] studying 324 SCs identified two periods of enhanced SC formation at 160Myr and 630Myr, with the former probably linked to a close encounter between the SMC and LMC.

The youngest clusters in the SMC seem to reside in supergiant shells, giant shells, intershell regions, and toward regions with a high Hα content, suggesting that their formation is related to expansion and shell-shell interaction. Piatti et al. [2007] found indications that many young clusters are located closer to the centre of the SMC. There are also young clusters still embedded in HII regions, which have been misidentified as HII regions alone in the past [Stanghellini et al., 2003].

Deep photometric data have been extensively used to derive the ages of intermediate and old SCs. Piatti (2012, 2012b, 2011, 2011, 2007, 2005, 2001) studied intermediate age SCs using accurate Washington photometry. By combining their data with other in the literature, they derived an age distribution of 43 well known SMC clusters older than 1 Gyr. They identified two enhanced cluster formation periods, at $\sim 2Gyr$ and at $\sim 5Gyr$. The most recent peak occurs at a time that may correspond to a very close encounter between SMC and LMC (at least according to the LMC-SMC orbit known at the time of these publications). They also suggested that from the birth of the SMC cluster system until approximately the first 4Gyr of its lifetime, the cluster formation rate seems to have been constant (Piatti et al. 2011). Parisi et al. [2014] studied 15 star clusters based on data taken with the VLT and they confirmed (using also data for another 35 clusters from previous studies) the existence of two periods of enhancement of cluster formation at 2 and 5 Gyr ago, while they disproved an age gradient as clusters younger than 3.5 Gyr were found to be located at several galactocentric distances and not only near the center. They also derived the cluster age-metallicity relation (also presented in a systematic manner for a smaller sample of clusters by Da Costa and Hatzidimitriou 1998) and concluded that for clusters younger than 4Gyr, it is in reasonable agreement with the bursting model of Pagel and Tautvaisiene [1998]. Other authors, Mighell et al. [1998], Glatt et al. [2008], Girardi et al. [2013], have also studied intermediate age and old clusters using photometric data obtained with the HST, or other ground based telescopes (e.g. Dias et al. (2014, 2016).

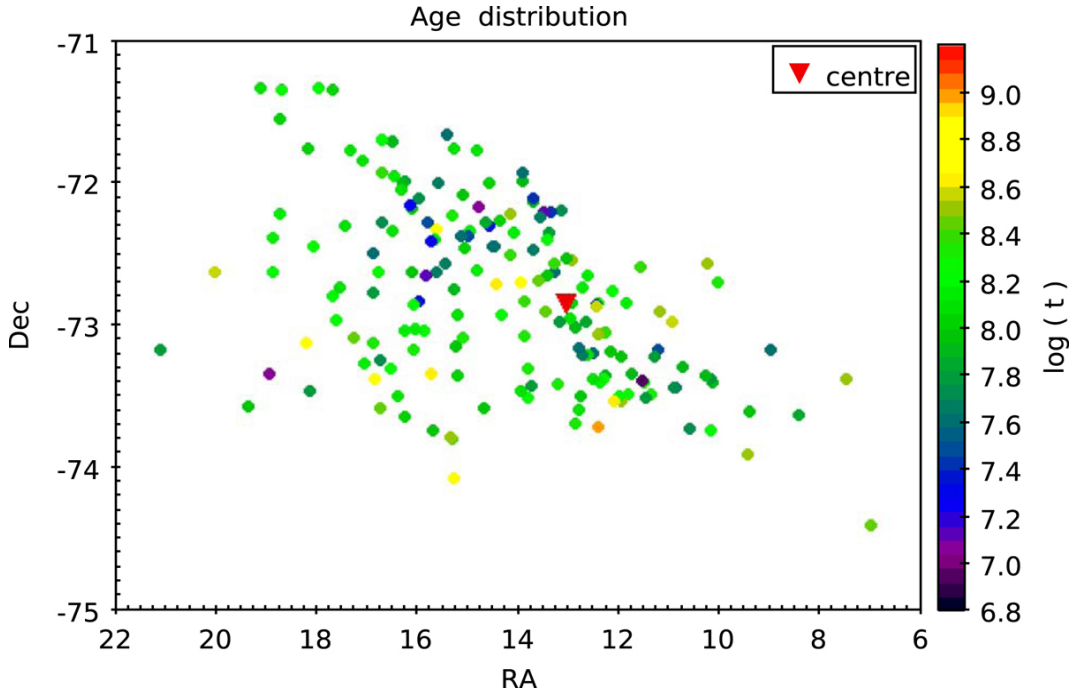

Figure 7: Spatial distribution of star clusters in the SMC as a function of age. (Nayak et al. 2018).

A more recent extensive study of the age distribution of star clusters in the SMC is presented in Nayak et al. [2018]. They studied 179 SCs using data from the OGLE III survey and a semi automated quantitative method developed by Nayak et al. [2016] to estimate cluster parameters. They derived the spatio-temporal distribution of SMC clusters by combining previous studies with their catalogue. The SCs located in the southern part of the SMC were found to be in the age range of 600Myr - 1.25Gyr, while those younger than 100Myr were mostly found in the northern part of the SMC, with the central parts of the SMC showing continuous cluster formation (Fig. 7). The peak of the cluster age distribution was determined to be at $130 \pm 35 Myr$, close to the age of the peak in the LMC SC age distribution (Nayak et al. [2016]), which suggests that the burst of cluster formation in both Clouds may have a common origin, presumably the LMC-SMC interaction. Additionally, 90% of their studied sample was found to have masses $<1700 M_{\odot}$ suggesting that the SMC SC population is dominated by low mass clusters as also suggested a few decades ago by the seminal study of Kontizas [1980] who concluded that the SMC SCs that they studied were on average about 10 times less massive than those in our Galaxy. A recent study by Maia et al. [2014] provided masses for 29 young and intermediate age clusters within the range 300-3000 $M_{\odot}$. Another extended recent study of the spatial and age distribution of SCs is by Bitsakis et al. [2018]. Their results suggested that the bulk of the clusters in both MCs were formed approximately 300Myr ago, probably during a direct collision of two galaxies.

1.5 High mass X-ray binaries in the SMC

There are many types of astrophysical objects which emit X-rays, such as active galactic nuclei, binary stellar systems, stars, etc. A binary stellar system contains two stars that orbit around the common center of mass. Binaries that emit X-rays (X-ray binaries - XRBs) consist of a non-degenerate star (donor) and a degenerate star (accretor) such as a white dwarf, neutron star or black hole, that are close enough for mass transfer to occur from the normal star to the dense collapsed star, that results in X-ray emission.

There are two main types of X-ray binaries, depending on the mass of the donor star: *High Mass X-ray Binaries (HMXBs):* In this case the donor is an early type massive star. Optically, only the donor star can be observed. *Low Mass X-ray Binaries (LMXBs):* The donor star is a low mass star that has evolved to fill its Roche lobe and is transferring material through the inner Lagrangian point Ł$_1$ onto the compact object (Seward and Charles 1995, Casares et al. 2017).

According to van den Heuvel [2019] HMXBs can be classified in three main types. The first type is the supergiant HMXB that have been discovered by Schreier et al. [1972] and Webster and Murdin [1972]. An O- or early B- type supergiant star is the donor of this system and is close to filling its Roche lobe. These systems have orbital periods shorter than 15 days and the X-ray emission is mostly powered by the capture of matter from the strong stellar wind of the supergiant companion. The compact star is a neutron star. The second class is called Be-emission X-Ray Binary (BeXRB). Maraschi et al. [1976] first recognized and suggested this type of system. A Be-star is the companion (donor) star and it lies very close to the main sequence. The characteristic of these stars is the variable emission-line spectrum of hydrogen. The donor star is surrounded in its equatorial plane by a rapidly rotating disk where the emission lines are formed. Most of HMXBs are of the BeXRB type and particularly in the SMC there are at least 120 (**?**, Antoniou et al. 2019) such systems. Usually the compact object in these binaries is neutron star and only one black hole BeXRB is known (Casares et al. 2014). The third type has the fewest members. In this case the companion is a Wolf-Rayet star, so the binary system is called Wolf-Rayet X-Ray Binary (WRXB). All of them except CygX-3 have been discovered in external galaxies (Esposito et al. [2015]). They have very short orbital periods (about a day). Emission lines of He, C, N are characteristic of these stars and they are produced in an external strong radiation-driven stellar wind with mass-loss rates around 10^{-5} $M_{\odot}$ amd velocities 2000-5000 km s^{-1} (Hamann et al. 2006, Crowther 2007). The SMC due to the short distance is an ideal target to study the population of the HXRBs.

In LMXBs material is transferred from a slightly evolved late type star into the compact

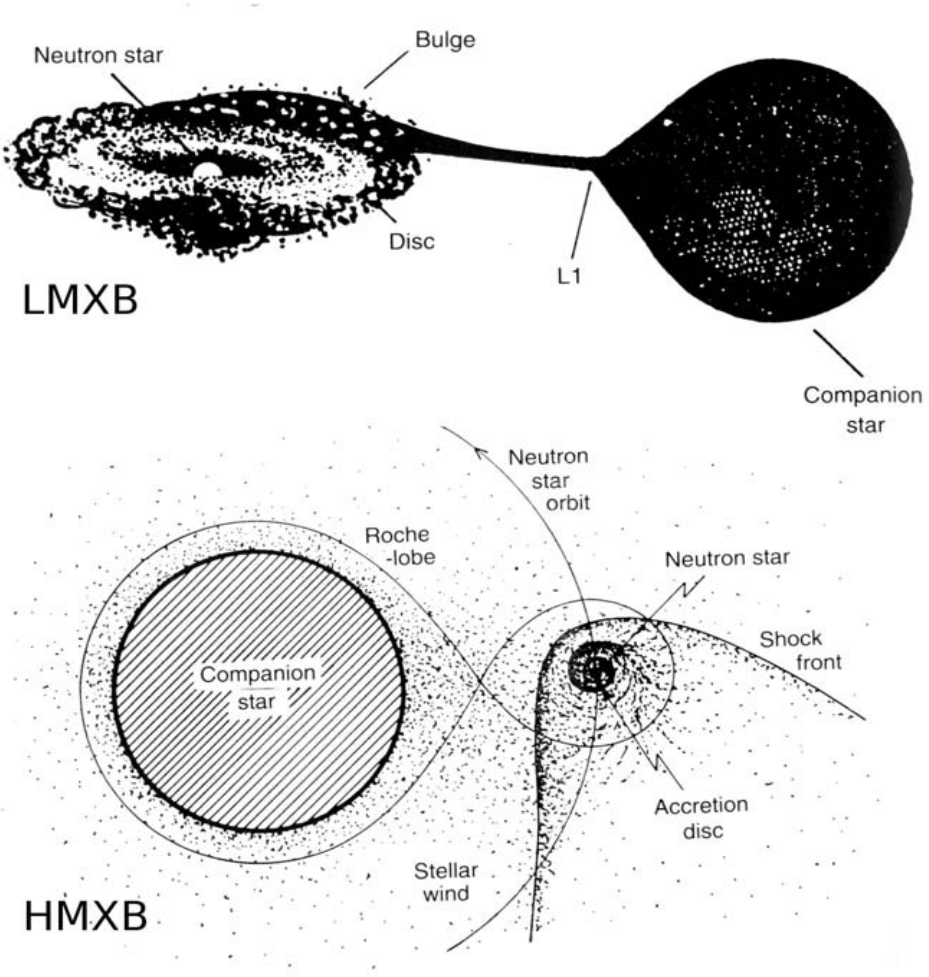

Figure 8: The two mechanisms by which matter is transferred onto a compact object in a binary system. *Upper panel:* An evolved lower mass star is loosing mass to its companion star because it fills its Roche lobe and mass flows through the L_1 point. Matter flowing out of the star forms a stream that impacts the accretion disk and by viscous forces is gradually accreted onto the compact where the X-rays are generated. *Lower Panel:* A compact object is orbiting a massive star which is losing mass through a powerful stellar wind accreted by the compact object and producing X-rays (Seward and Charles 1995).

object. An accretion disk is formed around the compact object due to the angular momentum of the material which leaves the star and cannot fall directly onto the compact object. The major difference between high and low mass XRBs is in how the matter is transferred from the normal star onto the compact object. The stars of the LMXBs direct its mass into the gravitational influence of the compact object in order to yield detectable X-rays. On the other hand the material in case of HMXB is transferred through the stellar wind. One of the most exciting areas of the X-ray astronomy is the search fro low mass X-ray binaries. Very few are known in the Magellanic Clouds (Seward and Charles 1995, Moe and Di Stefano 2015).

The SMC has been studied by many authors in X-rays. A first study was presented by Bruhweiler et al. [1987] using Deep Einstein IPC imagery of $\sim 50\%$ of the main body and Wing of the SMC and yielding a list of 25 X-ray sources. Wang and Wu [1992] did a comprehensive analysis of the Einstein data in the SMC covering a large area and provided a catalogue of 70 sources. Seward and Mitchell [1981], using also Einstein data, studied a 40 square degree region. ROSAT satellite observations from 1990 to 1998 were used by Sasaki et al. [2000] to

derive a catalogue of 121 discrete sources and from 1991 to 1994 by Haberl et al. [2000] to derive 517 discrete sources. A 4yr X-ray monitoring survey by Laycock et al. [2005] used the Rossi X-Ray Timing Explorer to study the long-term behaviour of X-ray pulsars. A catalogue of 106 discrete sources was obtained from an extensive study of 22 observations fully covering the main body and the eastern Wing, by the end of the ASCA mission by Yokogawa et al. [2003]. Another extensive survey covering the SMC Bar and Wing, was carried out with the XMM-Newton space observatory by Haberl et al. [2012], and Sturm et al. [2013]. A more recent study by Coe and Kirk [2015] present ~ 70 X-ray emitting binary systems that contain Be stars as the mass donor to a neutron star accretor. A large homogeneous sample of HMXBs was also provided by Haberl and Sturm [2016] who investigated their properties and confirmed 148 objects.

The stellar mass of a galaxy may be associated with the XRB formation rate. Lehmer et al. [2010] based on Chandra observations studied 17 luminous infrared galaxies. The imaging and X-ray spectral information allowed them to measure separately the X-ray contributions from active galactic nuclei and normal galaxy processes. Furthermore, Mineo et al. [2012], based on a homogeneous set of X-ray, infrared and ultraviolet data, studied populations of HMXBs in a sample of star-forming galaxies and explored their connection to star-formation rate. They agreed that HMXBs and their collective luminosity are good tracers of the recent star formation activity in their host galaxy. Antoniou et al. [2019] performed a deep Chandra X-ray Visionary Project survey of SMC regions with different ages of stellar populations and studied the number of HMXBs as a function of the local star-formation rate, and the stellar mass produced during the specific star-formation burst, as well as a function of the age of their parent stellar populations. Each of these indicators serves a different role, but in all cases they found that the HMXB formation efficiency increases as a function of time (following a burst of star formation) up to $\sim$40–60 Myr, and then gradually decreases.

It is commonly accepted that the occurence of BeXRBs is affected by metallicity. Linden et al. [2010] found the population of young and bright HMXBs to be a strongly metallicity depent. The connection of X-ray binaries and metallicity has also been suggested by many other authors like Dray [2006], Antoniou et al. [2010], Fragos et al. [2013], Antoniou and Zezas [2016].

2 Observations

Observations of five fields in the SMC were obtained with the 6.5m Magellan Telescope at the Las Campanas Observatory in Chile on October 4th, 2004, using the Inamori Magellan Areal Camera and Spectrograph (IMACS) [Dressler et al., 2011]. IMACS is a wide-field imager and multi-object spectrograph with an eight CCD mosaic. In its f/2 configuration it provides a 0.44 deg diameter field of view with 0.2" pixel size. The images were taken through B, V, I and R standard Johnson-Cousins filters.

In Table 1 the logs of observations are shown. The first column gives the Universal Time (U.T.) of each observation, the second column the name of the field, columns 3 and 4 the coordinates of the center of the field, column 5 the total exposure time, column 6 the filter and column 7 the airmass. The exposure time was 90s long in V, 120 s in B and 30s in R and I. Each image was constructed using the package of SWARP, from a total of 8 dithered single exposures in V, 6 in B, and 2 in R and I.

Table 1: Logs of observations

U.T.	**Field**	**RA** (J2000)	**DEC** (J2000)	**Exp. Time** (s)	**Filter**	**Air Mass**
00:13:32'	SMC3	0:56:53.6'	-72:17:17.6'	90	V	1.768
00:19:26'	SMC3	0:56:53.4'	-72:17:17.2'	90	V	1.749
00:22:59'	SMC3	0:56:50.1'	-72:17:16.7'	90	V	1.737
00:26:06'	SMC3	0:56:50.2'	-72:17:16.3'	90	V	1.727
00:29:15'	SMC3	0:56:50.1'	-72:17:46.4'	90	V	1.718
00:32:18'	SMC3	0:56:50.1'	-72:17:46.4'	90	V	1.708
00:37:13'	SMC3	0:56:53.3'	-72:17:48.7'	90	V	1.694
00:40:24'	SMC3	0:56:53.4'	-72:17:49.1'	90	V	1.685
00:47:29'	SMC5	0:53:19.8'	-72:17:42.7'	90	V	1.657
00:52:03'	SMC5	0:53:19.9'	-72:17:42.5'	90	V	1.649
00:54:18'	SMC5	0:53:16.5'	-72:17:42.3'	90	V	1.639
00:57:26'	SMC5	0:53:16.5'	-72:17:42.2'	90	V	1.631
01:00:44'	SMC5	0:53:16.4'	-72:17:13.1'	90	V	1.623
01:03:47'	SMC5	0:53:16.4'	-72:17:12.9'	90	V	1.616
01:08:37'	SMC5	0:53:19.7'	-72:17:13.0'	90	V	1.604
01:11:42'	SMC5	0:53:19.7'	-72:17:12.9'	90	V	1.597
01:15:55'	SMC6	0:53:14.9'	-72:42:05.8'	90	V	1.591
01:19:06'	SMC6	0:53:14.9'	-72:42:05.4'	90	V	1.584
01:22:49'	SMC6	0:53:11.5'	-72:42:05.5'	90	V	1.576
01:25:53'	SMC6	0:53:11.5'	-72:42:05.4'	90	V	1.570
01:29:05'	SMC6	0:53:11.6'	-72:42:05.6'	90	V	1.563
01:32:08'	SMC6	0:53:11.7'	-72:42:05.6'	90	V	1.557
01:35:22'	SMC6	0:53:15.3'	-72:42:05.8'	90	V	1.551
01:38:25'	SMC6	0:53:15.2'	-72:42:05.6'	90	V	1.545
01:42:31'	SMC7	0:49:16.6'	-72:44:56.0'	90	V	1.530
01:45:35'	SMC7	0:49:16.7'	-72:44:56.0'	90	V	1.525
01:56:33'	SMC7	0:49:13.4'	-72:44:55.6'	90	V	1.506
02:00:25'	SMC7	0:49:13.3'	-72:44:55.5'	90	V	1.500
02:03:37'	SMC7	0:49:13.3'	-72:44:26.0'	90	V	1.495
02:06:40'	SMC7	0:49:13.3'	-72:44:25.8'	90	V	1.490
02:09:56'	SMC7	0:49:16.8'	-72:44:25.2'	90	V	1.485
02:12:59'	SMC7	0:49:16.9'	-72:44:25.4'	90	V	1.481
02:16:15'	SMC4	0:49:36.0'	-72:16:18.1'	90	V	1.487
02:20:50'	SMC4	0:49:36.0'	-72:16:18.5'	90	V	1.481
02:24:45'	SMC4	0:49:32.4'	-72:16:18.3'	90	V	1.476

02:27:48’	SMC4	0:49:32.5’	-72:16:18.4’	90	V	1.472
02:34:37’	SMC4	0:49:32.4’	-72:15:50.6’	90	V	1.464
02:37:40’	SMC4	0:49:32.5’	-72:15:50.7’	90	V	1.460
02:41:03’	SMC4	0:49:36.0’	-72:15:50.4’	90	V	1.456
02:44:06’	SMC4	0:49:36.1’	-72:15:50.5’	90	V	1.453
04:50:58’	SMC3	0:56:53.6’	-72:17:16.7’	120	B	1.371
04:56:53’	SMC3	0:56:53.6’	-72:17:16.6’	120	B	1.372
05:00:27’	SMC3	0:56:53.8’	-72:17:16.2’	120	B	1.373
05:04:09’	SMC3	0:56:53.8’	-72:17:16.1’	30	R	1.373
05:06:22’	SMC3	0:56:53.8’	-72:17:16.4’	30	I	1.374
05:12:52’	SMC3	0:56:50.8’	-72:16:46.2’	30	I	1.375
05:24:11’	SMC3	0:56:50.7’	-72:16:46.3’	30	R	1.379
05:26:38’	SMC3	0:56:50.7’	-72:16:46.3’	120	B	1.380
05:30:12’	SMC3	0:56:50.7’	-72:16:46.2’	120	B	1.382
05:33:45’	SMC3	0:56:50.7’	-72:16:46.1’	120	B	1.383
05:54:44’	SMC5	0:53:19.8’	-72:26:42.4’	120	B	1.402
05:58:17’	SMC5	0:53:19.8’	-72:26:42.5’	120	B	1.405
06:01:50’	SMC5	0:53:19.8’	-72:26:42.1’	120	B	1.407
06:06:06’	SMC5	0:53:19.7’	-72:26:42.2’	30	R	1.411
06:08:30’	SMC5	0:53:19.7’	-72:26:41.6’	30	I	1.413
06:25:37’	SMC5	0:53:22.7’	-72:26:06.5’	30	I	1.429
06:27:42’	SMC5	0:53:22.6’	-72:26:06.4’	30	R	1.432
06:29:58’	SMC5	0:53:22.7’	-72:26:06.8’	120	B	1.434
06:33:31’	SMC5	0:53:22.6’	-72:26:07.1’	120	B	1.438
06:37:04’	SMC5	0:53:22.7’	-72:26:07.2’	120	B	1.442
07:53:20’	SMC4	0:49:36.1’	-73:16:18.0’	120	B	1.589
07:57:02’	SMC4	0:49:36.1’	-73:16:18.2’	120	B	1.597
08:00:48’	SMC4	0:49:36.1’	-73:16:18.3’	120	B	1.605
08:07:53’	SMC4	0:49:36.3’	-73:16:18.3’	30	R	1.621
08:09:49’	SMC4	0:49:36.3’	-73:16:18.5’	30	I	1.626
08:14:55’	SMC4	0:49:29.2’	-73:15:48.4’	30	I	1.638
08:16:08’	SMC4	0:49:29.3’	-73:15:48.4’	30	R	1.641
08:19:41’	SMC4	0:49:29.3’	-73:15:48.6’	120	B	1.648
08:22:14’	SMC4	0:49:29.3’	-73:15:48.7’	120	B	1.657
08:26:42’	SMC4	0:49:29.3’	-73:15:48.8’	120	B	1.666
08:34:42’	SMC6	0:53:14.9’	-72:42:05.5’	120	B	1.671
08:38:21’	SMC6	0:53:14.9’	-72:42:06.1’	120	B	1.681
08:41:54’	SMC6	0:53:14.9’	-72:42:06.1’	120	B	1.691
08:45:44’	SMC6	0:53:15.0’	-72:42:06.4’	30	R	1.702
08:47:50’	SMC6	0:53:15.0’	-72:42:06.8’	30	I	1.708
08:49:55’	SMC6	0:53:11.6’	-72:41:36.6’	30	I	1.714
08:52:32’	SMC6	0:53:11.6’	-72:41:36.6’	30	R	1.722
08:54:40’	SMC6	0:53:11.6’	-72:41:36.3’	120	B	1.728
08:58:18’	SMC6	0:53:11.7’	-72:41:36.3’	120	B	1.740
09:01:51’	SMC6	0:53:11.7’	-72:41:36.5’	120	B	1.751
09:08:04’	SMC7	0:49:16.8’	-72:44:56.2’	120	B	1.784
09:11:37’	SMC7	0:49:16.9’	-72:44:56.2’	120	B	1.796
09:15:11’	SMC7	0:49:16.8’	-72:44:56.2’	120	B	1.809
09:18:59’	SMC7	0:49:16.8’	-72:44:55.9’	30	R	1.822
09:21:09’	SMC7	0:49:16.9’	-72:44:56.1’	30	I	1.830
09:24:00’	SMC7	0:49:13.5’	-72:44:25.2’	30	I	1.840
09:38:23’	SMC7	0:49:16.6’	-72:44:25.1’	30	R	1.895
09:26:40’	SMC7	0:49:16.5’	-72:44:25.3’	120	B	1.850
09:30:13’	SMC7	0:49:16.5’	-72:44:25.0’	120	B	1.863

09:33:46’	SMC7	0:49:16.6’	-72:44:24.8’	120	B	1.878

Fig. 9 presents the locations of the five fields studied in this work on a Spitzer - MIPS 24 μ map of the SMC. The circles indicate the field of view of the IMACS data. The radius of each circle is $\sim$ 0.21 degrees.

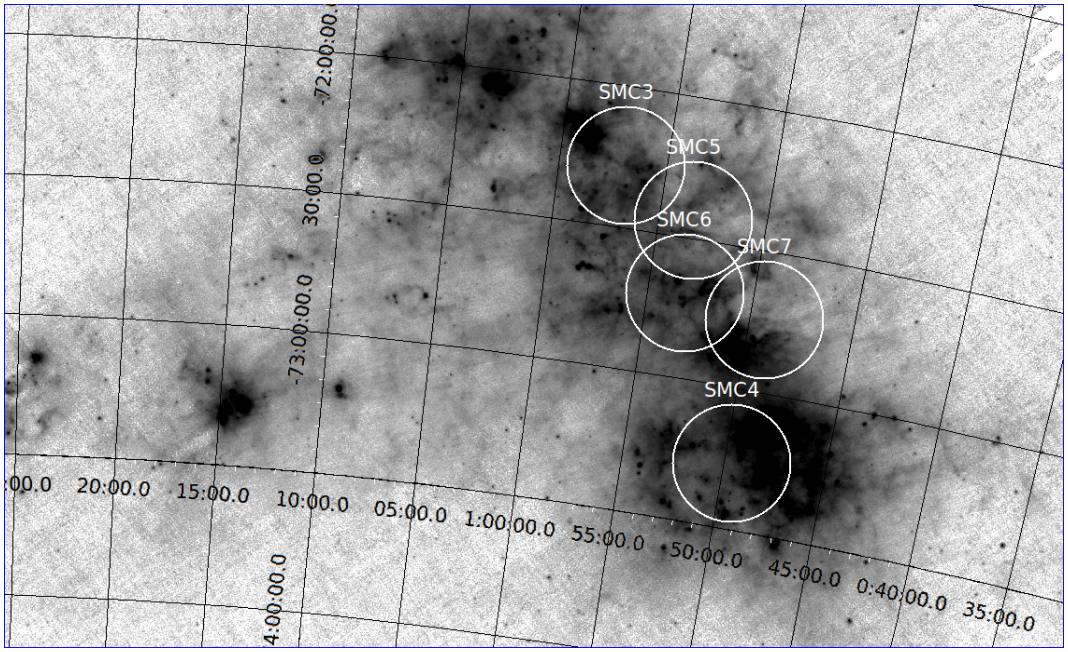

Figure 9: The location of the five studied fields marked on a Spitzer-MIPS 24μ map of the SMC.

3 Data Reduction

3.1 Bias Subtrsaction-Flat fielding

In this section we discuss the techniques used to pre-process the images. Initially, we derived the mean value of the overscan strip section at the edges of the image and we subtracted this constant value from the entire frame. Using the task CCDRPOC of the package IRAF/CCDRED we trimmed the image of the overscan region and edge lines and columns. Below we show the parameters of the task CCDPROC (for CCD8 of a field, as an example).

PACKAGE = ccdred
TASK = ccdproc

images = c8.fits List of CCD images to correct
(output = c8db.fits) List of output CCD images
(ccdtype= CCD) image type to correct
(max cac= 0) Maximum image caching memory
(noproc = no) List processing steps only
(fixpix = no) Fix bad CCD lines and columns
(oversca= yes) Apply overscan strip correction
(trim = yes) Trim the image?
(zerocor= no) Apply zero level correction?
(darkcor= no) Apply dark count correction?
(flatcor= no) Apply flat field correction?
(biassec= [2049:2111,4097:4160]) Overscan strip image section
(trimsec= [1:2048,1:4096]) Trim data section
(zero =) Zero level calibration image
(dark =) Dark count calibration image
(flat =) Flat field images

A sample of BIAS frames with zero exposure time were also obtained during the observing day, with the purpose of combining them to derive a high S/N bias frame with which to correct all other images (including calibration images). A BIAS image is a zero exposure time frame, giving for each pixel the electronic offset of the system, which is inherent in the structure of the CCD. We subtracted the averaged BIAS frame from each image. The process is also called "zero correction". We used again the task CCDROC, with parameter values as shown in the following.

PACKAGE = ccdred
TASK = ccdproc

images = c8db.fits List of CCD images to correct
(output = c8dbc.fits) List of output CCD images
(ccdtype= CCD) image type to correct
(max cac= 0) Maximum image caching memory
(noproc = no) List processing steps only
(fixpix = no) Fix bad CCD lines and columns
(oversca= no) Apply overscan strip correction
(trim = no) Trim the image
(zerocor= yes) Apply zero level correction
(darkcor= no) Apply dark count correction

(flatcor= no) Apply flat field correction
.....
(biassec=) Overscan strip image section
(trimsec=) Trim data section
(zero = BIASc8.fits) Zero level calibration image
(dark =) Dark count calibration image
(flat =) Flat field images
.....

The final step of pre-processing is flat fielding. Flat fielding corresponds to correcting the combined optical-system and CCD throughput at each pixel so that each pixel on the CCD would respond equally to a source with the same photon flux. Flat fielding removes the effect of the pixel-to-pixel sensitivity variations across the array as well as the effect of dust or scratches on the CCD window, and vignetting by the telescope or camera lens optics. A flat field frame must be produced for each filter. The flat-field frames are obtained by exposing the CCD array to an evenly illuminated target at very close range (and therefore out of focus) or by imaging the twilight sky.

The Flat-field effect is multiplicative, thus to correct for uneven response/sensitivity, we needed to divide each science or calibration image with the normalised flat field image (obtained through the same filter), after it was corrected for BIAS. This was done using the task CCDPROC.

PACKAGE = ccdred
TASK = ccdproc

images = c8dbc.fits List of CCD images to correct
(output = c8dbcff.fits) List of output CCD images
(ccdtype= CCD) image type to correct
(max cac= 0) Maximum image caching memory
(noproc = no) List processing steps only
(fixpix = no) Fix bad CCD lines and columns
(oversca= no) Apply overscan strip correction
(trim = no) Trim the image
(zerocor= no) Apply zero level correction
(darkcor= no) Apply dark count correction
(flatcor= yes) Apply flat field correction
.....
(biassec=) Overscan strip image section
(trimsec=) Trim data section
(zero =) Zero level calibration image
(dark =) Dark count calibration image
(flat FLATc8Bourflats.fit) Flat field images
.....

3.2 Astrometry

Position measurement of a star is one of the most basic measurements of astronomy. An image in the World Coordinate System (WCS) links each pixel to a specific direction in the sky. Here we describe the process to derive an astrometric solution that will map our pixel locations in the WCS system.

First, we need to derive the transformation between the (x,y) pixel coordinates and equatorial coordinates (Right Ascension -RA and Declination -Dec). To do this, we first identified a set of 25-30 stars common on each one of our images and SAO-DSS, which has accurate astrometry. For this set of common stars, we created a file having one star per line, and four columns, the first two giving the (x,y) pixel coordinates on our image and the last two giving the RA Dec coordinates from SAO-DSS. To compute the transformation between the pixel and celestial coordinates we applied the task CCMAP, from the IRAF/IMCOORDS package. The task was run in interactive mode which allows us to control the fitting process (e.g. to change the order of the fit, reject outliers if necessary, display the data and repeat the fitting with updated parameters). The derived astrometric solution is attached to the image file (.db), which is now astrometrically calibrated. The solution attached to the image file is updated every time a new fit is performed. The parameters for this task are shown below.

PACKAGE = imcoords
TASK = ccmap
input = c8xyradec.dat The input coordinate files
database= c81guide.db The output database file
(solutio=) The database plate solution names
(images = c8dbcffwcs.fits) The input images
(results=) The optional results summary files
(xcolumn= 1) Column containing the x coordinate
(ycolumn= 2) Column containing the y coordinate
(lngcolu= 3) Column containing the ra / longitude
(latcolu= 4) Column containing the dec / latitude
.....
(project= tan) Sky projection geometry
(xxorder= 2) Order of xi fit in x
(xyorder= 2) Order of xi fit in y
(xxterms= half) Xi fit cross terms type
(yxorder= 2) Order of eta fit in x
(yyorder= 2) Order of eta fit in y
(interac= yes) Fit the transformation interactively
.....

Generally, this first astrometric fit had an rms (root-mean square) in x, y less than $\simeq$0.4. The second step was to fine-tune the astrometric solution using the 2MASS point source catalogue (Skrutskie et al. [2006]). We first downloaded the catalog of 2MASS point sources that lie within the image studied. Using the task CCFIND we located these sources on the output CCMAP image created earlier. The output includes a list of the objects located, with the input (2MASS) celestial coordinated and the corresponding (matched) x,y pixel coordinates. CCMAP is run again to improve on the transformation solution. In the first iteration of the task CCFIND, the parameters "sbox" and "cbox", are set equal to 21 and 9, respectively; "sbox" is the search box (width in pixels) that defines the region on the input image searched for a match and used to compute the initial source centers x and y; "cbox" is the centering box (width in pixels), that defines the region of the input (CCMAP) image used to compute the final x and y values. In subsequent iterations the parameter "sky projection" is set to "tnx" (rather than "tan" used for the first iteration). Only objects whose coordinates are successfully located on the image are written to the output coordinate file. The parameters for the task CCFIND are shown below.

PACKAGE = imcoords
TASK = ccfind
input = c81602masssex.dat The list input celestial coordinate files
output = c81602masssexout.dat The output matched coordinates files
images = ccd0160c8dbcffwcs.fits The input images
(lngcolu= 1) Column containing the ra / longitude
(latcolu= 2) Column containing the dec / latitude
(lngunit= hours) Input ra / longitude units
(latunit= deg) Input dec / latitude units
(insyste= j2000) Input celestial coordinate system
(usewcs = yes) Locate objects using the existing image wcs ?
.....
(project= tnx) Sky projection geometry
(center = yes) Center the pixel coordinates ?
(sbox = 21) Search box width in pixels
(cbox = 9) Centering box width in pixels
.....

The task CMAP is repeated with the updated coordinates from CCFIND, but using "sbox"=16 and "cbox"=6. The rms of the final accepted astrometric solution is <0.3.

Combination of the separate images is most certainly the most critical step in creating a CCD mosaic. For this purpose we used the program "SWarp" (Bertin [2010]) and obtained the final images by resampling and co-adding the fitted images using the astrometric projection defined in the WCS.

3.3 Photometric Analysis

Photometry may be performed within IRAF in a number of different ways. In this project we used the package DAOPHOT [Stetson, 1987]. DAOPHOT is a fortran software package for crowded field photometry, which has been incorporated in IRAF as a subpackage within NOAO.DIGIPHOT. The main tasks we used were:

1. DAOFIND: searches the IRAF images for local over-densities above the local background and writes out a list of detected objects.

2. PHOT: computes accurate centers, sky values and magnitudes for the list of objects in the DAOFIND output file. PHOT computes accurate centers for each object using the centering parameters defined in CENTERPARS. It computes an accurate sky value for each object, using the sky fitting parameters defined in FITSKYPARS. Finally, it computes magnitudes using the photometric parameters defined in PHOTPARS. PHOT is an aperture photometry routine. The image data characteristics are specified in DATAPARS.

3. PSTSELECT: selects candidate isolated stars in order to estimate the Point Spread Function (PSF). It reads the input photometry file and extracts the ID, the coordinates of the center, and the magnitude of the selected PSF stars.

4. PSF: builds the PSF for the specified image using the output list of PSTSELECT. Suitable PSF stars are selected interactively using the image display and image cursor. A good PSF star should not be too close to the edge of the image (as defined by parameters *datamin* and *datamax*) in the DATAPARS task and it should not contain bad pixels. The output PSF image contains parameters which define the centroid, magnitude and size of the PSF model and also the analytic components of the PSF (the PSF is an analytic function which approximates the light distributions in the cores of the selected stars).

5. ALLSTAR: computes x and y centers, sky values and magnitudes using the output list of PHOT and fitting with the PSF groups of stars on the image. Initial estimates of the centers, sky values and magnitudes are read from the phot0metry list. ALLSTAR groups the stars dynamically, performing a regrouping operation after every operation. ALLSTAR computes a weighted fit to the PSF. The weight of each pixel is computed from the radial weighting function, with weights derived from the random errors. The ALLSTAR error predictions are based on the detector noise which is characterised by the DATAPARS parameters *readnoise* and *epadu*. Finally, ALLSTAR computes two statistical parameters which characterise the goodness of fit, "chi" and "sharp". The "chi" parameter is essentially the ratio of the observed pixel to pixel scatter in the fitting residuals to the expected scatter derived from the DATAPARS parameters *readnoise* and *epadu*. It is important, therefore, for these values to be set correctly. A plot of "chi" versus magnitude should scatter around unity with no significant trend in "chi" with magnitude. "Sharp" is roughly defined as the difference between the square of the width of the object and the square of the width of PSF. "Sharp" has values close to zero for single stars, large positive values for blended doubles and partially resolved galaxies and large negative values for cosmic rays and blemishes.

Some of the IRAF tasks used here, only provide values for the parameters used by other tasks. We can recognize these tasks by the character @ at the end of their names. These tasks are:

- CENTERPARS: sets the centering algorithm parameters that control the action of the centering algorithms.
- DAOPARS: edits the DAOPHOT parameters required by all tasks which compute the PSF model.
- DATAPARS: sets the image data dependent parameters. These parameters are functions of the instrument optics, the noise characteristics and range of the linearity of the detector and the observing conditions.
- FINDPARS: edits the object detection parameters where are used by DAOFIND.
- FITSKYPARS: edits the sky fitting algorithm parameters that control the action of the sky fitting algorithms.
- PHOTPARS: edits the aperture photometry parameters. The integral of the flux within the circular apertures specified by the aperture sizes is computed by summing pixels in the aperture with the specified weighting function.

Using the previous tasks we defined the parameters for the relevant tasks. In the case of CENTERPARS the default parameter values have been proven to produce reasonable results in the majority of cases, and were adopted throughout our analysis. These parameter values are:

PACKAGE = daophot
TASK = centerpars
(calgori= none) Centering algorithm
(cbox = 5.) Centering box width in scale units
(cthresh= 0.) Centering threshold in sigma above background
(minsnra= 1.) Minimum signal-to-noise ratio for centering algo
(cmaxite= 10) Maximum iterations for centering algorithm
(maxshif= 1.) Maximum center shift in scale units
(clean = no) Symmetry clean before centering
(rclean = 1.) Cleaning radius in scale units
(rclip = 2.) Clipping radius in scale units
(kclean = 3.) K-sigma rejection criterion in skysigma

(mkcente= no) Mark the computed center
(mode = ql)

The PSF function defined in DAOPARS was *function*=auto. There are six different PSF functions that can be selected to derive the best possible matches for the cores of the selected stars. The analytic function and six look-up tables are used to compute the PSF model. The PSF model is quadratically variable over the image, with terms proportional to 1, x, y, x**2, xy, y**2. The parameter *psfrad*=13, is the radius of the circle within which the PSF model is defined. Psfrad should be a pixel or two larger than the radius at which the intensity of the brightest star of interest fades into the noise. The other parameters are default.

PACKAGE = daophot
TASK = daopars
(functio= auto) Form of analytic component of psf model
(varorde= 2) Order of empirical component of psf model
(nclean = 0) Number of cleaning iterations for computing psf
(saturat= no) Use wings of saturated stars in psf model comput
(matchra= 3.) Object matching radius in scale units
(psfrad = 13.) Radius of psf model in scale units
(fitrad = 3.) Fitting radius in scale units
(recente= yes) Recenter stars during fit
(fitsky = no) Recompute group sky value during fit
(groupsk= yes) Use group rather than individual sky values
(sannulu= 0.) Inner radius of sky fitting annulus in scale uni
(wsannul= 11.) Width of sky fitting annulus in scale units
(flaterr= 0.75) Flat field error in percent
(proferr= 5.) Profile error in percent
(maxiter= 50) Maximum number of fitting iterations
(clipexp= 6) Bad data clipping exponent
(clipran= 2.5) Bad data clipping range in sigma
(mergera= INDEF) Critical object merging radius in scale units
(critsnr= 1.) Critical S/N ratio for group membership
(maxnsta= 10000) Maximum number of stars to fit
(maxgrou= 60) Maximum number of stars to fit per group
(mode = ql)

The parameter describing the full width at half maximum of the PSF is *fwhmpsf*. From a statistical analysis it was found that a value of 5 or 6 for filter B and 4 for filter I are good choices. The standard deviation "Sigma" of the sky counts was estimated using a large number of small background regions, and it was found to be between 20 and 35. In the parameters file shown here we have set sigma=30, as an example. The parameters *Datamax* and *Datamin* are used to detect and remove bad data from the sky. In all cases we adopted *datamin*=0 in order to allow detection of as faint stars as possible, and *datamax*=42000, just below the saturation limit of the detector in order to ensure linearity. The parameter *readnoise* is the detector's electron noise and *epadu* is the detector's gain per ADU (Analog Digital Unit). We adopted *readnoise*=5 and *epadu*=0.8, as recommended in the technical characteristics pages of the Magellan Telescope website.

PACKAGE = daophot

TASK = datapars
(scale = 1.) Image scale in units per pixel
(fwhmpsf= 5) FWHM of the PSF in scale units
(emissio= yes) Features are positive
(sigma = 30.) Standard deviation of background in counts
(datamin= 0.) Minimum good data value
(datamax= 42000) Maximum good data value
(noise = poisson) Noise model
(ccdread=) CCD readout noise image header keyword
(gain =) CCD gain image header keyword
(readnoi= 5.) CCD readout noise in electrons
(epadu = 0.8) Gain in electrons per count
(exposur=) Exposure time image header keyword
(airmass=) Airmass image header keyword
(filter =) Filter image header keyword
(obstime=) Time of observation image header keyword
(itime = 1.) Exposure time
(xairmas= INDEF) Airmass
(ifilter= INDEF) Filter
(otime = INDEF) Time of observation
(mode = ql)

In the task DATAPARS we provided the appropriate value for the parameter threshold, which denotes how many units of sigma above of local sky background can a star be to be detected by DAOFIND. The other parameters are set to their default values. Finally, in the two remaining tasks FITSKYPARS and PHOTPARS all parameters are also set to their default values.

PACKAGE = daophot
TASK = findpars
(thresho= 4.) Threshold in sigma for feature detection
(nsigma = 1.5) Width of convolution kernel in sigma
(ratio = 1.) Ratio of minor to major axis of Gaussian kernel
(theta = 0.) Position angle of major axis of Gaussian kernel
(sharplo= 0.2) Lower bound on sharpness for feature detection
(sharphi= 1.) Upper bound on sharpness for feature detection
(roundlo= -1.) Lower bound on roundness for feature detection
(roundhi= 1.) Upper bound on roundness for feature detection
(mkdetec= no) Mark detections on the image display?
(mode = ql)

The photometric analysis was performed individually for each one of the 8 CCDs constituting each field. This choice was dictated by the positional variations of the point spread function (PSF) and of the background. The PSF was determined from 150 bright unsaturated stars using PSTSELECT. PSF photometry was then performed for all sources detected in each CCD mosaic using ALLSTAR by applying the corresponding PSF. The detection threshold was set at 4σ above the background. The recovery of faint and/or partially blended sources was achieved by repeating the procedure with the same PSF (after removing the already measured sources) four times. The measurement of the magnitudes was performed on the initial image using the complete list of the detected stars with the threshold reduced to 3σ above background for the last two repetitions. The distributions of the instrumental magnitude, of the error of

the magnitude, of the sharpness and of the chi square of four iterations are presented in Fig. 10. Fig. 11 shows the magnitude error versus magnitude, using different colours for the different iterations (data from CCD2 in field SMC5 are shown here as an example). Using this iterative method we detected fainter stars. As expected errors increase with magnitude.

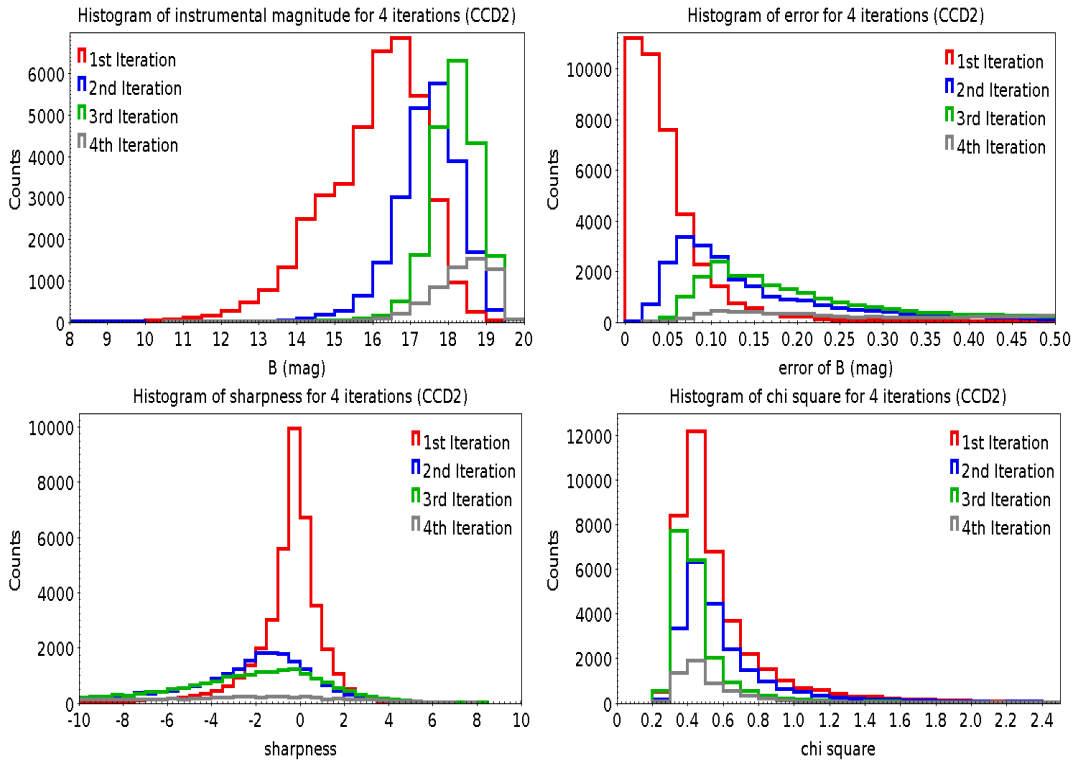

Figure 10: Distributions of the instrumental B magnitudes and the corresponding errors, sharpness and chi square values, for CCD2 in field SMC5. Different colours are used to indicate the different iterations.

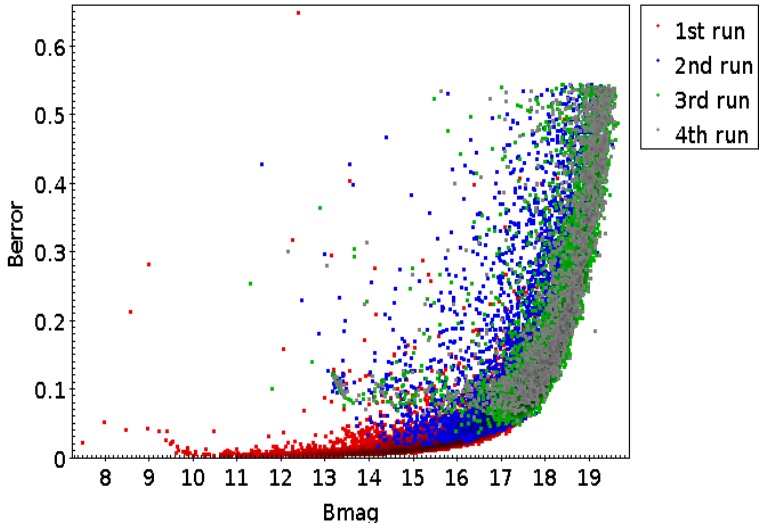

Figure 11: Errors of the instrumental magnitudes versus magnitude for the four iterations.

As discussed above, the final photometric magnitudes (as well as the corresponding errors,

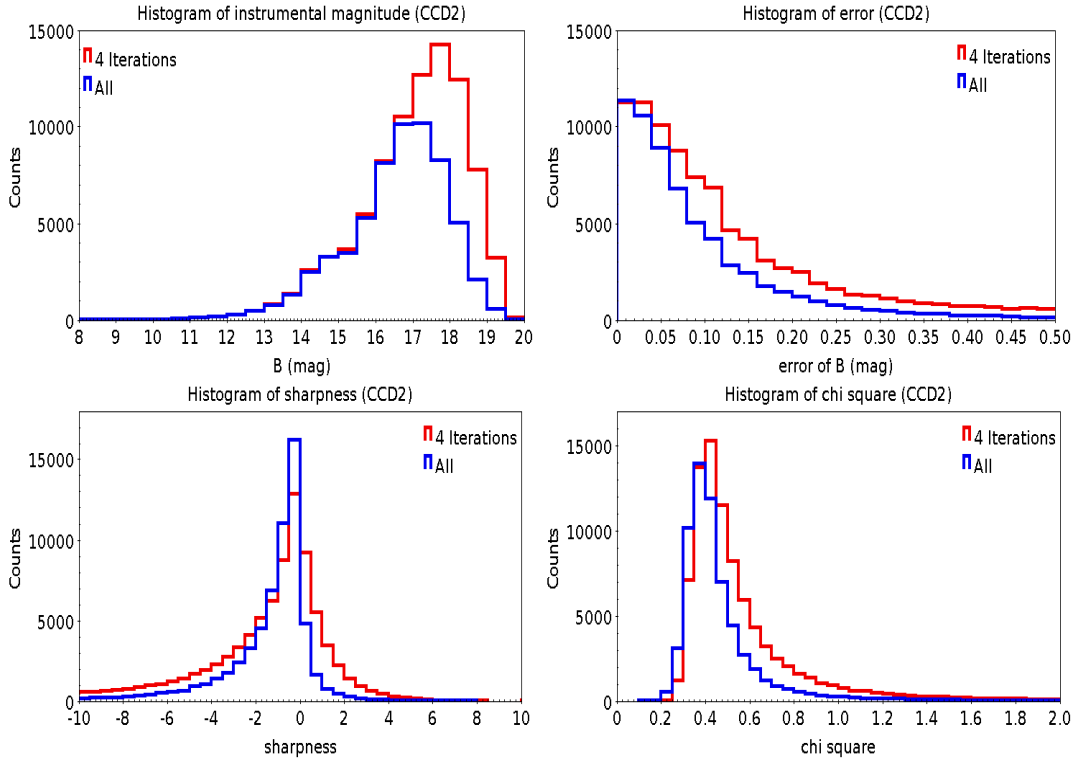

Figure 12: *Blue lines*: distribution of the photometric parameters (magnitude, error, sharpness, chi square) derived from the initial image using the combined source catalog; *Red lines:* distribution of the photometric parameters resulting from the combination of the photometry derived in the invididual iterations from the subtracted images. The histograms shown here as an example are for CCD2 in field SMC5.

sharpness and the chi square values) were derived from the initial image using as input the combination of all 4 catalogs of stars detected in the individual iterations. In Fig. 12 we show a comparison between the photometric parameters (magnitude, error, sharpness, chi square) that were derived from the initial image using the combined source catalog (blue lines) with the parameters resulting from the combination of the photometry derived in the invididual iterations from the subtracted images (red lines). In Fig. 13 we compare the error distributions for the two methods (same colour coding as in the previous figure). It is clear that the method of using the combined lists directly on the original image gives better results.

Absolute photometric calibration was achieved by using a set of secondary standards selected from isolated relatively bright stars ($B < 17.5$mag and $I < 18$mag) in the Zaritsky et al. [2002] photometric catalog. It must be noted that a significant percentage of stars in the Zaritsky catalog were actually resolved into at least two sources in our data. Clearly, such cases were not included in the sample used for the photometric calibration. The calibration correction was performed separately for each CCD image and involved only a zero-point term, as the colour term was negligible. In Table 2 we report, for the different CCDs the range of zero-point values obtained (column 3) per field (column 1) and filter (column 2), as well as the total number of sources detected, N_{tot} (column 4) and the number of sources for which the error in the instrumental magnitude was below 0.2mag, $N_{\sigma \leq 0.2}$ (column 5). By applying the zero-point corrections for each CCD we derived the B and I magnitudes of the stars within the CCD. In the rest of our analysis we have retained stars with photometric instrumental errors below 0.2 mag. In most cases more than 85% of the complete source list fulfilled this criterion. The final errors include both instrumental magnitude errors and zero-point uncertainties. The saturation limit for all fields corresponds to $\simeq 14$ mag.

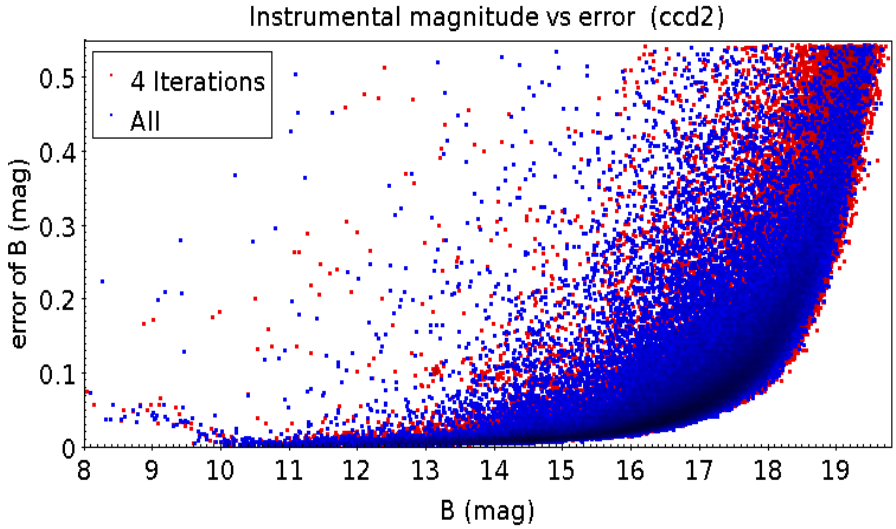

Figure 13: Instrumental errors versus instrumental magnitudes for the B filter data using the two different combination methods, as described in the text. Colour coding is the same as in Fig. 12. Data for CCD2 of field SMC5 are shown as an example.

Table 3 lists the photometric results for a total of 1,068,803 sources [1]. Column 1 gives the field number, column 2 the CCD number within the specified field, column 3 lists the unique ID of the source, columns 4 and 5 give the J2000 coordinates for each star, and columns 6-7 and 8-9 provide the magnitudes and magnitude errors (including zero point error) for the B and I filters, respectively. In Fig. 14 we show the CCD numbering system in each field. It is noted that the orientation was different for field SMC6 (the field of view was turned by 90 degrees counterclockwise, for guiding reasons).

Table 2: The range of average photometric zero points per field and filter, the total number of sources detected and the number of sources with instrumental error less than 0.2 mag.

Field	Filter	Zero Point range	N_{tot}	$N_{\sigma \leq 0.2}$
SMC3	B	6.051 ± 0.009 - 6.391 ± 0.013	411074	365703
SMC3	I	4.636 ± 0.010 - 4.833 ± 0.009	391140	331254
SMC4	B	4.813 ± 0.016 - 5.112 ± 0.010	338836	317232
SMC4	I	4.324 ± 0.007 - 4.547 ± 0.010	415748	349697
SMC5	B	5.506 ± 0.010 - 5.743 ± 0.009	417994	369608
SMC5	I	4.783 ± 0.016 - 5.000 ± 0.013	467574	377979
SMC6	B	5.172 ± 0.007 - 5.314 ± 0.011	327808	299546
SMC6	I	4.043 ± 0.006 - 4.220 ± 0.013	287903	247182

B Images: In each field, the final B image consists of six dithered frames with a total exposure time of 720s. Each frame had an exposure time of 120s. The photometric parameters, derived with the method described above, are shown in Fig. 15. It is noted that the FWHM of the PSF was somewhat different in the different fields, as was ascertained using the IRAF IMEXAM package in a sample of isolated stars. We found FWHMPSF=5 for SMC3, SMC5 and SMC6 and FWHMPSF=6 (SMC4), and sigma=20. The instrumental error and sharpness distributions are similar in all fileds. Field SMC5 seems to go a bit deeper than the other fields. It also has somewhat higher errors which may be due to the detection of fainter blended stars.

[1] The table is provided in its entirety in electronic form only in the Strantzalis et al. [2019]

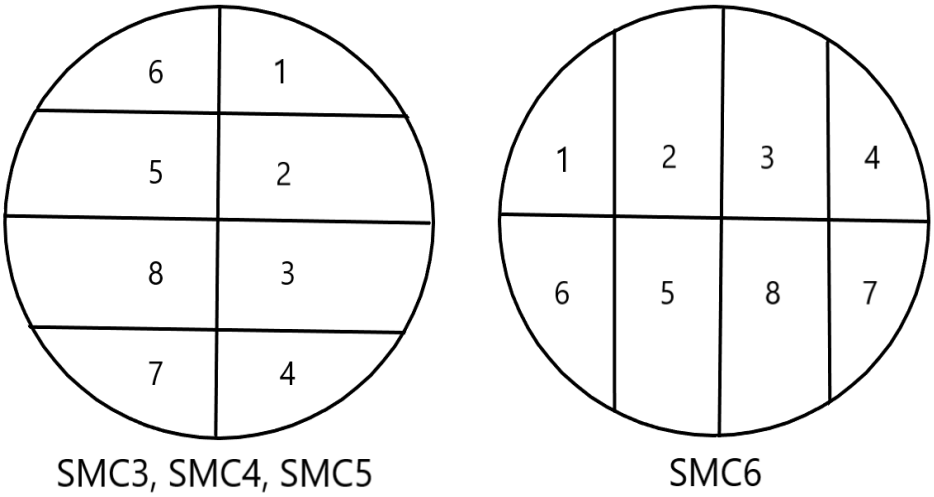

Figure 14: The CCD mosaic orientation for each field

Table 3: Catalogue of detected sources (the full catalogue is available in electronic form).

Field	CCD	Source-ID	RA (J2000)	DEC (J2000)	Bmag	e_Bmag	Imag	e_Imag
3	1	1	13.81901	-72.11543	17.855	0.013	18.022	0.015
3	1	2	13.89466	-72.11497	17.274	0.013	17.541	0.014
3	1	3	13.72003	-72.15316	16.807	0.013	17.000	0.019
3	2	19356	13.95725	-72.27774	19.050	0.013	19.016	0.017
3	2	19357	14.01589	-72.27467	22.627	0.05	21.48	0.10
4	1	283237	12.35343	-73.14637	17.966	0.012	16.631	0.016
4	1	283238	12.37794	-73.14379	19.292	0.013	19.213	0.04
4	1	283239	12.29457	-73.14603	22.31	0.05	22.02	0.17

It is noted that in field SMC3 the chi-square values are systematically higher than in the other fields, possibly indicating a mismatch with the adopted point spread function.

I Images: In each field, the final I image consists of two dithered frames. Each frame had an exposure time of 30s, thus the final image had a total exposure time of 60s. The values used for the parameters FWHMPSF and sigma were 4 and 30, respectively, for all fields. The distribution of the instrumental magnitudes, errors, sharpness and chi square values are shown in Fig. 16. It is noted that instrumental errors are slightly larger in SMC3 and SMC5. In both of these fields the photometry is deeper. It is possible that the detection and measurement of fainter, generally blended, stars increases the noise level, explaining the observed effect. Also, in all fields the chi square values are higher than for the B images.

R Images: The final R image consists of two dithered frames. Each frame had an exposure time of 30s, thus the final image had a total exposure time of 60s. The parameters FWHMPSF and sigma were set to 4 and 40, respectively, for all fields. Fig. 17 shows the distribution of the derived photometric parameters for each field. The instrumental errors are generally higher than in B, although the chi square and sharpness values are similar. Using B and R instrumental magnitudes we could construct deeper colour magnitude diagrams (see Section XX). However, the R magnitudes could not be calibrated using secondary standards, as the Harris and Zaritsky [2004] catalogue used for B and I do not provide R magnitudes. No other existing catalogue provides appropriate secondary standards. For example, the catalogue of Massey [2002] does provide R magnitudes, but their stars are too bright, generally above the

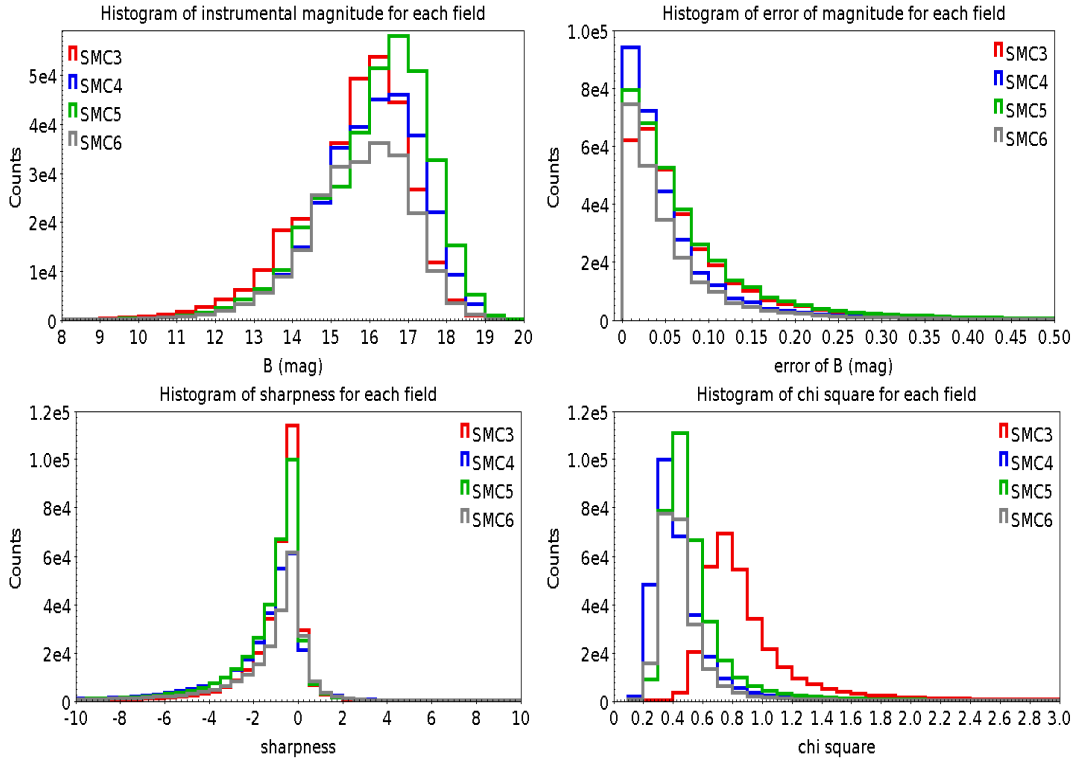

Figure 15: Distribution of instrumental magnitudes, errors, sharpness and chi square values for the B images in the four fields, denoted in different colours (red for SMC3, blue for SMC4, green from SMC5 and grey for SMC6).

saturation limit of the IMACS images. For this reason we did not further use the R data in this study.

V Images: The final V images consist of 8 dithered frames. Each frame had an exposure time of 90s, thus the total exposure time was 720s. Although the V images are deep and in principle they would be very useful in our analysis, they had to be rejected, as they suffer from severe systematic errors probably related to erroneous application of adaptive optics corrections, on site. An example of these systematic effects is shown in Fig. 18, where a systematic colour term is introduced to the photometry in different regions across the field of view. The error is severe and could not be corrected for, therefore the V data were not further used in our study. The same systematics were present in all fields.

Finally, it is noted that one more field was observed, field "SMC7". However, the images for this field were obtained during twilight and suffer from very high and variable background, leading to shallower photometry and larger errors shown in magenta in Fig. 19. The results for this field were not further considered in our study.

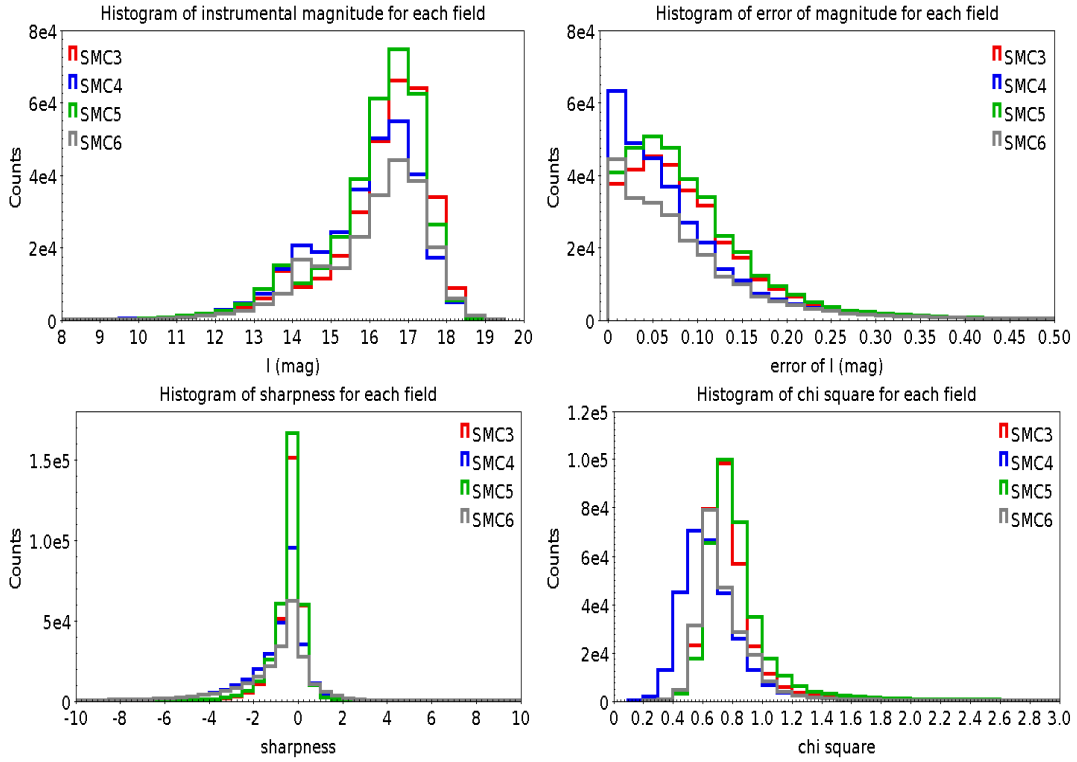

Figure 16: Distribution of instrumental magnitudes, errors, sharpness and chi square values for the B images in the four fields, denoted in different colours, as in Fig. 15.

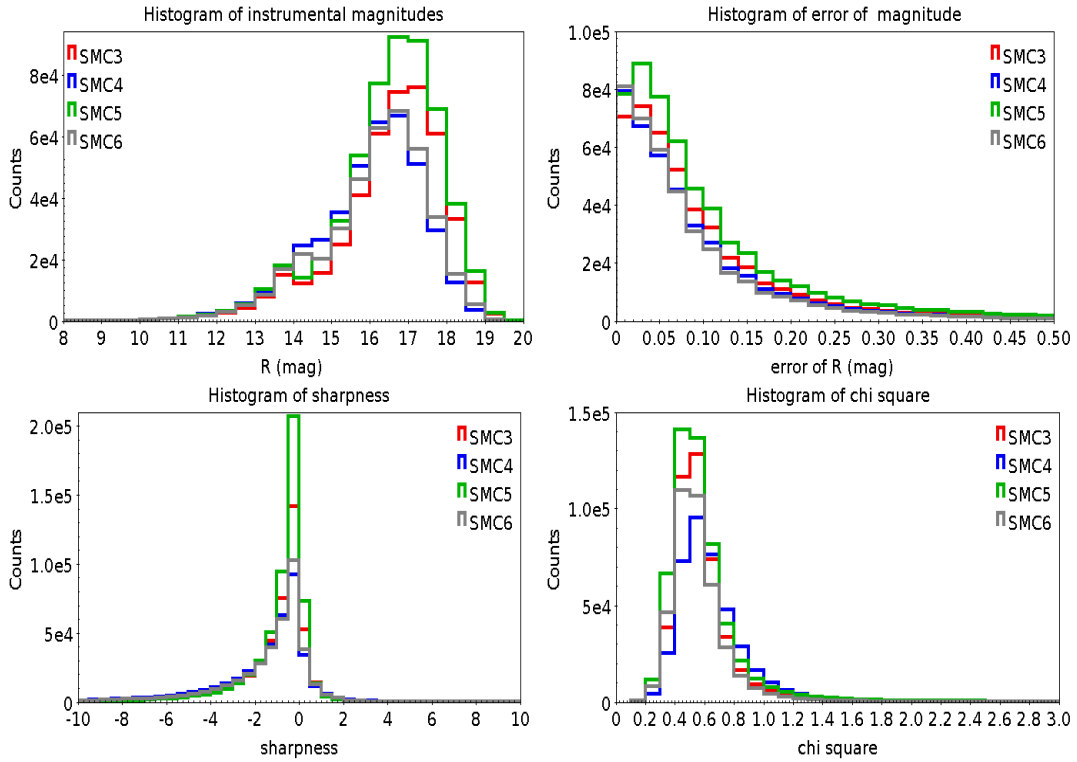

Figure 17: Distribution of instrumental magnitudes, errors, sharpness and chi square values for the R images in the four fields, denoted in different colours, as in Fig. 15.

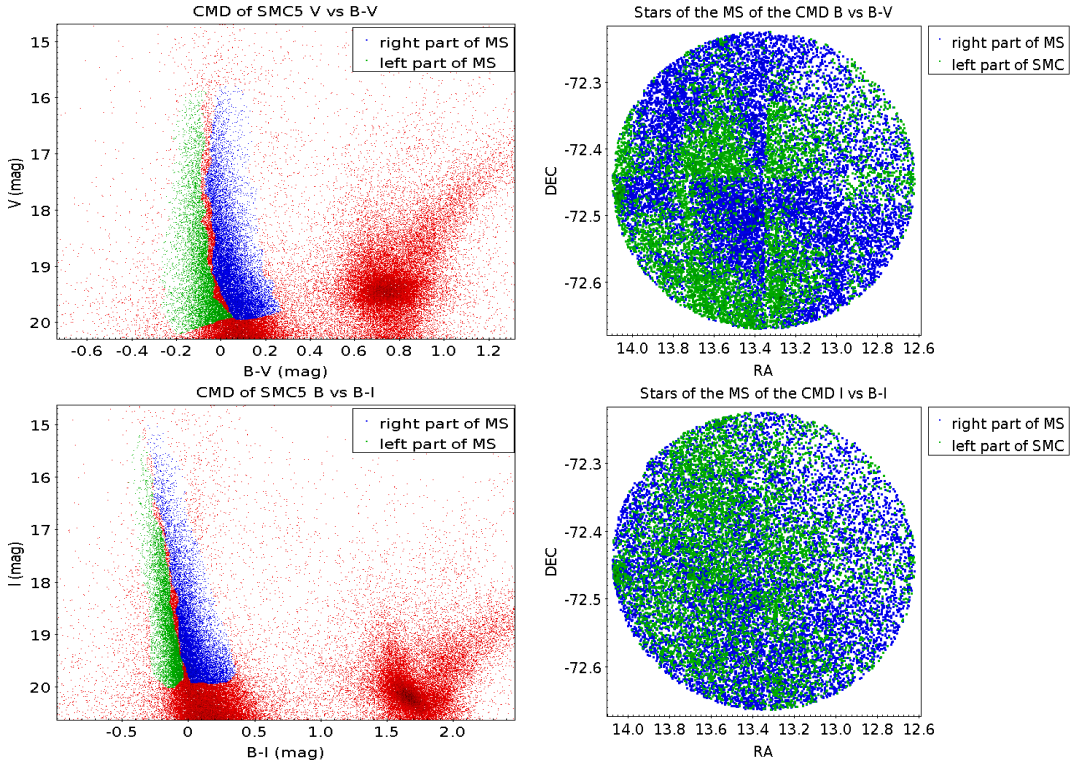

Figure 18: Systematic effects present in the V images. On the top panels we show the Colour magnitude diagram in a field in V. The left and right parts of the main sequence, marked in different colours are plotted on the field of view on the right panel. The same is repeated for I and B-I in the bottom two panels, for comparison.

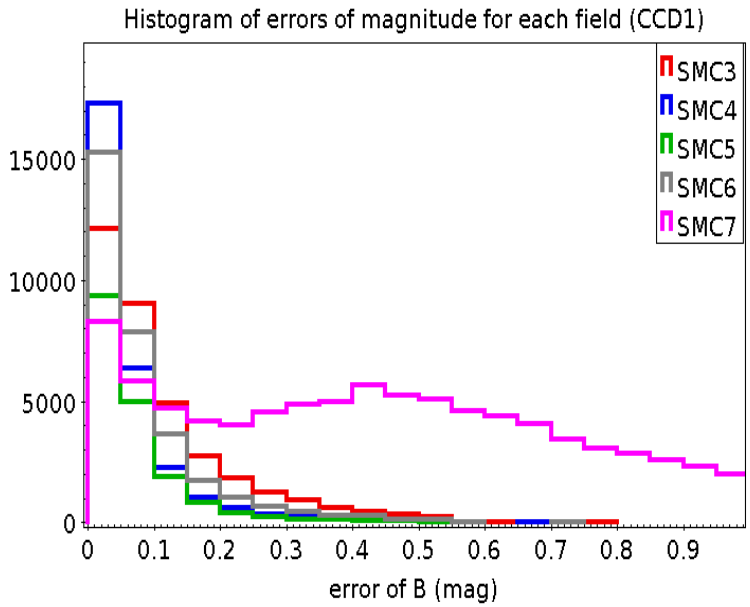

Figure 19: The B magnitude instrumental error distribution in all fields, showing that in SMC7 the errors are much larger.

3.4 Completeness Evaluation

The term "completeness" is used to signify the percentage of stars recovered by the reduction process. This percentage is expected to decrease with increasing magnitude and increasing star number density. Interpretation of the colour magnitude diagrams in terms of star formation history requires a good undestanding of the photometric completeness in different magnitude bins. To achieve this we followed the method of artificial star experiments: "Artificial" stars of different magnitudes, constructed from the observed PSF, are added in the actual images, and then run through the reduction pipeline. The completeness is estimated from the number of artificial stars recovered, in each magnitude bin. We used the standard artificial star package in DAOPHOT, ADDSTAR. The PSF model adopted for the artificial stars was identical to the one derived for the observed stars in each CCD. In order to minimize source confusion, the number of the artificial stars added per CCD was limited to 8% of the total number of sources detected in the particular area, in order not to change significantly the star number density. The artificial stellar magnitudes were equally distributed within the instrumental magnitude range of the observed stars. The artificial stars were randomly placed on the images, which were subsequently analyzed in exactly the same way as described in the previous subsection. An artificial star was considered as recovered by the detection and photometric reduction process, if its final position lay within 0.7 pixels from the original one, where 0.7 pixels correspond to more than twice the positional scatter of the astrometric solution. The percentage of recovered stars defines the completeness, per magnitude bin. The same procedure was repeated 10 times in order to increase the statistical sample and estimate the uncertainty in the completeness values derived. In Table 4 we give the range of the B and I magnitudes for which completeness falls to 50% and 20%, in the four fields studied. The 50% completeness level ranges from 23.2 mag (in B, for field SMC3) to 20.3 mag (in I, for field SMC4).

Table 4: The range of 50% and 20% completeness levels in each filter and field.

Field	Filter	Completeness 50% (mag)	Completeness 20% (mag)
SMC3	B	22.4-23.2	22.9-23.9
SMC3	I	21.3-22.1	22.0-22.5
SMC4	B	20.9-21.4	21.7-22.2
SMC4	I	20.3-21.1	21.0-21.5
SMC5	B	21.5-22.9	22.5-23.5
SMC5	I	21.5-22.2	22.1-22.6
SMC6	B	21.0-21.8	21.5-22.4
SMC6	I	20.8-21.1	21.2-21.5

It is noted that the I data are shallower than the B data in all fields, and therefore the 50% completeness levels occur at brighter magnitudes. We also investigated the dependence of completeness on location across the CCD mosaic, in each field. To this purpose, we divided, the corner CCDs into 4 regions and the central CCDs into 8 regions of equal area, and estimated the completeness in each one of these subregions.

Fig. 20 and Fig. 21 show the spatial distribution of the 50% and 20% completeness levels in the four fields. The colour scale is in colour bins that correspond to about (or somewhat more than) 1 σ.

Finally, we investigated the dependence of completeness on star number density. Fig. 22 shows the dependence of the 50% and 20% level of completeness on the projected surface density for the 8 different CCDs constituting the mosaic of the four different fields. As we can see there is no significant correlation. It should be mentioned here that completeness levels can be much lower in dense star clusters. Such high densities were not considered in this analysis.

In addition to these artificial star experiments, which are sufficient for the present study, we also embarked on the execution of much more extended artificial star experiments which

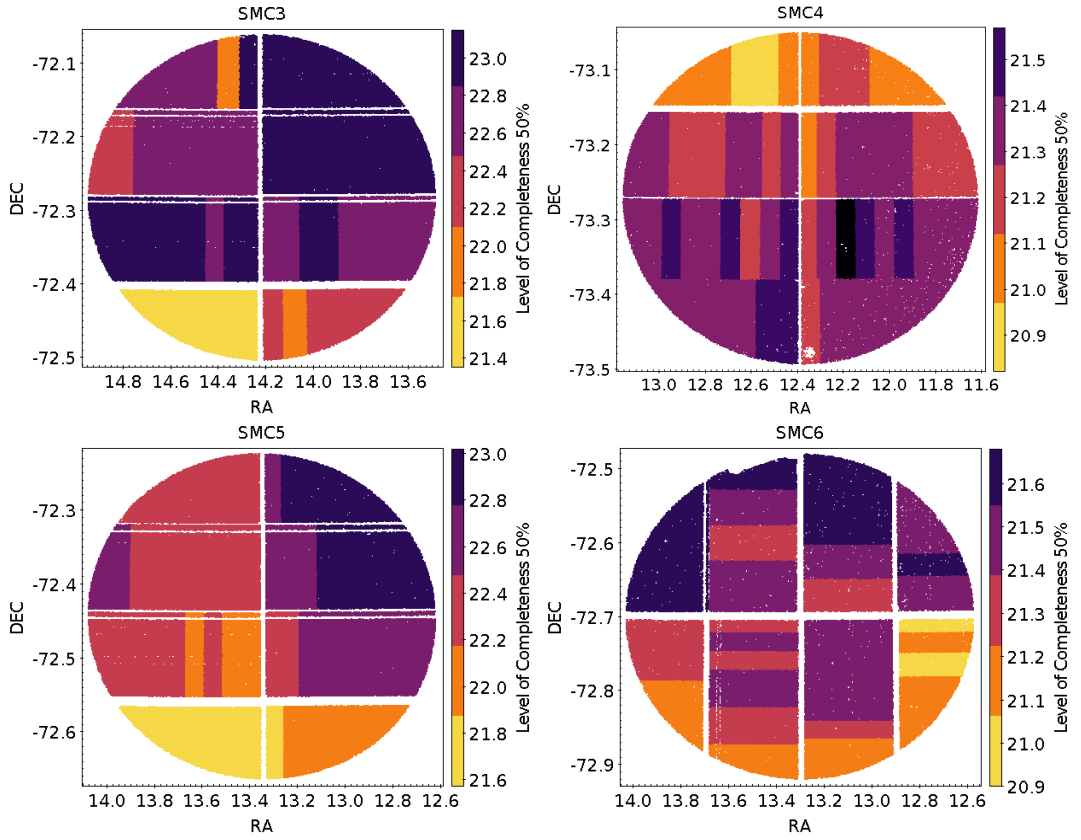

Figure 20: The distribution of the 50% completeness level in B. The colours change in steps of one sigma.

are necessary for the full Star Formation History analysis that is planned as a follow-up of the present work, following the method described in Cole et al. [2014] (see also Lianou and Cole 2013, Cignoni et al. 2012, Cole et al. 2007). For each CCD, the sample of the artificial stars used was increased to about 700000, with 250000 stars brighter than 18.5mag and 450000 stars fainter than this magnitude level. A total of 22400000 artificial stars were added in all four fields. The input distribution of magnitudes of the artificial stars is shown on the top panel of Fig. 24, while on the bottom panels the recovered distribution of magnitudes is shown for B and I (for CCD2 in SMC3 as an example). A total of 87% of artificial stars were recovered in B and 84% in I (for the example of SMC3- CCD2). Fig. 23 shows the colour magnitude diagram of the injected (ADDSTAR magnitudes) and recovered (DAOPHOT) magnitudes. In these experiments an artificial star was considred as "recovered" if its final position lay within 5 pixels from the original one.

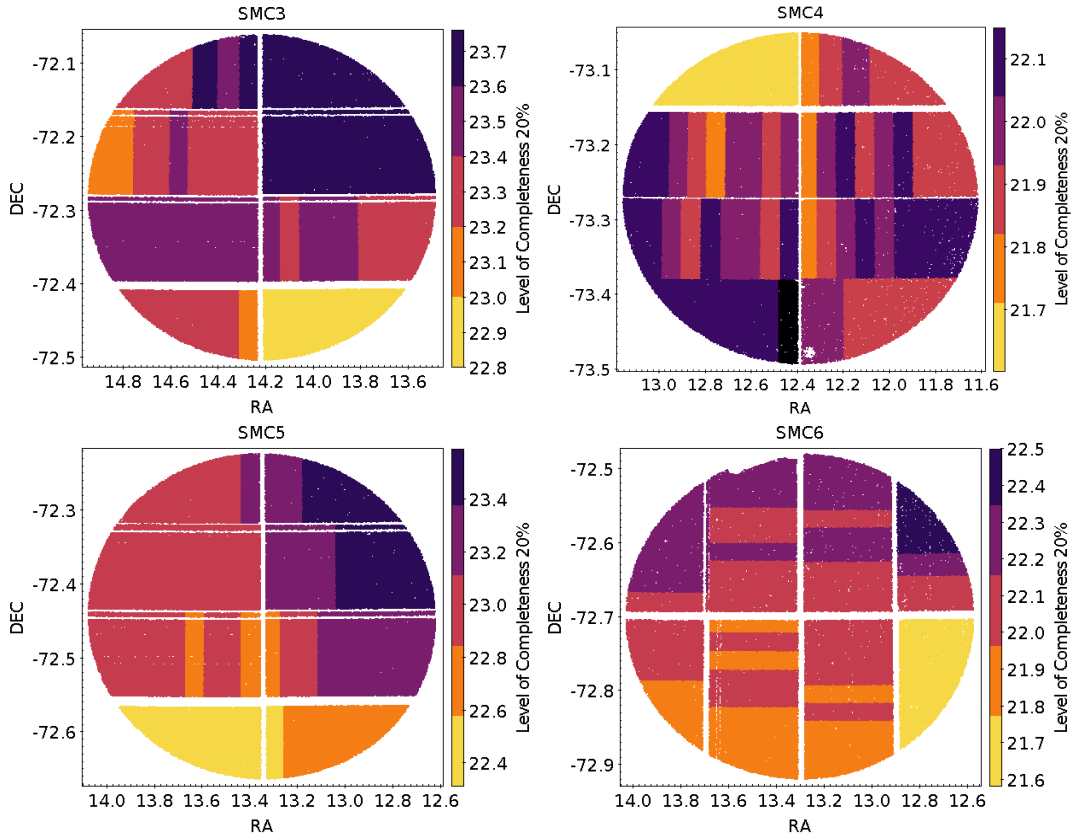

Figure 21: The distribution of the 20% completeness level in B. The colours change in steps of one sigma.

3.5 Colour Magnitude Diagrams

We constructed B versus $B-I$ colour-magnitude diagrams (CMDs) for the four fields (Fig. 25, 26, 27, 28). Each CMD corresponds to a 0.152 square-degree area. The error bars shown on the left side of the CMDs denote representative photometric uncertainties, which include both instrumental errors and the uncertainty in the zero-point correction. The differences in limiting magnitude and completeness between fields SMC3 and SMC5 on the one hand and SMC4 and SMC6 on the other, which have been discussed in the previous section, are also apparent on the CMDs.

The CMDs show a well defined main sequence (MS) reaching up to the saturation magnitude of $B \simeq 14$ mag, indicating the presence of young populations in these fields. The subgiant (SG) and red giant (RGB) branches are clearly defined. The red clump (RC) is also evident, as well as its vertical extension to brighter magnitudes caused by the presence of younger stellar populations in the fields studied. It is noted that in the case of field SMC4, the RC appears to be strongly elongated (and strongly inclined, essentially along the reddening vector) towards redder colours. This is caused by differential interstellar reddening, which is particularly severe in this field. Fig. 30 shows the effect of differential reddening on the CMD for each CCD. The RC and the MS show larger scatter in CCDs 1,2,3 than in CCDs 4,8,7. The MS turnoff region corresponding to intermediate age and older populations, between 22mag and 23mag is also clearly delineated, especially in fields SMC3 and SMC5. It is evident, therefore, that stellar populations of different generations are present in the SMC Bar. This is better demonstrated in Fig. 29 where indicative PARSEC isochrones [PAdova and TRieste Stellar Evolution Code Bressan et al., 2012, Marigo et al., 2017] of different ages are overlayed on the CMD of SMC3, as an example. We have assumed here a distance modulus of 18.96 mag [Scowcroft et al., 2016],

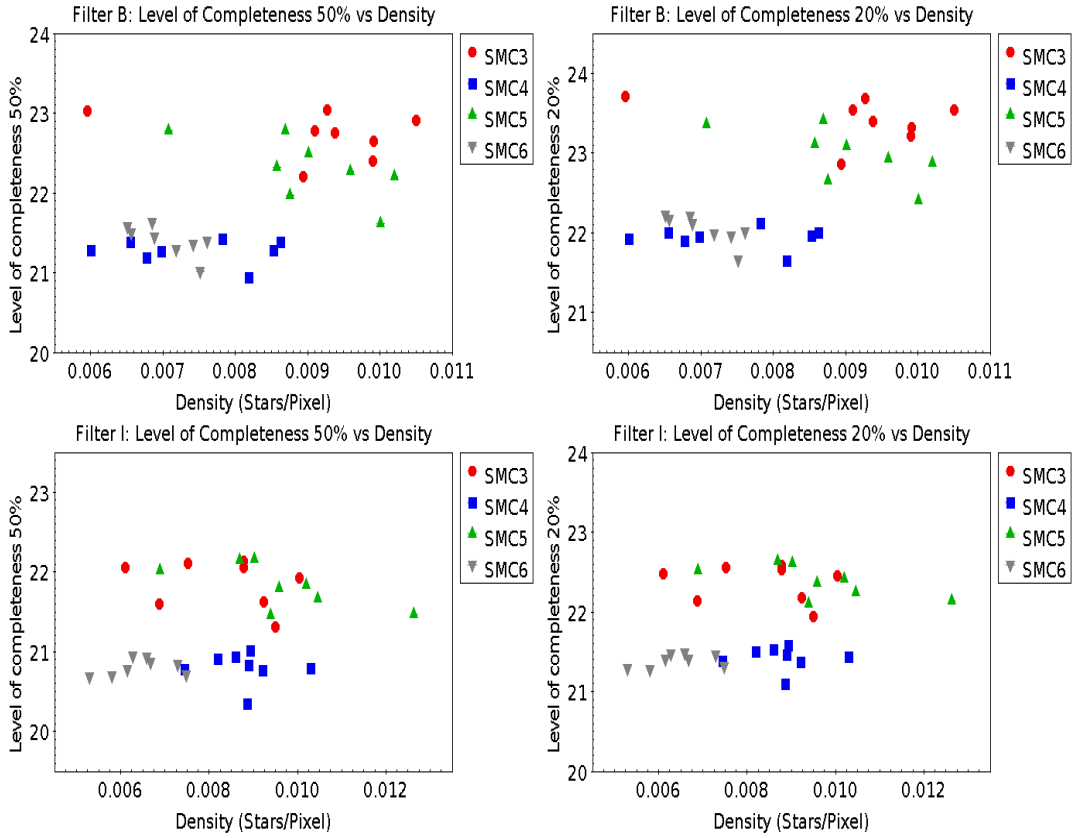

Figure 22: The dependence of completeness on star number density in the four fields studied.

an interstellar reddening value of $E(B-I) = 0.08$mag (with a dispersion of 0.04mag) as derived from the Haschke et al. [2011] extinction map for this region. These authors have adopted a Milky-Way like dust extinction curve (for which $R_B \approx 1.83$) to derive the interstellar absorption A_B. Recently, Yanchulova Merica-Jones et al. [2017] found a larger value of $R_{B475} = 2.65 \pm 0.11$ in the SMC Bar. Assuming this higher value, interstellar absorption towards field SMC3 is estimated to be $A_B \simeq 0.21$mag, for $E(B-I) = 0.08$mag.

The isochrones shown have ages of 4 and 7 Gyr (green lines), and 40 Myr and 80 Myr (blue lines)[2]. Although these isochrones are only indicative, we have assumed a lower metallicity of Z=0.0009 for the older isochrones and a higher metallicity of Z=0.004 for the two younger ones. These assumptions are not intended to constitute an accurate representation of the age-metallicity relation of the SMC, however, they are in broad agreement with the age-metallicity relations derived for SMC clusters and field populations (e.g. Da Costa and Hatzidimitriou 1998, Kayser et al. 2007, Rubele et al. 2018), assuming $Z_{\odot}$=0.0152 [Bressan et al., 2012]. It is clear that the MSTO region is well bracketed by the 4 and 7 Gyr isochrones, suggesting enhanced star formation during this period.

It is noted that although for the purposes of this analysis we have used an average value for the distance modulus, it is well known that the SMC displays large line-of sight depth which needs to be taken into account when interpreting a CMD in terms of populations of different ages. For example in Field 5, using RR-Lyrae variables from Kapakos and Hatzidimitriou [2012], we find a dispersion of about 7 kpc, which is consistent with the values derived for Cepheids in this region by Subramanian and Subramaniam [2015]. Such a range in distance would correspond to an age spread of about $\pm$0.5Gyr (for the older isochrones shown here).

[2]The isochrones shown do not change significantly when using the MIST [Dotter, 2016], or the Dartmouth models [Dotter et al., 2008]

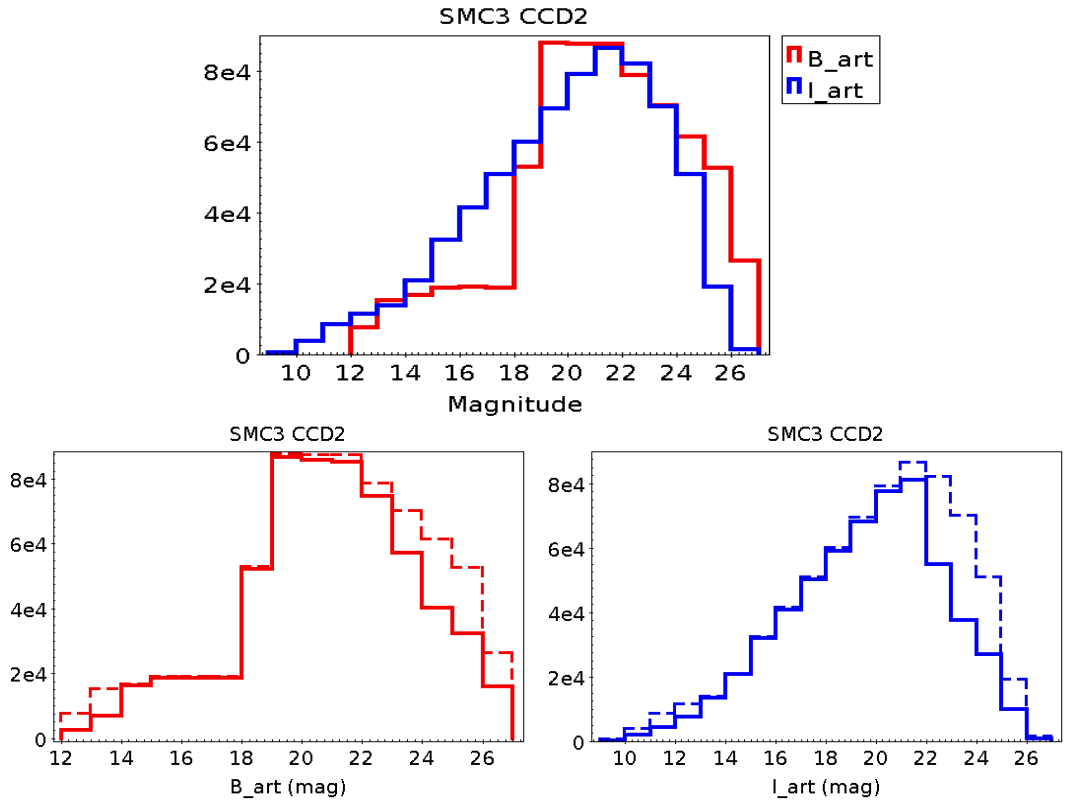

Figure 23: Top panel. The magnitude distribution of artificial stars added in CCD2-SMC3 (red line for B and blue line for I). Bottom panels. Distribution of recovered artificial star magnitudes for the CCD2-SMC3, in B and I, shown in solid lines. The dotted lines show the injected distribution of artificial stars, as in the top panel.

4 Star Formation History

We used the method of Dohm-Palmer et al. [1997] to estimate the Star Formation History (SFH), i.e. the star formation rate as a function of look-back time, in the four fields studied here. The method is applied to MS stars and it is useful for studying the relatively recent SFH, as the time resolution and accuracy degrade with increasing look-back time. We apply the following equation to the MS stars.

$$C(M_v, B-I) = \int_{logm_1}^{logm_2} \int_{t_1(logm)}^{t_2(logm)} \phi(logm, t) R(t) dt dlogm \quad (1)$$

where ϕ is the initial mass function (IMF) normalized to unity, m is the stellar mass in $M_\odot$, $R(t)$ is the star formation rate in of ${M_\odot}^{-1}$ and t is look-back time. We assume that the IMF is independent of time and that the MS is simply a function of magnitude and not colour. In order to account for the decrease in completeness as fainter magnitudes are considered, we assigned to each star a weight depending on completeness (so a larger statistical weight is given to fainter stars). For example for a star with a magnitude corresponding to the 50% completeness level, we give a weight of 2, so we would count it as two stars.

We divided the CMD in discrete bins along the MS. The stars in a single bin along the MS are assumed to have the same initial mass. However, each bin may include stars of different ages. For example, assuming that there is a MS turnoff at a specified magnitude, the MS bin at that magnitude level would include stars of that age, and stars of the same mass but belonging to younger generations. Eq. 1 can be rewritten as,

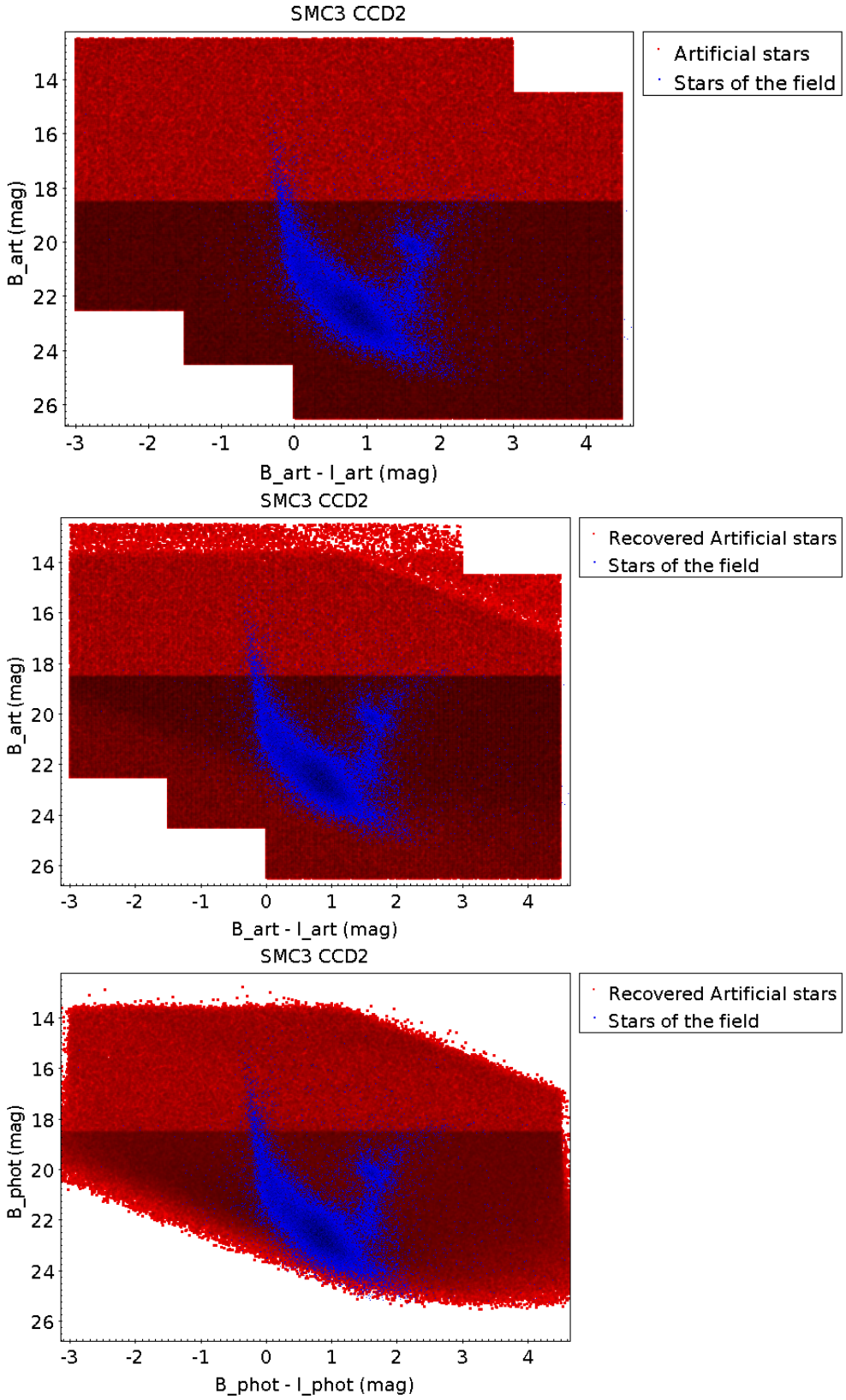

Figure 24: CMD of the field stars of SMC3, CCD2 with *Top panel*: additional $\sim$ 700000 artificial stars, *Middle panel*: recovered artificial stars, *Bottom panel*: recovered artificial stars using the derived magnitudes from DOPHOT.

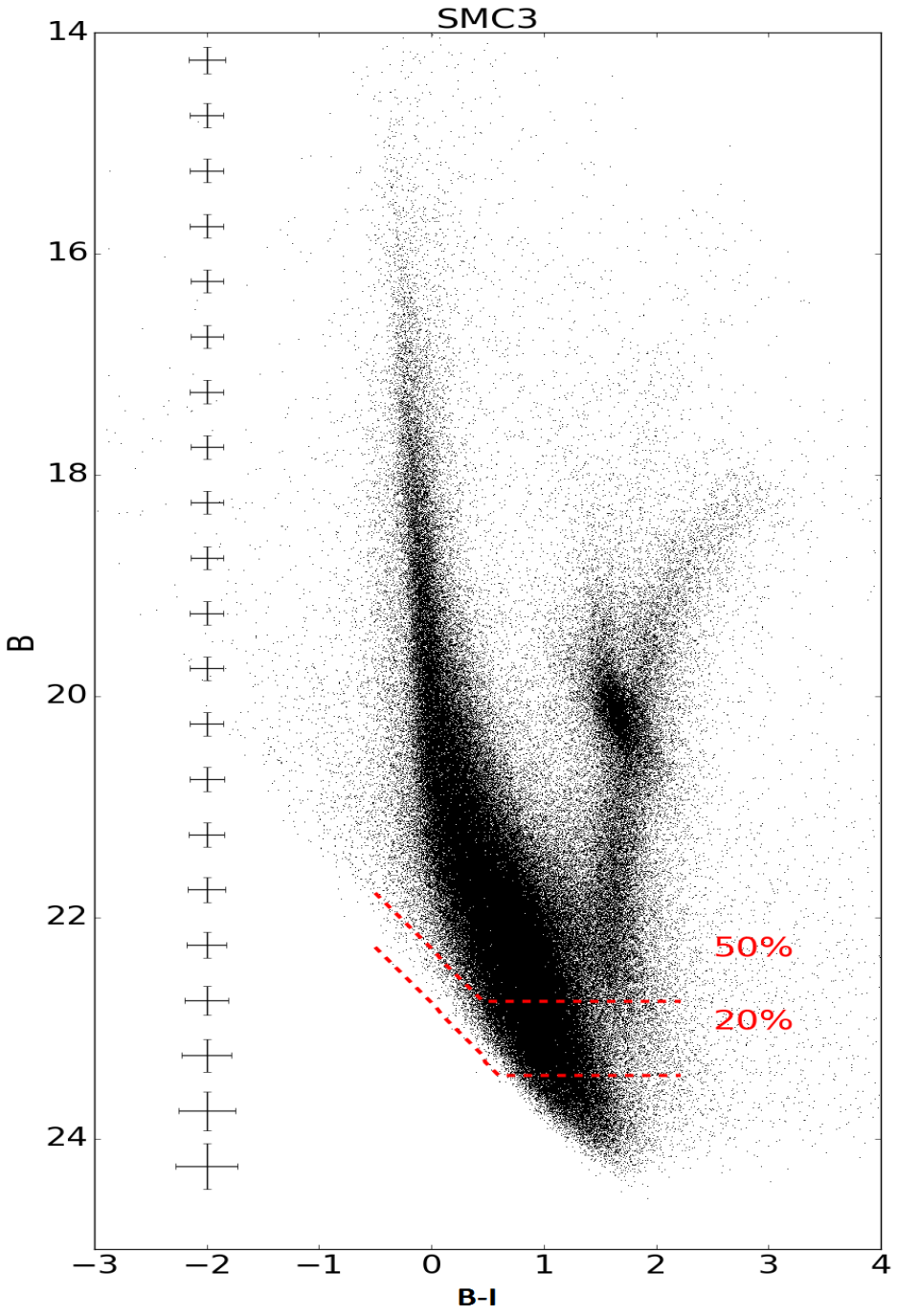

Figure 25: B versus $B - I$ colour magnitude diagram of field SMC3. The red dashed lines indicate the corresponding 50% and 20% completeness levels.

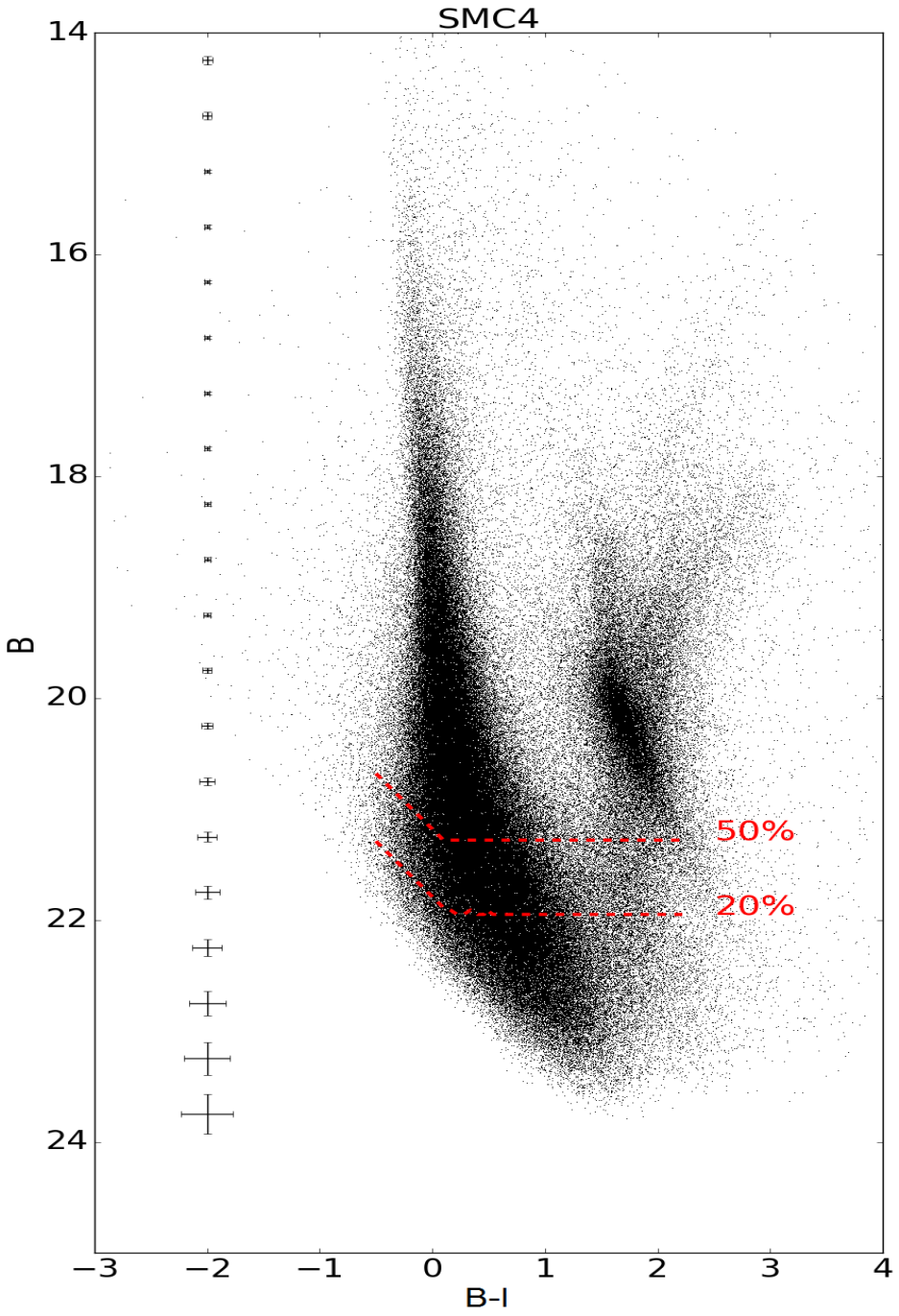

Figure 26: B versus $B - I$ colour magnitude diagram of field SMC4. The red dashed lines indicate the corresponding 50% and 20% completeness levels.

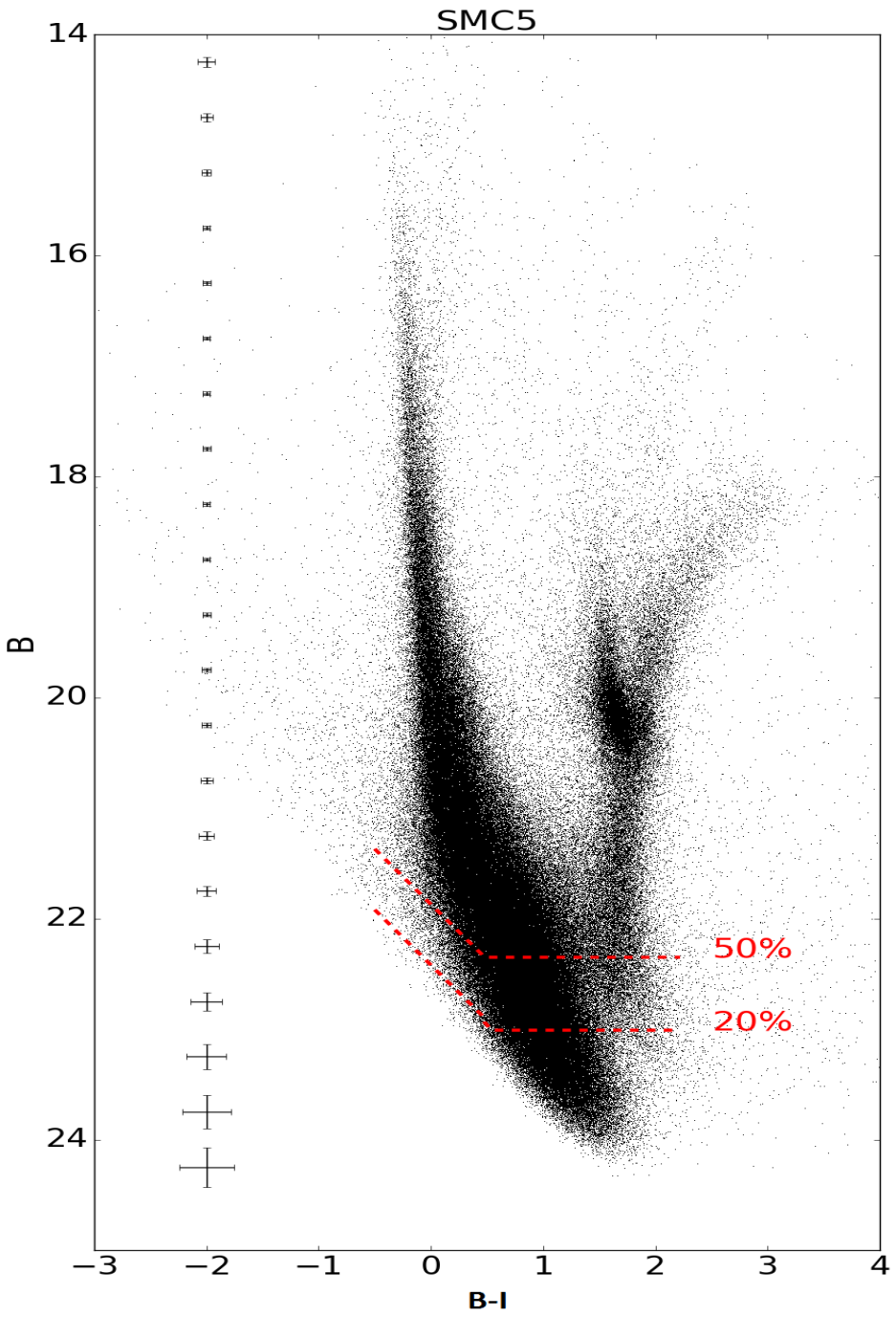

Figure 27: B versus $B - I$ colour magnitude diagram of field SMC5. The red dashed lines indicate the corresponding 50% and 20% completeness levels.

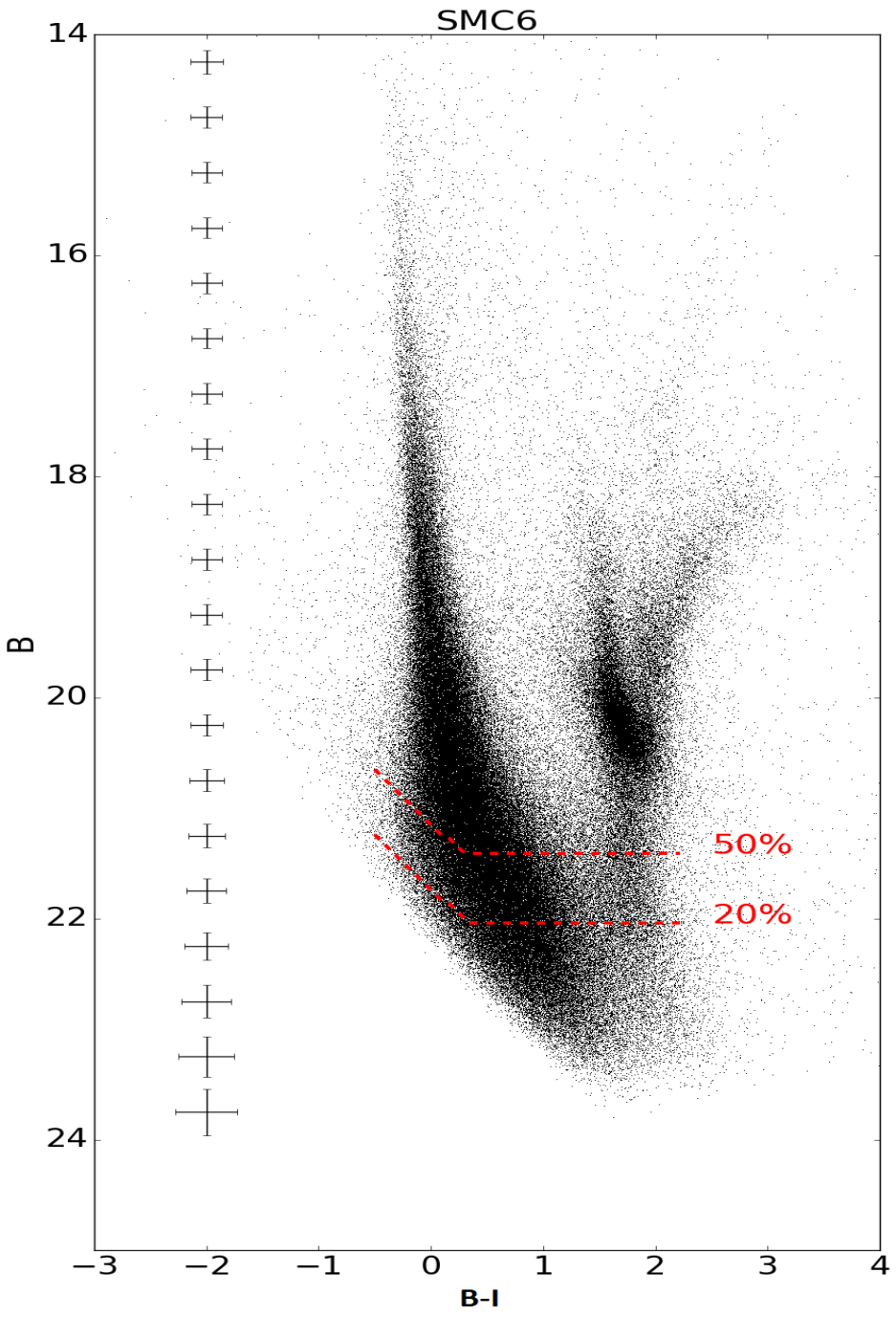

Figure 28: B versus $B - I$ colour magnitude diagram of field SMC6. The red dashed lines indicate the corresponding 50% and 20% completeness levels.

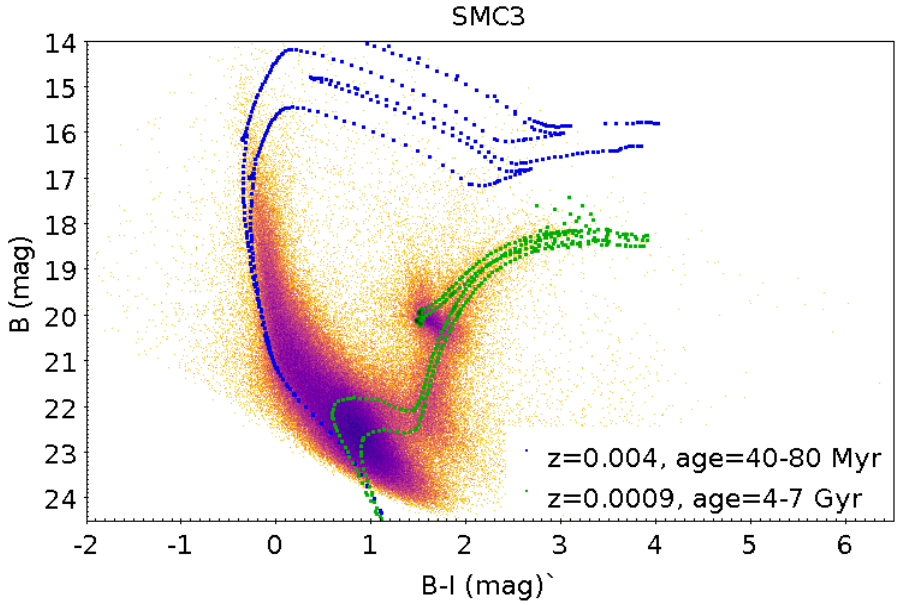

Figure 29: CMD of field SMC3 with PARSEC isochrones overlayed. The older isochrones shown have ages of 4 and 7 Gyr and a metallicity of Z=0.0009 (green lines). The younger isochrones shown have ages of 40 and 80 Myr and Z=0.004 (blue lines).

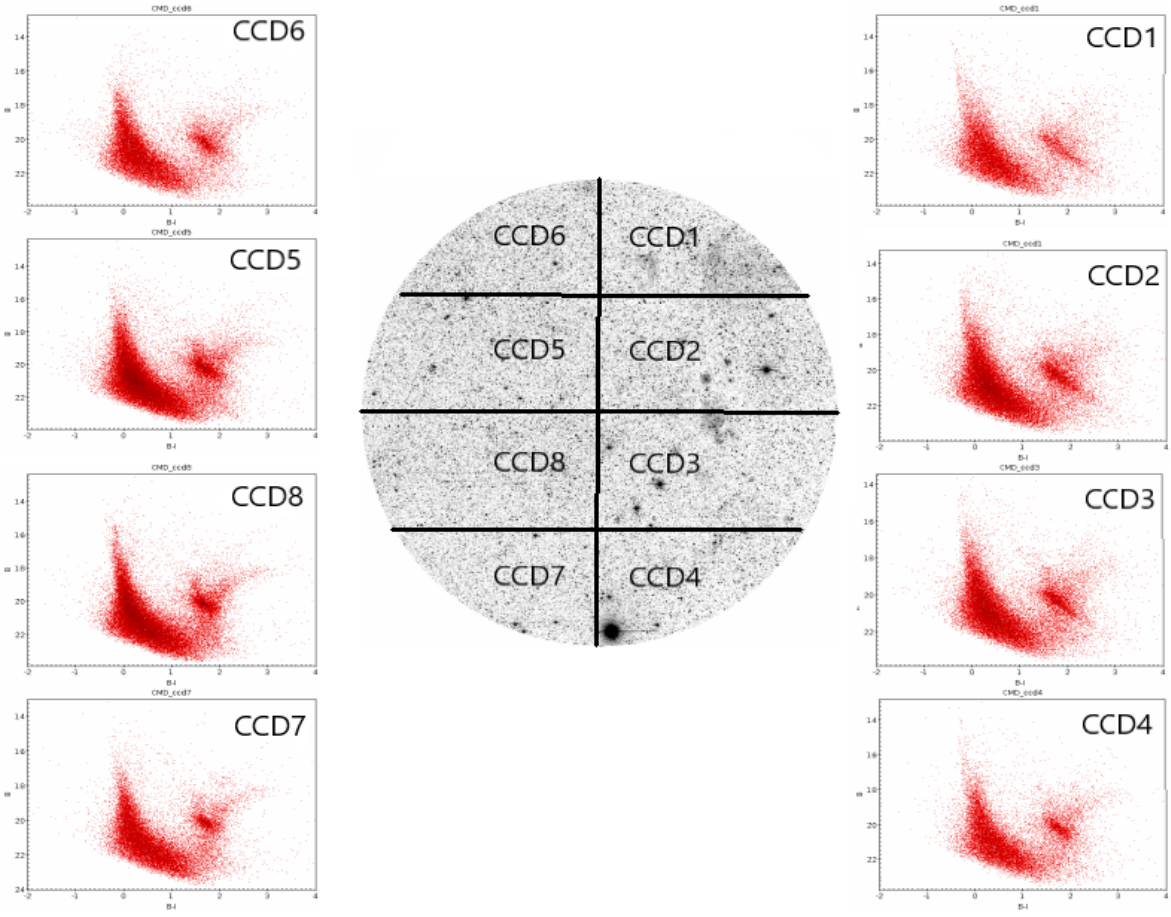

Figure 30: CMDs for each CCD of the field SMC4.

$$C_n(M_n) = \phi(logm_n)\Delta logm_n \sum_{n=o}^{TO} R_n \Delta t_n \tag{2}$$

where n is the bin number. $\Delta \log m_n$ and $\Delta\ t_n$ depend on the bin size. $\Delta \log m_n$ can be expressed as

$$\Delta logm_n \equiv \left(\frac{dlogm}{\Delta M_v}\right)_n \Delta M_v \tag{3}$$

where the ΔM_v is the bin width and the fraction $d(logm)/(dM_v)$ results from the relationship between M_v and $logm$ along the MS. Δt_n is the difference TO_n-TO_{n-1} in turnoff ages for consecutive bins. So Eq. 3 yields for the n-th bin

$$\begin{aligned} C_n(M_v) = \phi(logm_n)\left(\frac{dlogm}{\Delta M_v}\right)_n \Delta M_v \,(R_1 TO_1 + \ldots \\ + R_2(TO_2 - TO_1) + R_n(TO_n - TO_{n-1})) \end{aligned} \tag{4}$$

where R_1 is the SFR for the youngest bin and R_2 is the next youngest.

It is clear that in this method we have to know the SFR for the youngest bin. Working backward in time, we can calculate the SFR as a function of look-back time. One disadvantage of this procedure is the fact that the calculation of the SFR for the fainter/older bins depends on the ones determined for the younger bins. The brighter bins are usually sparse, thus statistical errors are high and they propagate all the way through to the older/fainter bins.

Along with the SFR values for different look-back times, we estimated the corresponding uncertainties, by taking into account the statistical uncertainty in the stellar number counts and in the completeness levels derivation.

Another issue is that occasionally negative SFRs are derived, due to over-subtraction, caused by statistical fluctuations. Examples are shown in Fig. 31 for field SMC3, and in(Fig. 32) for SMC4, SMC6, for ages older than 8 Gyr. Generally, the low number of counts in the youngest bins contribute to the uncertainties in the calculated SFR in all bins. An additional caveat that needs to be mentioned is related to the saturation limit of our photometry at $B \simeq 14$mag, which leads to an overestimation of the SFR in the first MS bin considered.

In order to calculate C for a specific bin using Eq. 4, we need three functions. The first function provides the relation between absolute magnitude M_v and stellar mass m along the MS. The second function gives the relation between M_v and turnoff age along the MS. Both these functions were derived using the PARSEC evolutionary tracks and are shown below:

$$logm = -0.141 M_v + 3.21, R^2 = 0.9919 \tag{5}$$

and

$$log(age) = 0.354 M_v + 1.80, R^2 = 0.9982 \tag{6}$$

The third function is the initial mass function (IMF). In this work we adopted a power law IMF, with a Salpeter [1955] slope of Γ=-1.35 for the mass range from 0.5 to 100 $M_\odot$. Our SFR results do not depend strongly on the assumed IMF, for the mass range of interest. Indeed, application of the Kroupa [2001] or the Chabrier [2003] IMFs, for stellar masses down to $\simeq 0.8 M_\odot$, yielded very similar results.

Clearly the calculated SFRs depend on the evolutionary tracks used. The models we used here did not include treatment of convection and mass loss, and did not take rotation into account. The effect of these assumptions on our results are difficult to quantify. The uncertainties we provide for the SFRs are only random errors. Another possible source of bias is our assumption that the IMF is the same for all ages and metallicities.

It is noted that we used normalized IMF functions. The normalization constant was chosen so that the integral over all masses is unity. The following equation gives the normalized Salpeter IMF used:

$$\phi(logm)dlogm = 0.394\left(\frac{m}{M_{\odot}}\right)^{-1.35} dlogm \quad (7)$$

Fig. 31 and Fig. 32 show the resulting SFH in the four fields, assuming two values for the metallicity, Z=0.004 (red triangles) which is more appropriate for ages below 1Gyr and Z=0.0009 which better matches the metallicity of older populations (black circles). The choice of these two metallicities has been discussed in the previous section. We indicate on the diagrams the location of the 50% and 20% completeness limits with vertical dotted lines. We also show for comparison the SFH for the same regions from Harris and Zaritsky [2004], who used a Salpeter IMF and a metallicity of Z=0.001, and from Rubele et al. [2018] who used a Kroupa IMF and a varying metallicity. It is clear that the SFR for the younger populations derived here are too high compared to these studies. This is mainly due to the caveat mentioned earlier, i.e. the fact that we "start" building our SFH for populations older than about 10 Myr, ignoring younger stars, which are present in the fields, but not included in the CMDs due to saturation. Therefore, our results can be used to discuss trends of the SFR with time, but not to derive absolute values of the SFRs.

Despite the differences in completeness, a general conclusion that can be drawn from Fig. 31 and Fig. 32 is that in all four fields star formation has been more intense recently (<1Gyr). From about 1 to about 3 Gyr ago SF activity seems to have been lower, while it also peaked between 4 and 8 Gyr ago. This is in excellent agreement with the appearance of the MSTO region on the field-scale CMDs discussed in the previous section. In the two fields with fainter completeness limits (fields SMC3 and SMC5) the peak in SFR occurs close to an age of 6-7 Gyr. The SFH beyond the 50% completeness limit is less reliable, therefore for fields SMC4 and SMC6 the displacement to somewhat different ages of the SFR peaks beyond 4 Gyr is probably an artifact. Small differences can also be expected from variations in interstellar reddening and line-of-sight distance in the different fields. Field SMC4 (and less so, field SMC6) is on average further away than field SMC3 (and less so, than field SMC5) by at least 5kpc, due to the inclination of the SMC Bar Scowcroft et al. [2016]. In addition, interstellar reddening is higher (and variable) particularly in field SMC4, as previously mentioned. Using a larger average distance (68 kpc) and average reddening (E(B-I)=0.15 mag) value for SMC4 we recalculated the SFH, which was found to be identical within the errors. Therefore, our adoption of a uniform value for the distance and reddening of all fields does not compromise our results.

In Fig. 33 and Fig. 34, we show the SFH for stars younger than 1Gyr, in all four fields. These diagrams are zoomed-in versions of the diagrams shown in Fig. 31 and Fig. 32, with the bin width being smaller. In all fields, the SF activity seems to have been intense over the past $\simeq$ 100 Myr, decreasing rapidly over a period of few hundred Myr (look-back time). Moreover, in fields SMC4 and SMC6, there appears to have been a small enhancement in SF around 700-800 Myr ago.

Generally, many recent studies agree that there are (at least) two major periods of intense SF activity in the SMC main body, one very recently and one around 4-6 Gyr ago Rezaeikh et al. [2014], Weisz et al. [2013], Cignoni et al. [2012], Noël et al. [2009]. The fact that SF activity has been very intense over the past 100-200Myr is also corroborated by the burst of cluster formation observed over roughly the same period Bitsakis2018,Nayak2018. It is interesting to compare our rough estimate of the SFH of the SMC Bar with the results of the full analysis of Rubele2018 for the same fields. These authors derived the spatially resolved star formation history across the entire main body and Wing of the SMC, using the VISTA survey of the Magellanic Clouds (VMC), in the YJK_s filters and a CMD reconstruction method. As it can be seen in their Fig. 33 and Fig. 34, the SFR decreased from 5Myr to about 300Myr ago (with a small increase around 200 Myr), showed a small enhancement around 800 Myr ago, and then a more significant increase between 3 and 8 Gyr ago. These results are in very good agreement with our findings. On the other hand the results of Harris and Zaritsky [2004], which suffer from much larger uncertainties particularly in the crowded regions studied here, display much poorer agreement with our results.

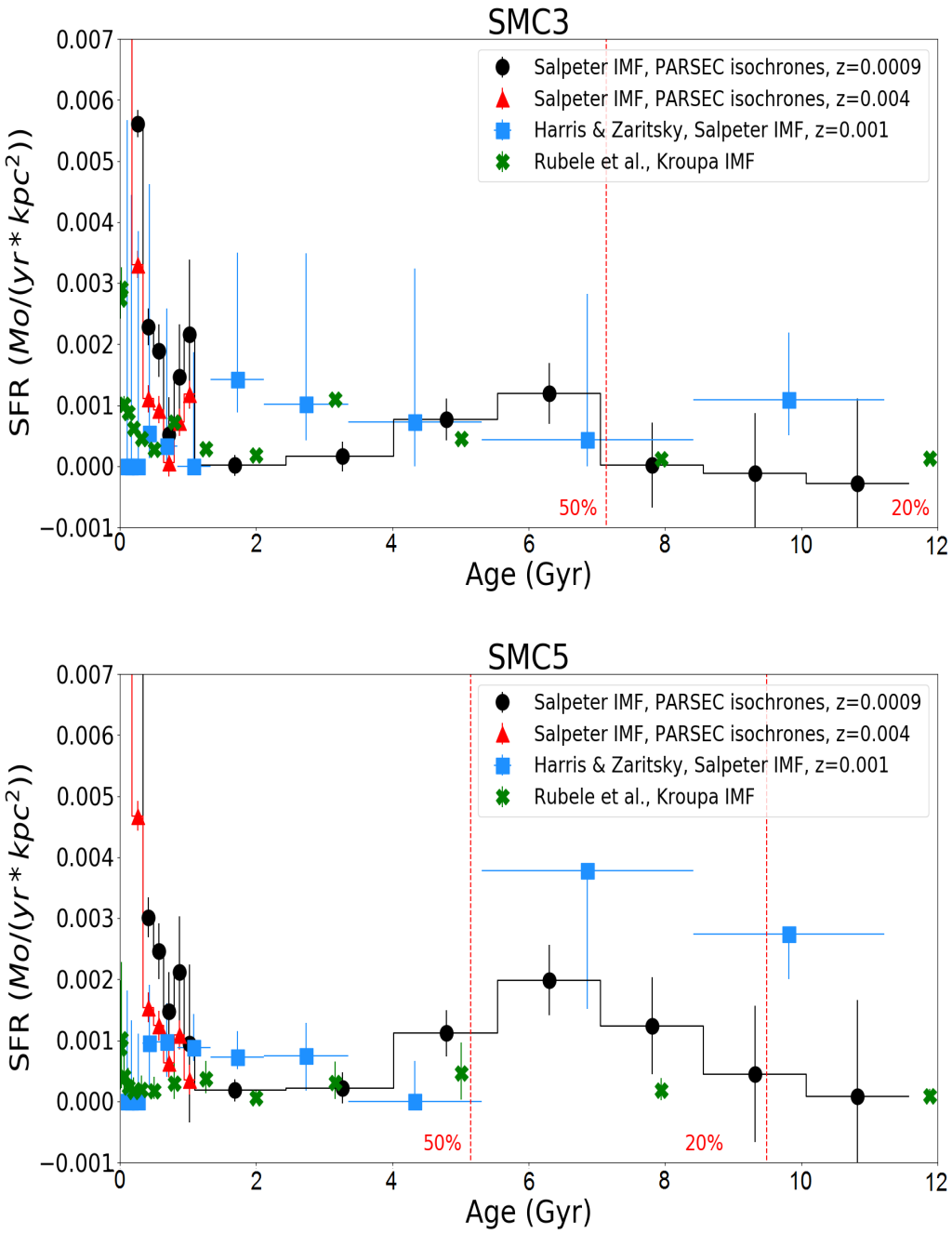

Figure 31: SFRs as a function of look-back time for fields SMC3 and SMC5, up to 12Gyr ago, derived from the completeness-corrected luminosity functionc of MS stars. We used the PARSEC stellar evolutionary tracks, adopting a metallicity of Z=0.0009 (black line) and of Z=0.004 (red line). Orange points correspond to the results of Harris and Zaritsky [2004] for the same fields, and green points correspond to the results of Rubele et al. [2018].

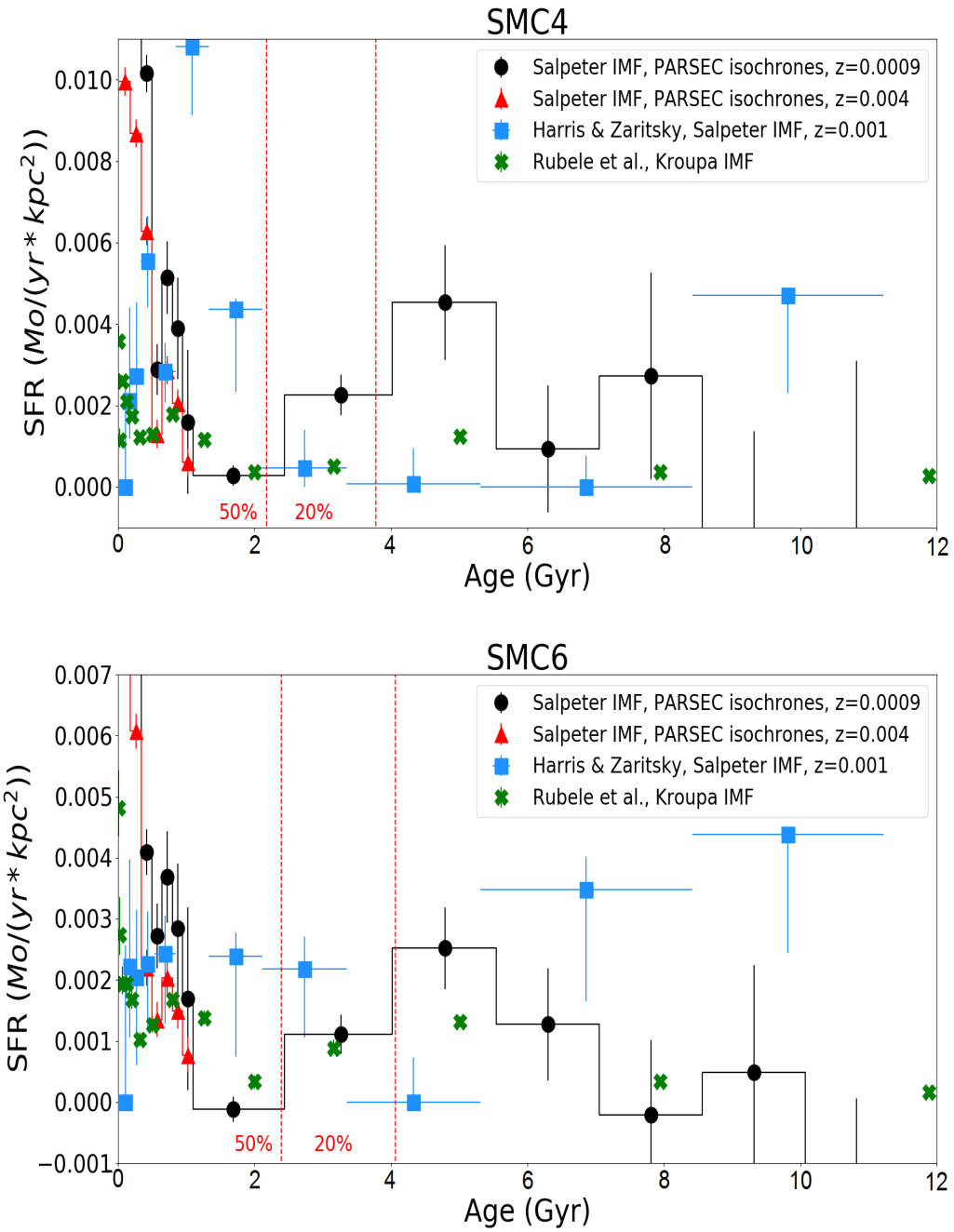

Figure 32: SFRs as a function of look-back time for fields SMC4 and SMC6, up to 12Gyr ago, derived from the completeness-corrected luminosity functionc of MS stars. We used the PARSEC stellar evolutionary tracks, adopting a metallicity of Z=0.0009 (black line) and of Z=0.004 (red line). Orange points correspond to the results of Harris and Zaritsky [2004] for the same fields, and green points correspond to the results of Rubele et al. [2018].

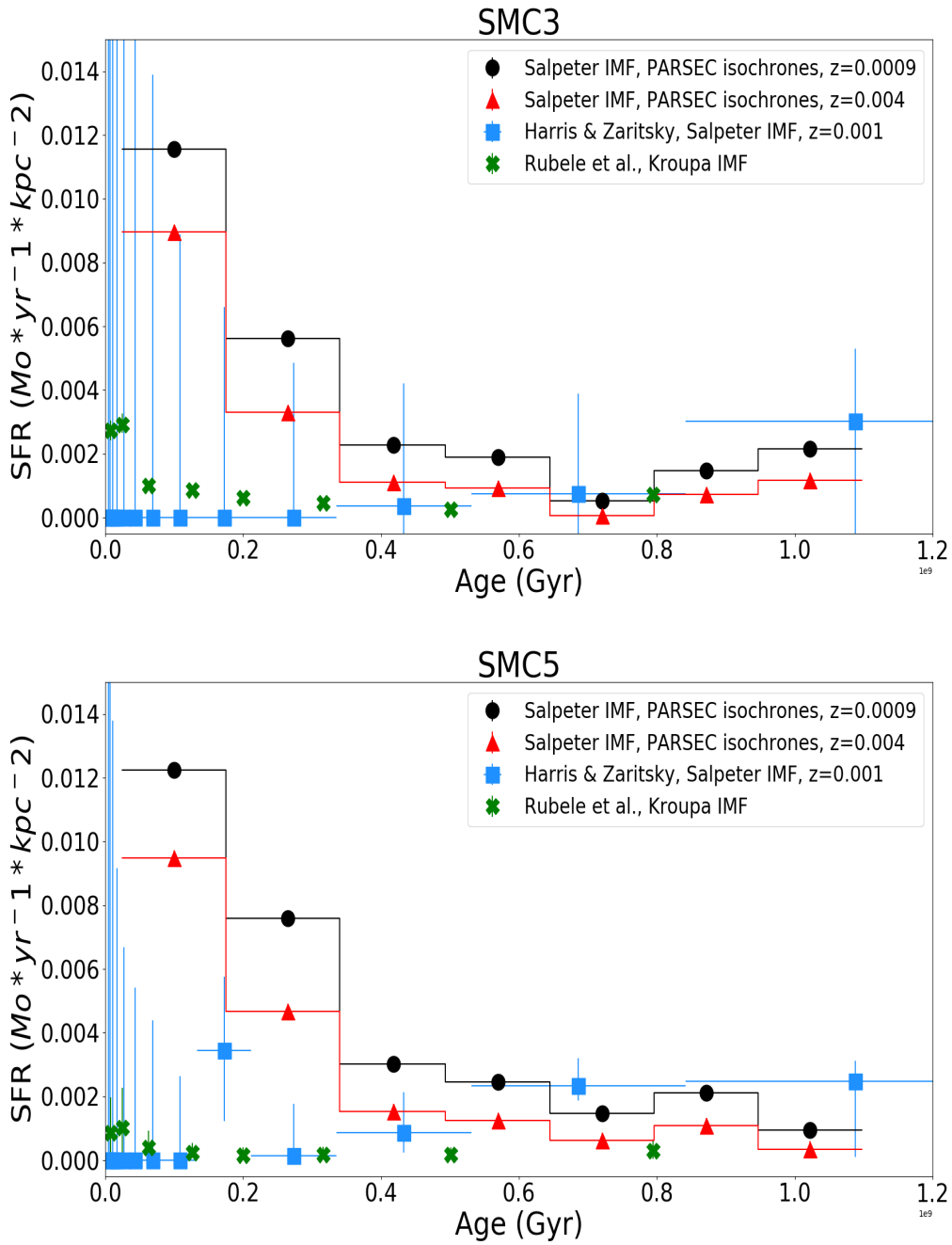

Figure 33: SFRs in fields SMC3 and SMC5 up to 1.2 Gyr ago, derived from the completeness-corrected luminosity function of MS stars. We used the PARSEC stellar evolutionary tracks adopting a metallicity of Z=0.0009 (black line) and Z=0.004 (red line). Orange points correspond to the results of Harris and Zaritsky [2004] for the same fields, and green points correspond to the results of Rubele et al. [2018].

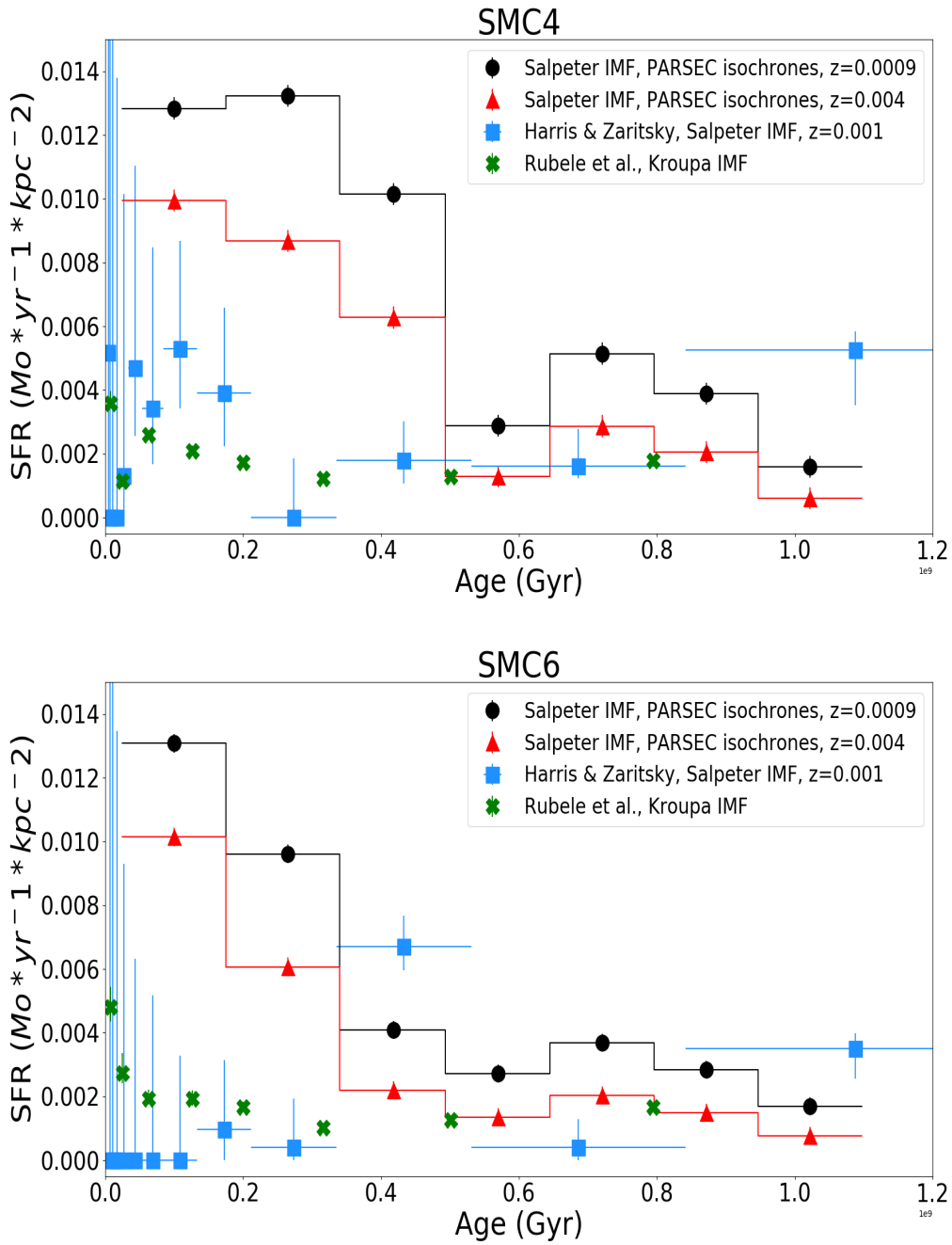

Figure 34: SFRs in fields SMC4 and SMC6 up to 1.2 Gyr ago, derived from the completeness-corrected luminosity function of MS stars. We used the PARSEC stellar evolutionary tracks adopting a metallicity of Z=0.0009 (black line) and Z=0.004 (red line). Orange points correspond to the results of Harris and Zaritsky [2004] for the same fields, and green points correspond to the results of Rubele et al. [2018].

5 Luminosity Functions

The Luminosity Function (LF) is a fundamental descriptor of stellar populations, serving as a census of stars of different magnitudes, M. Specifically, it measures the number of stars in the interval M, M+dM for a given wavelength band and a given volume element (Gilmore and Roberts 1988). In this section we utilise the LF of the MS stars alone, to search for differences in the mixture of populations of different ages across the fields studied here. The MS luminosity function was derived by counting the number of stars in each one of the cells defined along the MS ridge line, shown as black and red areas in Fig. 35. All these cells are equal in area (magnitude × colour) and have the same magnitude range.

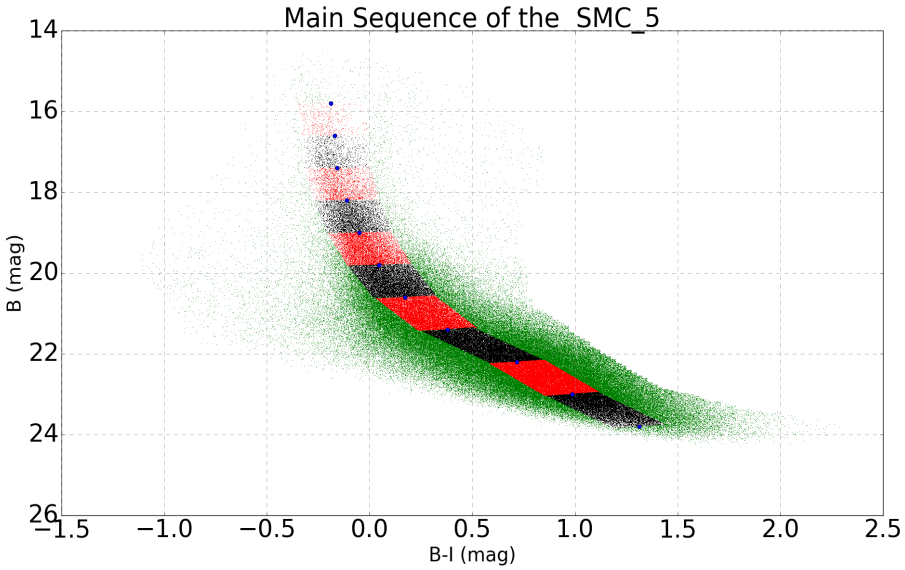

Figure 35: The MS of the field SMC5 divided into equal area cells. The blue points correspond to the MS ridge line.

The MS LF were corrected for completeness, as described in section 4. The completeness corrected LF (CCLF) for field SMC5 can be seen in the bottom panel of Fig. 36, while in the top panel we show the uncorrected MS LF, and in the middle panel the dependence of completeness on magnitude for the B data in SMC5.

The MS CCLF can be used for a rough comparison of the mixture of stellar populations of different ages present in the different fields. Fig. 37 (top left panel) shows the MS CCLFs for the four studied fields. The CCLFs have been normalized to the total number of stars with magnitudes fainter than 21.6 mag in B. This normalisation assumes that older populations are more evenly distributed than younger ones. It is immediately apparent that fields SMC3 and SMC5 have a higher contribution from younger populations compared to fields SMC4 and SMC6. This difference was confirmed (at a significance level of 0.05) with the application of a two-sample Kolmogorov-Smirnov test to the cumulative luminosity functions. It must also be noted that in the overlap region between fields SMC5 and SMC6, the derived CCLFs are identical within the errors (top right panel of Fig. 37. Therefore, the difference between the global CCLF of fields SMC5 and SMC6 cannot be accounted for by uncertainties in completeness and normalisation. It is noted that fields SMC3 and SMC5 are located to the North-Northeast of the Bar, while fields SMC4 and SMC6 are located towards the South-SouthWest. Younger populations therefore, seem to be more abundant in the North-North Eastern regions of the Bar.

One way of quantifying the spatial variation of the CCLF is to investigate the change of its slope in different locations. To this purpose, we divided each CCD in smaller regions (4 for the

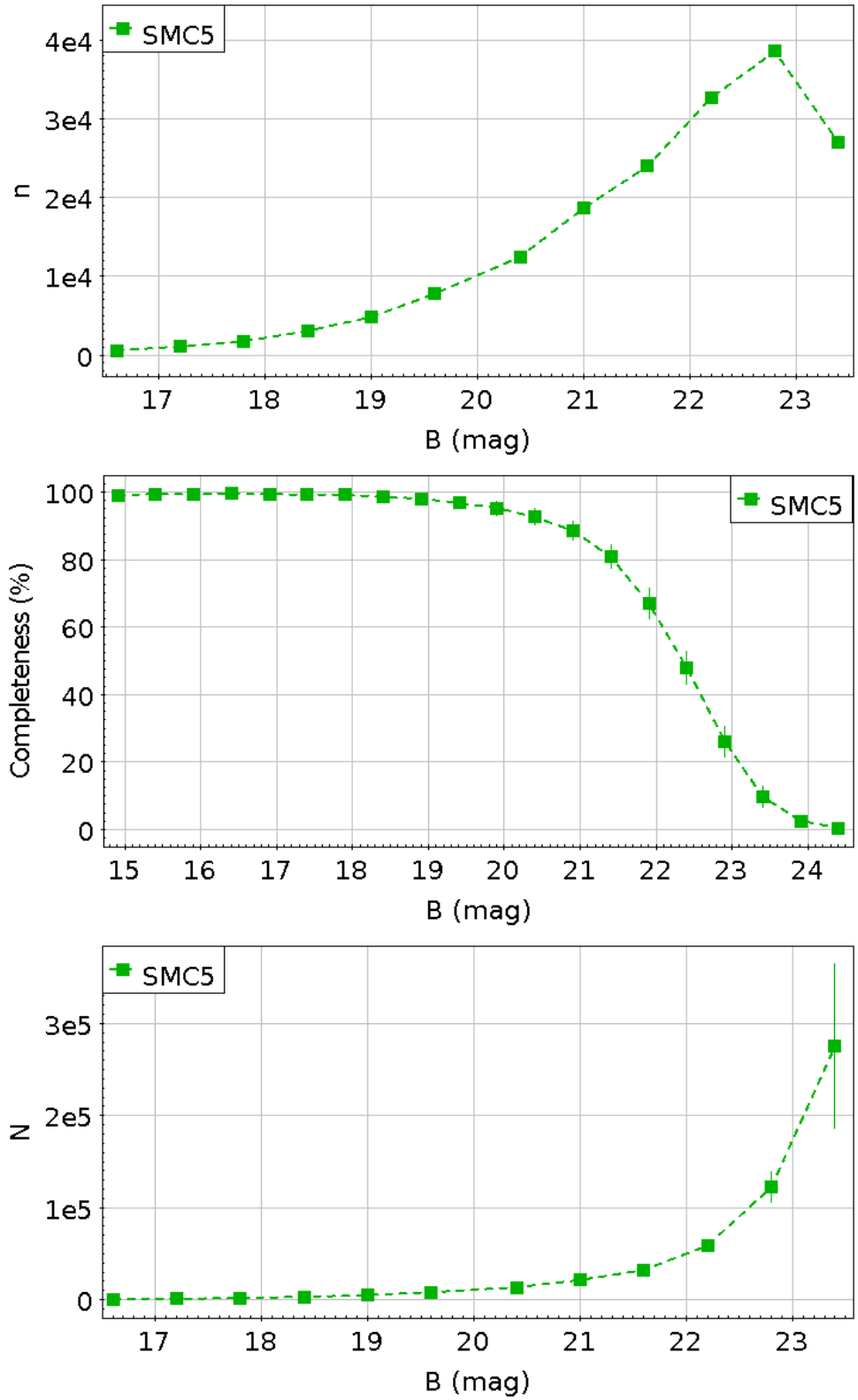

Figure 36: *Upper panel*: Luminosity Function of Main Sequence stars in field SMC5; *Middle panel*: Variation of completeness as a function of B magnitude; *Lower panel*: Main sequence completeness-corrected Luminosity Function.

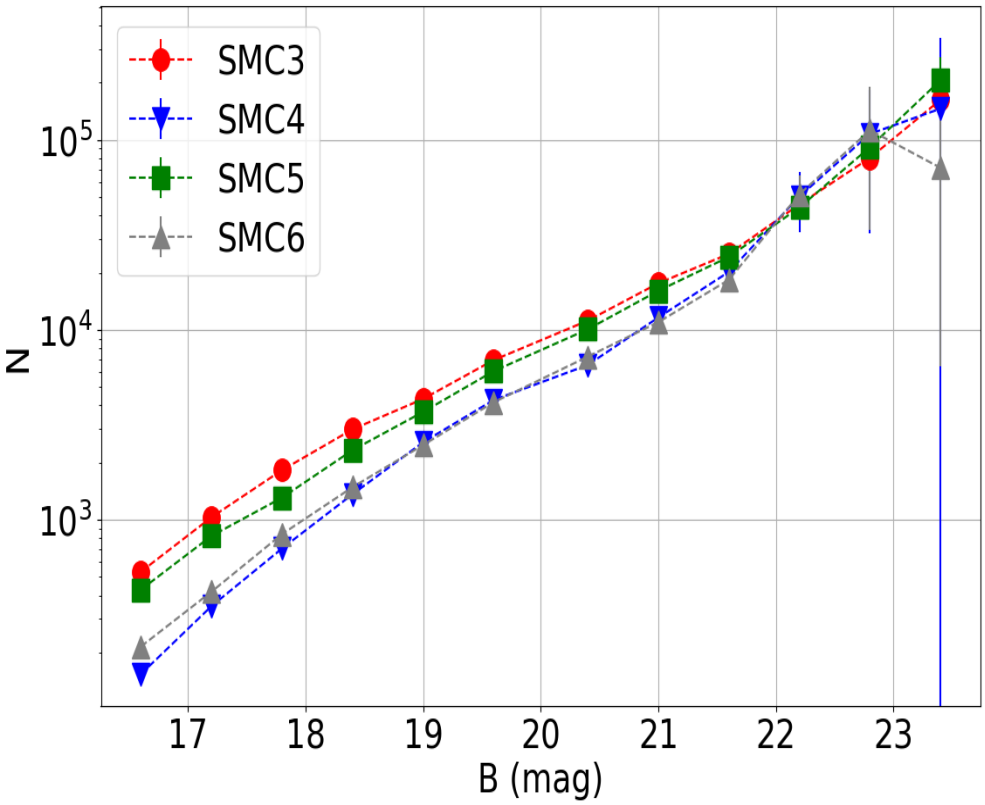

Figure 37: CCLFs of the four fields.

corner CCDs, 8 for the rest), constructed the CCLF for each subregion and then calculated its slope using a weighted linear regression in log scale. The slope was determined within a certain magnitude range, starting from the 17.8mag at the bright end and reaching different magnitude limits at the faint end. We used the overlap regions between SMC5 and SMC6 and between SMC5 and SMC3 to investigate the possible presence of systematics between fields, that would limit the usefulness of the LF slope as a diagnostic. We calculated the LF slope with a range of different faint limits, in each overlapping region. In Fig. 38 we show the change of the slope values as a function of the faint magnitude limit used, in the overlapping regions between SMC5 and SMC6 (left panel) and between SMC3 and SMC5 (right panel), In the first case, the slope values are consistent for the entire magnitude range, while in the second case there are significant variations beyond $\simeq$ 21.5mag. This result indicates that safe comparisons across the fields can be performed using a faint magnitude limit of $\leq$ 21.5mag.

A steeper LF, i.e. larger slope, indicates a larger percentage of older populations. In Fig. 39 we show colour maps showing the variation of the LF slope in the four fields, using two different faint limits, 21.5 and 21.0 mag. Lower values of the slope, indicating significant presence of younger populations are shown in light yellow, while large values of the slope, indicating a dominance of older populations are indicated in magenta. The errors in the slopes are shown in the colour maps of Fig. 40, where in this case different colours correspond to different error values. Lighter colours indicate smaller errors. It is clear that for the slopes calculated with the faint limit of 21.5mag, the errors are smaller, as expected (larger samples involved). It is noted that the difference between slopes that give adjacent colours in the colour maps is of the order of 1σ. As shown in the colour maps the larger percentage of young populations (light

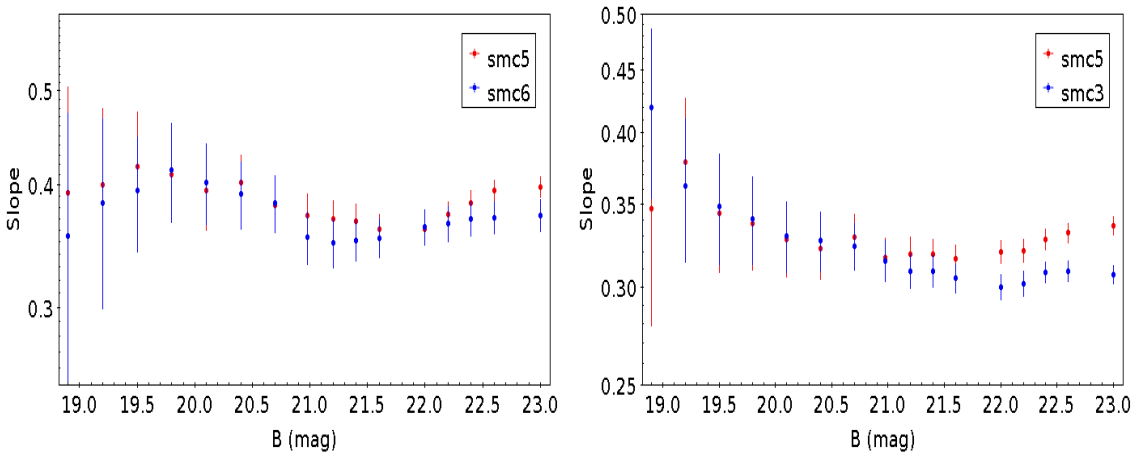

Figure 38: Comparison of the CCLF slope for different faint magnitude limits for the overlapping areas between SMC5-SMC5 *left panel* and between SMC3-SMC5 *right panel*

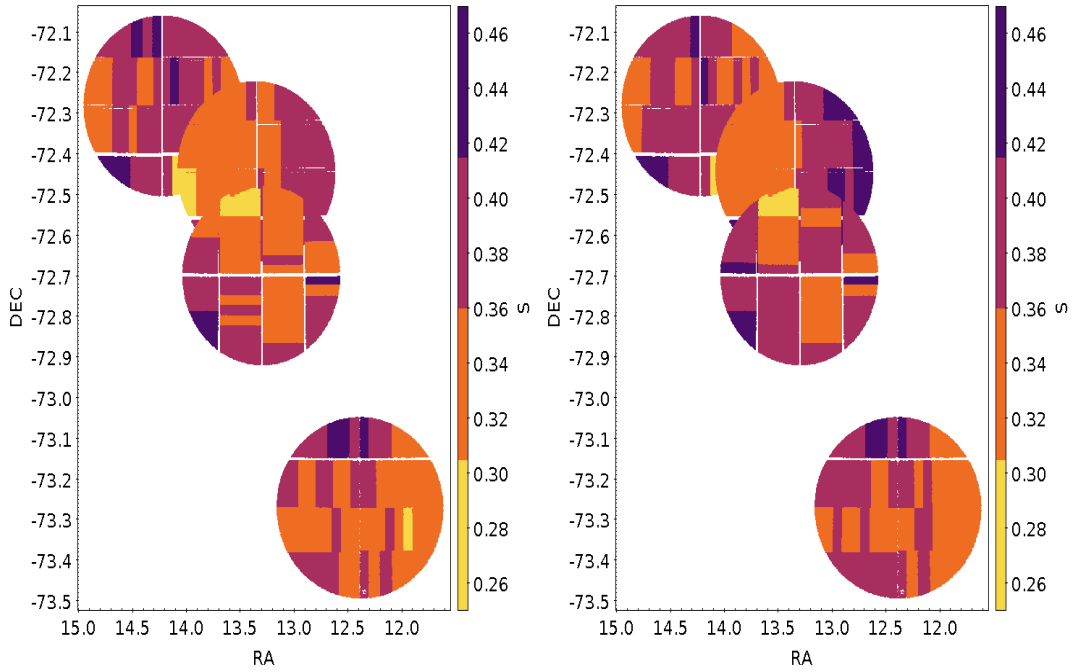

Figure 39: Colour maps showing the distribution of the values of the LF slopes, using two different faint limits, 21.5mag (left) and 21.0mag (right). Increase of the slope changes the colour from yellow to magenta.

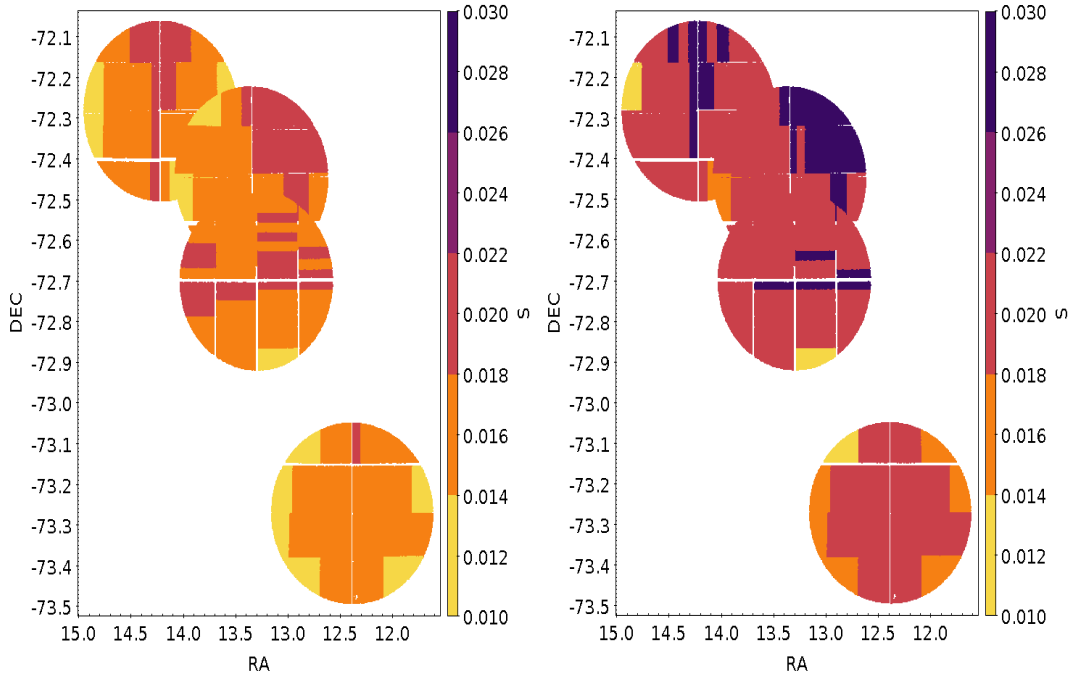

Figure 40: Colour maps showing the distribution of the errors in the values of the LF slopes, using two different faint limits, 21.5mag (left) and 21.0mag (right). Increase of the error changes the colour from yellow to magenta.

colour) is encountered in the central areas of the Bar (eastern half of SMC5 and top half of SMC6).

Although the LF slope is only indicative of the mixture of stellar populations present in the SMC Bar, it is clear that this mixture (and hence the history of Star Formation) is not uniform across the "Bar".

6 Discrete Star Formation Events

6.1 Peaks of Star Formation at 2.7Gyr and 4Gyr

In this section we focused on fields SMC3 and SMC5 due to the low photometric errors and relatively low differential reddening (which strongly affects the CMDs in SMC4). CMDs over relatively extended regions suer from differential interstellar absorption, small but non-negligible residual systematic photometric errors and possible distance variations All these factors limit the age resolution and the possibility to identify distinct SF periods.

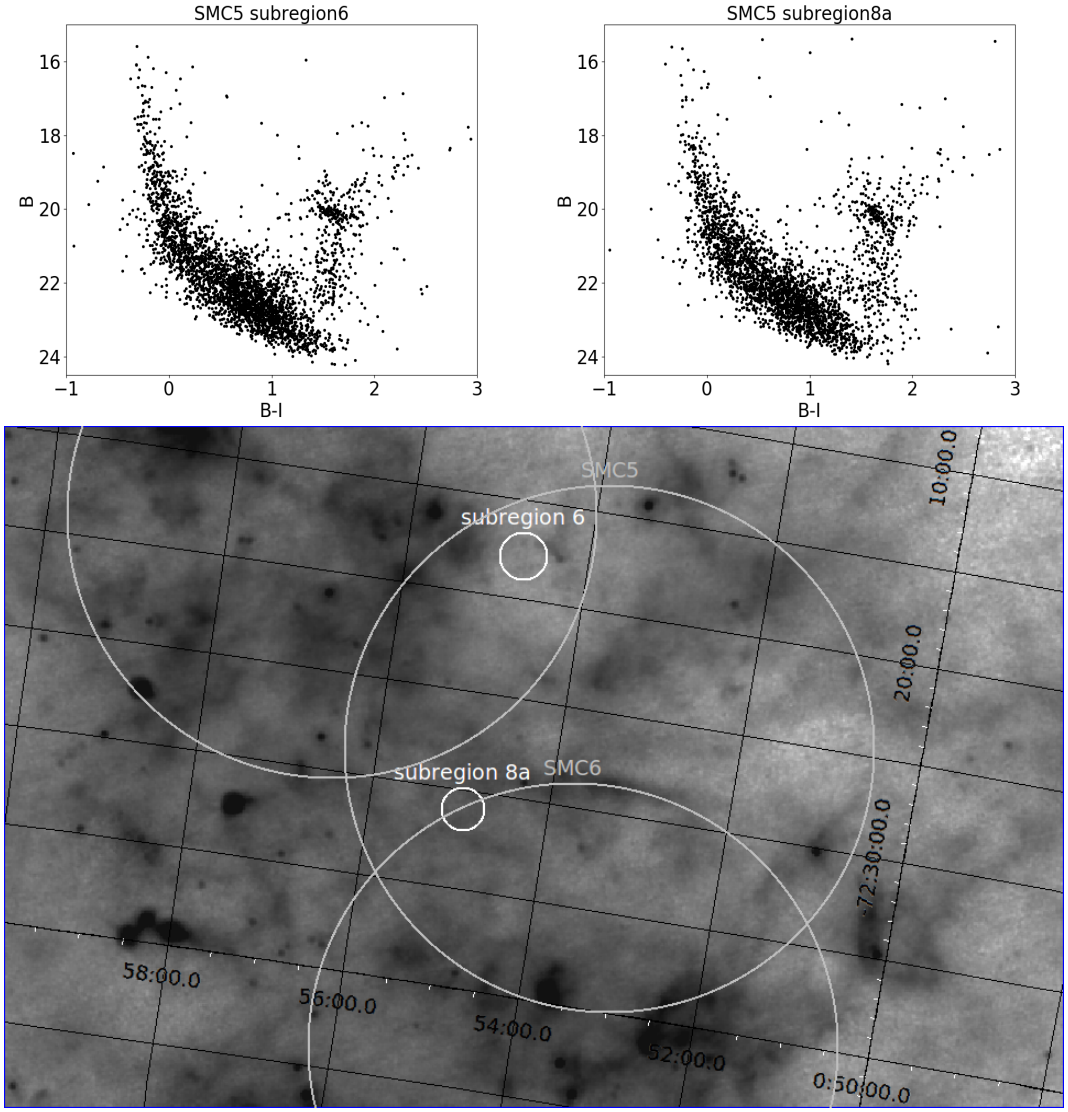

Figure 41: *Upper left panel*: CMD of subregion 6. *Upper right panel*: CMD of subregion 8a *Lower panel*: The position of subregions 6 and 8a on on a Spitzer-MIPS 24μ map of the SMC.

By selecting smaller regions (with still acceptable numbers of stars allowing statistical analysis) with sizes between 0.9 and 1.1 arcmin in radius, devoid of extended dust absorption and star clusters, we were able to uncover clear indications of distinct main-sequence turnos on the CMDs, suggesting isolated relatively short-lasting star formation events, as indicated by the two examples of Fig. 41 (CMDs of subregions 6 and 8a in SMC5, top panels). The position of the subregions are shown at the bottom of the Fig. 41.

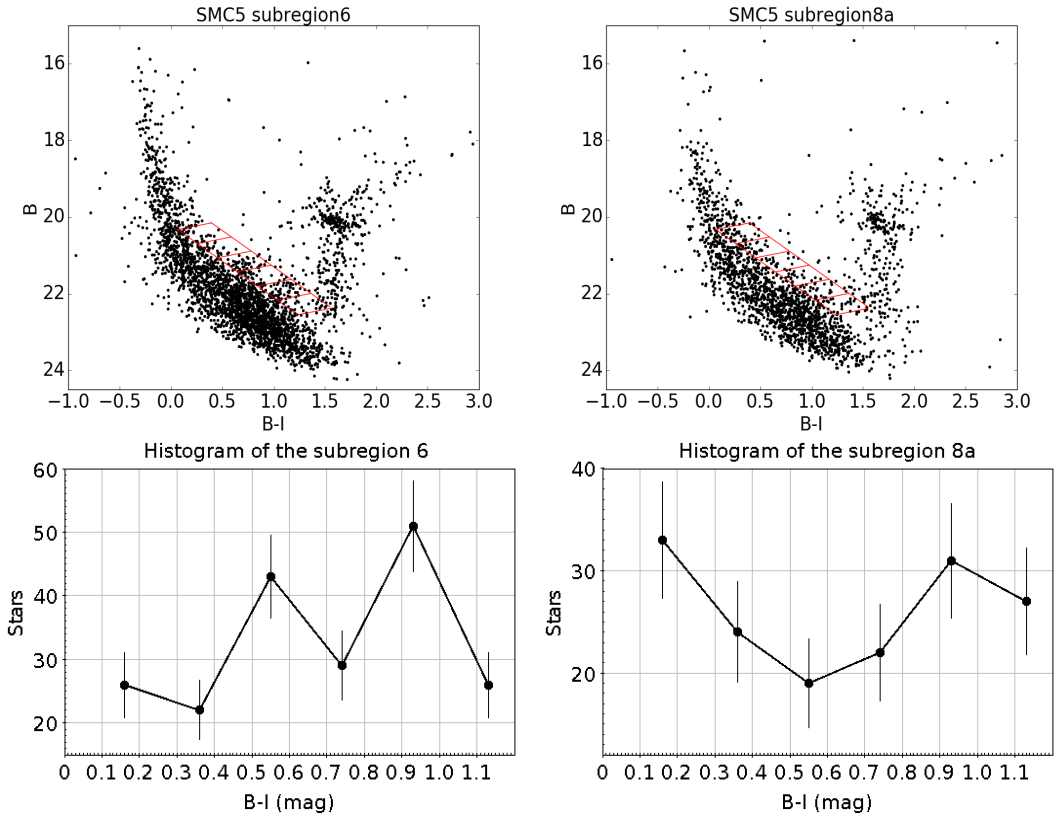

Figure 42: CMDs of subregions 6 and 8a (*upper panels*), and the distributions of counts of the red cell (*lower panel*), as it is defined in the CMDs.

The method we used to identify different MS TOs is to construct number distributions of stars lying along and redwards of the main sequence, as shown with the red cells in the top panels of Fig. 42, for the same regions displayed in Fig. 41. The width of each cell is 0.2mag, larger than the mean error in this magnitude range (<22.5mag). In the bottom panels of Fig. 42 we see the corresponding number distributions. The errors shown are equal to the square root of the number of stars counted in a particular cell. In these diagrams, MS turnoffs would appear as peaks. The CMD on the left and the corresponding number distribution, show two clear peaks, one at (B-I)=0.35mag and another at (B-I)=0.55mag. No such peaks can be seen on the CMD and corresponding number distribution on the right. In this case there appears to be a possible peak around (B-I)=0.95 mag,

We attempted to estimate the average ages of the populations corresponding to these two MS TOs through comparison with PARSEC isochrones with a metallicity of Z=0.0009, which is consistent with the metallicity of the intermediate age and old stellar populations in the SMC [e.g., Da Costa and Hatzidimitriou, 1998, Piatti, 2012a]. We have assumed a local interstellar reddening value of E(B-I)=0.08 and a distance modulus of 18.96 mag. On the left panel of Fig. 43 we have overplotted on the CMD of subregion 6 two indicative isochrones of 2.7 and 4Gyr, which appear to represent sufficiently well the average populations corresponding to the two MS TOs. On the right panel, only the older isochrone is overplotted, indicating the position of the turnoff that is visible on the CMD of subregion 8a. Similar results are obtained using the Dartmouth (Dotter et al. 2008) and the MIST (Dotter 2016,Choi et al. 2016) isochrones. These age estimates are only indicative. A full analysis of the SFH will be presented in Strantzalis et al. (2021, in preparation), following the method of Cole (Cole et al. 2014, Lianou and Cole 2013, Cignoni et al. 2012, Cole et al. 2007).

We have investigated the entire area of Fields SMC3 and SMC5 in the same way. We

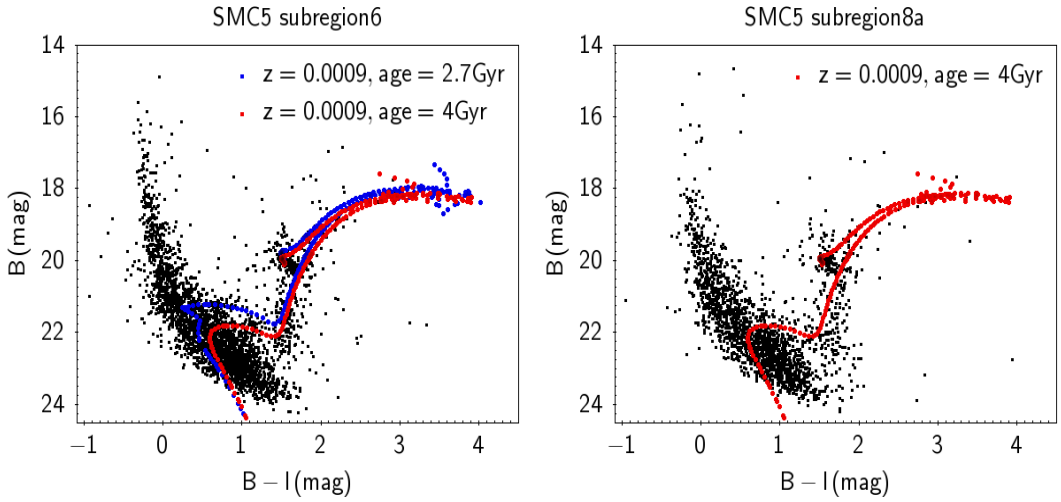

Figure 43: CMDs of subregions 6 and 8a, with a 2.7Gyr and 4Gyr PARSEC isochrone overplotted.

found that there are several small regions, usually clear of severe interstellar absorption (see below), that also show similar behaviour to the two prototypical regions of Fig. 41. The top two panels of Fig. 44 show the "MS turnoff" number distributions of fields SMC3 and SMC5 (upper panels). The bottom panel shows and the sum of the number distributions of the subregions that present one peak along the MSTO area around (B-I)=0.95 mag, similar to subregion 8a. Furthemore, there is one more subregion (subregions 7) in the field SMC5 that presents two peaks, similar to subregion 6, one at (B-I)=0.55mag and one at (B-I)=0.95mag.

The spatial distribution of subregions on a image of SMC (Spitzer-MIPS 24 μ map) is shown on the top panel of Fig. 45. The radius of circle of subregions (top panel) is equal with the radius of the study subregion. Subregions with peak at (B-I)=0.95mag are red, with peak at (B-I)=0.75mag are blue and with two peaks are black. It is not safe to draw conclusions without see the position of the subregions on the colour maps of the 50% and slope of the luminosity function (Fig. 46). We see that the colours or the class of the subregions does not depend on completeness. It would be an explanation that in the regions with lower completeness it would be impossible to detect the enhanced number of stars along the MSTOs. So, seems that the present of discrete populations through of these distributions is more believable. Also, the subregions with two (6, 7) peaks have a range of the slope of the luminosity function 0.011-0.013 and the subregions with one peak (8a, 2m, 2, 5b) have a range about 0.0125-0.0145. Based on conclusion of section 5 (LF), the subregions 6, and 7 which have the first peak is overplotted by an isochrone at 2.7Gyr, are located in regions which are dominated by younger stars, while subregions 8a, 2, 2m, 5b (peak is overplotted by an isochrone at 4.0Gyr) are covered by regions dominated by older stars.

The peak at (B-I)=0.55mag as we see in the Fig. 43 by using PARSEC isochrones is overlaid by ages 2.7 Gyr. The 2.7 Gyr peak is probably coincident with the 2.5 Gyr SF enhancement identied by Harris and Zaritsky [2004]. Interestingly, they also did not nd this star formation event smoothly distributed but rather located within a ring structure. The relatively small extent of our study cannot conrm the ring geometry, but we have found indications of non-uniformity in the spatial distribution of this population (contrary to the conclusion of Rubele et al. 2018). Regarding the second peak, several studies have shown enhanced star formation at 4-5 Gyr, ago (e.g. Cignoni et al. [2012], Noël et al. 2009 and McCumber et al. 2005). What is new in the present study is that we could actually identify distinct main sequence turnos that allow a better estimate of the duration of the SF events.

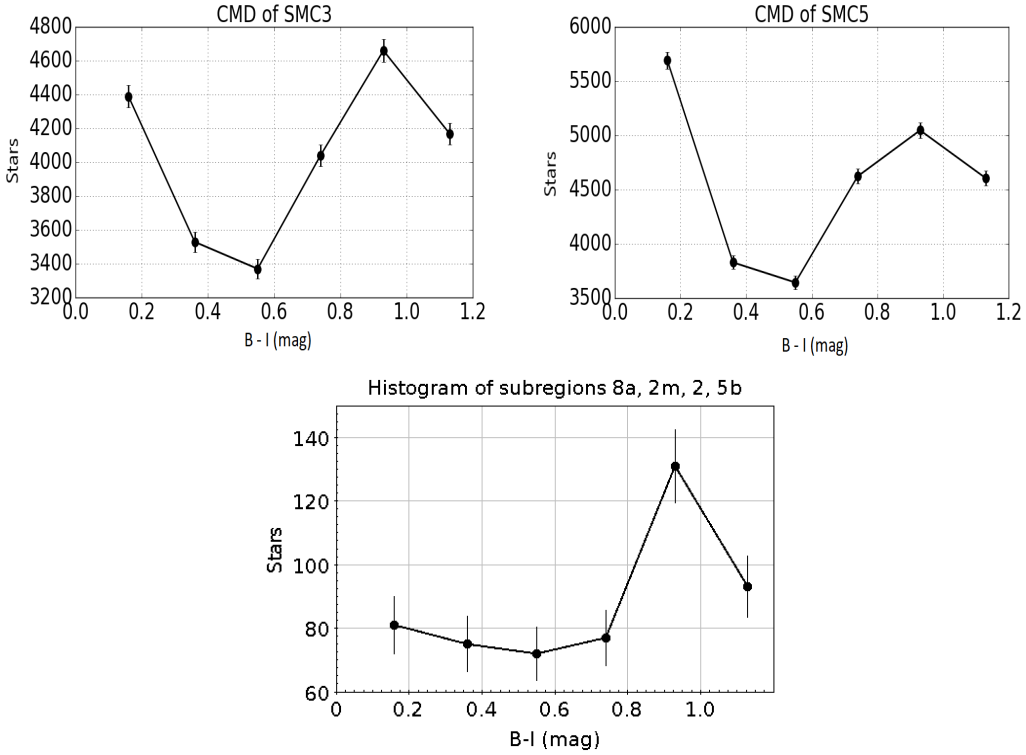

Figure 44: *Upper panels*:MS turnoff number distributions for fields SMC3 and SMC5. *Bottom panel*:The sum of the number distributions of the subregions that show the same peak as for subregion 8a.

6.2 The ≃90 Myr Star Formation period

On the CMDs of all fields, shown in Fig. 25, 26, 27, 28, there is clear evidence of a MS turnoff around $B = 17$mag, with a sequence of stars branching out to the red of the zero age MS. In the following we will concentrate on field SMC5 where this population is most clearly seen.

The left panel of Fig. 47 zooms in to the brighter part of the CMD in SMC5, clearly showing this MS turn off. On the CMD we have overplotted two PARSEC isochrones [PAdova and TRieste Stellar Evolution Code Bressan et al., 2012, Marigo et al., 2017] corresponding to ages of 56 Myr and 120Myr, yielding an average age of about 90Myr. We have assumed a reddening of $E(B-I)$=0.3 (corresponding to $E(B-V) = 0.13$), a metallicity of $Z = 0.004$, and a distance modulus of 18.96 mag. The isochrones are only indicative. Stars lying on the zero-age main sequence are marked in red, while stars consistent with the older population to the red, are marked in blue. On the right panel of Fig. 47 we show the colour distribution of stars defined in the figure on the left panel. The red and blue bins on the right panel correspond to red and blue coloured stars in the left panel. The histograms show a secondary peak which moves to redder colours for brighter magnitudes, confirming the presence of the 56-120Myr old population.

Therefore, apart from the very young stellar population exemplified by the zero-age main sequence stars (red points) there is a distinct population aged between 56 and 120Myr present in the SMC Bar. This was also shown in our SF history analysis based on the MS Luminosity Function in Section XX. Ennhanced SF for this period was also reported by Harris and Zaritsky [2004], Rubele et al. [2015] and Auchettl et al. [2019] who showed that a large fraction of the supernova remnants in the SMC indicated a burst of star formation between 50 and 200 Myr ago.

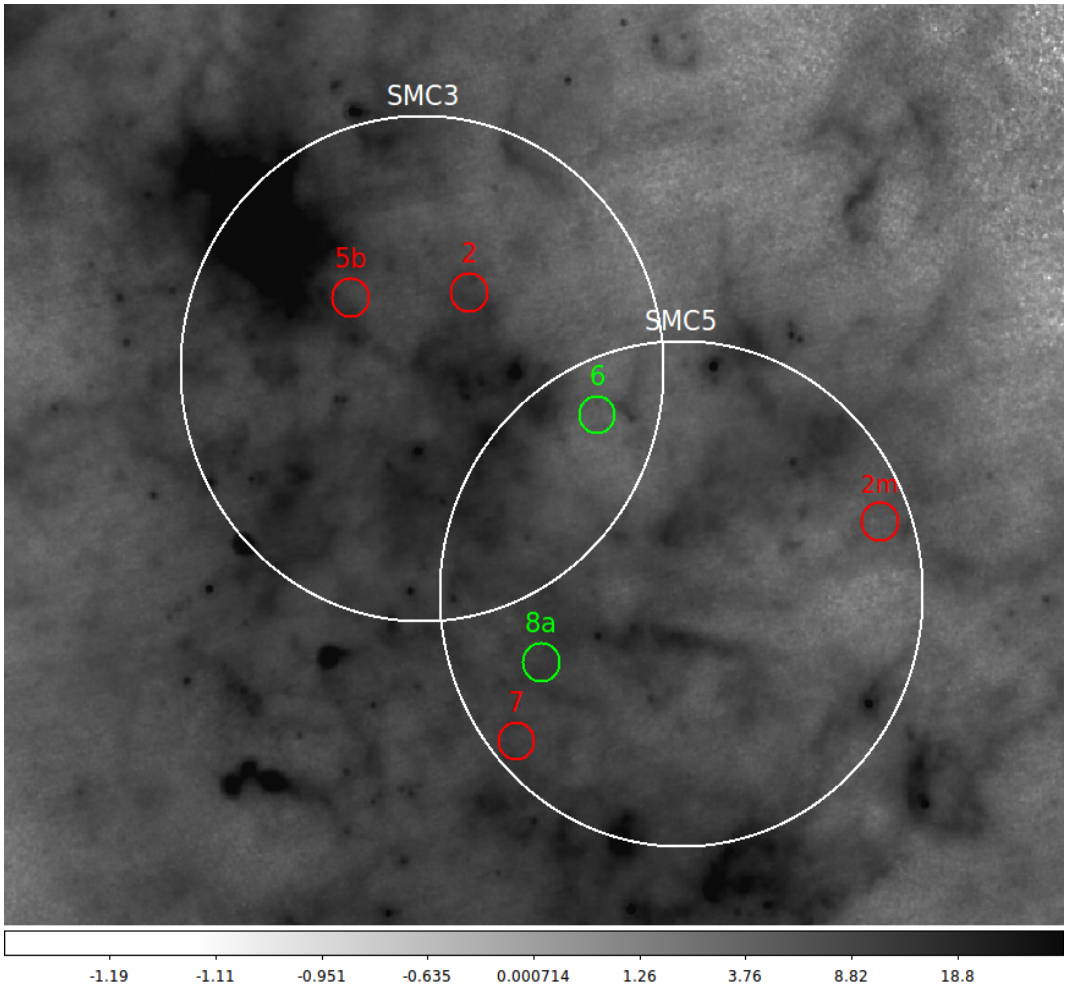

Figure 45: The position of all subregions of the fields SMC3 and SMC5 on a Spitzer-MIPS 24μ map of the SMC. Green regions are the prototypical subregions 6, 8a and the red subregions have similar behaviour to the two green.

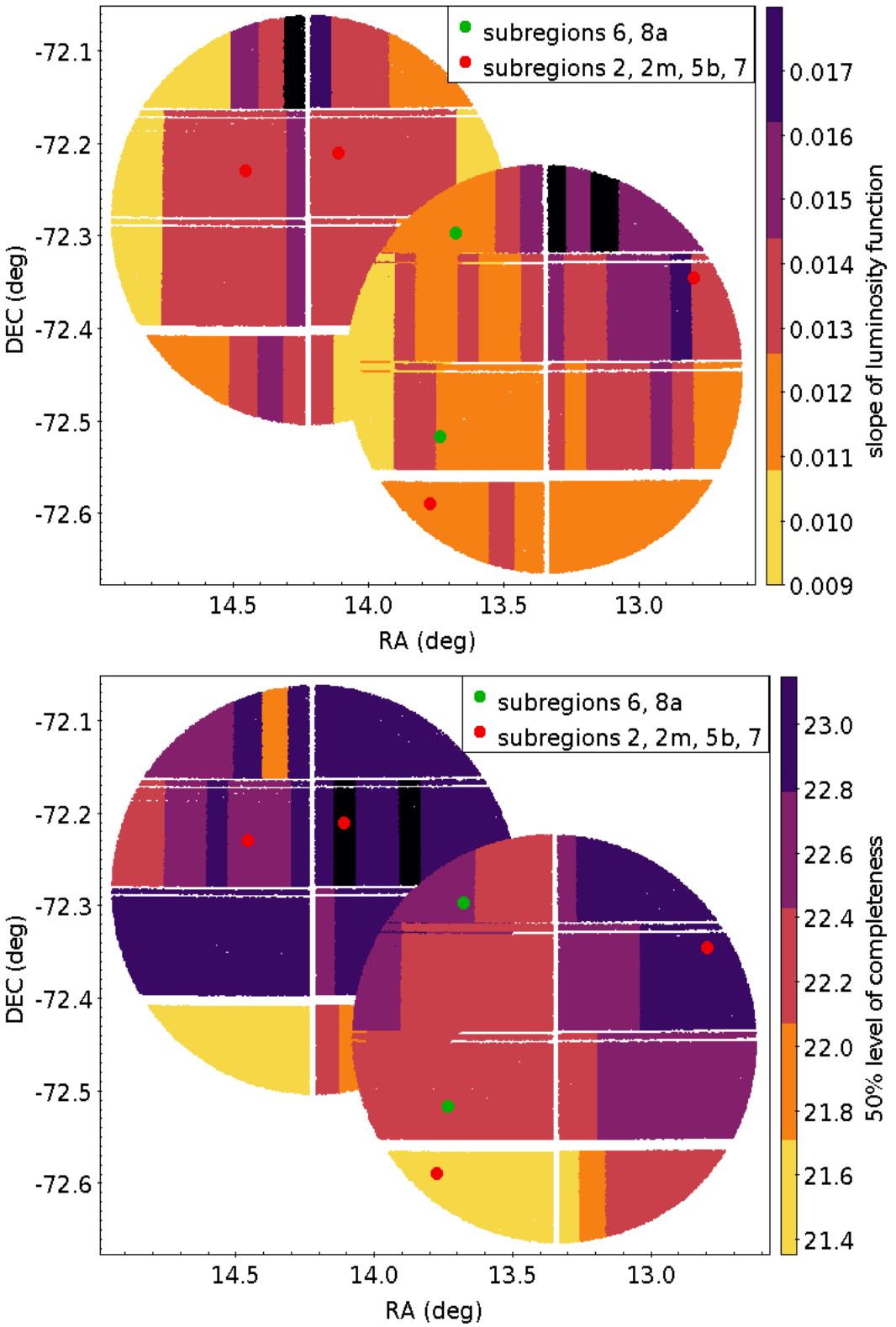

Figure 46: The spatial distribution of the subregions on the colour maps of the slope of the luminosity function (*top panel*) and of the Completeness levels 50% (*bottom panel*). Green regions are the prototypical subregions 6, 8a and the red subregions have similar behaviour to the two green.

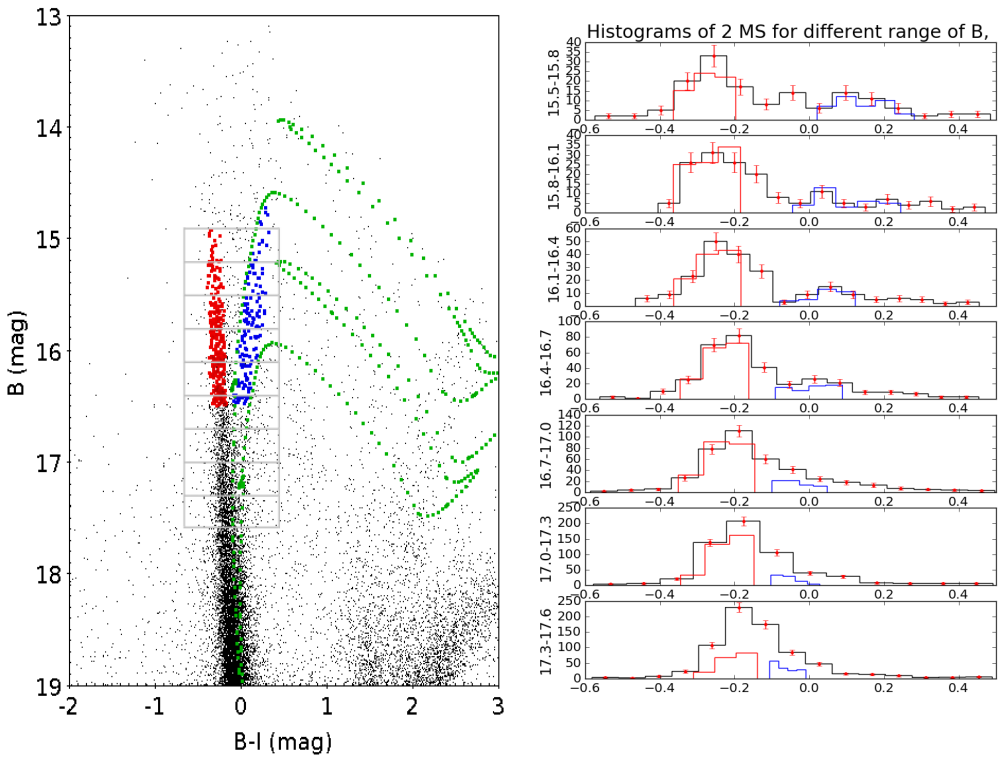

Figure 47: *Left panel* The CMD in region SMC5 for stars brighter than B=19mag, with two PARSEC isochrones of ages 56Myr, 120Myr overplotted. Stars on the zero age main sequence are indicated in red, while stars consistent with the older population (as delineated by the overplotted isochrones) are marked in blue. The coloured points correspond to stars that are included in the kinematic study of the two populations. The black cells mark the regions used to create the histograms shown on the right panel. *Right Panel* Colour distributions of stars in the black cells shown in the middle panel.

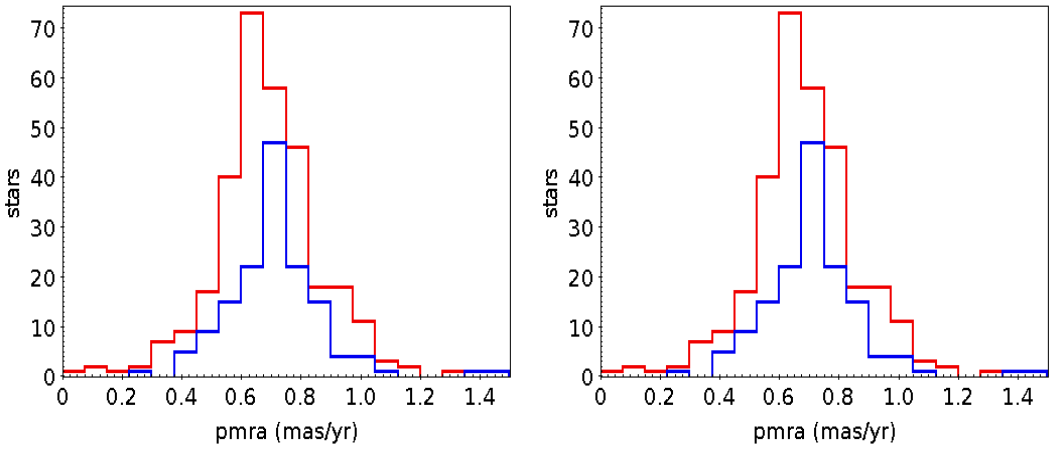

Figure 48: Histogram of the parameters of the catalogue of Gaia Data Release 2 of the two discrete MSs. The stars are brighter than B=16.5mag

6.2.1 Kinematical study of the 90Myr population using Gaia DR2 data

Driven by studies that have reported kinematically distinct populations in the SMC (e.g. De Leo et al. 2020), we have investigated the kinematic behaviour of the two different age groups. To this purpose, we used proper motion measurements derived from Gaia Data Release 2 (Gaia Collaboration et al. 2016, Gaia Collaboration et al. 2018a). As very few stars have radial velocity estimates in Gaia DR2, we limited our study to proper motions. Parallaxes were only used to filter out foreground (galactic) stars, by demanding that the parallax should be less than 0.25mas. We also limited our kinematic study to stars with proper motion errors less than 0.15mas/yr, which corresponds to a magnitude cutoff of $B < 16.5$mag ($G < 16.7$mag). This is why the "red" and "blue" sequences indicated in Fig. 47 reach 16.5mag at the faint end. The final sample (the "blue" and "red" stars) contains stars with proper motions in right ascension (pmRA) in the range of 0.2 to 1.7 mas/yr and proper motions in declination (pmDEC) in the range of -1.9 to -0.6 mas/yr. There are known spatially correlated proper motion errors in the Gaia DR2 catalog (Gaia Collaboration et al. 2018b), on small (1 degree) and large scales. However, given the limited spatial extent of the data used here and more importantly the fact that the populations considered here are spatially well mixed (see discussion in the next paragraph), our results are not expected to be affected by these systematic effects. There are also known colour related systematic trends in the parallax determination (Arenou et al. 2018, Lindegren et al. 2018), which are quantified using "chromaticity", calculated from the effective wavenumber. In our case, the range of the effective wavenumber values is small (1.73-1.93), therefore we do not expect significant colour related trends in parallaxes, although we only use them as a filter to exclude galactic stars.

The total number of stars in the blue and red sequences shown on the left panel of Fig. 47, for which proper motions were available, is 460. In Fig. 48 we compare the distribution of pmRA and pmDec of the stars belonging to the two different populations (red and blue in Fig. 47). On average we derived a mean pmRA of 0.70±0.01 mas/yr and pmDec of -1.29±0.01 mas/yr. Taking into account the uncertainties, these values are consistent with the known proper motion of the SMC (e.g. Kallivayalil et al. 2013 and van der Marel and Sahlmann 2016).

Inspection of the histograms suggests that the two populations may have different net kinematics, with the difference being more pronounced in pmdec. Indeed, application of the Kolmogorov Smirnov (K-S) test (significance level a=0.05) for stars with B$\leq$16.5 yielded a p-value of 1.3×10^{-4} for the pmdec distributions, and 0.031 for the pmra distributions. Therefore, the kinematics of the $\simeq$90Myr population seem to be distinguishable from the younger stars. Of course, the K-S test cannot preclude the presence of systematic errors in the Gaia DR2 data, although according to the official astrometry papers, these errors are expected to be negligible in our case. Nonetheless, we have searched for a systematic correlation of proper motions with stellar colour for all stars brighter than B$\simeq$16.5mag, and found none. The difference in the mean value of pmdec for the two groups of stars is $\simeq$0.1mas/yr which corresponds to $\simeq$30km/s assuming that the distance of the SMC is 62kpc (Inno et al. 2013, de Grijs and Bono 2015).

The spatial distribution of young populations (especially those younger than $\simeq$100Myr) is highly inhomogeneous (e.g. Sabbi et al. [2009]). It is therefore relevant to examine the spatial distribution of the two populations under study. Fig. 49 shows the spatial distribution of the two populations, retaining the colour coding of the previous figures. Although the distributions in RA and DEC are not identical (as shown in the histograms at the top and on the right of Fig. 49), the two populations are generally well mixed (in projection), at least within the 470pc area covered by field SMC5.

We have also attempted to investigate the kinematics of the two populations along the line of sight using bibliographic radial velocities of bright stars. Using the catalogue of Evans and Howarth [2008] we found radial velocities for a total of twelve stars, six stars in each age group. The weighted mean values for the radial velocities was 159.4±15km/s and 159.8±32km/s, respectively. The small samples do not allow us to extract safe conclusions. Indeed a simple simulation experiment showed that more than 200 stars are needed for the K-S test to distinguish safely between mean radial velocities differing by 20-30km/s, for a velocity dispersion

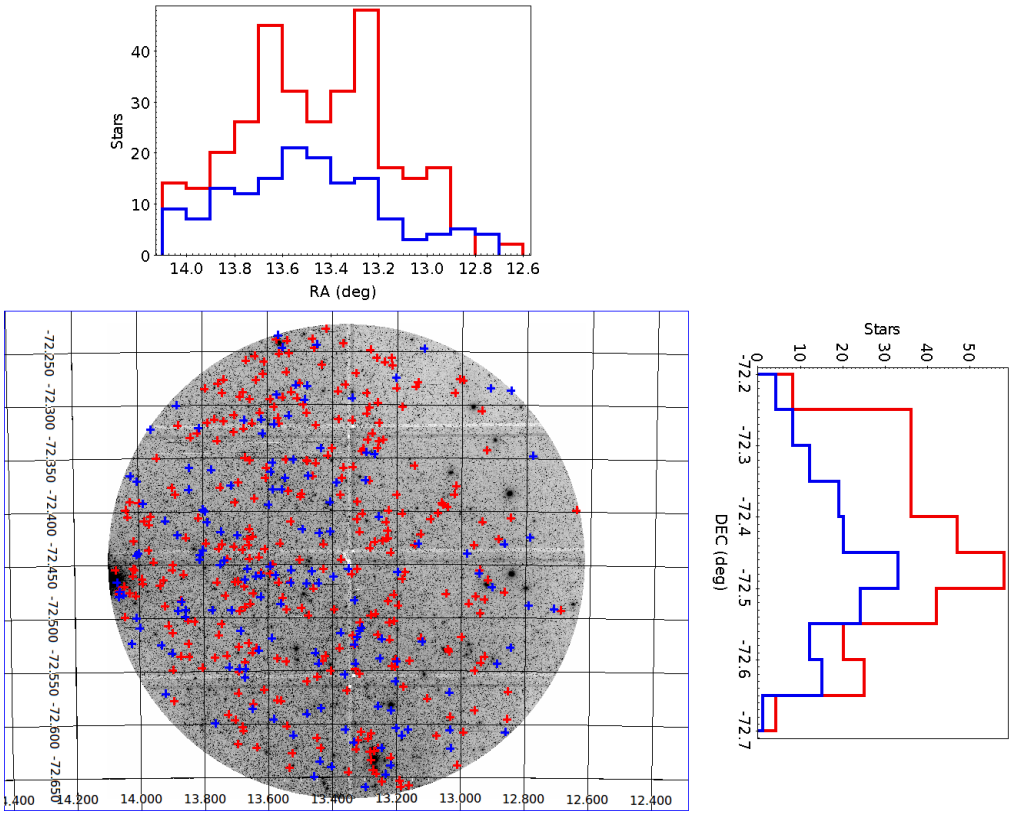

Figure 49: The spatial distribution of the stars in the two populations (the first exemplified by the very young stars on the ZAMS and and the second being ≃90Myr old). The same colour coding is used, as in Fig. 47. At the top, a histogram of the distribution of the RA values is shown, and on the right, the corresponding distribution for Dec.

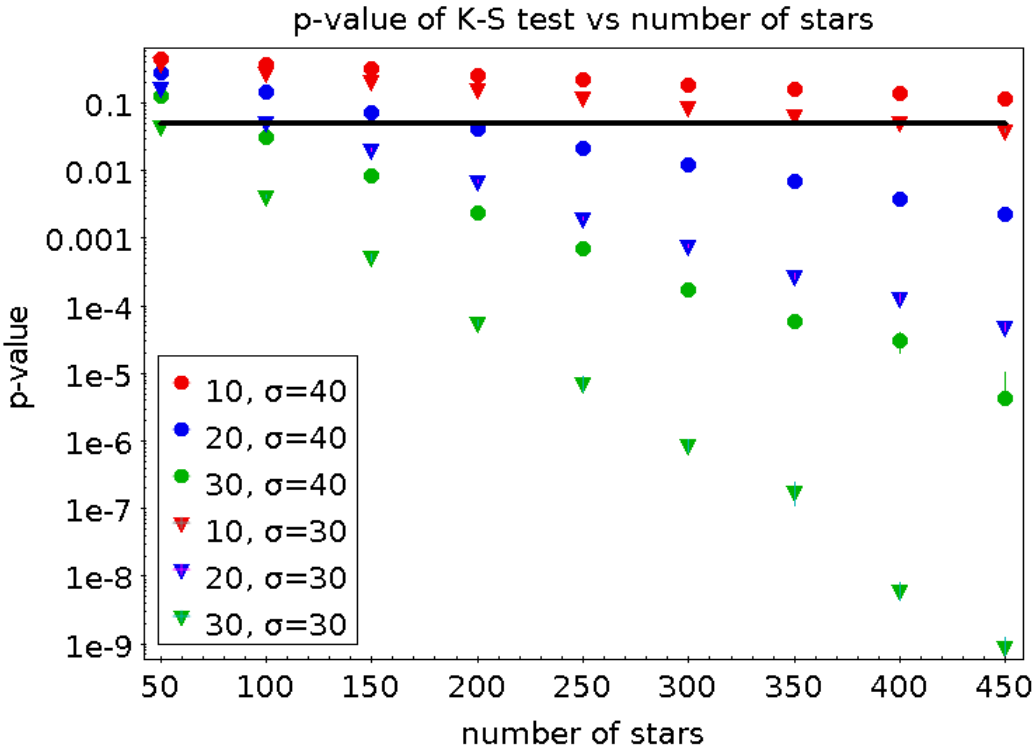

Figure 50: Simulations of the p-value of the K-S test versus number of stars in two groups of stars with radial velocities following normal distributions having peaks that differ by 10,20 and 30km/s, with a dispersion of 30 or 40km/s.

of 30-40km/s in each group (following the estimates for the radial velocity disprsion in young populations in the SMC by Bekki and Chiba [2009].

We assumed that we have two populations with radial velocities following normal distributions with six scenarios about the difference in the average radial velocity (10, 20 and 30km/s) for two different radial velocity dispersion of 30 and 40km/s. We also assumed, that the total number of stars in the first population is twice as large as in the second one. The ratio of the number of the two populations is n_1/n_2=2 in any case. The number of stars in both populations together varied from 50 to 450. We applied the K-S test and derived the p-value for six different scenarios, and for the different sample sizes. The experiment was repeated 10000 times.The resulting p-values as a function of sample size (averaged over the 10000 iterations) are shown in Fig. 50. It is clear that more than 250-300 stars are needed to safely distinguish the two populations for radial velocity differences ¿20km/s. Smaller differences are not distinguishable, for the assumed radial velocity dispersion.

In conclusion, the kinematical investigation we conducted indicated that the two different age groups, one very young and one around 90Myr may also be kinematically distinct. This tentative result alludes to the presence of distinct substructures proposed by Murray et al. [2019] who also found that non-rotational motions are prevalent throughout the SMC. These results need to be confirmed using more accurate proper motions and radial velocities, expected in Gaia DR3.

7 Identification of Star Clusters in the SMC

As outlined in the introduction, star clusters constitute an important component of a galaxy and play a crucial role in our understanding of star formation, stellar evolution and galactic dynamics. The identification of star clusters (mostly small clusters) in the SMC is an ongoing endeavour. As already mentioned, the quest for SMC star clusters started almost a century ago, and has been largely based on visual inspection originally of photographic plates and subsequently of CCD images. It is only relatively recently that machine learning and data mining methods and techniques have been employed to detect star clusters in the Magellanic Clouds. Actually, one of the first attempts to automate star cluster detection in the SMC was by Pietrzynski et al. [1998] who used an algorithm based on the detection of overdensities in OGLE II data. The method was similar to the one applied by Zaritsky et al. [1997] in the LMC. Piatti and Bica [2012] showed evidence that some of the candidate star clusters detected with this algorithm, amounting to 10% of the total number, were in fact spurious.

In a more recent study Piatti et al. [2016] combined near-infrared data from the VMC survey Vista survey with machine learning (using suitable kernel estimators for appropriate ranges of radii and stellar densities) to search for clusters in regions of high extinction in the main body of the SMC. They validated their results using near infrared CMDs. Out of 143 candidates, they could confirm 38 new clusters. One year later Piatti [2017] applied the same method to search for new star clusters in the periphery of the Magellanic Clouds using data from the Magellanic Stellar History (SMASH) Survey. They discovered 24 new stellar cluster candidates distributed in 11 different SMASH fields, most of them located in the outer regions of the LMC and SMC disks.

Another automated method, based on star counts to identify overdensities with respect to the local background, was adopted by Bitsakis et al. [2018], who reported a total of 1319 star clusters distributed over an area of 18 deg^2 in and around the SMC. They also estimated the ages of the detected clusters. Only a small percentage of these clusters were known before (less than 50% overlap with the Bica et al. [2008] catalog).

At the beginning of 2020, Bica et al. [2020] published an updated compilation of 2741 star clusters, associations and related extended objects in the SMC and the Magellanic Bridge, based on all existing catalogs. Their new catalog included a factor of 2 more objects than Bica et al. [2008]. They re-assessed the cluster or association classification of each object by inspecting digital atlases and imaging surveys in various bands. In particular, they cross-identified recent cluster samples from the Visible and Infrared Survey Telescope for Astronomy (VISTA) near-infrared YJKs survey of the Magellanic System, the Optical Gravitational Lensing Experiment IV (OGLE IV), and the Survey of the MAgellanic Stellar History (SMASH) surveys, confirming new clusters, reclassifying others and pointing out common objects. To classify the objects they considered their angular sizes, stellar densities, contrast to the field, contaminants, presence of cluster pairs or multiplets, hierarchical effects (i.e. a cluster included in a larger structure), shape and astrophysical parameters, when available. They also assessed the presence of dust and gas emission (Bica et al. 2019), when applicable. Finally, they estimated (improved) central coordinates and angular dimensions of the clusters, and classified them as C: cluster, CA: cluster association, CN: cluster nebula, A: association, AC: association cluster, AN: association.

Our data provide a unique opportunity to investigate the validity of these identifications and classifications, as they were obtained with a 6.5m telescope and with adaptive optics and have superior spatial resolution to most data used to date to search for star clusters.

We identified the objects in the Bica et al. [2020] catalogue of classes C, CA, and CN, that lie in our fields. There are 108 such objects (out of a total of 625). This list contains two star clusters from Chiosi et al. [2006] with the designation CVH and 19 clusters from Piatti et al. [2016] with the acronym VMC. None of the 45 newly discovered faint clusters and candidates in Bica et al. [2020] were located in our fields.

In Fig. 51 we show the spatial distribution of star clusters (red circles) from the catalogue of Bica et al. [2020] overlayed on a Spitzer-MIPS 24m image. The radii of the red circles correspond to the cluster radii. The white circles mark our four fields. In field SMC4 there is

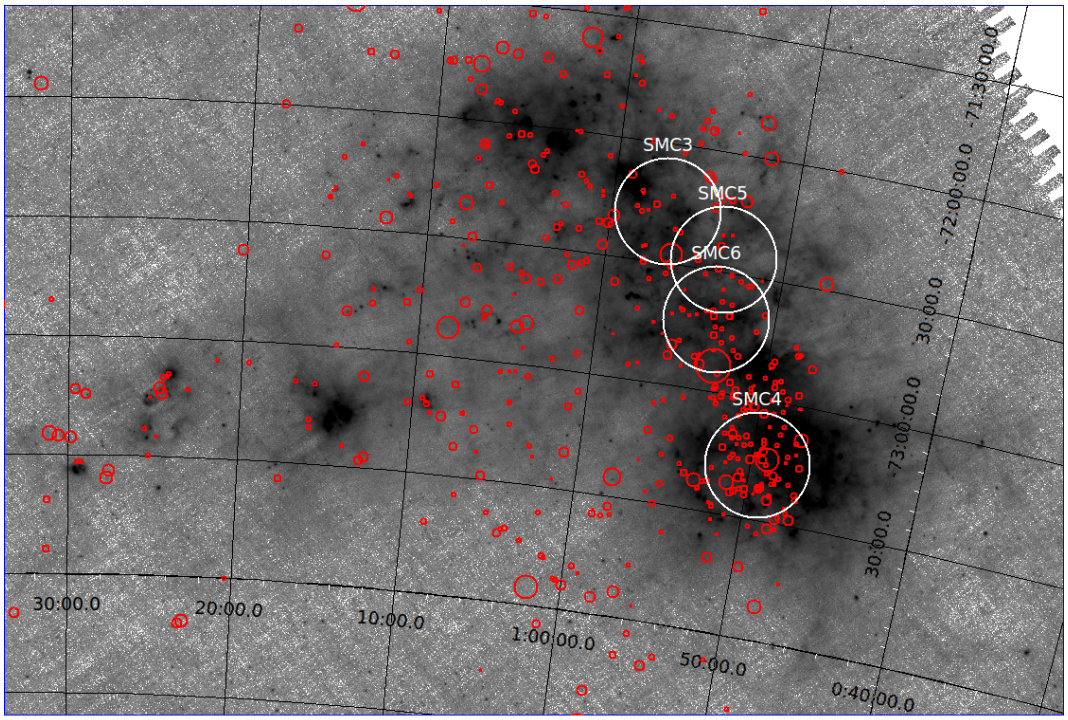

Figure 51: Spatial distribution of the stars clusters from the catalog of Bica et al. [2020] overlayed on an image of the SMC obtained with Spitzer-MIPS at 24m.

a larger number of clusters than in the other fields, but many of them have only been detected in the near infrared (in the VISTA data, Piatti2016). It is noted that SMC4 has significant interstellar extinction.

As already mentioned we have only considered objects assigned a "C", "CA" or "CN" class by Bica et al. The objects classified as associations, should not be confused with associations of young stars, which is the customary use of the term. In the Bica classification "associations" ("A", "AC" and "AN") are loose and extended concentrations of stars, which have on average rather large ages, contrary to what one would anticipate. Fig. 52 shows the radius and age distribution of clusters (C/CA/CN) and associations (A/AC/AN). Objects classified as clusters are generally smaller than 20-30pc, while objects classified as associations can be as large as 70pc. What is unexpected is the age distribution of "associations", which includes a significant percentage of old objects, even older than star clusters. Associations are unbound structures and should not be detectable at large ages, and indeed at ages larger on average than the bound clusters.

We have inspected the 108 "clusters" from the Bica et al. [2020] catalogue and re-classified them using a suite of criteria based on visual inspection on the IMACS images, their radial profiles and CMDs.

We have classified our clusters into four classes: *class 3*: are clusters that are considered as certain, *class 2*: probable clusters, *class 1*: probably not clusters and *class 0* definitely not clusters.

Visual inspection involves examination of the images around the published central coordinates of a cluster, to confirm or otherwise the existence of a stellar overdensity in that location. As the images used are all in the optical, embedded clusters cannot be properly characterised. In these cases near-infrared data should be used. In Fig. 53 we show the IMACS images of 8 clusters as examples, two of class 3 (NGC306 and B55), two of class 2 (BS39 and H86-128), two of class 1 (H86-170 and BS254) and finally two of class 0 (H86-166 and BS259). The

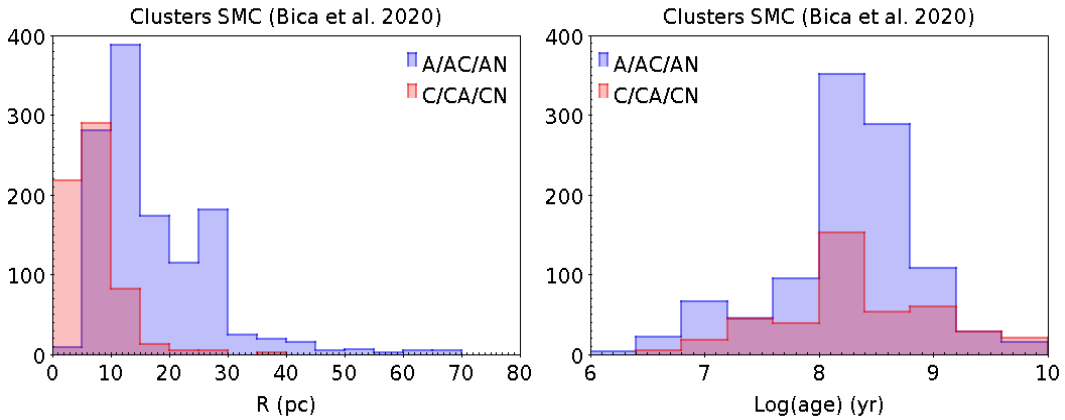

Figure 52: Distribution of radii (left) and ages (right) of star clusters (red line) and associations (blue line) from Bica et al. [2020].

superior spatial resolution of our data is well suited to confirm the classification of an apparent stellar concentration as a star cluster. Many older catalogues of star clusters include false cluster identifications, due to the overlap of very few bright stellar images, which gave the false appearance of significant density increase. For example, objects NGC306 and B55 show a clear concentration of stars at their center, while objects H86-166 and BS259 seem to have a negligible number of stars at the center. In the case of BS39 and H86-128 the surface density of the stars at the center is relatively high but visual inspection is not conclusive. Objects H86-170 and BS254 show no evidence of increased star number density.

The second criterion involves the examination of the radial profiles of the Bica et al. [2020] clusters. The radial profiles were constructed from the surface number density of the stars in concentric rings around the published cluster center. The radial bin size of each ring is 15 pixels corresponding to 3 arcsec. The radial profiles of objects of class 2 and 3 were fitted with King profiles (King 1962), as given in equation (8).

$$f(r) = k[1/\sqrt{(1+(r/r_c)^2)} - 1/\sqrt{(1/(r_t/r_c)^2)}]^2 + f_b \quad (8)$$

where f_b is the surface density of the background, r_c is a scale factor that is called core radius and r_t is the value of r which the f reaches zero.

While the radial profiles of candidate star clusters NGC306, B55, BS39, H86-128 present a clear overdensity in their central region, H86-166 and BS259 present a constant surface density as a function of radius (Fig. 54).

Star clusters have almost "simple population" CMDs characteristic of the age and metallicity of the cluster and usually distinguishable from the surrounding field. In Fig. 55 we present the CMDs of star clusters NGC306, B55, BS39, H86-128, H86-170, BS254, H86-166, BS259 using our IMACS photometry. All stars lying within the radius of the cluster, as published in Bica et al. [2020], are included in these CMDs and are marked in blue. The red symbols indicate field stars in an equal area annulus beyond the cluster radius. In cases of small clusters, the contrast between the cluster and field CMDs is far from obvious. Moreover, increased incompleteness in the high density regions in the cluster core decrease the contrast even further, especially for the fainter stars. Therefore, correction for the field star contribution is not a trivial task. The method we adopted to correct the CMDs for the field contribution utilises the Hess diagrams of the clusters and corresponding fields. A Hess diagram is a relative density map of occurrence of stars at differing color–magnitude positions on a CMD. Fig. 56 shows CMD density maps (Hess diagrams) for the star cluster NGC306. The top left panel is the Hess diagram of the cluster (including all stars within the cluster radius) and the top right is the corresponding diagram for the background field (stars in an equal area annulus). The bottom two diagrams show the results of the subtraction of the background diagram from the

cluster diagram using Bayesian analysis, adapting the algorithm designed by Park et al. [2006]. This algorithm (Bayesian Estimation of Hardness Ratios, BEHR) was originally designed to estimate the hardness ratios of X-ray sources and their uncertainties (see also Hou et al. 2020, Connor et al. 2020 etc), which requires the removal of a background. Technically the problem is the same as removing the background from the Hess diagram of a cluster.

BEHR is based on Poisson assumptions in a fully model based statistical approach. We can evaluate the fully posterior probability distribution of the subtraction, which provides reliable estimates and correct confidence limits, even when the number of stars of either the cluster or the background, or both, is very low. In particular, the method is not limited to "detectable" stars and can properly calculate upper and lower limits. As already mentioned, we used the algorithm in order to subtract the background from the cluster Hess diagrams. The Hess diagrams were constructed by binning the CMD in magnitude-colour bins somewhat larger in size than the corresponding errors. For each bin in the cluster diagram, we subtracted the background contribution. The bottom left panel of Fig. 56 shows the mean subtracted Hess diagram of the cluster, while on the bottom right we show the subtracted diagram with the minimum possible number of retained stars.

Table 2: Star clusters in the Bica et al. [2020] catalogue that lie in the SMC fields studied here.

Name	**Field**	**RA** (J2000)	**DEC** (J2000)	**Type**	**amin** (arcmin)	**amax** (arcmin)	**log(age)** (yr)	**class**
B90	SMC3	0:57:55.6	-72:17:31	C	0.45	0.35	7.9	1
BS269	SMC3	0:58:20.3	-72:13:18	CA	0.4	0.3	8.3	0
BS270	SMC3	0:58:23.7	-72:12:46	CA	0.55	0.5	8.03	0
H86-166	SMC3	0:56:00.6	-72:21:54	CA	0.7	0.5	8.1	0
H86-170	SMC3	0:56:20.3	-72:21:15	C	0.5	0.5	0.0	1
H86-171	SMC3	0:56:39.3	-72:13:03	C	0.55	0.35	0.0	1
H86-175	SMC3	0:57:50.3	-72:26:25	C	0.4	0.4	8.0	1
H86-179	SMC3	0:57:57.0	-72:26:42	C	0.4	0.35	7.5	1
H86-181	SMC3	0:58:19.0	-72:17:57	C	0.65	0.65	7.6	2
H86-183	SMC3	0:58:33.5	-72:16:50	C	0.55	0.55	7.65	2
L56	SMC3	0:57:30.2	-72:15:51	C	0.95	0.95	7.63	3
NGC306	SMC3	0:54:15.0	-72:14:29	C	1.1	1.1	7.7	3
NGC330	SMC3	0:56:18.7	-72:27:48	C	2.8	2.5	7.63	3
B47	SMC4	0:48:33.0	-73:18:25	C	1.0	1.0	9.11	3
B48	SMC4	0:48:37.0	-73:24:53	CA	1.3	1.1	7.7	1
B50	SMC4	0:49:02.5	-73:21:57	C	0.55	0.55	7.0	1
B53	SMC4	0:50:03.7	-73:22:57	C	0.95	0.95	8.27	1
B54	SMC4	0:50:28.4	-73:12:11	C	0.65	0.65	8.2	3
B55	SMC4	0:50:22.1	-73:23:13	C	0.7	0.6	8.21	3
B56	SMC4	0:50:54.9	-73:12:06	C	0.45	0.45	7.75	1
B60	SMC4	0:51:41.5	-73:13:39	CN	0.95	0.75	7.9	1
BS251	SMC4	0:51:25.9	-73:17:08	CA	0.4	0.35	8.1	0
BS38	SMC4	0:48:23.2	-73:19:42	CN	0.4	0.2	0.0	0
BS39	SMC4	0:50:12.0	-73:20:53	C	0.45	0.4	7.5	1
BS42	SMC4	0:49:16.0	-73:14:57	CN	1.0	1.0	7.15	0
BS43	SMC4	0:49:16.0	-73:22:11	CA	1.1	0.8	6.8	1
BS43nw	SMC4	0:49:17.8	-73:22:20	CA	0.65	0.55	0.0	3
BS43se	SMC4	0:49:13.8	-73:22:03	C	0.7	0.55	0.0	0
BS48	SMC4	0:50:42.0	-73:23:49	CA	0.85	0.55	8.0	0
BS54	SMC4	0:52:08.3	-73:19:00	CA	0.55	0.5	6.7	1
CVH2	SMC4	0:49:02.9	-73:14:37	CA	2.9	2.9	7.4	1
CVH3	SMC4	0:51:09.3	-73:22:05	CA	1.9	1.9	8.2	1

H86-104	SMC4	0:49:12.1	-73:06:30	C	0.4	0.4	9.0	2
H86-106	SMC4	0:50:32.2	-73:20:14	CA	1.1	1.1	0.0	0
H86-107	SMC4	0:50:02.0	-73:15:24	CA	1.1	0.8	7.6	2
H86-108	SMC4	0:50:52.6	-73:24:25	CN	1.0	1.0	7.0	0
H86-112	SMC4	0:50:07.7	-73:11:27	C	0.65	0.55	8.0	1
H86-121	SMC4	0:51:21.6	-73:08:18	C	0.55	0.55	8.8	0
H86-123	SMC4	0:51:44.1	-73:10:01	C	0.55	0.55	8.3	0
H86-87	SMC4	0:47:04.9	-73:22:16	C	0.8	0.7	8.3	1
H86-89	SMC4	0:47:06.1	-73:15:26	CA	0.85	0.65	8.3	0
H86-91	SMC4	0:47:32.1	-73:26:01	C	0.4	0.4	0.0	1
H86-92	SMC4	0:47:34.3	-73:20:02	CA	0.5	0.3	8.1	0
H86-93	SMC4	0:47:24.4	-73:12:21	CN	0.4	0.4	7.6	0
H86-97	SMC4	0:47:52.2	-73:13:19	C	0.7	0.6	8.37	3
L39	SMC4	0:49:03.1	-73:21:40	C	0.7	0.55	8.01	3
MA222	SMC4	0:48:22.7	-73:05:59	CN	0.55	0.45	0.0	0
MA351	SMC4	0:50:18.4	-73:19:31	CN	0.45	0.4	7.4	2
NGC290	SMC4	0:51:14.9	-73:09:40	C	1.1	1.1	7.4	3
SOGLE193	SMC4	0:48:37.0	-73:10:45	CA	0.5	0.5	8.7	0
SOGLE196	SMC4	0:49:27.0	-73:23:55	C	0.35	0.35	8.23	0
SOGLE53	SMC4	0:49:18.5	-73:12:42	C	1.0	0.8	7.3	1
SOGLE55	SMC4	0:49:21.6	-73:11:02	C	0.6	0.6	8.0	1
VMC11	SMC4	0:48:32.5	-73:08:04	CN	0.5	0.5	7.8	-
VMC12	SMC4	0:48:33.2	-73:20:42	C	0.5	0.5	8.7	-
VMC13	SMC4	0:48:33.6	-73:23:31	C	0.6	0.6	8.2	-
VMC16	SMC4	0:48:55.1	-73:18:18	C	0.5	0.5	9.0	-
VMC18	SMC4	0:49:04.1	-73:15:56	CN	0.6	0.6	7.9	-
VMC22	SMC4	0:49:24.1	-73:09:53	C	0.6	0.6	8.4	-
VMC23	SMC4	0:49:42.0	-73:14:00	C	0.7	0.7	7.8	-
VMC25	SMC4	0:50:00.1	-73:24:30	C	0.8	0.8	7.6	-
VMC26	SMC4	0:50:27.0	-73:09:41	C	0.8	0.8	8.1	-
VMC27	SMC4	0:50:27.2	-73:18:42	C	0.8	0.8	8.1	-
VMC30	SMC4	0:50:43.0	-73:15:41	C	0.5	0.5	8.8	-
VMC32	SMC4	0:50:53.9	-73:10:30	C	0.6	0.6	8.1	-
VMC35	SMC4	0:51:05.1	-73:14:54	C	0.6	0.6	7.5	-
VMC37	SMC4	0:51:10.0	-73:15:49	C	0.6	0.6	7.3	-
VMC38	SMC4	0:51:18.0	-73:10:47	C	0.6	0.6	8.4	-
VMC4	SMC4	0:47:33.7	-73:09:27	C	0.6	0.6	8.9	-
VMC6	SMC4	0:47:55.9	-73:14:34	CN	0.4	0.4	9.0	-
VMC7	SMC4	0:48:11.3	-73:18:50	CN	0.6	0.6	8.9	-
VMC8	SMC4	0:48:21.6	-73:20:41	C	0.4	0.4	9.0	-
B69	SMC5	0:53:05.8	-72:37:26	C	0.65	0.65	7.5	3
B79	SMC5	0:54:47.5	-72:27:57	C	0.8	0.6	7.47	3
BS259	SMC5	0:54:55.6	-72:26:46	C	0.55	0.5	7.75	0
H86-118	SMC5	0:51:03.6	-72:30:42	CA	0.3	0.2	0.0	0
H86-119	SMC5	0:51:36.0	-72:32:25	C	0.65	0.55	7.0	1
H86-127	SMC5	0:51:47.8	-72:32:30	C	0.6	0.4	8.4	1
H86-129	SMC5	0:52:12.5	-72:31:51	C	0.65	0.45	7.7	2
H86-132	SMC5	0:52:31.9	-72:37:51	C	0.5	0.4	8.4	0
H86-135	SMC5	0:52:47.9	-72:30:42	C	0.55	0.55	8.7	3
H86-136	SMC5	0:53:06.7	-72:20:38	C	0.45	0.45	0.0	0
H86-138	SMC5	0:53:09.4	-72:34:27	C	0.45	0.45	8.6	1
H86-142	SMC5	0:53:34.7	-72:29:25	C	0.9	0.9	8.0	0
H86-145	SMC5	0:53:36.4	-72:21:07	C	0.45	0.45	7.8	1
H86-146	SMC5	0:53:39.2	-72:23:34	C	0.9	0.9	8.2	2

H86-149	SMC5	0:54:16.2	-72:31:11	C	0.55	0.45	8.8	0
SOGLE220	SMC5	0:55:14.1	-72:36:04	C	0.35	0.35	9.0	1
B59	SMC6	0:51:43.7	-72:50:27	CN	0.8	0.6	8.1	3
B66	SMC6	0:52:47.3	-72:47:44	C	0.6	0.45	8.6	1
B71	SMC6	0:53:18.0	-72:46:00	C	0.85	0.85	7.4	2
BS253	SMC6	0:52:14.9	-72:45:58	CA	0.6	0.4	7.1	1
BS254	SMC6	0:52:51.7	-72:44:11	C	0.5	0.4	7.15	0
BS256	SMC6	0:53:16.8	-72:44:03	C	0.5	0.45	7.78	0
BS69	SMC6	0:53:55.5	-72:51:25	CA	0.35	0.35	8.8	1
BS72	SMC6	0:54:10.6	-72:52:03	CA	0.75	0.6	8.8	1
H86-114	SMC6	0:50:34.1	-72:39:03	C	0.75	0.65	8.2	1
H86-128	SMC6	0:52:02.8	-72:49:05	C	0.55	0.55	8.3	1
H86-133	SMC6	0:52:33.2	-72:40:49	C	0.75	0.75	7.4	1
H86-137	SMC6	0:52:33.0	-72:40:50	C	0.9	0.9	0.0	1
H86-139	SMC6	0:53:08.4	-72:49:58	C	0.35	0.3	0.0	0
H86-140	SMC6	0:53:08.1	-72:49:59	C	0.45	0.4	7.8	0
H86-143	SMC6	0:53:31.0	-72:40:04	C	0.8	0.8	7.8	1
H86-147	SMC6	0:53:49.0	-72:53:43	C	1.2	1.2	8.53	1
H86-148	SMC6	0:53:53.1	-72:40:22	C	0.5	0.5	8.8	1
H86-158	SMC6	0:55:08.5	-72:48:40	C	0.5	0.5	7.6	1
H86-159	SMC6	0:55:11.9	-72:40:58	C	0.5	0.4	9.0	1
H86-160	SMC6	0:55:20.5	-72:40:30	C	0.4	0.4	0.0	0
L41	SMC6	0:50:55.8	-72:43:35	C	0.65	0.65	8.1	3

According to our criteria, out of the 108 objects from the catalogue of Bica et al. [2020] that are located in our fields, 47 are of class 0, 38 of class 1, 8 of class 2 and only 15 are of class 3. The list of all 108 objects is presented in Table 2. Col.1 gives the name of the cluster, Col.2 the field in which the cluster is located, Cols 3 4 the J2000 coordinates of the cluster centre, Col.5 the cluster classification in Bica et al. [2020], Cols 6 7 the extent of the cluster along the minor and major axes respectively, Col.8 the age of the cluster and finally Col. 9 our classification of the cluster. From the 47 objects of class 0, 18 originate from the new catalogue of Piatti et al. [2016], which includes star clusters that were identified on near infrared images and are hardly recognizable in optical data. If we exclude these clusters, the number of class 0 objects is 29, i.e. 37% of the objects that have been characterized as C/CA/CN by Bica et al. [2020]. More specifically, of these 29 objects, 15 have been characterized as "C", 9 objects as "CA" and 5 objects as "CN". In the top panel of Fig. 60 we show the spatial distribution of the objects of classes 3, 2 as blue circles and of classes 1, 0 as red circles, in the four fields studied. Fig. 61 shows the distributions of the radii (left panel) and of the ages (right panel) of the 108 objects from the catalogue of Bica et al. [2020], The red bins correspond to class 1,2, and 3, and blue corresponds to class 0.

Using the same criteria, we also classified the 179 objects of Bitsakis et al. [2018] that lie in our fields. Of these, 11 are of class 3 (6.1%), 3 of class 2 (1.7%), 8 of class 1 (4.4%) and 157 of class 0 (87.7%). All clusters of class 3 and 2 are known clusters, except for one object of class 2 which is new. The spatial distribution of the candidate star clusters from Bitsakis et al. [2018] located in our fields is shown on the bottom panel of Fig. 60. The red circles are classes 0, 1 and the blue circles are classes 2, 3. The radii of the circles are the suggested radii of clusters given by the authors.

Another useful diagnostic for classifying apparent overdensities as likely star clusters is based on a comparison between the magnitude and colour distributions of stars lying along the MS of the candidate cluster and corresponding field regions. In Fig. 62 we show examples for two objects, B55 and BS259. Three diagrams are shown for each cluster: The CMD, where stars in the cluster area are denoted with blue points, while stars in the field area with red points; a histogram of the distribution of the B-magnitude of stars along the MS, shown on

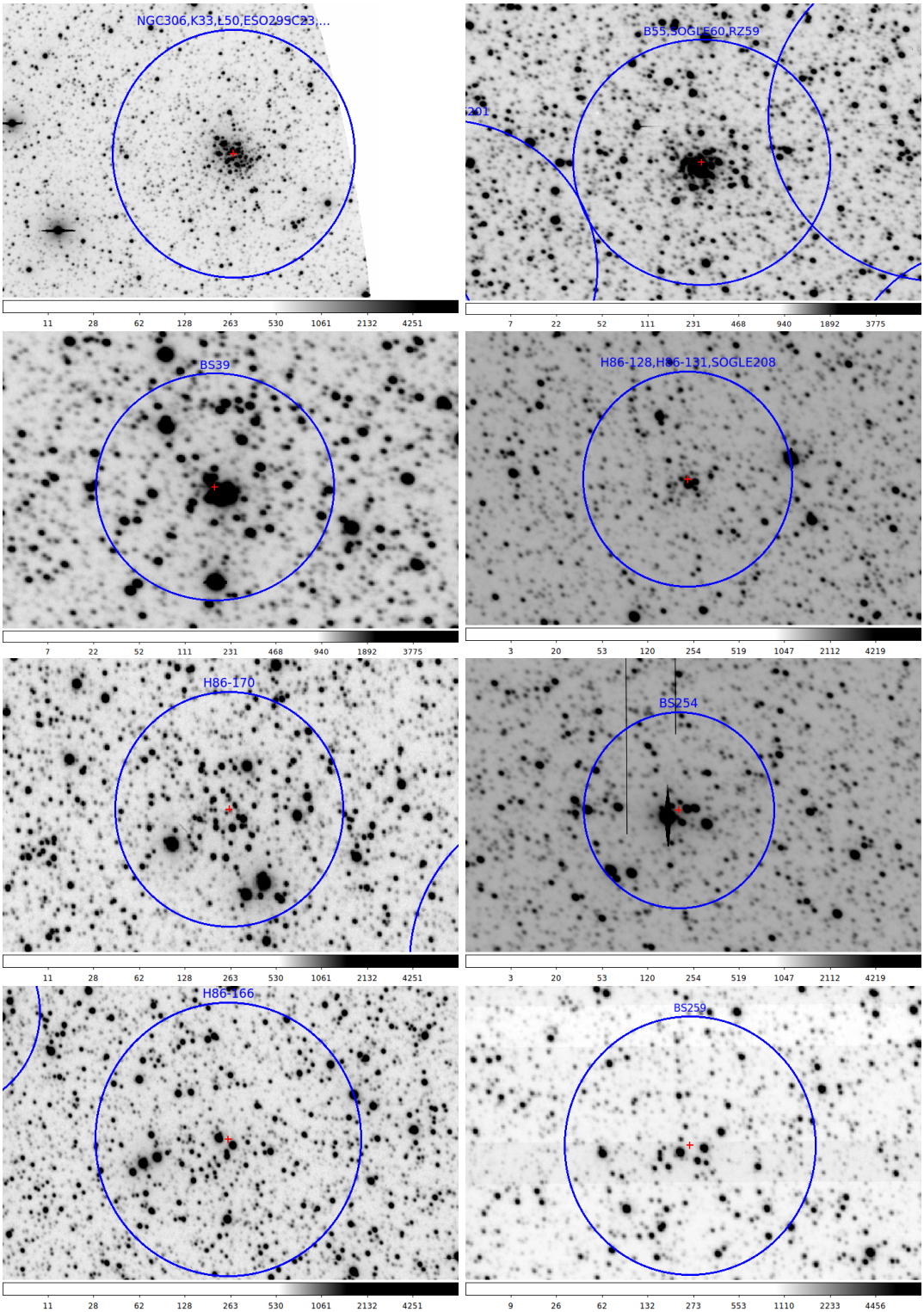

Figure 53: Clusters of all three classes, NGC306, B55, BS39, H86-128, H86-170, BS254, H86-166, BS259, as seen on IMACS B images. The blue circle has a radius equal to the published radius (major axis).

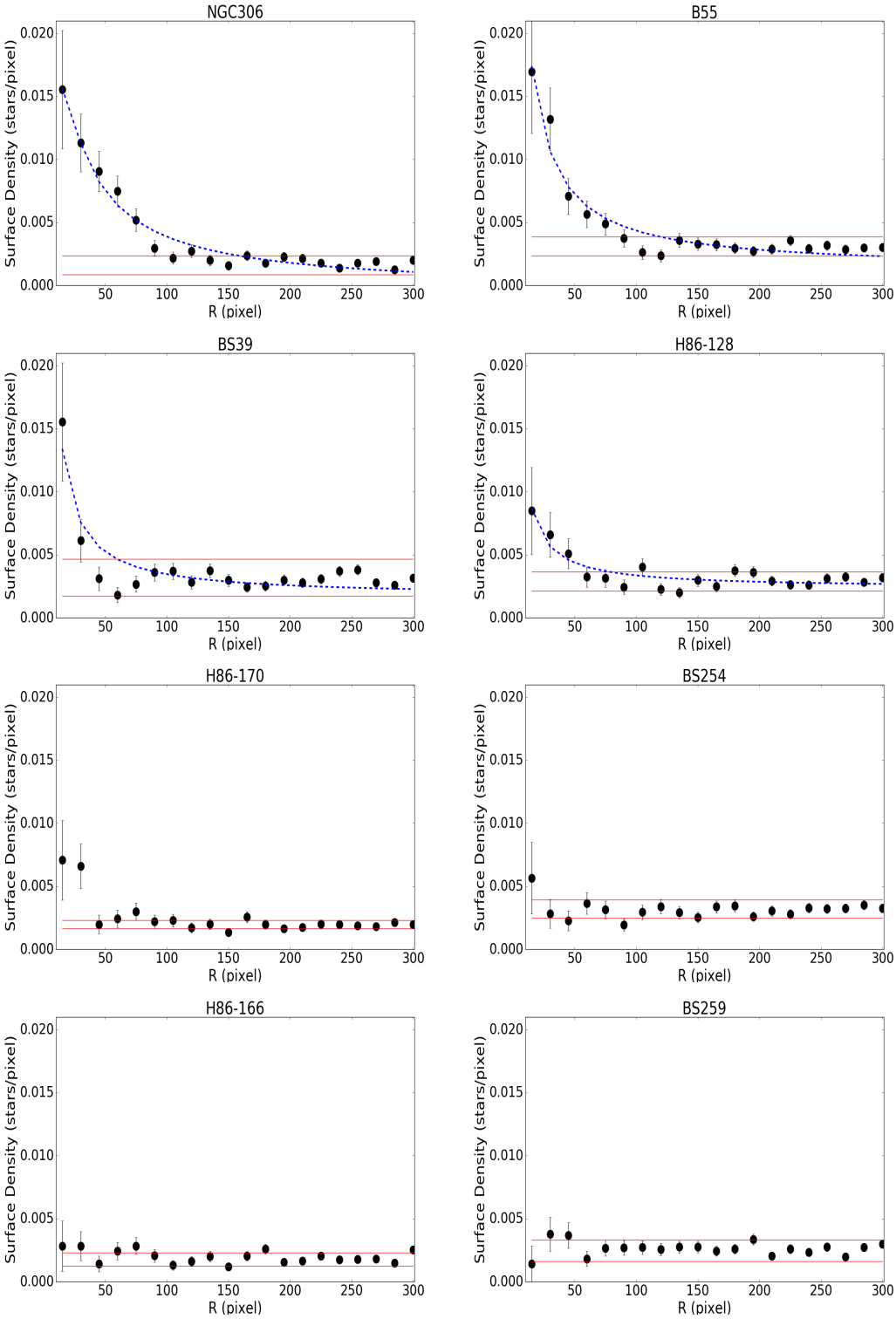

Figure 54: The radial profiles of NGC306, B55, BS39, H86-128, H86-170, BS254, H86-166, and BS259. The blue line is the best fit of a King empirical profile. The red lines indicate the three sigma range ($\pm 3\sigma$) around the average background surface density.

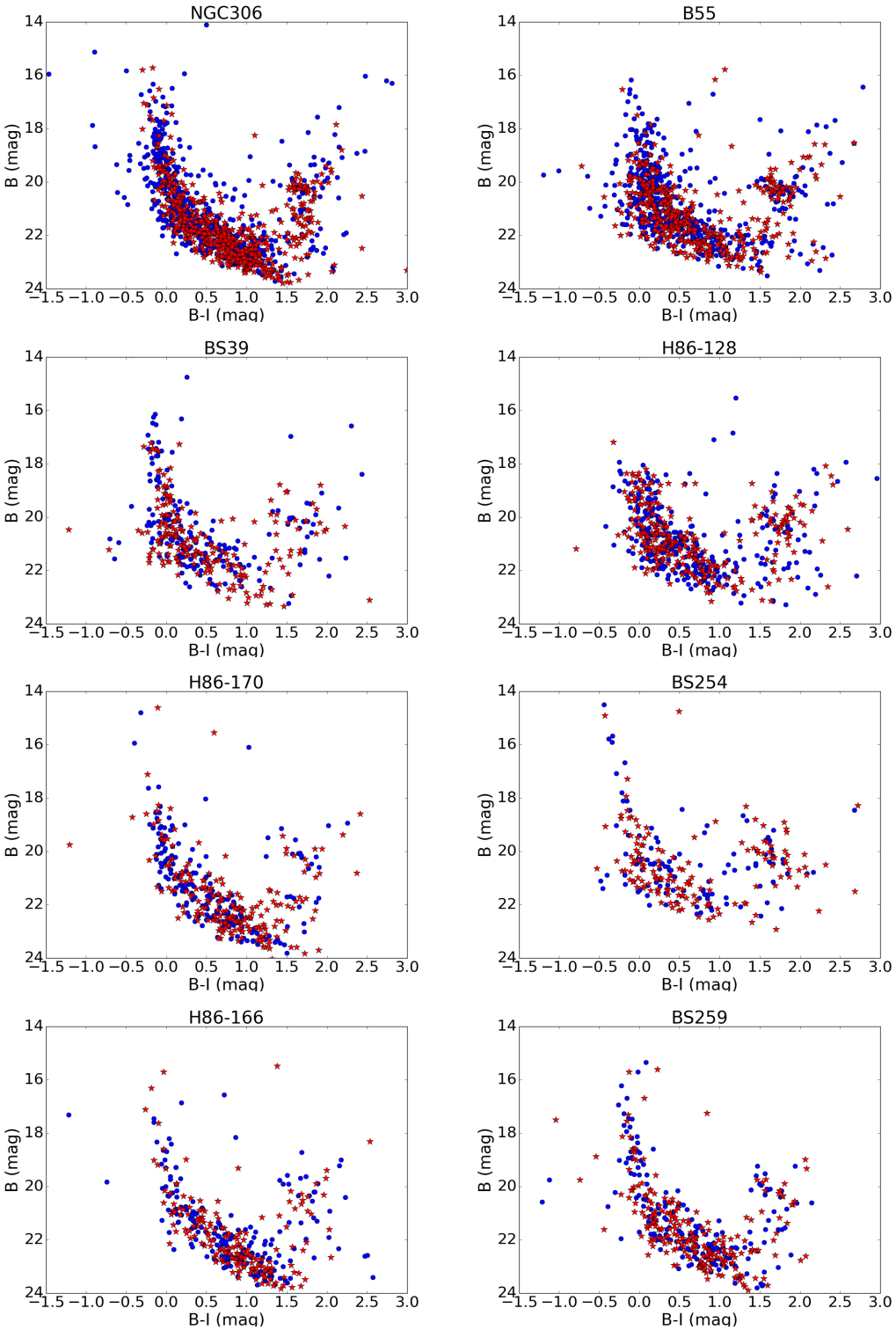

Figure 55: CMDs of star clusters NGC306, B55, BS39, H86-128, H86-170, BS254, H86-166, BS259 (blue points) and of background (red stars).

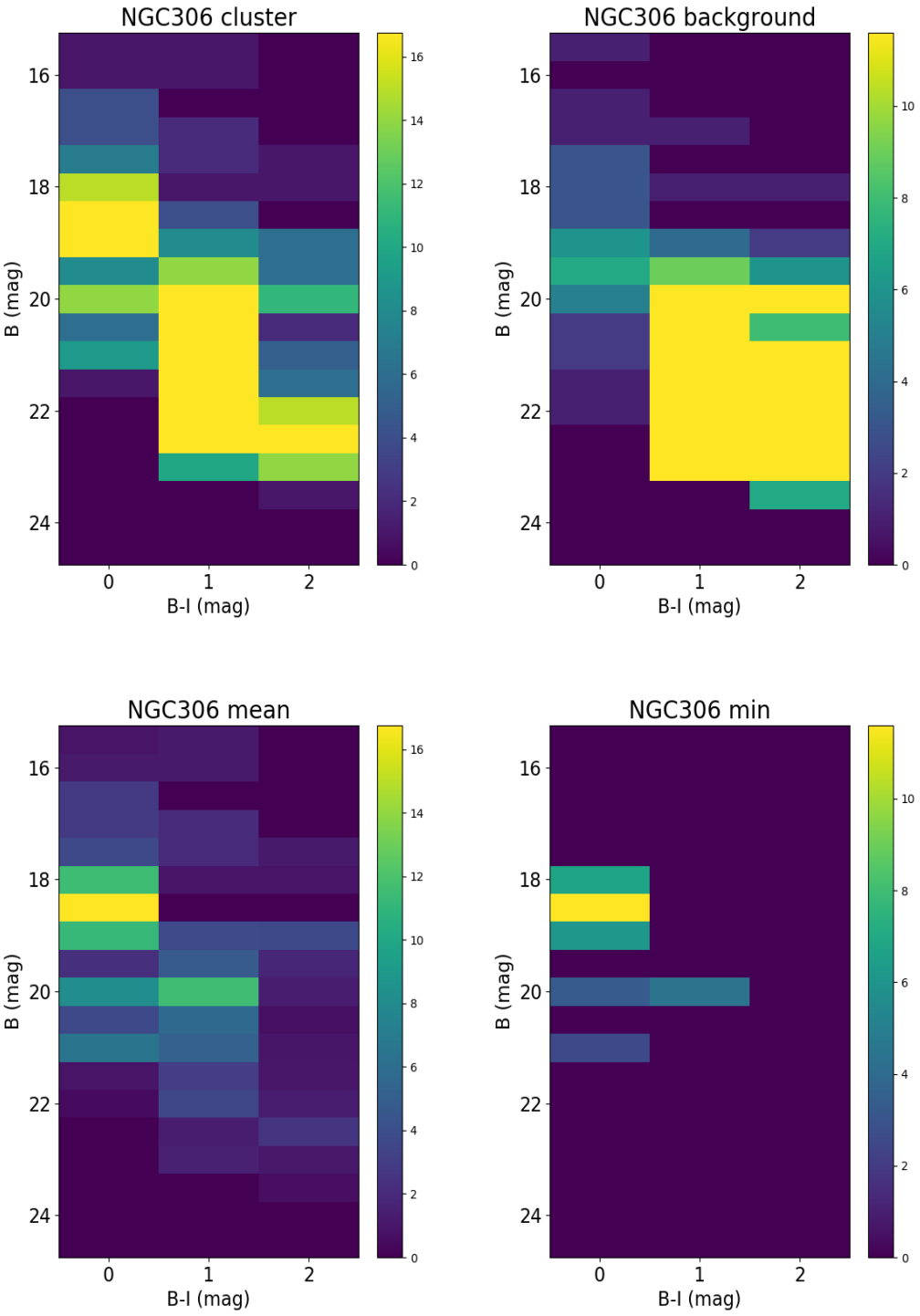

Figure 56: colour density maps of the CMDs of NGC306.

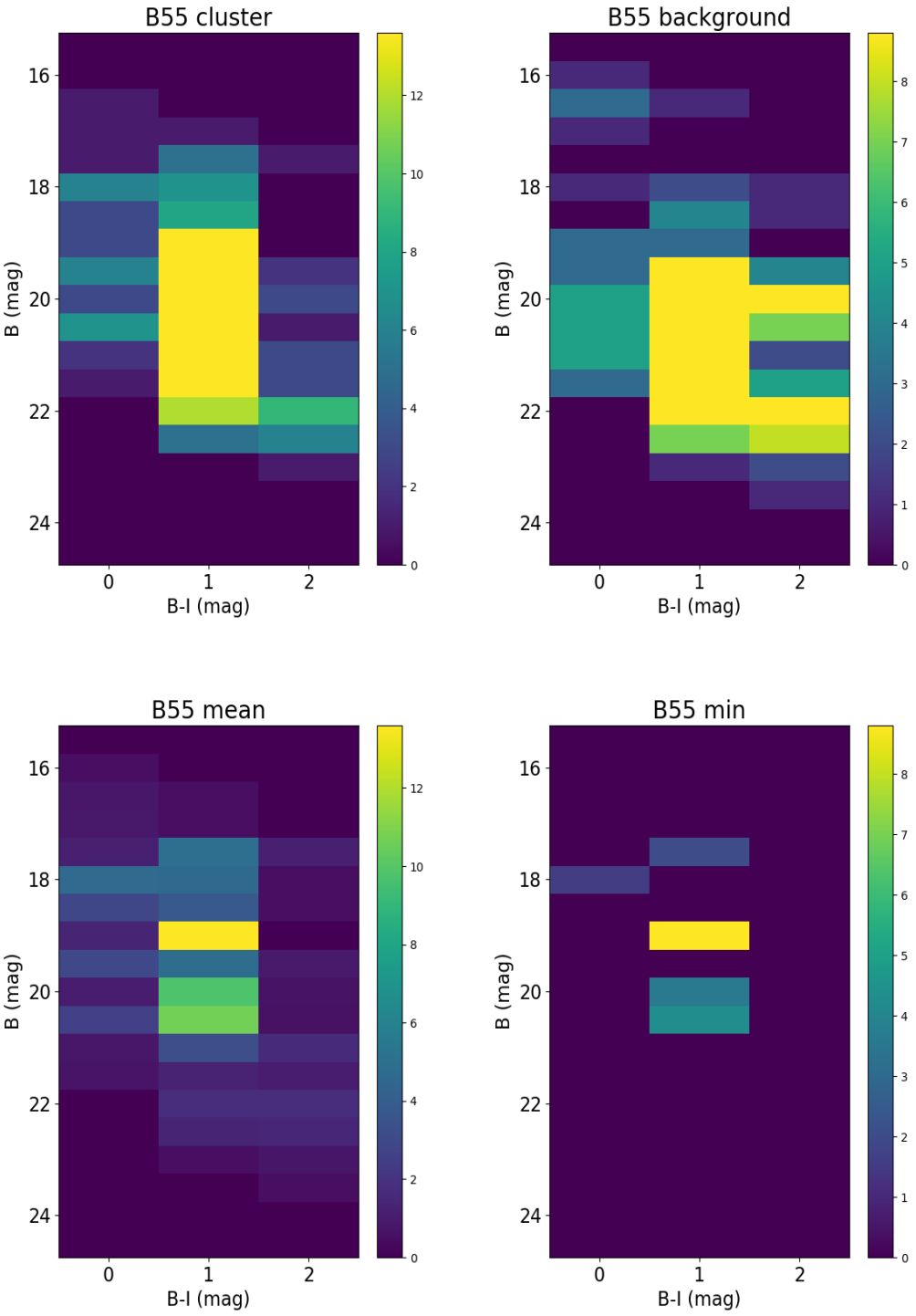

Figure 57: colour density maps of the CMDs of B55.

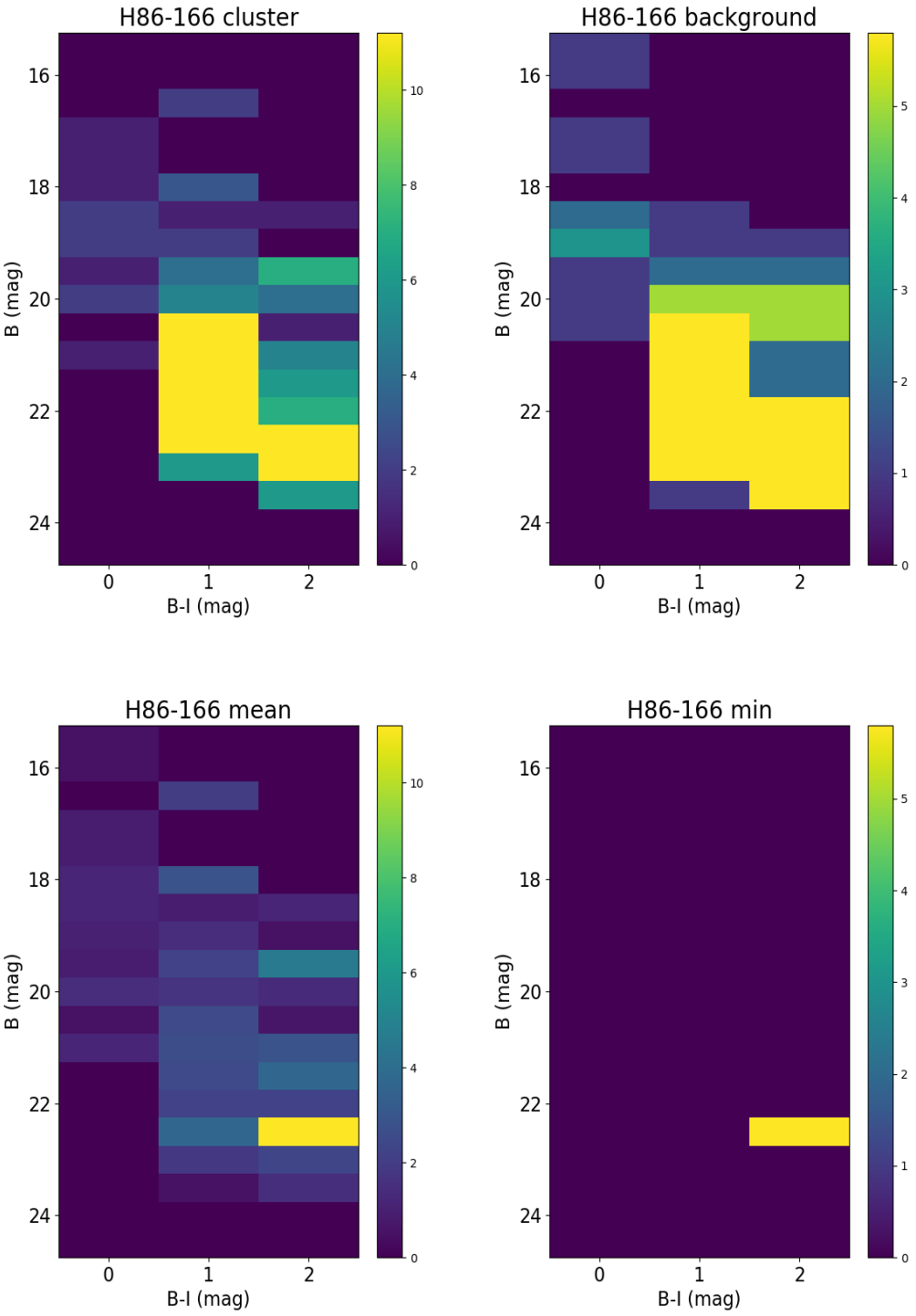

Figure 58: colour density maps of the CMDs of H86-166

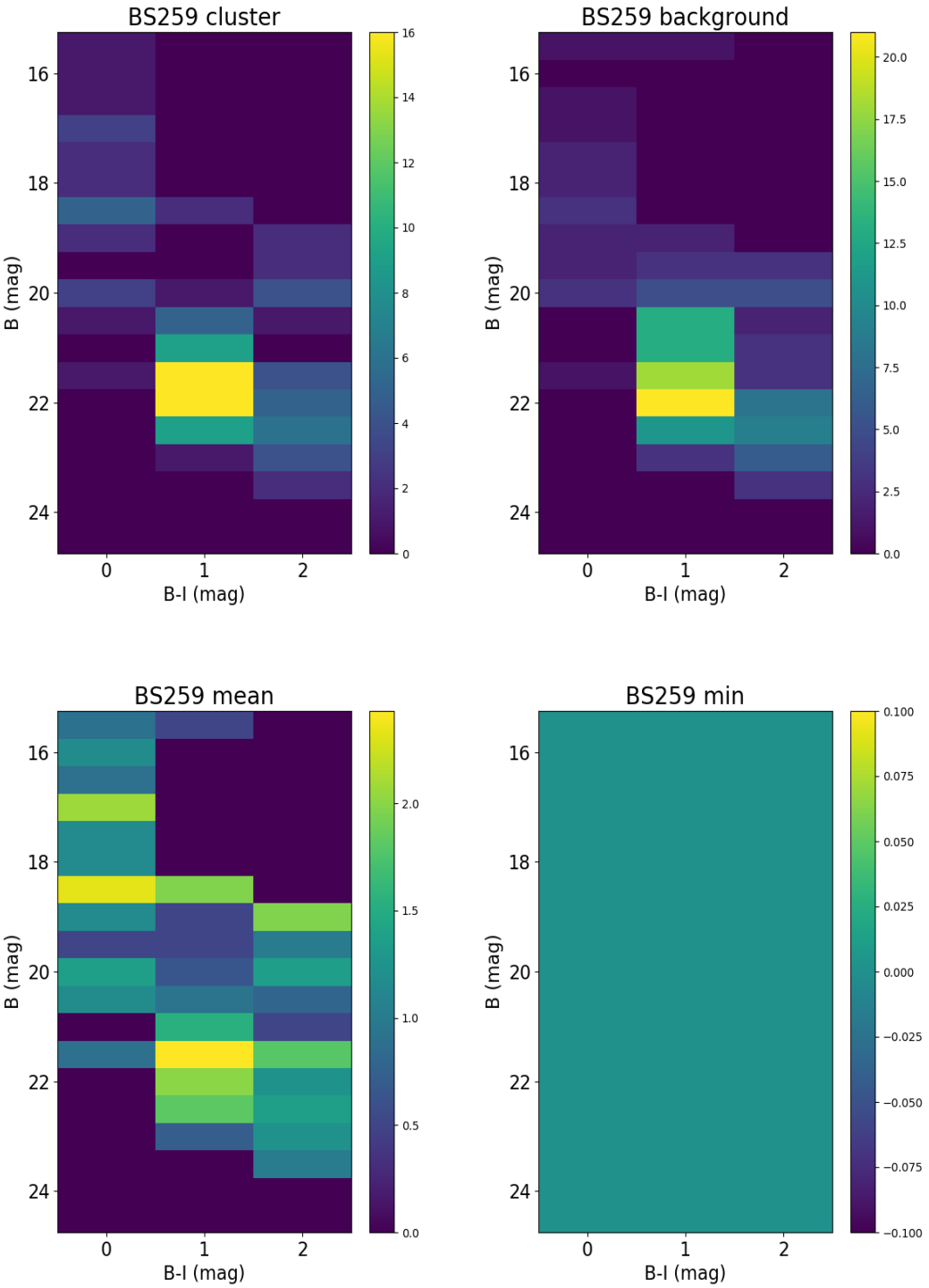

Figure 59: colour density maps of the CMDs of BS259

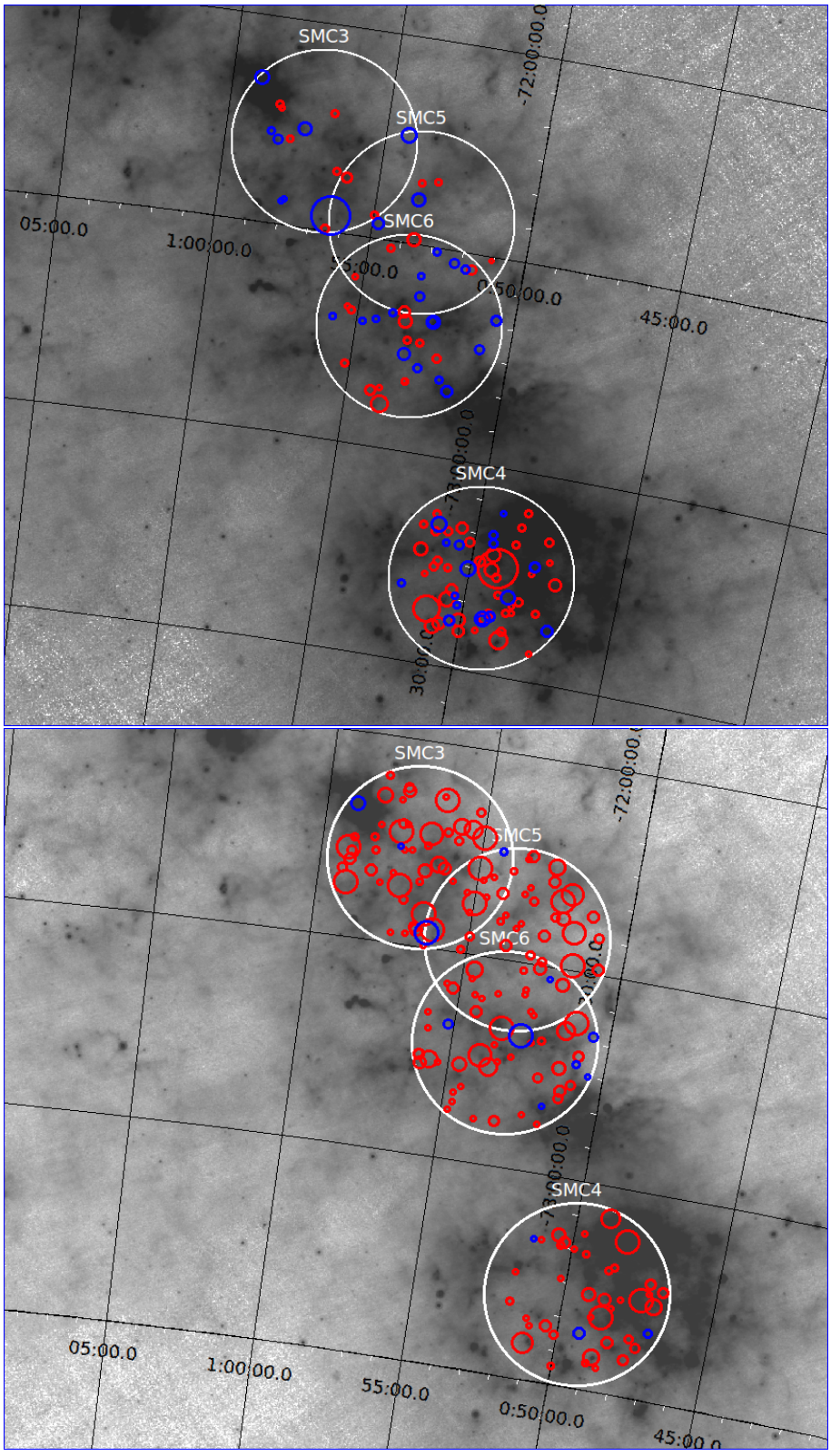

Figure 60: Spatial distribution of the stars clusters from the catalog of Bica et al. [2020] *top panel* and from the catalogue of Bitsakis et al. [2018] *bottom panel*. The blue circles have been classified as classes 3, 2 and the red circles as classes 1, 0.

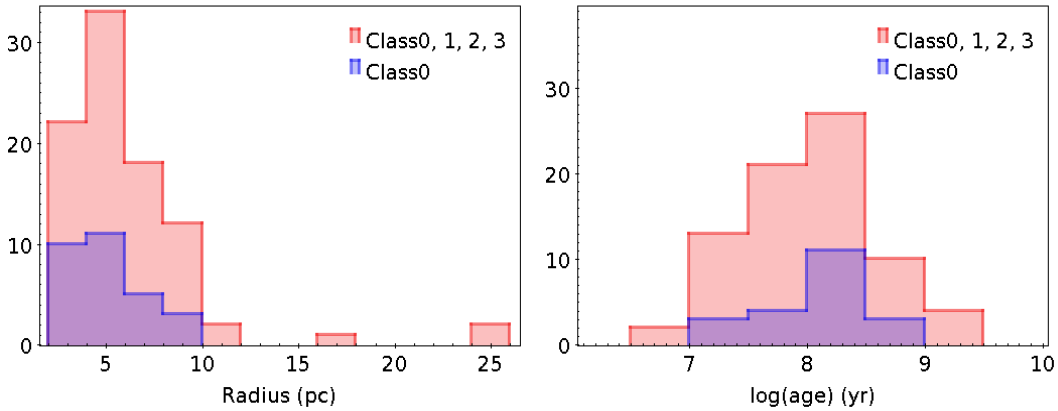

Figure 61: Comparison of radius and age distribution of star clusters class0, with all clusters of the catalog of Bica et al. [2020]

the left of each CMD, with the blue line corresponding to the cluster region, and the red to the field region; and finally, a histogram of the distribution of B-I colours of MS stars in the cluster (blue) and field (red) regions. The comparison between the "blue" and "red" distributions, i.e. between cluster and field, is performed using the Kolmogorov-Smirnov 2-sample test (K-S). The null hypothesis is that the two distributions (cluster and field) are drawn from the same population. This is rejected if the p-value is less than the predefined significance level, e.g. 0.05. P-values derived from the comparison between the cluster and field B-magnitude distributions are symbolised with p1 while the p-values derived for the $B-I$ colour distributions with p2. In Fig. 63 we plot the resulting $-logp2$ versus $-logp1$ values for different clsses of candidate clusters: on the top left we show the distribution of class 0 and 1 objects in red and class 2 and 3 objects in green, while on the top right, we only show class 0 (red) and class 3 (green) objects. It can be clearly seen that for the great majority of class 2 and 3 objects, the hypothesis that the cluster and field come from the same population is rejected with very high confidence (even higher for class 3). There are few exceptions, corresponding to cases with very small numbers of stars on the MS. Therefore, the $-logp2$ versus $-logp1$ diagram can be used as a diagnostic to confirm or otherwise the classification of an object as a star cluster. The size of the sample of stars used is crucial. The bottom two panels of Fig. 63 show the same plots when the sample size is larger than 300.

We also investigated automatic algorithms to identify star clusters. Schmeja [2011] presented a comparison between four such algorithms, testing them with artificial star clusters of different sizes and morphologies. The algorithms tested were (i) stellar density mapping, (ii) the Nearest Neighbour algorithm, (iii) the Voronoi Tessellation and (iv) the the Minimum Spanning Trees algorithm. While distinct, centrally concentrated, clusters were detected by all methods, clusters with low density or highly hierarchical structure were only reliably detected by methods with inherent smoothing (star counts and nearest neighbour method). It was also noted that the algorithms differed strongly in computation time and additional parameters they provided.

The first algorithm that we employed for star cluster identification was Friend of Friend (FoF). The code used was developed by P. Drazinos (Drazinos et al. 2013) and searches for pairs of objects that are closer than a cut off distance limit. The main aim of the method is to apply an objective criterion to the stellar structure identification process. Two stars belong to the same group only if they lie at a distance less or equal to a predefined value of search radius. The algorithm was applied to IMACS data, but due to the gaps in the spatial distribution (in the regions between CCDs; this problem was only partially rectified by dithering, during the observations, leaving lower sensitivity strips between CCDs in any observed field), the FoF code did not render reliable results. The code provided a large number of candidate clusters, with the great majority being false positives. The problem persisted over a wide range of values

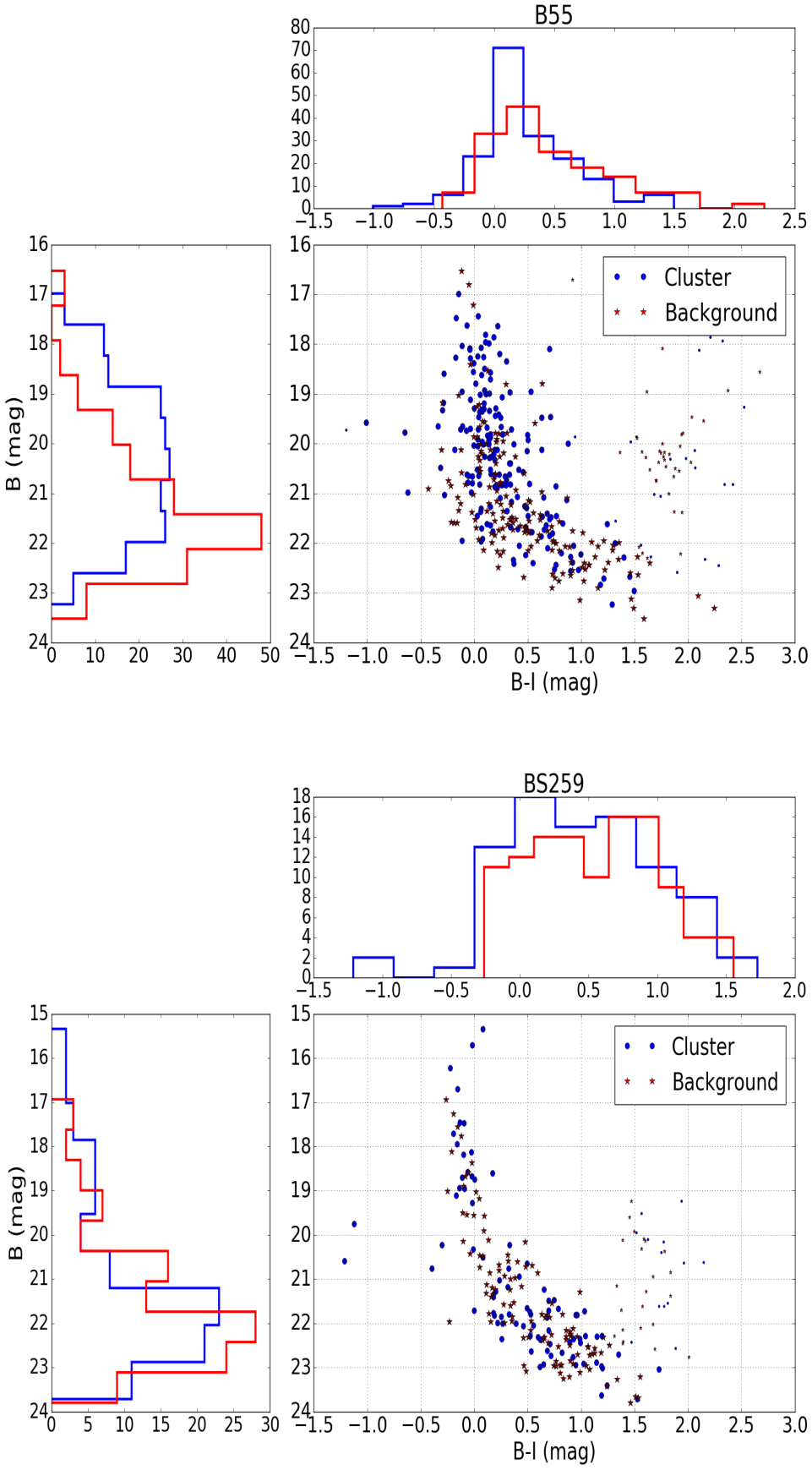

Figure 62: Histograms of the MN stars of the magnitude B and colour of clusters B55, BS259.

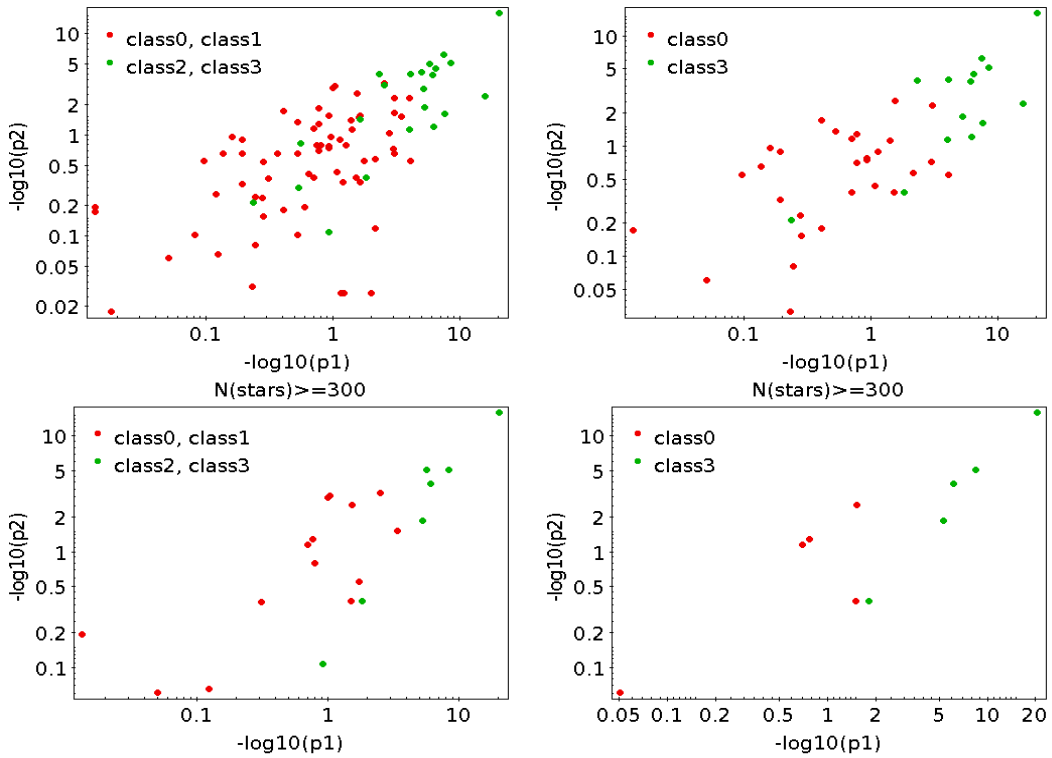

Figure 63: Diagram of the p values of two sample K-S test of the distribution of the magnitude B and colour B-I.The K-S test was applied to the populations of cluster's area and background MS's stars. Bica et al. [2020]

tested for the various parameters used in the algorithm, such as linking length and minimum group size. We also used supervised machine learning, trained on known clusters in one subfield, to classify candidates automatically identified in the rest of the area. This method also failed to satisfactorily flag false positives.

The second method we tested was "Density-based Spatial Clustering of Applications with Noise" (DBSCAN). DBSCAN is a well-known data clustering algorithm that is commonly used in data mining and machine learning (Zari et al. 2019, Price-Jones and Bovy 2019). It is a non-parametric algorithm based on density: given a set of points in some space, it groups together points that are closely packed together (points with many nearby neighbors), marking as outliers points that lie alone in low-density regions (whose nearest neighbors are too far away). DBSCAN is one of the most commonly used clustering algorithms and also most cited in the scientific literature.

DBSCAN clustering depends on 2 parameters:"MinPts" that represents the minimum number of core points and "eps" that represents the radius of a circle where MinPts are to be found. It is clear that when increasing MinPts one gets fewer but denser clusters, while omitting smaller ones. The initial value assigned to "MinPts" was 25, i.e. a cluster will have at least 25 stars, usually many more than that. As with FoF, we performed additional runs with more (and fewer) MinPts in order to check our assumptions and understand the algorithm's capacity to capture star clusters more effectively. As far as the optimization of the eps parameter is concerned, we calculated the kNN (k nearest neighbors) distances for a given k, where k=MinPts. The kNN distance plot (see left panel of Fig. 64) is useful in general since it provides the density distribution of the dataset. From this plot we can find a suggested value for the distance parameter eps from the maximum curvature or the point where a sharp change occurs (like "knee"). There might be none, one or more than one "knees" in general; this depends on our data. In the dataset we had available, the distribution of distances using

the kNN method was clear enough allowing us to select an optimal eps. Using this algorithm we can identify (see right panel of Fig. 64) all clusters of class 3 and almost all of class 2 (except one in field SMC5). We can conclude here that the DBSCAN algorithm confirms the classification resulting from the use of the three criteria described above. The combined use of the two methods is a very useful tool for the discovery and verification of star clusters. Although star clusters of the class 1 are not discovered by the DBSCAN algorithm, some of them are not rejected by all three criteria. A full analysis and description of these results will be presented in detail in Strantzalis et al. (2021, in preparation).

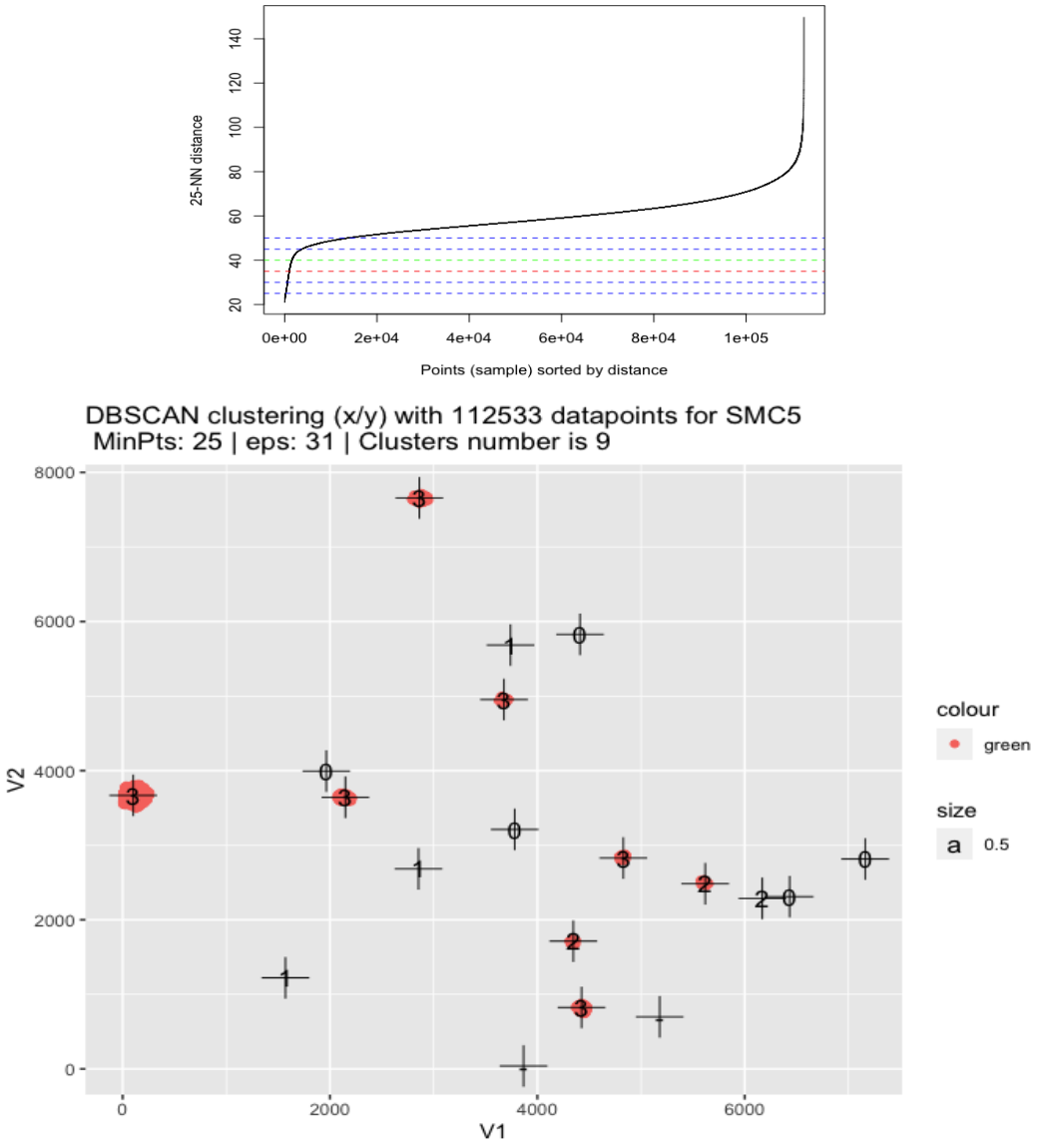

Figure 64: *Left Panel:* knn diagram for field SMC5, We use a range of values of the eps (dashed lines) to select the value of eps. From the red line and upper there are many false positive objects, so we choose a value before (eps=31).*Right Panel:* Candidate cluster locations using DBSCAN for SMC5. The quality class of the cluster 0,1,2,3 appear at the location of each cluster. The orange-coloured patches indicate the location of the DBSCAN candidate overdensities.

8 X-ray sources in the SMC

High-mass X-ray binaries (HMXBs) are binary stellar systems consisting of a massive, early-type donor star (of O or B spectral type) and a compact object (which can be a neutron star or a stellar black hole), which is the accretor. Mass loss can occur either via the donor's stellar wind (in the case of supergiants) or via a circumstellar disc created from equatorial mass loss (forming a decretion disk) of the rapidly rotating Be stars. In the first case the HMXB is of the sgXRB type and in the second case of the BeXRB type. In BeXRBs the donor is a non-supergiant O or B star and the accretor is usually a pulsar. Depending on the mass of the decretion disk and the system's orbital parameters, the X-ray emission can be persistent or variable,on timescales of days up to several months. Most BeXRB are variable sources, with X-ray fluxes that can reach up to $\simeq 10^{38}$ergs^{-1}. BeXRBs are identified as variable or transient X-Ray sources, with an optical counterpart that is an early type non-supergiant massive star of O or B type that shows (or has shown in the past) Balmer emission.

The SMC is known to contain a large number of HMXRBs (e.g. Townsend et al. 2011, Haberl and Sturm 2016, Antoniou et al. 2010). The great majority of the SMC HMXBs are of the BeXRB type (Coe et al. 2005), many more per unit stellar mass than in the LMC, or in the Milky Way (McBride et al. 2008, Yokogawa et al. 2003). This high incidence of BeXRBs is probably connected to the star formation history of the SMC (Antoniou et al. 2009,Antoniou et al. 2010), as well as its low metallicity McBride et al. [2008].

The Deep *Chandra* X-ray Visionary Project (XVP) is a survey of 11 selected SMC regions that are known to contain young ($\leq$100 Myr) stellar populations of different ages. The X-ray exposures are of 100 ks in order to reach limiting fluxes well within the regime of X-ray emission from quiescent XRBs ($10^{32} ergs^{-1}$) and in this way to obtain as complete a picture as possible of the HMXB populations of the SMC. These observations were performed from December 2012 to February 2014, utilizing the *Chandra* ACIS-Imaging mode. Additionally, there are 3 archival observations reaching the same depth (exposure time of 100 ks). Two of these fields (PI A. Zezas; observed in 2006) overlap partially with fields from the XVP survey, and the third is centered on the star cluster NGC346 (PI M. Corcoran; observed in 2001), (Antoniou et al. 2019).

The spatial distribution of the observed fields of the XVP survey is shown in Fig.65 overlaid on a Magellanic Cloud Emission Survey (MCELS) Hα image. The colour of each field corresponds to the age of its younger stellar population as derived by Harris and Zaritsky [2004] (orange: 11 Myr, blue: 34 Myr, cyan: 42 Myr, magenta: 67 Myr) except for three fields that have two distinct stellar populations: DF11 (red: 7 Myr and 42 Myr), DF02A (green: 42 Myr and 167.9 Myr) and NGC346 (maroon: 5 Myr and 42 Myr). The final catalogue presented by Antoniou et al. [2019] contained 2393 X-ray sources down to a limiting flux of 2.6×10^{-16}erg cm^2 s^1 in the full (0.5–8.0keV) band (50% complete at 7.94×10^{16}erg cm ^{2}s ^{1}). The spatial distribution of the sources is shown on a Spitzer-MIPS 24μ map in Fig. 66.The four IMACS fileds are indicated with white circles.

A subset of the catalogued sources are expected to be HMXRBs. To identify candidate HMXBs, we cross-correlated the X-ray source catalogue of Antoniou et al. [2019] with the IMACS photometric catalogue. Because of the relatively large positional errors of the X-ray sources and the relatively large surface stellar number density particularly in the inner regions of the SMC, false correlations are likely. Therefore, to interpret the results of the cross-correlation it is important to first calculate statistical tables of chance coincidence in different regions of the CMD. We followed a procedure similar to that presented in Antoniou et al. [2010] and in Antoniou and Zezas [2016]. The CMD was divided in colour-magnitude cells. For each cell, we calculated the "chance coincidence", i.e. the probability to detect one or more optical matches (inside the specified cell) to a X-ray source, within a search radius determined by the positional uncertainty. To this purpose a code was written in Python (see Appendix) that simulates 100 random samples of X-ray sources by applying to the position of each source a random offset in RA and DEC. The new position of X-ray source had to be outside the search radius, while the maximum offset was limited in order to avoid regions with different stellar density. Fig. 67 shows the grid of cells used. The cell size is not constant but depends on the number of stars.

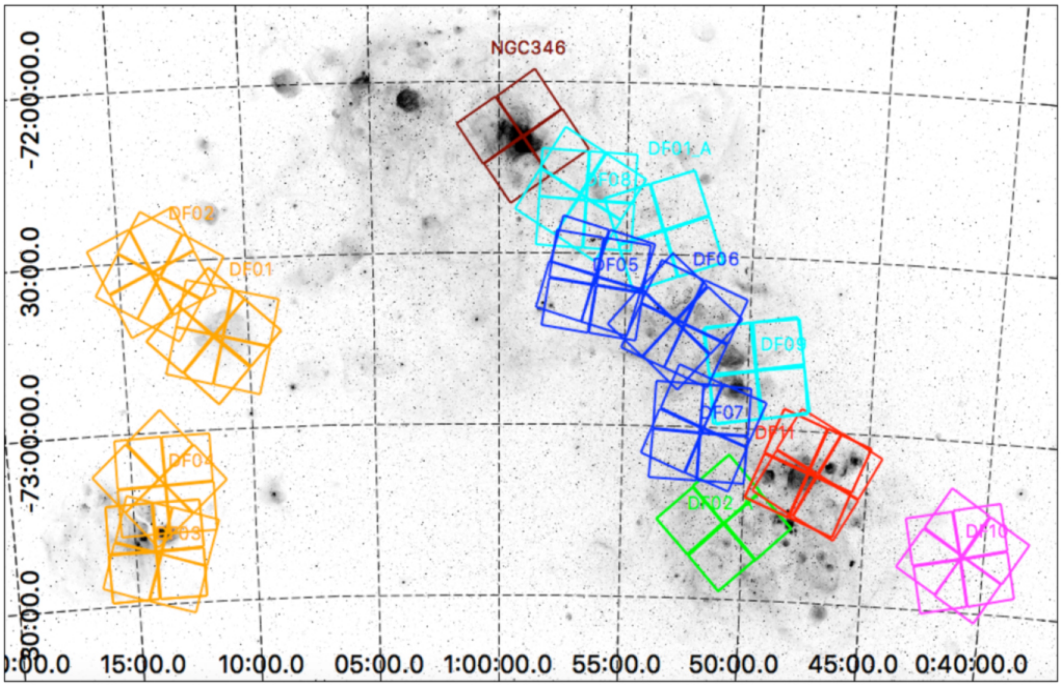

Figure 65: The 14 Chandra fields analyzed by Antoniou et al. [2019]. The colour of each box is related with the age of stellar population.The figure is reproduced from Antoniou et al. [2019].

So the cells are larger in sparse areas of the CMD. For example, in a high stellar density region of the CMD the cell size is 0.5 mag in magnitude (B) and 0.5 mag in colour (B-I). In lower density regions the cell size is 1 mag in B and 1 mag in B-I.

We cross-correlated the original catalogue of X-ray sources, as well as the one with offset positions as described above (this procedure was repeated 100 times, so 100 tables with offset positions were created), with the optical catalogue of stars from IMACS, using three different search radii for the cross-matching, 1, 2, or 3 arcsec. It is noted that 13% of the 2393 X-ray sources have positional errors larger than 3 arcsec, and 26% larger than 2 arcsec. The resulting chance coincidence probabilities in the various CMD cells for different search radii are displayed in Fig. 68. Each chance coincidence probability value is followed by the standard error derived from the different values obtained for the 100 iterations.

As expected, the chance coincidence probability is higher for regions of the CMD with high stellar density, and increases with increasing search radius. For example, the chance coincidence for a search radius of 1 arcsec is 4.7% for a stars with $0 \leq (B\text{-}I) \leq 0.5$ and $20 \leq B \leq 21$. This probability drops to 1.6% for stars with $0 \leq (B\text{-}I) \leq 0.5$ and $19 \leq B \leq 20$, a region on the CMD with lower stellar number density. As also noted by Antoniou et al. [2019] cross matches with brighter main sequence stars have lower chance coincidence, which means that the brightest match for X-ray sources with multiple matches is the most likely optical counterpart.

Antoniou et al. [2019] have published a catalogue of HMXB candidates that resulted from a cross correlation of the XVP X-ray source catalogue with the OGLE III catalogue of stars in the SMC (Udalski et al. 2008). The radius used for the cross-correlation was set equal to the positional error. Sources with an optical counterpart within the OB-star locus on the CMD (according to the spectroscopic catalogue of Bonanos et al. 2010) were considered to be HMXB candidates (see also Antoniou et al. [2010], Antoniou and Zezas [2016]). The locus of BeXRBs on the CMD is extended to redder colours to account for the circumstellar disk absorption. The final catalogue of candidate HMXRBs presented by Antoniou et al. [2019] contained 123 objects, 92 of which lie in the IMACS fields studied here.

Leveraging on the high photometric quality of the IMACS data, we revisited the identifica-

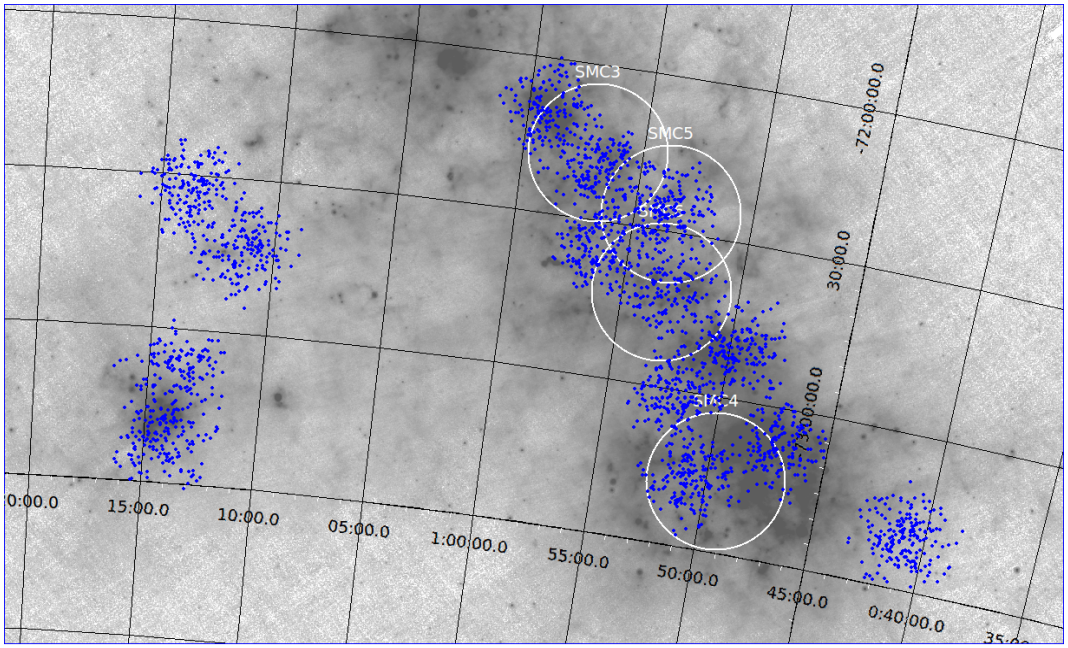

Figure 66: Spatial distribution of the X-ray sources in the SMC (overlayed on a Spitzer 24μm image).The white circles indicate the four IMACS fields analysed in this thesis.

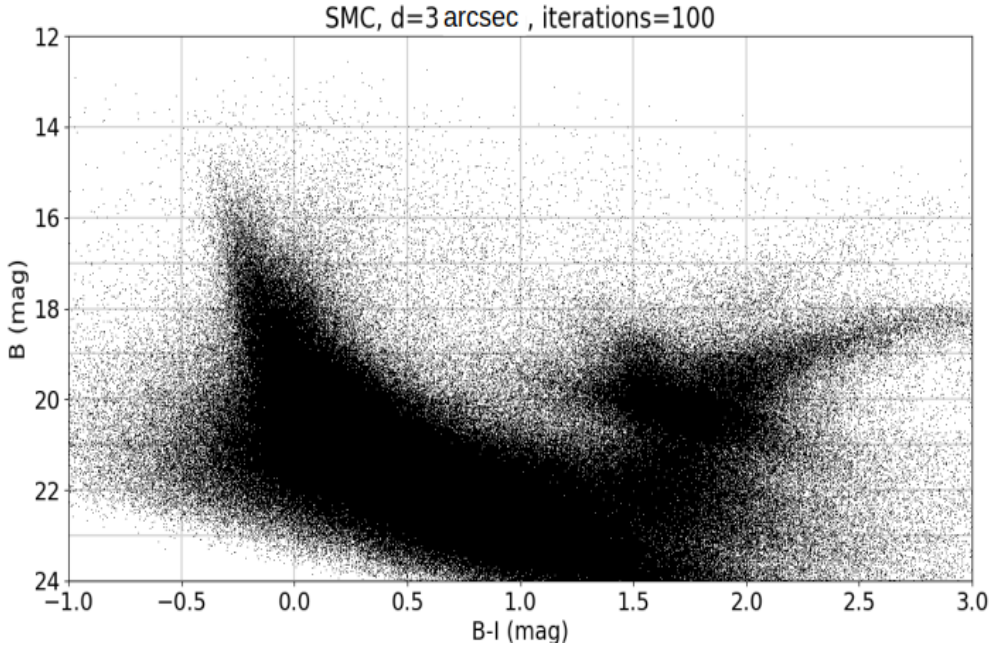

Figure 67: Example of CMD grid used for the calculation of chance coincidence probabilities.

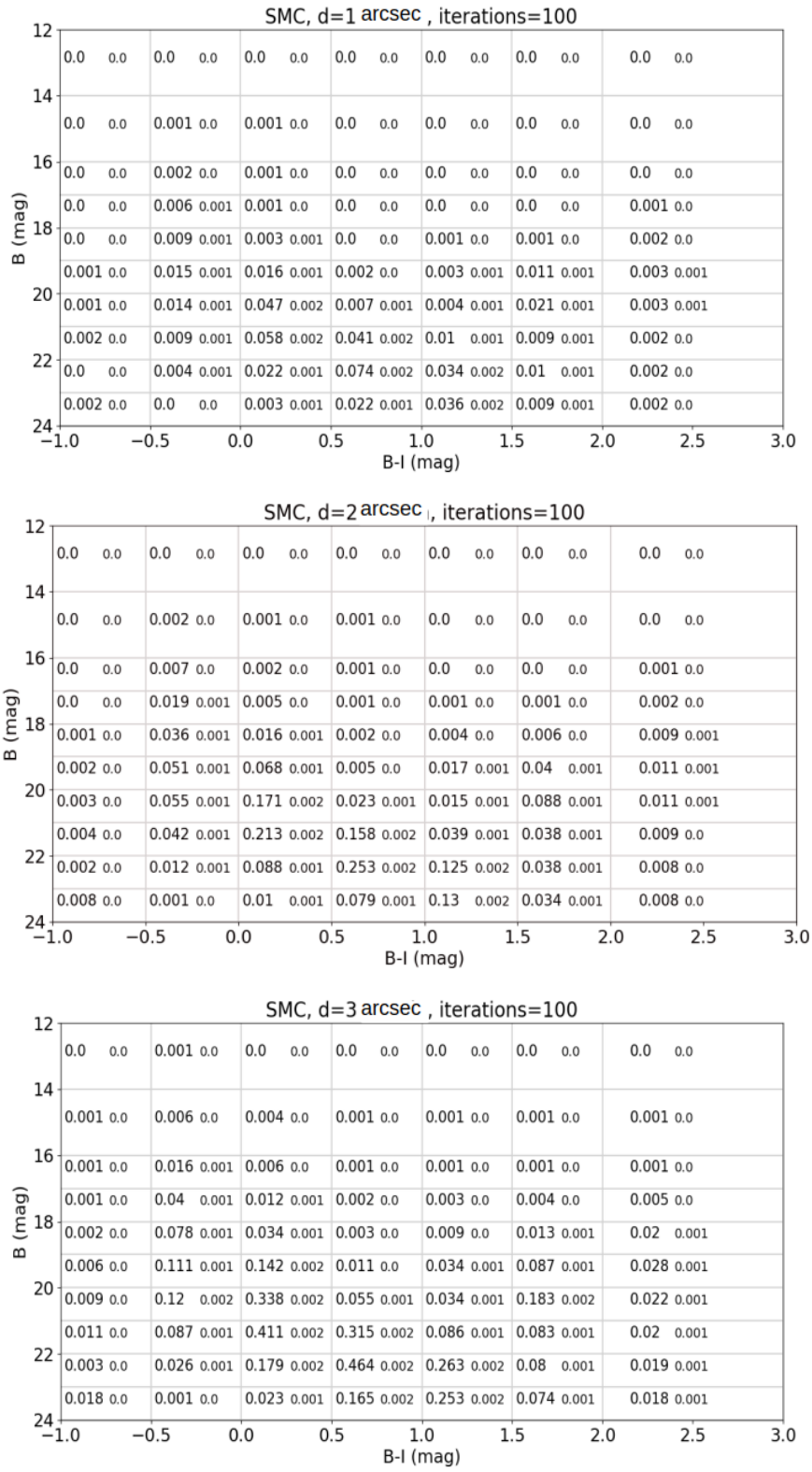

Figure 68: Chance coincidence probabilities and corresponding standard errors calculated for each colour-magnitude cell, for three different search radii (top panel, for a search radius of 1 arcsec, middle for 2 arcsec, and bottom for three arcsec).

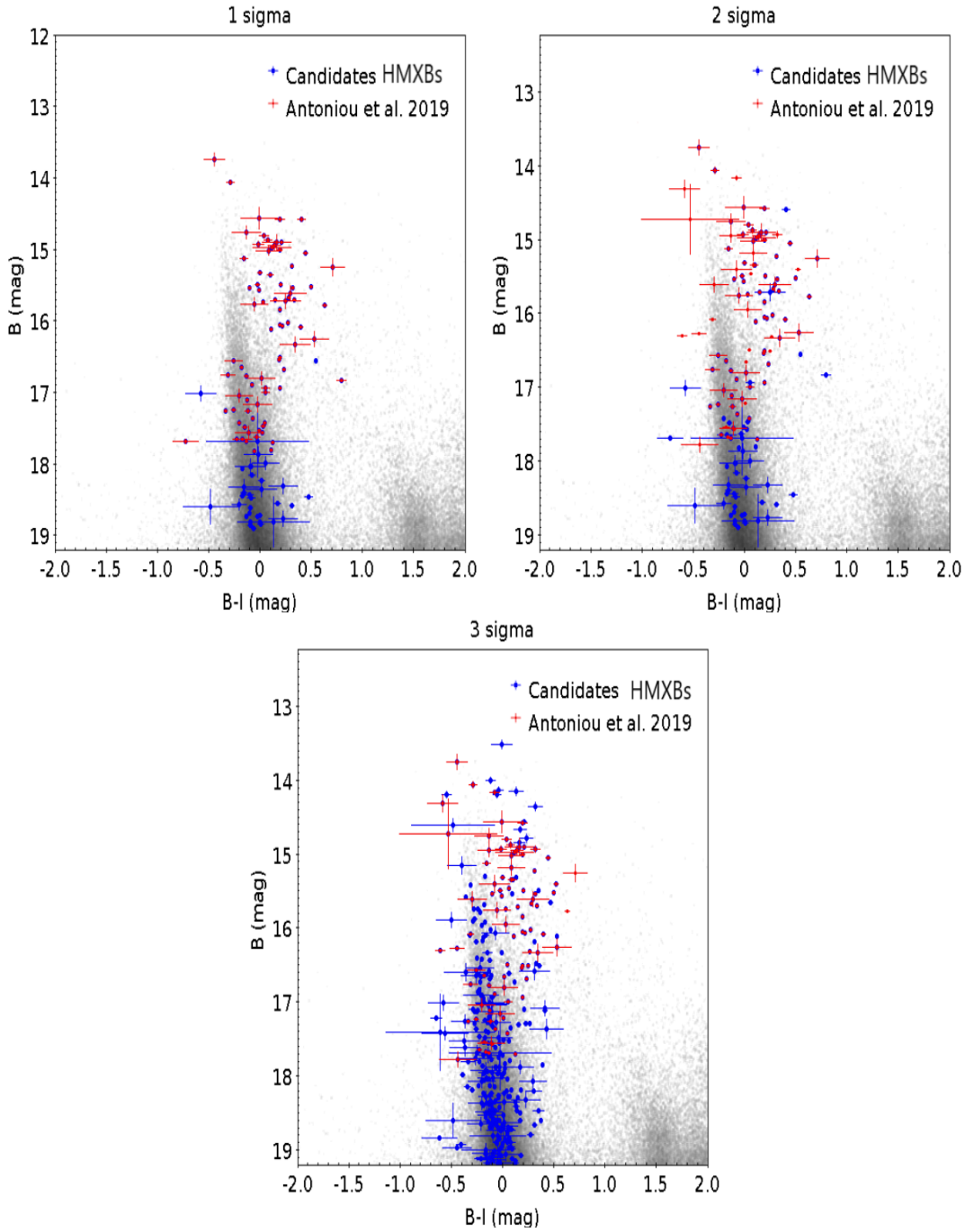

Figure 69: Candidates Bes stars for different search radius (*left upper panel* 1 sigma, *right upper panel* 2 sigma, *lower panel* 3 sigma) on the CMD. For our study take into account only candidates for magnitudes B*leq*18mag.

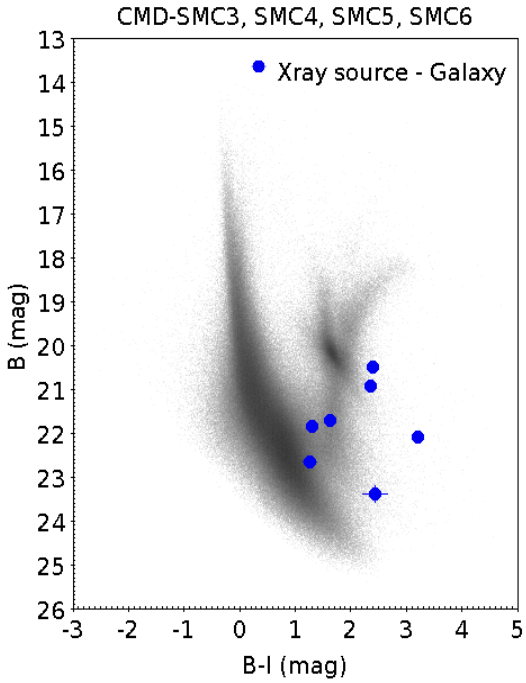

Figure 70: Xray sources it seems to be related with galaxy emission.

tion of HMXBs in the SMC based on the XVP survey. Following the procedures described in Antoniou et al. [2019], we cross correlated the catalogue of the 960 X-ray sources that are located in the four IMACS fields with the IMACS photometric catalogue. As candidate HMXBs we considered objects with counterparts with B $\leq$ 18 mag, I $\leq$ 18 and $-0.7 \leq$ B $-I \leq 0.9$ mag. This is the "extended" O, B, Oe, Be star region as defined in Antoniou et al. [2019]. The results are shown in Fig. 69 for various search radii. As previously mentioned if there is more than one optical counterpart to an X-ray source, the star with the lower chance coincidence is retained as a possible match. The search radius is 1,2 or 3 times the positional error. In the first case (top left panel), we recovered all candidates in Antoniou et al. [2019] (it is noted however that in this paper a larger search radius was used) and discovered 4 new candidates. For a search radius of two sigma (top right panel) we found 17 new candidates and for a search radius of three sigma (bottom panel) we found 85 new candidates. The candidates from the catalogue of Antoniou et al. [2019] are marked with red.

Antoniou et al. [2019] correlated the incidence of BeXRBs with star formation rate at different ages, and estimated the efficiency of BeXRB formation as a function of age. They found that the BeXRB formation efficiency increases as a function of look back time up to $\sim 40 - 60Myr$ ago. They also estimated the BeXRB formation peak to be at $\sim 30 - 40Myr$ with an average formation rate of $N(HMXB)/SFR = 339_{-83}{}^{+78}(\mathrm{M}_{\odot}/yr)^{-1}$ and $N(HMXB)/M_{*} = 8.74_{-1.0}{}^{+0.92}10^{-6}(\mathrm{M}_{\odot}/yr)^{-1}$. These estimates can be revised using the new results presented here. For a search radius of one sigma, we have 4 new candidates, which need to be added to the 94 objects that are located within our fields from the sample of Antoniou et al. [2019], leading to an increase of $\sim 4.2\%$. For a search radius of two sigma, there are 17 new candidates (increase of $\sim 18\%$) so the new rates need to be modified as follows: $N(HMXB)/SFR \sim 400(M_{\odot}/yr)^{-1}$ and $N(HMXB)/M_{*} \approx 10M_{\odot}^{-1}$. A full analysis and more detailed calculations of the formation efficiency of BeXRBs will be presented in Strantzalis et al. (2021).

Many authors have presented candidate HMXBs or BeXRBs of the SMC. Using light curves of about 2 million stars Mennickent et al. [2002] found a sample of ∼1000 candidates. Liu et al. [2005] presented a catalogue of 128 HMXBs and Haberl and Sturm [2016] merged previous lists and represented a catalogue of 148 confirmed and candidate HMXBs. We compared our new

candidates with these earlier catalogues and found that for 1 sigma search radius we do not have any new candidates, for two sigma we have 9 new candidates and for 3 sigma we have 70 new candidates.

A large percentage of the X-ray sources in the direction of the SMC are expected to be active galactic nuclei. Using the very high resolution images of the HST it is possible distinguish stars from AGNs. From the sample of 960 X-ray sources which are located in the fields studied, 193 have been imaged with the HST. We found 11 sources, i.e. 5.7%, that have a galaxy within the positional error of the X-ray source. From this sample of 11 galaxies, 7 have IMACS photometry. The location of the 7 galaxies on the CMD is shown in Fig. 70. They are generally red objects and fainter than 20 mag (in B). Assuming that the sample of sources with HST imaging is representative, we estimate that from the 2293 sources, about 140 could be associated with a galaxy. This is only a lower limit, as there are AGN that cannot be distinguished even with the HST.

In conclusion, we developed new tables of chance coincidence for the CMD of the SMC using deep photometric data of IMACS. Using the catalogue of the X-ray sources by Antoniou et al. [2019], we found new candidate HMXBs in the SMC. We also estimated a lower limit of the number of galaxies (AGN) that are expected in the sample of X-ray sources.

References

V. Antoniou and A. Zezas. Star formation history and X-ray binary populations: the case of the Large Magellanic Cloud. , 459(1):528–553, June 2016. doi: 10.1093/mnras/stw167.

V. Antoniou, A. Zezas, D. Hatzidimitriou, and J. C. McDowell. The Chandra Survey of the Small Magellanic Cloud "Bar". II. Optical Counterparts of X-ray Sources. , 697(2):1695–1716, June 2009. doi: 10.1088/0004-637X/697/2/1695.

V. Antoniou, A. Zezas, D. Hatzidimitriou, and V. Kalogera. Star Formation History and X-ray Binary Populations: The Case of the Small Magellanic Cloud. , 716(2):L140–L145, June 2010. doi: 10.1088/2041-8205/716/2/L140.

V. Antoniou, A. Zezas, J. J. Drake, C. Badenes, F. Haberl, N. J. Wright, J. Hong, R. Di Stefano, T. J. Gaetz, K. S. Long, P. P. Plucinsky, M. Sasaki, B. F. Williams, P. F. Winkler, and SMC XVP collaboration. Deep Chandra Survey of the Small Magellanic Cloud. III. Formation Efficiency of High-mass X-Ray Binaries. , 887(1):20, Dec. 2019. doi: 10.3847/1538-4357/ab4a7a.

F. Arenou, X. Luri, C. Babusiaux, C. Fabricius, A. Helmi, T. Muraveva, A. C. Robin, F. Spoto, A. Vallenari, T. Antoja, T. Cantat-Gaudin, C. Jordi, N. Leclerc, C. Reylé, M. Romero-Gómez, I. C. Shih, S. Soria, C. Barache, D. Bossini, A. Bragaglia, M. A. Breddels, M. Fabrizio, S. Lambert, P. M. Marrese, D. Massari, A. Moitinho, N. Robichon, L. Ruiz-Dern, R. Sordo, J. Veljanoski, L. Eyer, G. Jasniewicz, E. Pancino, C. Soubiran, A. Spagna, P. Tanga, C. Turon, and C. Zurbach. Gaia Data Release 2. Catalogue validation. , 616: A17, Aug. 2018. doi: 10.1051/0004-6361/201833234.

K. Auchettl, L. A. Lopez, C. Badenes, E. Ramirez-Ruiz, J. F. Beacom, and T. Holland - Ashford. Measurement of the Core-collapse Progenitor Mass Distribution of the Small Magellanic Cloud. , 871(1):64, Jan. 2019. doi: 10.3847/1538-4357/aaf395.

K. Bekki and M. Chiba. Origin of Structural and Kinematic Properties of the Small Magellanic Cloud. , 2009.

V. Belokurov and S. E. Koposov. Stellar streams around the Magellanic Clouds. , 456(1): 602–616, Feb. 2016. doi: 10.1093/mnras/stv2688.

E. Bertin. Swarp: Resampling and co-adding fits images together. *Astrophysics Source Code Library*, pages 10068–, 10 2010.

G. Besla, N. Kallivayalil, L. Hernquist, B. Robertson, T. J. Cox, R. P. van der Marel, and C. Alcock. Are the Magellanic Clouds on Their First Passage about the Milky Way? , 668 (2):949–967, Oct. 2007. doi: 10.1086/521385.

G. Besla, N. Kallivayalil, L. Hernquist, R. P. van der Marel, T. J. Cox, and D. Kereš. Simulations of the Magellanic Stream in a First Infall Scenario. , 721(2):L97–L101, Oct. 2010. doi: 10.1088/2041-8205/721/2/L97.

G. Besla, N. Kallivayalil, L. Hernquist, R. P. van der Marel, T. J. Cox, and D. Kereš. The role of dwarf galaxy interactions in shaping the Magellanic System and implications for Magellanic Irregulars. , 421(3):2109–2138, Apr. 2012. doi: 10.1111/j.1365-2966.2012.20466.x.

G. Besla, D. Martínez-Delgado, R. P. van der Marel, Y. Beletsky, M. Seibert, E. F. Schlafly, E. K. Grebel, and F. Neyer. Low Surface Brightness Imaging of the Magellanic System: Imprints of Tidal Interactions between the Clouds in the Stellar Periphery. , 825(1):20, July 2016. doi: 10.3847/0004-637X/825/1/20.

E. Bica, C. Bonatto, C. M. Dutra, and J. F. C. Santos. A general catalogue of extended objects in the Magellanic System. , 389(2):678–690, Sept. 2008. doi: 10.1111/j.1365-2966.2008.13612.x.

E. Bica, D. B. Pavani, C. J. Bonatto, and E. F. Lima. A Multi-band Catalog of 10978 Star Clusters, Associations, and Candidates in the Milky Way. , 157(1):12, Jan. 2019. doi: 10.3847/1538-3881/aaef8d.

E. Bica, P. Westera, L. d. O. Kerber, B. Dias, F. Maia, J. Santos, João F. C., B. Barbuy, and R. A. P. Oliveira. An Updated Small Magellanic Cloud and Magellanic Bridge Catalog of Star Clusters, Associations, and Related Objects. , 159(3):82, Mar. 2020. doi: 10.3847/1538-3881/ab6595.

E. L. D. Bica and H. R. Schmitt. A Revised and Extended Catalog of Magellanic System Clusters, Associations, and Emission Nebulae. I. Small Magellanic Cloud and Bridge. , 101: 41, Nov. 1995. doi: 10.1086/192233.

T. Bitsakis, P. Bonfini, R. A. González-Lópezlira, V. H. Ramírez-Siordia, G. Bruzual, S. Charlot, G. Maravelias, and D. Zaritsky. A Novel Method to Automatically Detect and Measure the Ages of Star Clusters in Nearby Galaxies: Application to the Large Magellanic Cloud. , 845(1):56, Aug. 2017. doi: 10.3847/1538-4357/aa8090.

T. Bitsakis, R. A. González-Lópezlira, P. Bonfini, G. Bruzual, G. Maravelias, D. Zaritsky, S. Charlot, and V. H. Ramírez-Siordia. The Distribution and Ages of Star Clusters in the Small Magellanic Cloud: Constraints on the Interaction History of the Magellanic Clouds. , 853(2):104, Feb 2018. doi: 10.3847/1538-4357/aaa244.

A. Z. Bonanos, D. J. Lennon, F. Köhlinger, J. T. van Loon, D. L. Massa, M. Sewilo, C. J. Evans, N. Panagia, B. L. Babler, M. Block, S. Bracker, C. W. Engelbracht, K. D. Gordon, J. L. Hora, R. Indebetouw, M. R. Meade, M. Meixner, K. A. Misselt, T. P. Robitaille, B. Shiao, and B. A. Whitney. Spitzer SAGE-SMC Infrared Photometry of Massive Stars in the Small Magellanic Cloud. , 140(2):416–429, Aug. 2010. doi: 10.1088/0004-6256/140/2/416.

A. Bressan, P. Marigo, L. Girardi, B. Salasnich, C. Dal Cero, S. Rubele, and A. Nanni. PARSEC: stellar tracks and isochrones with the PAdova and TRieste Stellar Evolution Code. , 427:127–145, Nov. 2012. doi: 10.1111/j.1365-2966.2012.21948.x.

M. T. Bruck. The cluster system in the Small Magellanic Cloud. , 173:327–338, Nov. 1975. doi: 10.1093/mnras/173.2.327.

F. C. Bruhweiler, I. Klinglesmith, Daniel A., T. R. Gull, and S. Sofia. Deep Einstein X-Ray Imagery of the Small Magellanic Cloud. , 317:152, June 1987. doi: 10.1086/165263.

J. Casares, I. Negueruela, M. Ribó, I. Ribas, J. M. Paredes, A. Herrero, and S. Simón-Díaz. A Be-type star with a black-hole companion. , 505(7483):378–381, Jan. 2014. doi: 10.1038/nature12916.

J. Casares, P. G. Jonker, and G. Israelian. *X-Ray Binaries*, page 1499. 2017. doi: 10.1007/978-3-319-21846-$5_1$11.

G. Chabrier. Galactic Stellar and Substellar Initial Mass Function. , 115(809):763–795, Jul 2003. doi: 10.1086/376392.

E. Chiosi, A. Vallenari, E. V. Held, L. Rizzi, and A. Moretti. Age distribution of young clusters and field stars in the Small Magellanic Cloud. , 452(1):179–193, June 2006. doi: 10.1051/0004-6361:20054559.

J. Choi, A. Dotter, C. Conroy, M. Cantiello, B. Paxton, and B. D. Johnson. Mesa Isochrones and Stellar Tracks (MIST). I. Solar-scaled Models. , 823(2):102, Jun 2016. doi: 10.3847/0004-637X/823/2/102.

M. Cignoni, A. A. Cole, M. Tosi, J. S. Gallagher, E. Sabbi, J. Anderson, E. K. Grebel, and A. Nota. Star Formation History in Two Fields of the Small Magellanic Cloud Bar. , 754(2): 130, Aug 2012. doi: 10.1088/0004-637X/754/2/130.

M. Cignoni, A. A. Cole, M. Tosi, J. S. Gallagher, E. Sabbi, J. Anderson, E. K. Grebel, and A. Nota. Mean Age Gradient and Asymmetry in the Star Formation History of the Small Magellanic Cloud. , 775(2):83, Oct. 2013. doi: 10.1088/0004-637X/775/2/83.

M. R. L. Cioni, L. Girardi, P. Marigo, and H. J. Habing. AGB stars in the Magellanic Clouds. III. The rate of star formation across the Small Magellanic Cloud. , 452(1):195–201, June 2006. doi: 10.1051/0004-6361:20054699.

M. R. L. Cioni, G. Clementini, L. Girardi, R. Guand alini, M. Gullieuszik, B. Miszalski, M. I. Moretti, V. Ripepi, S. Rubele, G. Bagheri, K. Bekki, N. Cross, W. J. G. de Blok, R. de Grijs, J. P. Emerson, C. J. Evans, B. Gibson, E. Gonzales-Solares, M. A. T. Groenewegen, M. Irwin, V. D. Ivanov, J. Lewis, M. Marconi, J. B. Marquette, C. Mastropietro, B. Moore, R. Napiwotzki, T. Naylor, J. M. Oliveira, M. Read, E. Sutorius, J. T. van Loon, M. I. Wilkinson, and P. R. Wood. The VMC survey. I. Strategy and first data. , 527:A116, Mar. 2011. doi: 10.1051/0004-6361/201016137.

M. J. Coe and J. Kirk. Catalogue of Be/X-ray binary systems in the Small Magellanic Cloud: X-ray, optical and IR properties. , 452(1):969–977, Sept. 2015. doi: 10.1093/mnras/stv1283.

M. J. Coe, W. R. T. Edge, J. L. Galache, and V. A. McBride. Optical properties of Small Magellanic Cloud X-ray binaries. , 356(2):502–514, Jan. 2005. doi: 10.1111/j.1365-2966.2004.08467.x.

A. A. Cole, E. D. Skillman, E. Tolstoy, I. Gallagher, John S., A. Aparicio, A. E. Dolphin, C. Gallart, S. L. Hidalgo, A. Saha, and P. B. Stetson. Leo A: A Late-blooming Survivor of the Epoch of Reionization in the Local Group. , 659(1):L17–L20, Apr 2007. doi: 10.1086/516711.

A. A. Cole, D. R. Weisz, A. E. Dolphin, E. D. Skillman, A. W. McConnachie, A. M. Brooks, and R. Leaman. Delayed Star Formation in Isolated Dwarf galaxies: Hubble Space Telescope Star Formation History of the Aquarius Dwarf Irregular. , 795(1):54, Nov 2014. doi: 10.1088/0004-637X/795/1/54.

B. C. Conn, R. R. Lane, G. F. Lewis, M. J. Irwin, R. A. Ibata, N. F. Martin, M. Bellazzini, and A. V. Tuntsov. The Anglo-Australian Telescope/Wide Field Imager survey of the Monoceros Ring and Canis Major dwarf galaxy - II. From l = (280-025). , 390(4):1388–1398, Nov. 2008. doi: 10.1111/j.1365-2966.2008.13847.x.

T. Connor, E. Bañados, C. Mazzucchelli, D. Stern, R. Decarli, X. Fan, E. P. Farina, E. Lusso, M. Neeleman, and F. Walter. X-Ray Observations of a [C II]-bright, z = 6.59 Quasar/Companion System. , 900(2):189, Sept. 2020. doi: 10.3847/1538-4357/abaab9.

T. W. Connors, D. Kawata, and B. K. Gibson. N-body simulations of the Magellanic stream. , 371(1):108–120, Sept. 2006. doi: 10.1111/j.1365-2966.2006.10659.x.

P. A. Crowther. Physical Properties of Wolf-Rayet Stars. , 45(1):177–219, Sept. 2007. doi: 10.1146/annurev.astro.45.051806.110615.

G. S. Da Costa and D. Hatzidimitriou. Ca II Triplet Spectroscopy of Giants in Small Magellanic Cloud Star Clusters: Abundances, Velocities, and the Age-Metallicity Relation. , 115:1934–1945, May 1998. doi: 10.1086/300340.

R. de Grijs and G. Bono. Clustering of Local Group Distances: Publication Bias or Correlated Measurements? III. The Small Magellanic Cloud. , 149(6):179, June 2015. doi: 10.1088/0004-6256/149/6/179.

M. De Leo, R. Carrera, N. E. D. Noël, J. I. Read, D. Erkal, and C. Gallart. Revealing the tidal scars of the Small Magellanic Cloud. , 495(1):98–113, Apr. 2020. doi: 10.1093/mnras/staa1122.

S. Deb, K. Kurbah, H. P. Singh, S. M. Kanbur, C.-C. Ngeow, B. J. Medhi, and S. Kumar. Morphology of the Small Magellanic Cloud using multiwavelength photometry of classical Cepheids. , 489(3):3725–3738, Nov. 2019. doi: 10.1093/mnras/stz2328.

B. Dias, L. O. Kerber, B. Barbuy, B. Santiago, S. Ortolani, and E. Balbinot. Self-consistent physical parameters for five intermediate-age SMC stellar clusters from CMD modelling. , 561: A106, Jan. 2014. doi: 10.1051/0004-6361/201322092.

B. Dias, L. Kerber, B. Barbuy, E. Bica, and S. Ortolani. SMC west halo: a slice of the galaxy that is being tidally stripped?. Star clusters trace age and metallicity gradients. , 591:A11, June 2016. doi: 10.1051/0004-6361/201527558.

J. D. Diaz and K. Bekki. The Tidal Origin of the Magellanic Stream and the Possibility of a Stellar Counterpart. , 750(1):36, May 2012. doi: 10.1088/0004-637X/750/1/36.

P. D. Dobbie, A. A. Cole, A. Subramaniam, and S. Keller. Red giants in the Small Magellanic Cloud - I. Disc and tidal stream kinematics. , 442(2):1663–1679, Aug. 2014. doi: 10.1093/mnras/stu910.

R. C. Dohm-Palmer, E. D. Skillman, A. Saha, E. Tolstoy, M. Mateo, J. Gallagher, J. Hoessel, C. Chiosi, and R. J. Dufour. The Dwarf Irregular Galaxy Sextans A. II. Recent Star Formation History. , 114:2527, Dec. 1997. doi: 10.1086/118665.

E. D'Onghia and A. J. Fox. The Magellanic Stream: Circumnavigating the Galaxy. , 54:363–400, Sept. 2016. doi: 10.1146/annurev-astro-081915-023251.

A. Dotter. MESA Isochrones and Stellar Tracks (MIST) 0: Methods for the Construction of Stellar Isochrones. , 222:8, Jan. 2016. doi: 10.3847/0067-0049/222/1/8.

A. Dotter, B. Chaboyer, D. Jevremović, V. Kostov, E. Baron, and J. W. Ferguson. The Dartmouth Stellar Evolution Database. , 178:89–101, Sept. 2008. doi: 10.1086/589654.

L. M. Dray. On the metallicity dependence of high-mass X-ray binaries. , 370(4):2079–2090, Aug. 2006. doi: 10.1111/j.1365-2966.2006.10635.x.

P. Drazinos, E. Kontizas, A. Karampelas, M. Kontizas, and A. Dapergolas. Star forming regions in a sample of HST spiral galaxies. , 553:A87, May 2013. doi: 10.1051/0004-6361/201220648.

A. Dressler, B. Bigelow, T. Hare, B. Sutin, I. Thompson, G. Burley, H. Epps, A. Oemler, Jr., A. Bagish, C. Birk, K. Clardy, S. Gunnels, D. Kelson, S. Shectman, and D. Osip. IMACS: The Inamori-Magellan Areal Camera and Spectrograph on Magellan-Baade. , 123:288, Mar. 2011. doi: 10.1086/658908.

P. Esposito, G. L. Israel, D. Milisavljevic, M. Mapelli, L. Zampieri, L. Sidoli, G. Fabbiano, and G. A. Rodríguez Castillo. Periodic signals from the Circinus region: two new cataclysmic variables and the ultraluminous X-ray source candidate GC X-1. , 452(2):1112–1127, Sept. 2015. doi: 10.1093/mnras/stv1379.

C. J. Evans and I. D. Howarth. Kinematics of massive stars in the Small Magellanic Cloud. , 386(2):826–834, May 2008. doi: 10.1111/j.1365-2966.2008.13012.x.

T. Fragos, B. Lehmer, M. Tremmel, P. Tzanavaris, A. Basu-Zych, K. Belczynski, A. Hornschemeier, L. Jenkins, V. Kalogera, A. Ptak, and A. Zezas. X-Ray Binary Evolution Across Cosmic Time. , 764(1):41, Feb. 2013. doi: 10.1088/0004-637X/764/1/41.

Gaia Collaboration, T. Prusti, J. H. J. de Bruijne, A. G. A. Brown, A. Vallenari, C. Babusiaux, C. A. L. Bailer-Jones, U. Bastian, M. Biermann, D. W. Evans, L. Eyer, F. Jansen, C. Jordi, S. A. Klioner, U. Lammers, and e. a. Lindegren. The Gaia mission. , 595:A1, Nov. 2016. doi: 10.1051/0004-6361/201629272.

Gaia Collaboration, A. G. A. Brown, A. Vallenari, T. Prusti, J. H. J. de Bruijne, C. Babusiaux, C. A. L. Bailer-Jones, M. Biermann, D. W. Evans, L. Eyer, F. Jansen, and e. a. Jordi. Gaia Data Release 2. Summary of the contents and survey properties. , 616:A1, Aug. 2018a. doi: 10.1051/0004-6361/201833051.

Gaia Collaboration, A. Helmi, F. van Leeuwen, P. J. McMillan, D. Massari, and e. a. Antoja. Gaia Data Release 2. Kinematics of globular clusters and dwarf galaxies around the Milky Way. , 616:A12, Aug. 2018b. doi: 10.1051/0004-6361/201832698.

L. T. Gardiner and D. Hatzidimitriou. Stellar populations and large-scale structure of the Small Magellanic Cloud. IV. Age distribution studies of the outer regions. , 257:195–224, July 1992. doi: 10.1093/mnras/257.2.195.

G. Gilmore and M. S. Roberts. The stellar luminosity function and its derivative the initial mass function : are they universal ? *Comments on Astrophysics*, 12:123–129, Jan. 1988.

L. Girardi, P. Goudfrooij, J. S. Kalirai, L. Kerber, V. Kozhurina-Platais, S. Rubele, A. Bressan, R. Chandar, P. Marigo, I. Platais, and T. H. Puzia. An extended main-sequence turn-off in the Small Magellanic Cloud star cluster NGC 411. , 431(4):3501–3509, June 2013. doi: 10.1093/mnras/stt433.

K. Glatt, E. K. Grebel, E. Sabbi, I. Gallagher, John S., A. Nota, M. Sirianni, G. Clementini, M. Tosi, D. Harbeck, A. Koch, A. Kayser, and G. Da Costa. Age Determination of Six Intermediate-Age Small Magellanic Cloud Star Clusters with HST/ACS. , 136(4):1703–1727, Oct. 2008. doi: 10.1088/0004-6256/136/4/1703.

K. Glatt, E. K. Grebel, and A. Koch. Ages and luminosities of young SMC/LMC star clusters and the recent star formation history of the Clouds. , 517:A50, July 2010. doi: 10.1051/0004-6361/201014187.

F. Haberl and R. Sturm. High-mass X-ray binaries in the Small Magellanic Cloud. , 586:A81, Feb. 2016. doi: 10.1051/0004-6361/201527326.

F. Haberl, M. D. Filipović, W. Pietsch, and P. Kahabka. A ROSAT PSPC catalogue of X-ray sources in the SMC region. , 142:41–57, Feb. 2000. doi: 10.1051/aas:2000136.

F. Haberl, R. Sturm, J. Ballet, D. J. Bomans, D. A. H. Buckley, M. J. Coe, R. Corbet, M. Ehle, M. D. Filipovic, M. Gilfanov, D. Hatzidimitriou, N. La Palombara, S. Mereghetti, W. Pietsch, S. Snowden, and A. Tiengo. The XMM-Newton survey of the Small Magellanic Cloud. , 545: A128, Sept. 2012. doi: 10.1051/0004-6361/201219758.

W. R. Hamann, G. Gräfener, and A. Liermann. The Galactic WN stars. Spectral analyses with line-blanketed model atmospheres versus stellar evolution models with and without rotation. , 457(3):1015–1031, Oct. 2006. doi: 10.1051/0004-6361:20065052.

F. Hammer, Y. B. Yang, H. Flores, M. Puech, and S. Fouquet. The Magellanic Stream System. I. Ram-Pressure Tails and the Relics of the Collision Between the Magellanic Clouds. , 813(2): 110, Nov. 2015. doi: 10.1088/0004-637X/813/2/110.

J. Harris and D. Zaritsky. The Star Formation History of the Small Magellanic Cloud. , 127(3): 1531–1544, Mar 2004. doi: 10.1086/381953.

R. Haschke, E. K. Grebel, and S. Duffau. New Optical Reddening Maps of the Large and Small Magellanic Clouds. , 141:158, May 2011. doi: 10.1088/0004-6256/141/5/158.

D. Hatzidimitriou and M. R. S. Hawkins. Stellar populations and large-scale structure of the SMC - II. Geometry of the north-eastern and south-western outlying regions. , 241:667–690, Dec. 1989. doi: 10.1093/mnras/241.4.667.

D. Hatzidimitriou, R. D. Cannon, and M. R. S. Hawkins. Kinematics in the outer parts of the SMC. , 261:873–882, Apr. 1993. doi: 10.1093/mnras/261.4.873.

R. W. Hilditch, I. D. Howarth, and T. J. Harries. Forty eclipsing binaries in the Small Magellanic Cloud: fundamental parameters and Cloud distance. , 357(1):304–324, Feb. 2005. doi: 10.1111/j.1365-2966.2005.08653.x.

P. Hodge. Clusters of the Small Magellanic Cloud. I. A catalog of 213 new clusters. , 98: 1113–1122, Nov. 1986. doi: 10.1086/131907.

P. W. Hodge and F. W. Wright. Catalog of 86 new star clusters in the Small Magellanic Cloud. , 79:858–859, Aug. 1974. doi: 10.1086/111619.

M. Hou, Z. Li, and X. Liu. A Chandra X-Ray Survey of Optically Selected AGN Pairs. , 900(1): 79, Sept. 2020. doi: 10.3847/1538-4357/aba4a7.

L. Inno, N. Matsunaga, G. Bono, F. Caputo, R. Buonanno, K. Genovali, C. D. Laney, M. Marconi, A. M. Piersimoni, F. Primas, and M. Romaniello. On the Distance of the Magellanic Clouds Using Cepheid NIR and Optical-NIR Period-Wesenheit Relations. , 764(1):84, Feb. 2013. doi: 10.1088/0004-637X/764/1/84.

A. M. Jacyszyn-Dobrzeniecka, D. M. Skowron, P. Mróz, J. Skowron, I. Soszyński, A. Udalski, P. Pietrukowicz, S. Kozłowski, Ł. Wyrzykowski, R. Poleski, M. Pawlak, M. K. Szymański, and K. Ulaczyk. OGLE-ing the Magellanic System: Three-Dimensional Structure of the Clouds and the Bridge Using Classical Cepheids. , 66(2):149–196, June 2016.

N. Kallivayalil, R. P. van der Marel, and C. Alcock. Is the SMC Bound to the LMC? The Hubble Space Telescope Proper Motion of the SMC. , 652(2):1213–1229, Dec. 2006a. doi: 10.1086/508014.

N. Kallivayalil, R. P. van der Marel, C. Alcock, T. Axelrod, K. H. Cook, A. J. Drake, and M. Geha. The Proper Motion of the Large Magellanic Cloud Using HST. , 638(2):772–785, Feb. 2006b. doi: 10.1086/498972.

N. Kallivayalil, R. P. van der Marel, G. Besla, J. Anderson, and C. Alcock. Third-epoch Magellanic Cloud Proper Motions. I. Hubble Space Telescope/WFC3 Data and Orbit Implications. , 764(2):161, Feb. 2013. doi: 10.1088/0004-637X/764/2/161.

E. Kapakos and D. Hatzidimitriou. RR Lyrae variables in the Small Magellanic Cloud - II. The extended area: chemical and structural analysis. , 426:2063–2077, Nov. 2012. doi: 10.1111/j.1365-2966.2012.21834.x.

A. Kayser, E. K. Grebel, D. R. Harbeck, A. A. Cole, A. Koch, K. Glatt, J. S. Gallagher, and G. S. Da Costa. A spectroscopy-based Age-Metallicity Relation of the SMC. In A. Vazdekis and R. Peletier, editors, *Stellar Populations as Building Blocks of Galaxies*, volume 241 of *IAU Symposium*, pages 351–352, Aug. 2007. doi: 10.1017/S1743921307008411.

I. King. The structure of star clusters. I. an empirical density law. , 67:471, Oct. 1962. doi: 10.1086/108756.

M. Kontizas. Preliminary colour-magnitude diagrams of 20 star clusters and their adjoining fields in the Small Magellanic Cloud. , 40:151–189, May 1980.

P. Kroupa. On the variation of the initial mass function. , 322(2):231–246, Apr 2001. doi: 10.1046/j.1365-8711.2001.04022.x.

S. Laycock, R. H. D. Corbet, M. J. Coe, F. E. Marshall, C. Markwardt, and J. Lochner. Long-Term Behavior of X-Ray Pulsars in the Small Magellanic Cloud. , 161(1):96–117, Nov. 2005. doi: 10.1086/432884.

B. D. Lehmer, D. M. Alexander, F. E. Bauer, W. N. Brand t, A. D. Goulding, L. P. Jenkins, A. Ptak, and T. P. Roberts. A Chandra Perspective on Galaxy-wide X-ray Binary Emission and its Correlation with Star Formation Rate and Stellar Mass: New Results from Luminous Infrared Galaxies. , 724(1):559–571, Nov. 2010. doi: 10.1088/0004-637X/724/1/559.

S. Lianou and A. A. Cole. The star formation history of the Sculptor dwarf irregular galaxy. , 549:A47, Jan 2013. doi: 10.1051/0004-6361/201220193.

L. Lindegren, J. Hernández, A. Bombrun, S. Klioner, and e. a. Bastian. Gaia Data Release 2. The astrometric solution. , 616:A2, Aug. 2018. doi: 10.1051/0004-6361/201832727.

T. Linden, V. Kalogera, J. F. Sepinsky, A. Prestwich, A. Zezas, and J. S. Gallagher. The Effect of Starburst Metallicity on Bright X-ray Binary Formation Pathways. , 725(2):1984–1994, Dec. 2010. doi: 10.1088/0004-637X/725/2/1984.

Q. Z. Liu, J. van Paradijs, and E. P. J. van den Heuvel. High-mass X-ray binaries in the Magellanic Clouds. , 442(3):1135–1138, Nov. 2005. doi: 10.1051/0004-6361:20053718.

D. Mackey, S. Koposov, G. Da Costa, V. Belokurov, D. Erkal, and P. Kuzma. Substructures and Tidal Distortions in the Magellanic Stellar Periphery. , 858(2):L21, May 2018. doi: 10.3847/2041-8213/aac175.

F. F. S. Maia, A. E. Piatti, and J. F. C. Santos. Mass distribution and structural parameters of Small Magellanic Cloud star clusters. , 437(2):2005–2016, Jan. 2014. doi: 10.1093/mnras/stt2039.

L. Maraschi, A. Treves, and E. P. J. van den Heuvel. B-emission Stars and X-ray sources. , 259: 292, Jan. 1976. doi: 10.1038/259292a0.

P. Marigo, L. Girardi, A. Bressan, P. Rosenfield, B. Aringer, Y. Chen, M. Dussin, A. Nanni, G. Pastorelli, T. S. Rodrigues, M. Trabucchi, S. Bladh, J. Dalcanton, M. A. T. Groenewegen, J. Montalbán, and P. R. Wood. A New Generation of PARSEC-COLIBRI Stellar Isochrones Including the TP-AGB Phase. , 835:77, Jan. 2017. doi: 10.3847/1538-4357/835/1/77.

N. F. Martin, R. A. Ibata, B. C. Conn, G. F. Lewis, M. Bellazzini, M. J. Irwin, and A. W. McConnachie. Why the Canis Major overdensity is not due to the Warp: analysis of its radial profile and velocities. , 355(4):L33–L37, Dec. 2004. doi: 10.1111/j.1365-2966.2004.08521.x.

P. Massey. A UBVR CCD Survey of the Magellanic Clouds. , 141(1):81–122, July 2002. doi: 10.1086/338286.

D. S. Mathewson, M. N. Cleary, and J. D. Murray. The Magellanic Stream. , 190:291–296, June 1974. doi: 10.1086/152875.

D. S. Mathewson, V. L. Ford, and N. Visvanathan. The Structure of the Small Magellanic Cloud. , 301:664, Feb. 1986. doi: 10.1086/163932.

V. A. McBride, M. J. Coe, I. Negueruela, M. P. E. Schurch, and K. E. McGowan. Spectral distribution of Be/X-ray binaries in the Small Magellanic Cloud. , 388(3):1198–1204, Aug. 2008. doi: 10.1111/j.1365-2966.2008.13410.x.

N. M. McClure-Griffiths, D. J. Pisano, M. R. Calabretta, H. A. Ford, F. J. Lockman, L. Staveley-Smith, P. M. W. Kalberla, J. Bailin, L. Dedes, S. Janowiecki, B. K. Gibson, T. Murphy, H. Nakanishi, and K. Newton-McGee. Gass: The Parkes Galactic All-Sky Survey. I. Survey Description, Goals, and Initial Data Release. , 181(2):398–412, Apr. 2009. doi: 10.1088/0067-0049/181/2/398.

M. P. McCumber, D. R. Garnett, and R. J. Dufour. Stellar Populations in the Wing of the Small Magellanic Cloud from Hubble Space Telescope Photometry. , 130(3):1083–1096, Sep 2005. doi: 10.1086/432535.

R. X. McGee and L. M. Newton. HI in the Small Magellanic Cloud re-examined. *Proceedings of the Astronomical Society of Australia*, 4:189–195, Jan. 1981.

R. E. Mennickent, G. Pietrzyński, W. Gieren, and O. Szewczyk. On Be star candidates and possible blue pre-main sequence objects in the Small Magellanic Cloud. , 393:887–896, Oct. 2002. doi: 10.1051/0004-6361:20020916.

K. J. Mighell, A. Sarajedini, and R. S. French. WFPC2 Observations of Star Clusters in the Magellanic Clouds. II. The Oldest Star Clusters in the Small Magellanic Cloud. , 116(5): 2395–2414, Nov. 1998. doi: 10.1086/300591.

S. Mineo, M. Gilfanov, and R. Sunyaev. X-ray emission from star-forming galaxies - II. Hot interstellarmedium. , 426(3):1870–1883, Nov. 2012. doi: 10.1111/j.1365-2966.2012.21831.x.

M. Moe and R. Di Stefano. A New Class of Nascent Eclipsing Binaries with Extreme Mass Ratios. , 801(2):113, Mar. 2015. doi: 10.1088/0004-637X/801/2/113.

T. Muraveva, H. E. Delgado, G. Clementini, L. M. Sarro, and A. Garofalo. RR Lyrae stars as standard candles in the Gaia Data Release 2 Era. , 481(1):1195–1211, Nov. 2018. doi: 10.1093/mnras/sty2241.

C. E. Murray, J. E. G. Peek, E. M. Di Teodoro, N. M. McClure-Griffiths, J. M. Dickey, and H. Dénes. The 3D Kinematics of Gas in the Small Magellanic Cloud. , 887(2):267, Dec. 2019. doi: 10.3847/1538-4357/ab510f.

P. K. Nayak, A. Subramaniam, S. Choudhury, G. Indu, and R. Sagar. Star clusters in the Magellanic Clouds - I. Parametrization and classification of 1072 clusters in the LMC. , 463 (2):1446–1461, Dec. 2016. doi: 10.1093/mnras/stw2043.

P. K. Nayak, A. Subramaniam, S. Choudhury, and R. Sagar. Star clusters in the Magellanic Clouds. II. Age-dating, classification, and spatio-temporal distribution of the SMC clusters. , 616:A187, Sep 2018. doi: 10.1051/0004-6361/201732227.

J. R. Neeley, M. Marengo, W. L. Freedman, B. F. Madore, R. L. Beaton, D. Hatt, T. Hoyt, A. J. Monson, J. A. Rich, A. Sarajedini, M. Seibert, and V. Scowcroft. Standard Galactic field RR Lyrae II: a Gaia DR2 calibration of the period-Wesenheit-metallicity relation. , 490(3): 4254–4270, Dec. 2019. doi: 10.1093/mnras/stz2814.

D. L. Nidever, K. Olsen, A. R. Walker, A. K. Vivas, R. D. Blum, C. Kaleida, Y. Choi, B. C. Conn, R. A. Gruendl, E. F. Bell, G. Besla, R. R. Muñoz, C. Gallart, N. F. Martin, E. W. Olszewski, A. Saha, A. Monachesi, M. Monelli, T. J. L. de Boer, L. C. Johnson, D. Zaritsky, G. S. Stringfellow, R. P. van der Marel, M.-R. L. Cioni, S. Jin, S. R. Majewski, D. Martinez-Delgado, L. Monteagudo, N. E. D. Noël, E. J. Bernard, A. Kunder, Y.-H. Chu, C. P. M. Bell, F. Santana, J. Frechem, G. E. Medina, V. Parkash, J. C. Serón Navarrete, and C. Hayes. SMASH: Survey of the MAgellanic Stellar History. , 154(5):199, Nov. 2017. doi: 10.3847/1538-3881/aa8d1c.

D. L. Nidever, A. Dey, K. Olsen, S. Ridgway, R. Nikutta, S. Juneau, M. Fitzpatrick, A. Scott, and F. Valdes. First Data Release of the All-sky NOAO Source Catalog. , 156(3):131, Sept. 2018. doi: 10.3847/1538-3881/aad68f.

D. L. Nidever, K. Olsen, Y. Choi, T. J. L. de Boer, R. D. Blum, E. F. Bell, D. Zaritsky, N. F. Martin, A. Saha, B. C. Conn, G. Besla, R. P. van der Marel, N. E. D. Noël, A. Monachesi, G. S. Stringfellow, P. Massana, M.-R. L. Cioni, C. Gallart, M. Monelli, D. Martinez-Delgado, R. R. Muñoz, S. R. Majewski, A. K. Vivas, A. R. Walker, C. Kaleida, and Y.-H. Chu. Exploring the Very Extended Low-surface-brightness Stellar Populations of the Large Magellanic Cloud with SMASH. , 874(2):118, Apr. 2019. doi: 10.3847/1538-4357/aafaf7.

N. E. D. Noël, C. Gallart, E. Costa, and R. A. Méndez. Old Main-Sequence Turnoff Photometry in the Small Magellanic Cloud. I. Constraints on the Star Formation History in Different Fields. , 133(5):2037–2052, May 2007. doi: 10.1086/512668.

N. E. D. Noël, A. Aparicio, C. Gallart, S. L. Hidalgo, E. Costa, and R. A. Méndez. Old Main-Sequence Turnoff Photometry in the Small Magellanic Cloud. II. Star Formation History and its Spatial Gradients. , 705(2):1260–1274, Nov 2009. doi: 10.1088/0004-637X/705/2/1260.

B. E. J. Pagel and G. Tautvaisiene. Chemical evolution of the Magellanic Clouds: analytical models. , 299(2):535–544, Sept. 1998. doi: 10.1046/j.1365-8711.1998.01792.x.

M. C. Parisi, D. Geisler, G. Carraro, J. J. Clariá, E. Costa, A. J. Grocholski, A. Sarajedini, R. Leiton, and A. E. Piatti. Age Determination of 15 Old to Intermediate-age Small Magellanic Cloud Star Clusters. , 147(4):71, Apr. 2014. doi: 10.1088/0004-6256/147/4/71.

T. Park, V. L. Kashyap, A. Siemiginowska, D. A. van Dyk, A. Zezas, C. Heinke, and B. J. Wargelin. Bayesian Estimation of Hardness Ratios: Modeling and Computations. , 652(1): 610–628, Nov. 2006. doi: 10.1086/507406.

E. Patel, G. Besla, and S. T. Sohn. Orbits of massive satellite galaxies - I. A close look at the Large Magellanic Cloud and a new orbital history for M33. , 464(4):3825–3849, Feb. 2017. doi: 10.1093/mnras/stw2616.

A. E. Piatti. Towards a comprehensive picture of the star cluster age-metallicity relationship in the Small Magellanic Cloud. , 2011.

A. E. Piatti. The star field age-metallicity relationship of the Small Magellanic Cloud. , 2012a.

A. E. Piatti. Identification of a New Relatively Old Star Cluster in the Small Magellanic Cloud. , 2012b.

A. E. Piatti. Stellar Cluster Candidates Discovered in the Magellanic System. , 834(2):L14, Jan. 2017. doi: 10.3847/2041-8213/834/2/L14.

A. E. Piatti. Towards a comprehensive knowledge of the star cluster population in the Small Magellanic Cloud. , 478(1):784–790, July 2018. doi: 10.1093/mnras/sty1249.

A. E. Piatti and E. Bica. Washington photometry of candidate star clusters in the Small Magellanic Cloud. , 2012.

A. E. Piatti, J. F. C. Santos, J. J. Clariá, E. Bica, A. Sarajedini, and D. Geisler. Ages and metallicities of five intermediate-age star clusters projected towards the Small Magellanic Cloud. , 325(2):792–802, Aug. 2001. doi: 10.1046/j.1365-8711.2001.04503.x.

A. E. Piatti, A. Sarajedini, D. Geisler, J. Seguel, and D. Clark. Tracing the formation history of intermediate-age star clusters in the Small Magellanic Cloud. , 2005.

A. E. Piatti, A. Sarajedini, D. Geisler, D. Clark, and J. Seguel. Young star clusters immersed in intermediate-age fields in the Small Magellanic Cloud. , 2007.

A. E. Piatti, J. J. Clariá, E. Bica, D. Geisler, A. V. Ahumada, and L. Girardi. Washington photometry of 14 intermediate-age to old star clusters in the Small Magellanic Cloud. , 2011.

A. E. Piatti, V. D. Ivanov, S. Rubele, M. Marconi, V. Ripepi, M.-R. L. Cioni, J. M. Oliveira, and K. Bekki. The VMC Survey - XXI. New star cluster candidates discovered from infrared photometry in the Small Magellanic Cloud. , 460(1):383–395, July 2016. doi: 10.1093/mnras/stw1000.

G. Pietrzynski, A. Udalski, M. Kubiak, M. Szymanski, P. Wozniak, and K. Zebrun. Optical Gravitational Lensing Experiment. The Catalog of Clusters in the Small Magellanic Cloud. , 48:175–268, Apr. 1998.

N. Price-Jones and J. Bovy. Blind chemical tagging with DBSCAN: prospects for spectroscopic surveys. , 487(1):871–886, July 2019. doi: 10.1093/mnras/stz1260.

M. E. Putman, B. K. Gibson, L. Staveley-Smith, G. Banks, D. G. Barnes, R. Bhatal, M. J. Disney, R. D. Ekers, K. C. Freeman, R. F. Haynes, P. Henning, H. Jerjen, V. Kilborn, B. Koribalski, P. Knezek, D. F. Malin, J. R. Mould, T. Oosterloo, R. M. Price, S. D. Ryder, E. M. Sadler, I. Stewart, F. Stootman, R. A. Vaile, R. L. Webster, and A. E. Wright. Tidal disruption of the Magellanic Clouds by the Milky Way. , 394(6695):752–754, Aug. 1998. doi: 10.1038/29466.

S. Rezaeikh, A. Javadi, H. Khosroshahi, and J. T. van Loon. The star formation history of the Magellanic Clouds derived from long-period variable star counts. , 445(3):2214–2222, Dec 2014. doi: 10.1093/mnras/stu1807.

V. Ripepi, M. Marconi, M. I. Moretti, G. Clementini, M. R. L. Cioni, R. de Grijs, J. P. Emerson, M. A. T. Groenewegen, V. D. Ivanov, and A. E. Piatti. The VMC Survey. XIX. Classical Cepheids in the Small Magellanic Cloud. , 224(2):21, June 2016. doi: 10.3847/0067-0049/224/2/21.

V. Ripepi, M.-R. L. Cioni, M. I. Moretti, M. Marconi, K. Bekki, G. Clementini, R. de Grijs, J. Emerson, M. A. T. Groenewegen, V. D. Ivanov, R. Molinaro, T. Muraveva, J. M. Oliveira, A. E. Piatti, S. Subramanian, and J. T. van Loon. The VMC survey - XXV. The 3D structure of the Small Magellanic Cloud from Classical Cepheids. , 472(1):808–827, Nov. 2017. doi: 10.1093/mnras/stx2096.

S. Rubele, L. Girardi, L. Kerber, M.-R. L. Cioni, A. E. Piatti, S. Zaggia, K. Bekki, A. Bressan, G. Clementini, R. de Grijs, J. P. Emerson, M. A. T. Groenewegen, V. D. Ivanov, M. Marconi, P. Marigo, M.-I. Moretti, V. Ripepi, S. Subramanian, B. L. Tatton, and J. T. van Loon. The VMC survey - XIV. First results on the look-back time star formation rate tomography of the Small Magellanic Cloud. , 449(1):639–661, May 2015. doi: 10.1093/mnras/stv141.

S. Rubele, G. Pastorelli, L. Girardi, M.-R. L. Cioni, S. Zaggia, P. Marigo, K. Bekki, A. Bressan, G. Clementini, R. de Grijs, J. Emerson, M. A. T. Groenewegen, V. D. Ivanov, T. Muraveva, A. Nanni, J. M. Oliveira, V. Ripepi, N.-C. Sun, and J. T. van Loon. The VMC survey - XXXI: The spatially resolved star formation history of the main body of the Small Magellanic Cloud. , 478(4):5017–5036, Aug 2018. doi: 10.1093/mnras/sty1279.

E. Sabbi, J. S. Gallagher, M. Tosi, J. Anderson, A. Nota, E. K. Grebel, M. Cignoni, A. A. Cole, G. S. Da Costa, D. Harbeck, K. Glatt, and M. Marconi. Star Formation History of the Small Magellanic Cloud: Six Hubble Space Telescope/Advanced Camera for Survey Fields. , 703(1): 721–735, Sept. 2009. doi: 10.1088/0004-637X/703/1/721.

L. V. Sales, J. F. Navarro, N. Kallivayalil, and C. S. Frenk. Identifying true satellites of the Magellanic Clouds. , 465(2):1879–1888, Feb. 2017. doi: 10.1093/mnras/stw2816.

E. E. Salpeter. The Luminosity Function and Stellar Evolution. , 121:161, Jan. 1955. doi: 10.1086/145971.

M. Sasaki, F. Haberl, and W. Pietsch. ROSAT HRI catalogue of X-ray sources in the SMC region. , 147:75–91, Nov. 2000. doi: 10.1051/aas:2000290.

S. Schmeja. Identifying star clusters in a field: A comparison of different algorithms. *Astronomische Nachrichten*, 332(2):172, Feb. 2011. doi: 10.1002/asna.201011484.

E. Schreier, R. Levinson, H. Gursky, E. Kellogg, H. Tananbaum, and R. Giacconi. Evidence for the Binary Nature of Centaurus X-3 from UHURU X-Ray Observations. , 172:L79, Mar. 1972. doi: 10.1086/180896.

V. Scowcroft, W. L. Freedman, B. F. Madore, A. Monson, S. E. Persson, J. Rich, M. Seibert, and J. R. Rigby. The Carnegie Hubble Program: The Distance and Structure of the SMC as Revealed by Mid-infrared Observations of Cepheids. , 816(2):49, Jan 2016. doi: 10.3847/0004-637X/816/2/49.

F. D. Seward and P. A. Charles. *Exploring the X-Ray Universe*. 1995.

F. D. Seward and M. Mitchell. X-ray survey of the Small Magellanic Cloud. , 243:736–743, Feb. 1981. doi: 10.1086/158641.

H. Shapley and H. H. Wilson. The Magellanic Clouds, VI. Positions and Descriptions of 170 Nebulae in the Small Cloud. *Harvard College Observatory Circular*, 276:1–4, May 1925.

M. F. Skrutskie, R. M. Cutri, R. Stiening, M. D. Weinberg, S. Schneider, J. M. Carpenter, C. Beichman, R. Capps, T. Chester, J. Elias, J. Huchra, J. Liebert, C. Lonsdale, D. G. Monet, S. Price, P. Seitzer, T. Jarrett, J. D. Kirkpatrick, J. E. Gizis, E. Howard, T. Evans, J. Fowler, L. Fullmer, R. Hurt, R. Light, E. L. Kopan, K. A. Marsh, H. L. McCallon, R. Tam, S. Van Dyk, and S. Wheelock. The Two Micron All Sky Survey (2MASS). , 131(2):1163–1183, Feb. 2006. doi: 10.1086/498708.

I. Soszynski, A. Udalski, M. Szymanski, M. Kubiak, G. Pietrzynski, P. Wozniak, K. Zebrun, O. Szewczyk, and L. Wyrzykowski. The Optical Gravitational Lensing Experiment. Catalog of RRLyr Stars from the Small Magellanic Cloud. , 52:369–396, Dec. 2002.

L. Stanghellini, E. Villaver, R. A. Shaw, and M. Mutchler. Hubble Space Telescope Observations of Three Very Young Star Clusters in the Small Magellanic Cloud. , 598(2):1000–1004, Dec. 2003. doi: 10.1086/379121.

P. B. Stetson. DAOPHOT - A computer program for crowded-field stellar photometry. , 99: 191–222, Mar. 1987. doi: 10.1086/131977.

A. Strantzalis, D. Hatzidimitriou, A. Zezas, V. Antoniou, S. Lianou, and S. Tsilia. Discrete star formation events in the central bar of the Small Magellanic Cloud. , 489(4):5087–5097, Nov 2019. doi: 10.1093/mnras/stz2540.

R. Sturm, F. Haberl, W. Pietsch, J. Ballet, D. Hatzidimitriou, D. A. H. Buckley, M. Coe, M. Ehle, M. D. Filipović, N. La Palombara, and A. Tiengo. The XMM-Newton survey of the Small Magellanic Cloud: The X-ray point-source catalogue. , 558:A3, Oct. 2013. doi: 10.1051/0004-6361/201219935.

S. Subramanian and A. Subramaniam. Depth estimation of the Large and Small Magellanic Clouds. , 496(2):399–412, Mar. 2009. doi: 10.1051/0004-6361/200811029.

S. Subramanian and A. Subramaniam. The Three-dimensional Structure of the Small Magellanic Cloud. , 744(2):128, Jan. 2012. doi: 10.1088/0004-637X/744/2/128.

S. Subramanian and A. Subramaniam. Disk of the Small Magellanic Cloud as traced by Cepheids. , 573:A135, Jan. 2015. doi: 10.1051/0004-6361/201424248.

T. Tepper-García, J. Bland-Hawthorn, M. S. Pawlowski, and T. K. Fritz. The Magellanic System: the puzzle of the leading gas stream. , 488(1):918–938, Sept. 2019. doi: 10.1093/mnras/stz1659.

L. J. Townsend, M. J. Coe, R. H. D. Corbet, and A. B. Hill. On the orbital parameters of Be/X-ray binaries in the Small Magellanic Cloud. , 416(2):1556–1565, Sept. 2011. doi: 10.1111/j.1365-2966.2011.19153.x.

A. Udalski, M. K. Szymanski, I. Soszynski, and R. Poleski. The Optical Gravitational Lensing Experiment. Final Reductions of the OGLE-III Data. , 58:69–87, June 2008.

E. P. J. van den Heuvel. High-Mass X-ray Binaries: progenitors of double compact objects. *IAU Symposium*, 346:1–13, Dec. 2019. doi: 10.1017/S1743921319001315.

R. P. van der Marel and N. Kallivayalil. Third-epoch Magellanic Cloud Proper Motions. II. The Large Magellanic Cloud Rotation Field in Three Dimensions. , 781(2):121, Feb. 2014. doi: 10.1088/0004-637X/781/2/121.

R. P. van der Marel and J. Sahlmann. First Gaia Local Group Dynamics: Magellanic Clouds Proper Motion and Rotation. , 832(2):L23, Dec. 2016. doi: 10.3847/2041-8205/832/2/L23.

Q. Wang and X. Wu. A Comprehensive X-Ray Study of the Small Magellanic Cloud. , 78:391, Feb. 1992. doi: 10.1086/191632.

B. L. Webster and P. Murdin. Cygnus X-1-a Spectroscopic Binary with a Heavy Companion ? , 235(5332):37–38, Jan. 1972. doi: 10.1038/235037a0.

D. R. Weisz, A. E. Dolphin, E. D. Skillman, J. Holtzman, J. J. Dalcanton, A. A. Cole, and K. Neary. Comparing the ancient star formation histories of the Magellanic Clouds. , 431(1): 364–371, May 2013. doi: 10.1093/mnras/stt165.

P. Yanchulova Merica-Jones, K. M. Sandstrom, L. C. Johnson, J. Dalcanton, A. E. Dolphin, K. Gordon, J. Roman-Duval, D. R. Weisz, and B. F. Williams. The Small Magellanic Cloud Investigation of Dust and Gas Evolution (SMIDGE): The Dust Extinction Curve from Red Clump Stars. , 847(2):102, Oct 2017. doi: 10.3847/1538-4357/aa8a67.

J. Yokogawa, K. Imanishi, M. Tsujimoto, K. Koyama, and M. Nishiuchi. Review of Discrete X-Ray Sources in the Small Magellanic Cloud: Summary of the ASCA Results and Implication on the Recent Star-Forming Activity. , 55:161–189, Feb. 2003. doi: 10.1093/pasj/55.1.161.

E. Zari, A. G. A. Brown, and P. T. de Zeeuw. Structure, kinematics, and ages of the young stellar populations in the Orion region. , 628:A123, Aug. 2019. doi: 10.1051/0004-6361/201935781.

D. Zaritsky, J. Harris, and I. Thompson. A digital photometric survey of the magellanic clouds: First results from one million stars. , 114:1002–1013, Sept. 1997. doi: 10.1086/118531.

D. Zaritsky, J. Harris, I. B. Thompson, E. K. Grebel, and P. Massey. The Magellanic Clouds Photometric Survey: The Small Magellanic Cloud Stellar Catalog and Extinction Map. , 123: 855–872, Feb. 2002. doi: 10.1086/338437.

P. Zivick, N. Kallivayalil, G. Besla, S. T. Sohn, R. P. van der Marel, A. del Pino, S. T. Linden, T. K. Fritz, and J. Anderson. The Proper-motion Field along the Magellanic Bridge: A New Probe of the LMC-SMC Interaction. , 874(1):78, Mar. 2019. doi: 10.3847/1538-4357/ab0554.